

Mineralogie

Generation of basalt and the effect of carbon-bearing fluids on partial melting of peridotite and eclogite - from trace elements in olivine to petrological experiments

A thesis submitted for the degree of Doctor of Philosophy of Muenster University and Macquarie University

Inaugural-Dissertation
zur Erlangung des Doktorgrades der Naturwissenschaften
im Fachbereich Geowissenschaften
der Mathematisch-Naturwissenschaftlichen Fakultät
der Westfälischen Wilhelms-Universität Münster

vorgelegt von/presented by
Zairong Liu, MSc
aus/from Rizhao, China
Institut für Mineralogie, Universität Münster
Department of Earth and Environmental Sciences, Macquarie University

29th *March 2020*

Dekanin/Dekan: Prof. Harald Straus

Erstgutachter/-in: Prof. Stephan Klemme

Zweitgutachter/-in: Prof. Stephen Foley

Tag der mündlichen Prüfung: 18.06.2020

Tag der Promotion: 18.06.2020

Always be a beginner.

--Shunryū Suzuki

Statement of Originality

This thesis is being submitted to Macquarie University and Münster University in accordance with the Cotutelle agreement (24th March 2017).

To the best of my knowledge and belief, the thesis contains no material previously published or written by another person except where due reference is made in the thesis itself.

29th March 2020

Table of content

Summary	v
Zusammenfassung.....	vii
Acknowledgements/Danksagungen.....	ix
Chapter 1 Introduction.....	1
1 Objectives of the thesis	1
2 Outline of the thesis	4
Chapter 2 Identification of the source assemblages of basaltic rocks in southeastern Australia using trace elements in olivine	5
1 Introduction	7
1.1 Eastern Australian Mesozoic-Cenozoic volcanism	7
1.2 The use of trace elements in olivine for identifying source assemblages	9
2 Geological background	11
2.1 Sample area: orogenic history and lithosphere thickness.....	11
2.2 Previous work on basalts from the sampled localities	12
3 Analytical methods	16
3.1 Whole-rock analysis	16
3.2 Element concentrations in olivines	17
3.2.1 SEM:.....	17
3.2.2 EPMA:	17
3.2.3 ICP-MS:.....	18
4 Results.....	19
4.1. Petrography	19
4.2 Whole-rock analysis.....	21
4.2.1 Major elements	21
4.2.2 Trace elements.....	27

4.3 Analysis of olivine compositions.....	29
4.3.1 Characteristics and correlation of major elements in whole-rocks and olivines.....	29
4.3.2 Characteristics of minor and trace elements (EPMA data).....	30
5 Discussion	36
5.1. Distinguishing olivine xenocrysts and phenocrysts.....	36
5.2. Characterisation of the mantle source	38
5.2.1. Xenocrysts characterize the peridotite facies.....	38
5.2.2. Source determination based on olivine phenocrysts: Pyroxenite or peridotite?	39
5.2.3. Other parameters for identifying pyroxenite in the source	44
5.2.4. Possible influence of continental crustal material based on phenocrysts.....	46
5.2.5. Indicators and identification of metasomatism in the source	49
5.2.6. Redox conditions.....	54
6 Magmatic processes in the sources of New South Wales Cenozoic basaltic rocks	56
6.1. Mineralogy of the source assemblages	56
6.2. The possible role of a mantle plume based on whole-rock and olivine phenocryst analysis	56
6.3. Magmatic processes leading to metasomatism of the lithosphere.....	58
7 Conclusions	60
8 Appendix.....	62
Chapter 3 The effect of C-O-H fluids on partial melting of eclogite and lherzolite under moderately oxidizing and reducing conditions	75
1 Introduction	77
2 Methods.....	79
2.1 Starting materials.....	79
2.2 Experimental and analytical methods	80
2.3 Equilibrium and preliminary results.....	83
2.3.1 Attainment of equilibrium	84

2.3.2 Oxygen fugacity:	85
2.3.3 Iron loss:.....	86
2.4 Mass balance calculation:.....	87
2.4.1 Mass balance-modal calculation:	87
2.4.2 Graphic mass balance:	88
3 Results and discussion	89
3.1 C-bearing phases in experiments:	89
3.2 Peridotite melting experiments.....	90
3.2.1 Solidi of the mantle lherzolite with C-O-H fluids at different redox conditions:	90
3.2.2 Major compositions of all phases in the experiments:.....	91
3.2.3 Compositions of melts at different redox condition:.....	96
3.3 Eclogite melting experiments	107
3.3.1 Solidi of eclogite with C-O-H fluids at high pressures and temperatures:.....	107
3.3.2 Major element compositions of minerals and melts:.....	108
3.3.3 Melting reactions of the partial melting of eclogite experiments:.....	114
3.3.4 Melt compositions of partial melting experiments of eclogite	115
4 Implications:	118
4.1 Reducing fluids in the Earth's mantle	118
4.2 Mantle melting and water recycling under reducing conditions in the Archaean	118
4.3 Melting in the deep reducing mantle?	120
4.4 Melting under reducing conditions on other terrestrial planets.....	120
5 Conclusions.....	121
6 Appendix-Calculation of fO_2 :	122
Chapter 4 Summary and Conclusions	125
Chapter 5 References.....	129
Curriculum vitae	147

Summary

Primitive basalts are the main rock samples to probe mantle heterogeneity and understand the process of partial melting of the mantle. In comparison to the well-known Mid-Ocean Ridge Basalts and Ocean Island Basalts, the generation of intra-plate continent basalts is still controversial. In this study, I followed two approaches to understand the genesis of these basalts: (i) a study of intra-plate basalts from southeastern Australia, through trace element analyses of olivine in combination with whole-rock compositions, (ii) an experimental study focused on the effect of fluid compositions under different oxygen fugacity conditions on the partial melting of lherzolite and eclogite.

For the study of natural samples, I collected Cenozoic primitive basalts from various locations in New South Wales, Australia. Two locations (Dubbo and Bingara/Inverell (Central)) are close to a major step in thickness of the lithosphere, while two other localities lie close to small areas of anomalously thicker lithosphere (Ebor and Barrington). In addition, I used samples from Buckland in Queensland as a complement which lies in another province but also close to this lithosphere edge.

Based on a correlation between Mn/Fe and Ni/Mg ratios and concentrations of Ni, Ca, Ti, Zn and Li in olivine, and whole rock compositions, tholeiite from Dubbo was found to originate from a plume-type pyroxenite source which had experienced a low degree of carbonatitic metasomatism. Similarly, the alkali basalt from Dubbo and Ebor also comes from a pyroxenite-associated source. Basanite from Bingara/Inverell (Central) has experienced the highest degree of carbonatitic metasomatism in the source and the basanite from Barrington comes from a source formed by metasomatism of peridotite reacted with carbonate melt. Alkali basalt and basanite from Buckland have a similar source to Barrington.

Partial melting experiments were conducted on eclogite and lherzolite at conditions of 2 GPa and 6 GPa, 900–1500 °C. Starting compositions contained 5 wt.% H₂O for oxidizing conditions and 5 wt.% H₂O and CH₄ for reducing conditions. Based on the mineral and melt phases and solidus temperature obtained from the experiments, it turns out that under reducing conditions, both the solidi of eclogite and lherzolite with C-O-H fluids are subparallel to the anhydrous solidi and higher than those under oxidizing conditions. The mineralogy of eclogite and lherzolite residues depends on fO₂. At 2 GPa partial melting of lherzolite with 5% H₂O forms a basaltic melt while partial melting of lherzolite with 5% C-O-H fluids forms a basaltic andesite melt. In contrast, the melt from partial

melting of eclogite with 5% H₂O varies from basalt, through basaltic andesite to andesite with increasing temperature.

The generation depth of Cenozoic basalts from Southeastern Australia is close to the conditions of my experiments. The experiments showed that at this pressure and temperature range, hydrous metasomatism of eclogite does not lead to the formation of intra-plate basalts, whereas it is possible to form intra-plate basalts by partial melting of hydrated (> 1,000 ppm H₂O) peridotite. The Cenozoic basalts from Southeastern Australia were not formed through this latter mechanism, but were generated by partial melting of a pyroxenitic or plume-associated pyroxenitic source metasomatized by carbonatitic melts.

Zusammenfassung

Primitive Basalte sind die Gesteinsproben, die hauptsächlich verwendet werden, um die Heterogenität des Mantels zu untersuchen und den Prozess des partiellen Schmelzens des Mantels zu verstehen. Im Vergleich zu den bekannten Mittelozeanischen-Rücken-Basalten und Ozean-Insel-Basalten ist die Genese von kontinentalen Intra-Platten-Basalten immer noch umstritten. In dieser Arbeit verfolgte ich zwei Ansätze, um die Entstehung dieser Basalte zu verstehen: (i) eine Untersuchung von Intra-Platten-Basalten aus Südostaustralien durch Spurenelementanalysen von Olivin in Kombination mit Gesamtgesteinszusammensetzungen, (ii) eine experimentelle Studie, die sich auf die Wirkung von Fluidzusammensetzungen bei verschiedenen Sauerstoff fugazitäten auf das partielle Schmelzen von Lherzolit und Eklogit fokussiert.

Für die Untersuchung natürlicher Proben sammelte ich känozoische primitive Basalte an verschiedenen Orten in New South Wales, Australien. Zwei Standorte (Dubbo und Bingara/Inverell (Central)) befinden sich in der Nähe eines sprunghaften Anstiegs in der Dicke der Lithosphäre, während zwei andere Orte in der Nähe kleiner Gebiete mit anomal dickerer Lithosphäre liegen (Ebor und Barrington). Außerdem habe ich Proben aus Buckland in Queensland als Ergänzung verwendet, die in einem anderen Bundesstaat, aber auch in der Nähe dieses Randes der Lithosphäre liegt.

Basierend auf einer Korrelation zwischen Mn/Fe- und Ni/Mg-Verhältnissen und Konzentrationen von Ni, Ca, Ti, Zn und Li in Olivin und Gesamtgesteinszusammensetzungen habe ich herausgefunden, dass Tholeiit aus Dubbo aus einer Pyroxenitquelle vom Plume-Typ stammt, die einen geringen Grad an karbonatitischen Metasomatismus erfahren hatte. Alkalibasalt aus Dubbo und Ebor stammt ebenfalls aus einer Pyroxenit-assoziierten Quelle. Basanit aus Bingara/Inverell (Central) hat den höchsten Grad an karbonatitischen Metasomatismus in der Quelle erfahren. Basanit aus Barrington stammt aus einer Quelle, die durch Metasomatose von Peridotit gebildet wurde, der mit einer Karbonatschmelze reagiert ist. Alkalibasalt und Basanit aus Buckland stammen aus einer ähnlichen Quelle wie Barrington.

Partielle Schmelzexperimente wurden an Eklogit und Lherzolith bei Bedingungen von 2 GPa und 6 GPa bei 900 – 1500 °C durchgeführt. Die Ausgangszusammensetzungen enthielten 5 Gew.-% H₂O für oxidierende Bedingungen bzw. 5 Gew.-% H₂O und CH₄ für reduzierende Bedingungen. Basierend auf den Mineral- und Schmelzphasen sowie der Solidustemperatur, die aus den Experimenten erhalten wurden, stellt sich heraus, dass unter reduzierenden Bedingungen sowohl die Solidi von Eklogit als auch Lherzolit mit C-O-H-Fluiden subparallel zu den wasserfreien Solidi sind und höher

sind als diejenigen unter oxidierenden Bedingungen. Die Mineralogie von Eklogit- und Lherzolithresiuduen hängt von der Sauerstofffugazität ab. Bei 2 GPa bildet das partielle Schmelzen von Lherzolit mit 5% H₂O eine Basaltschmelze, während das teilweise Schmelzen von Lherzolit mit 5% C-O-H-Fluiden eine basaltische Andesitschmelze bildet. Im Gegensatz dazu variiert die Schmelze beim partiellen Schmelzen von Eklogit mit 5% H₂O mit zunehmender Temperatur von Basalt über Basaltandesit bis Andesit.

Die Tiefe, aus der die känozoischen Basalte aus Südostaustralien stammen, liegt nahe an den Bedingungen meiner Experimente. Die Experimente zeigten, dass in diesem Druck- und Temperaturbereich die Metasomatose von Eklogit nicht zur Bildung von Intra-Platten-Basalten führt, wohingegen es möglich ist, Intra-Platten-Basalte durch partielles Schmelzen von hydratisiertem (> 1.000 ppm H₂O) Peridotit zu bilden. Die känozoischen Basalte aus Südostaustralien wurden nicht durch diesen letzteren Mechanismus gebildet, sondern durch partielles Schmelzen einer pyroxenitischen oder Plume-assoziierten pyroxenitischen Quelle erzeugt, die durch karbonatitische Schmelzen überprägt wurde.

Acknowledgements/Danksagungen

First of all, I'd like to thank all my supervisors Stephen Foley, Stephan Klemme, Arno Rohrbach for giving me the chance to do a PhD with them and the supporting all the time! Thank you, Steve and Stephan, for the motivation, for your encouragement, for all kind of support all the time and being so kind and tolerant for me, and I appreciate a lot that you made it possible for me to study in two universities in different countries; it changed my life in a good way. I have learned a lot. One-year study in Australia motivated me a lot, and that time was so amazing! Thank you very much, Arno, for all the discussions, encouragement, and support, without those supporting I couldn't have managed the thesis.

I'd like to thank Yannick Bussweiler and Suzette Timmerman for the discussions, suggestions and corrections for my manuscript, and spiritual support! Thanks a lot Tobias Grützner and Fernanda for teaching me doing experiment when I started my PhD. I'd like to thank John Adam, Chunfei Chen, Josh Shea, Michael Förster, Michael Willig, Ilya Fomin, Xiong Wang, Fernanda Gervasoni for lots of discussion about my projects. I'd like to thank Dorrit Jacob, Yi Ren, Tracy Rushmer, Elena Belousova for the support and help with the Cotutelle program and my study!

I'm so grateful for the help from Jasper Berndt and Beate Schmitte with the EPMA, Christian Vollmer for the SEM, and Erik Scherer for the geochemical calculations (also coffee machine ;)). Many thanks also go to the people from the workshops of our institute, especially Michael Feldhaus, Jonas Kemmann and Maik Trogisch. I also thank Timothy Murphy, Yi-zhen Lai, Chao Shen for the EPMA, ICP-MS, and SEM at Macquarie University, thanks for the technical support.

And thanks also go to my family and my friends! I'd like to thank my brother who pushed me to come here and has been supportive all the time, thanks to my parents, my sister-in law, my little niece and nephew for the love and support. I'd like to thank my friends who helped me for with the thesis submission: Seema Kumari, Suzette Timmerman, Matthias Krug, and Marina Veter. I'm so grateful!

In addition, I'd like to thank all the friends I have made during the time of my PhD: Risa, Fer, Eve, Michaels, Stamatis, Tossin, Zaicong, Bothaiyna, Alanur, Lena, Eli, Stephan, Christina, Teresita, Ren, Xiurong, Huifang, Huiyu, Jingzi, Xenia, Xiao meng, Mari, Anqi, Alex, Mila, Coti, Rosa, Joyjit, Hindol, John, Kui, Thusitha, Laura, Stephanie, Jinxiang, Seema, Matthias, Misha, Dominik, Hacki, Carla, Chris, Malcolm, Marion, Thomas, Paula and Boofie,... etc. Because of you, I enjoyed my time in Muenster and Sydney a lot!! Many thanks from the bottom of my heart, to all of you!

I have grown a lot in last few years, and experienced a lot as well, good or bad. But I really appreciate deeply my supervisors and some friends who motivated me and lift me up. Some of them have changed my life in a better way and saved me when I was in a chanlangble situation. I will always remember you in heart and to be a better person. I'm very lucky to always have people like angels around me, hopefully one day I can be other people's angle as well! Unus pro omnibus, Omnes pro uno /人人为我，我为人人.

This research is supported by China Scholarship Council (CSC) and an Australian Government Research Training Program (RTP) Scholarship. Thanks for the support.

This thesis, in terms of 'material', is made 85-99% of Lindt Chocolate, with Coffee/Herb Tea as the fluid components and a bit salt as well.

Chapter 1 Introduction

1 Objectives of the thesis

Basaltic magma occurs in many geological settings on Earth and the origin of these magmas and the composition of their mantle sources have been studied for decades (Yoder Jr and Tilley, 1962; O'Hara, 1965; Green and Ringwood, 1967; Green and O'Hara, 1971; Frey et al., 1978; Green et al., 1987; Weaver, 1991). It is now widely accepted that basaltic magmas are derived from the mantle (Green and Ringwood, 1967) and melting of peridotite is the most important way to form basalt (O'Hara, 1965; Falloon et al., 1988; Takahashi et al., 1993). However, it has recently been proposed that some basaltic melts, especially those with a so-called garnet-signature (Hirschmann et al., 2003), may have affected by additional partial melting of garnet pyroxenite or eclogite (Klemme et al., 2002; Hirschmann et al., 2003; Kogiso et al., 2003; Pertermann and Hirschmann, 2003). Basaltic rocks are widely distributed on Earth, and they are the main rock samples that can provide us with information about the mantle source and the partial melting processes in the mantle (Reiners, 2002). Furthermore, basaltic volcanism is not only important to understand the partial melting process on Earth, but basalts are also formed during melting of the mantles of other terrestrial planetary bodies and their moons, such as Mars, Earth's Moon, and Io, the latter of which is one moons of Jupiter (ref: Mars: (Pieters, 1978; Greeley and Spudis, 1981; Wilson and Head III, 1981; Anderson et al., 2001; Jaeger et al., 2003; Grotzinger, 2013; Braden et al., 2014), and might be on Mercury as well (Palme, 2002).

In order to determine the mantle source rock composition and to unravel the partial melting processes that lead to the generation of basalts, one can either perform experiments to simulate melting processes in the laboratory (Kushiro et al., 1968; Green and O'Hara, 1971; Green, 1976; Kushiro, 2001) or one can analyse major elements, trace elements, and/or stable or radiogenic isotopes of natural basaltic rocks and/or mantle xenoliths (O'Reilly and Zhang, 1995; Stracke et al., 2000; McKenzie et al., 2004) (Fig. 1). Furthermore, as olivine is the first silicate phase to crystallize during differentiation of the mantle melt, trace elements in olivine have recently been used to infer information about the mantle source of basalts from different geological settings (Prelević and Foley, 2007; Foley et al., 2013; Jaques and Foley, 2018), i.e., intra-plate basalts in North China Craton (Liu et al., 2008; Yang et al., 2016; Geng et al., 2019), and oceanic basalts from Hawaii and the Canary Islands (Sobolev et al., 2005; Sobolev et al., 2007; Gómez-Ulla et al., 2017; Matzen et al., 2017). This

new approach, combined with the chemical compositions of basalts, has successfully been used to infer the origin of basalts and subsequent magmatic processes (Geng et al., 2019; Shea and Foley, 2019).



Fig.1: Left: A Mantle peridotite xenolith from Eifel volcano, Germany. Right: A basalt sample with olivine phenocrysts from Barrington, Australia.

An alternative approach to further our understanding of mantle melting processes, high pressure experiment can be conducted to investigate the origin of basaltic magmas (Yoder Jr and Tilley, 1962; O'Hara, 1965; Green and Ringwood, 1967; Green and O'Hara, 1971; Foley, 2010; Litasov et al., 2014). These experiments are usually conducted in the so-called piston cylinder apparatus ($P_{\text{max}} = 5 \text{ GPa}$, $T_{\text{max}} = 2100 \text{ }^{\circ}\text{C}$) which was introduced by Boyd and England (1960), the multi-anvil apparatus ($P_{\text{max}} = 27 \text{ GPa}$, $T_{\text{max}} = 3000 \text{ }^{\circ}\text{C}$) which was first introduced by Kawai and Endo (1970); and the diamond-anvil cell ($P_{\text{max}} = 560 \text{ GPa}$, $T_{\text{max}} = 6000 \text{ }^{\circ}\text{C}$) which was first constructed by Weir et al. (1959) and Jamieson et al. (1959). High pressure and high-temperature experiments are commonly used to obtain melting reactions, information about solidus and liquidus temperature, or fractionation of magmas during differentiation. In addition, high-pressure experiments can also be used to study the effects of fluids on melting relationships (e.g., Kushiro 2001, Litasov 2014).

In terms of chemical composition, basalt contains between 45-55 wt.% SiO_2 and 2-6 wt.% of total alkalis. and based on their geotectonic environment, basalts may be classified as mid-ocean ridge basalts (MORB), Oceanic island basalts (OIB), Island Arc basalts (IAB), Continental Arc basalts, and basalts in continental hot spots and rifts (i.e. Continental intraplate basalts). Basalts in different geological settings are products of different melting regimes and possible also different mantle sources (Yoder Jr and Tilley, 1962; O'Hara, 1965; Green and Ringwood, 1967; Green and O'Hara, 1971; Frey et al., 1978; Green et al., 1987; Weaver, 1991; Presnall et al., 2002). Whilst the genesis of the most common mid-ocean ridge basalts (MORB), which are formed by shallow partial melting of peridotite (Falloo and Green, 1987; Falloo et al., 1988) and oceanic island basalts (OIB), which

are often associated with mantle plumes that welled up from much greater depths (Lassiter and Hauri, 1998; Stracke et al., 2000; Dixon and Clague, 2001) are rather well understood, the genesis of intra-plate basalts is still under debate.

For example, intra-plate basalts were suggested to have originated from a mantle source with silica-deficient garnet pyroxenite components (Hirschmann et al., 2003; Kogiso et al., 2003), carbonated peridotite (Hirose, 1997; Dasgupta et al., 2007), partial melting of a metasomatized subcontinental lithospheric mantle (SCLM) (Zhang and O'Reilly, 1997), or a regional upwelling of deep hot mantle (O'Reilly and Zhang, 1995).

As to the formation of intra-plate basalts, it is still controversial (Hirschmann et al., 2003; Kogiso et al., 2003; Zeng et al., 2010; Niu et al., 2011) if intra-plate basalts are formed by melting of primitive or fertile mantle, or if the mantle source of intra-plate basalts has been modified by metasomatic processes (McKenzie and O'Nions, 1995; Liu et al., 2008; Pilet et al., 2008; Foley et al., 2009). Furthermore, it remains uncertain if melting processes or the mantle source composition changed over geological time, as it is well known that the redox conditions of the Earth's mantle changed since accretion of the Earth (Kasting et al., 1993; Kadik, 1997; Burgisser and Scaillet, 2007).

In this context, changing redox conditions over geological time must have affected partial melting of the mantle, as redox conditions control the speciation of C-O-H fluids, from CH₄ under reducing conditions to CO₂ and H₂O under oxidizing conditions. Moreover, C-O-H fluids are metasomatic agents that can change the mantle peridotite composition dramatically (Yaxley et al., 1991; Rudnick et al., 1993; Klemme et al., 1995; Dasgupta and Hirschmann, 2006; Dasgupta et al., 2007) and volatile-rich fluids are known to cause partial melting of eclogite and peridotite at much lower temperatures than in volatile-free conditions (Dasgupta et al., 2007; Green et al., 2010; Litasov et al., 2014; Rosenthal et al., 2014). In addition to partial melting of peridotite, partial melting of eclogite with C-O-H fluids shed light on the possible melting relations between the subducted basaltic lithosphere and the ambient peridotites, and the stability of ancient recycled oceanic crust at reducing environments. Since silica-deficient eclogite is one of the candidates for the genesis of intra-plate basalts (Hirschmann et al., 2003; Kogiso et al., 2003; Zeng et al., 2010), experiments on partial melting of eclogite with fluids provide an opportunity to test this hypothesis.

In order to further our understanding of melting of the mantle and the generation of basalt, the mantle source of basalts, especially inter-plate basalts, needs to be better constrained and the effect of redox conditions of melting relations in volatile-bearing mantle compositions needs to be evaluated. This research presented in this thesis aims to address these questions by using two approaches: (i) a geochemical study of natural basaltic and basanitic rocks from southeastern

Australia which aims to constrain the source of these volcanic rocks, and (ii) high- pressure, high- temperature experiments on the partial melting of peridotite and eclogite under different redox conditions and consequently different fluid components.

2 Outline of the thesis

In addition to the introduction, this thesis is composed of two major parts: the first parts aims to identify the source assemblages of basaltic rocks in Southeastern Australia using trace elements in olivine (Chapter 2). The second part (Chapter 3) focuses on the effect of C-O-H fluids on partial melting processes of eclogite and lherzolite at different redox conditions (Chapter 3). Both part 1 and 2 contain an introduction and background information specific to their topics. This thesis concludes with a summary chapter and a short conclusion (Chapter 4). All references of each chapter are combined together (Chapter 5).

Chapter 2 Identification of the source assemblages of basaltic rocks in southeastern Australia using trace elements in olivine

1 Introduction

1.1 Eastern Australian Mesozoic-Cenozoic volcanism

Extensive basaltic igneous activity occurred throughout the late Cretaceous and Cenozoic in eastern Australia, beginning at the end of the Cretaceous (70 Ma; Wellman and McDougall, 1974). The products of this volcanism are dominated by mafic rocks: slightly silica-undersaturated olivine basalts or hawaiite are prevalent in flows and intrusions of large volcanoes, while tholeiite, mugearite, trachybasalt and trachyte occur more rarely. Olivine basalts are predominant in extensive lava fields, frequently accompanied by hawaiite, picrite, nepheline basanite and basanite. In addition, one province which extends across central New South Wales consists of olivine leucitite (Wellman et al., 1970; Cundari, 1973).

Alkaline mafic volcanic rocks in continental provinces generally show a continuous range from alkali basalts through basanites and nephelinites to melilitites. This range of compositions was originally explained by melting of peridotite at different pressures and degrees of melting (Green et al., 1970; Green and O'Hara, 1971). Specifically for southeastern Australia, it was recognised from the trace element compositions of volcanic rocks and peridotite xenoliths that the origin of the more alkaline members of these series could not be explained without pre-enrichment of the source by mantle metasomatism (Frey and Green, 1974; Frey et al., 1978). Experiments showed that H₂O and CO₂ in the source were required to explain the composition, particularly the high degree of silica undersaturation of melilitites (Brey, 1978). Instead of the metasomatized peridotite, Foley (1992) suggested a model that: Those volcanic rocks derived from the melting of veins which are enriched in hydrous and carbonate minerals such as amphibole, mica and minor apatite with surrounding mantle peridotite in the lower lithosphere. Eastern Australian volcanic rocks are known to contain xenoliths rich in amphibole and apatite (Wass and Rogers, 1980; O'Reilly and Griffin, 2000). High-pressure experiments investigating melting of these ultramafic mantle assemblages have shown that melts of amphibole-rich pyroxenites are nephelinitic to basanitic (Yaxley et al., 1991; Foley et al., 1999; Pilet et al., 2008) with the nephelinite composition being contributed by the high mode of amphibole in the melting reaction (Foley et al., 1999). The mineralogy of the metasomatic assemblages is thought to result from the fractionation of basanitic melts that stall at mantle depths (Adam, 1990; Pilet et al., 2010, 2011).

The volcanic rocks are mainly distributed along the coastal margin of the Australian continent, situated in Phanerozoic orogens that lie to the seaboard side of thick lithosphere under the centre of the continent (160 km or more: Fig. 1). The earliest occurrences are in the south, including Tasmania, Victoria, and seamount chains in the Tasman Sea (Fig. 1b), whereas later volcanism has

been related to linear tracks decreasing in age from north to south (Davies et al., 2015). Some researchers have interpreted this pattern to represent plume tracks, marking the passage of the Australian plate over mantle plumes, based on age constraints from ^{40}Ar - ^{39}Ar and K-Ar dating (Cohen et al., 2007; Cohen et al., 2013) and zircon U-Pb dating (Sutherland et al., 2012). Other evidence, such as a low seismic velocity zone (Montelli et al., 2006) and abnormally high heat flow (O'Neill et al., 2003), has been used to locate a hotspot, currently lying under Bass Strait, which may be related to the volcanism expressed by these plume tracks. Plume control for the magmatism implies that the source for most of the melt would be produced in the plume head in the upwelling asthenosphere, and not in the lower lithosphere (O'Reilly and Zhang, 1995) according to the trace elements variation in flood basalts based on the mantle plume structure model (Campbell and Griffiths, 1990).

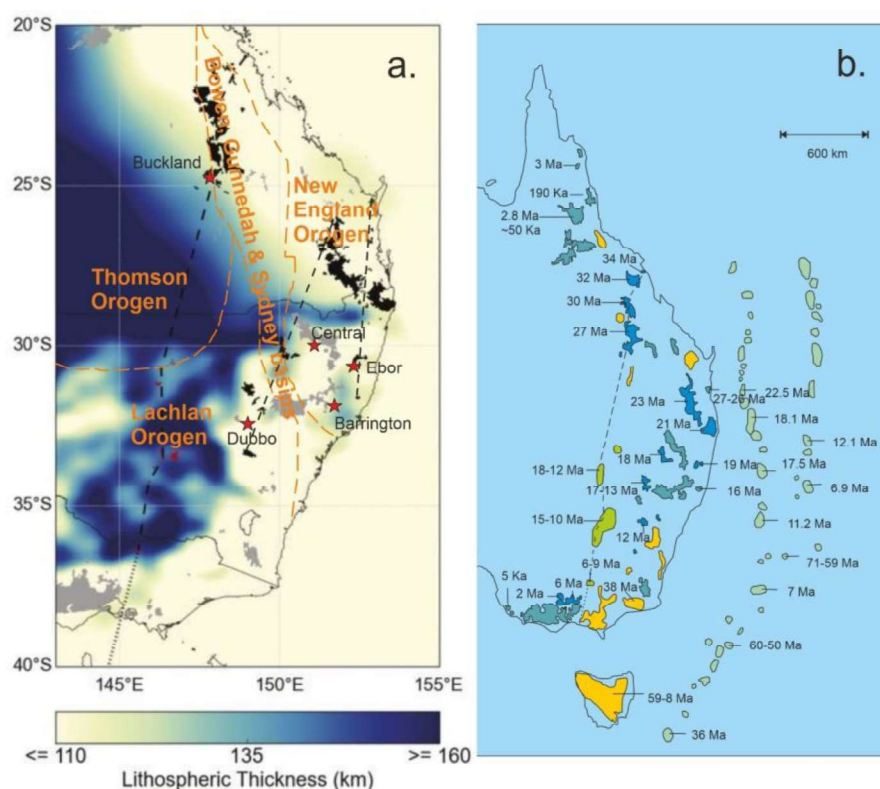


Fig. 1 Distribution of Cenozoic basaltic volcanism. a: Volcanic fields, hotspot tracks and sample areas and orogens in Eastern Australia (Glen et al. 2013; Davies et al. 2015); b: Basaltic distribution and age-trend in eastern Australia, revised after Meeuws et al. 2016. Green: Seamount, yellow: lava field remnants, blue: Bingara/Inverell (Central) shield volcano, cyan: lava field, lime: leucitite suite.

The thickness of the Australian lithosphere is thinning towards the seaboard (Fig. 1; Davies et al. 2015). Thus, they proposed that the distribution of Cenozoic magmatism is dominated by the lithospheric thickness, which controls the degree of mantle partial melting as recorded in the variation of concentration of incompatible trace elements in the volcanic rocks along the Cosgrove track. 3-D seismic tomography results indicate that the basalts in the Newer Volcanics Province (NVP)

of Victoria which is on the lithospheric step in South Australia was fed by the mantle upwelling with melt segregation at 3-4 GPa (Davies and Rawlinson, 2014). Price et al. (2014) applied the edge-driven convection caused by the migration of the Australian plate to explain the formation of basalts in the Older Volcanics of Victoria, south-eastern Australia. In contrast, the trace element and isotopic compositions of volcanic rocks have been used to constrain the source of these Cenozoic basaltic rocks as being located in the subcontinental lithospheric mantle (SCLM; O'Reilly and Zhang, 1995; Zhang and O'Reilly, 1997) since compositions were found to overlap with the geochemical characteristics of spinel lherzolite xenoliths from eastern Australia. For example, many basaltic rocks from New South Wales are enriched in Nb and Ta, with incompatible trace element patterns that show a gradual decrease towards the HREE. In addition, the ranges of 0.7029-0.7054 in $^{87}\text{Sr}/^{86}\text{Sr}$ and 0.51304-0.51257 in $^{143}\text{Nd}/^{144}\text{Nd}$ appear to characterize varied sources within the SCLM.

The sub-continental lithosphere can be characterized firsthand where mantle xenoliths are entrained, and these show that the SCLM beneath eastern Australia displays heterogeneous geochemical signatures and records a complicated evolutionary history (Yaxley et al., 1991; O'Reilly and Zhang, 1995; Zhang and O'Reilly, 1997). Experimental studies of basaltic rocks and partial melting of peridotites can provide further constraints, as can the relationship between local tectonism and magmatism. Experimental studies on a range of basaltic to melilititic rocks, as well as on partial melting of mantle peridotites, indicate depths of 70-130 km for most of these melt types (Bultitude and Green, 1971; Green and O'Hara, 1971; Green, 1973; Falloon et al., 1988; Adam, 1990).

However, previous studies have shown that neither bulk-rock major element and isotopic compositions nor geophysical observations alone can clearly decipher the source assemblages and melting conditions. Therefore, other approaches are required.

1.2 The use of trace elements in olivine for identifying source assemblages

The compositions of primitive basalts can record not only geochemical information about mantle reservoirs involved in the melting process, but also about the history and evolution of the SCLM (Zhang et al., 2001). Primary basaltic magma in continental settings is usually assumed to be formed either by upwelling of mantle plumes, or by melting at the base of the SCLM, or mixing of lithospheric and asthenospheric components generated by edge-driven convection (Demidjuk et al., 2007; Price et al., 2014). The magma composition can be modified on its way to the surface by interaction with surrounding wall rocks and/or thermal perturbation. Since olivine is usually the first silicate mineral to crystallize during cooling of magma, olivine phenocrysts in the most primitive

magmas should be the best witnesses of this process. Minor and trace elements in olivine such as Ni, Mn, Cr, and Ca, whose concentration in olivine is controlled by element partitioning, are influenced by pressure, temperature, and bulk composition of the melt (Simkin and Smith, 1970; Humayun et al. 2004; Foley et al., 2013). Thus, the abundance of these elements in olivine might be used to characterize the source mineral assemblages and geological settings that the magma has experienced. If trace element signatures are preserved well in olivine, and/or the zonation of elements are retained, their abundance and speciation are useful to decipher the mantle source environment of primitive magma and to track the magmatic history.

Nickel is the most compatible ‘trace elements’ in olivine, it has a higher partition coefficient for olivine than orthopyroxene in basaltic and alkaline melts (Beattie et al., 1991). For example, the partition coefficient of Ni for olivine/alkaline melts lies in the range 30-95 from experimental data (Foley et al., 2013), whereas the partition coefficient of Ni for orthopyroxene/basaltic melts is no more than 10 (Straub et al. 2008). Therefore, if there is residual olivine in the source, the magma generated from this source would have low Ni content. When the source runs out of olivine, Ni content in the magma will increase because the constraint from olivine was removed. Subsequently, the olivine crystallizing from this magma will be enriched in Ni. In this respect, Ni-enriched olivine in Hawaiian lavas was used to indicate a second-stage olivine-free pyroxenite source (Sobolev et al., 2005). In their model, the reaction between peridotite and recycled eclogite-derived melt results in the formation of pyroxene-rich rocks. When these rocks re-melt, they produce a melt enriched in Ni because the partitioning control of olivine is absent, and pyroxenes retain much less Ni during melting. Therefore, olivine phenocrysts that form near the surface in these melts will have higher Ni contents than normal.

However, other minerals such as garnet, spinel, phlogopite, and amphibole also affect the budget of mineral-specific minor and trace elements such as Mn, Sc, and Ti (Veter et al., 2017; Shea and Foley, 2019). For this reason, the combination of olivine trace element compositions with whole-rock compositions is necessary to arrive at well-constrained conclusions: this means that a conclusion made based on the trace element contents of olivines can be checked against predictions based on the major and trace element composition of the whole-rock.

Trace elements in olivine have been applied to interpret the mantle source of a variety of rock types and geological settings over the last few years, such as oceanic basalts (Sobolev et al., 2005; Sobolev et al., 2007; Gómez-Ulla et al., 2017; Matzen et al., 2017), intraplate basalts (Yang et al., 2016; Geng et al., 2019), ultramafic lamprophyres (Veter et al., 2017), leucitites and lamproites (Prelević and Foley, 2007; Ammannati et al., 2016; Shaikh et al., 2019). Only recently has this

approach been applied to decipher the petrogenesis of igneous rocks in Australia (Jaques and Foley, 2018; Shea and Foley, 2019).

Nowadays, high-precision electron microprobe (EPMA) analyses and the advancement of laser ablation inductively coupled plasma mass spectrometry (LA-ICP-MS) techniques make it possible to detect minor and trace elements in olivine at very low concentration (50 ppm by EPMA; <10 ppb by LA-ICP-MS (Foley et al., 2013).

This work aims to identify the probable source assemblages of the selected basaltic provinces in eastern Australia using trace element abundances in primitive olivine. The conclusions reached are backed up by whole-rock analyses in an attempt to assess whether melting of the rock types identified is associated with the passage of the Australian plate over a plume. We selected primitive basaltic samples from various locations in New South Wales: Dubbo is close to a major step in lithosphere thickness while Bingara/Inverell (Central) is a bit further away from the major lithospheric step (Fig.1a), and a third locality lies further to the east but close to anomalous small areas of thicker lithosphere (Barrington). These results are compared to those of the Buckland volcano in Queensland, which also lies close to a lithosphere ledge, but along one of the major eastern Australian hotspot tracks – the Cosgrove track (Davies et al., 2015).

2 Geological background

2.1 Sample area: orogenic history and lithosphere thickness

There are three main orogens in East Australia: the Thomson Orogen, the New England Orogen, and the Lachlan Orogen (Glen et al., 2013; Fig. 1). The Thomson and New England Orogens are separated by the Sydney Gennedah Bowen Basin. The Lachlan and the New England Orogens are Paleozoic orogens: the former has an age of Late Cambrian to Carboniferous and is suggested to have evolved simultaneously with the New England Orogen (Betts et al., 2002). The basement of the Lachlan Orogen was generally thought to consist mainly of oceanic lithosphere (Glen, 2005; Fishwick et al., 2008), and may include some fragments of continental basement from orogenic events. The New England Orogen is Carboniferous to earliest Triassic in age, and is composed of various volcanic arc, fore-arc and back-arc basins and subduction assemblages (Betts et al., 2002). The substrate beneath the New England Orogen is oceanic in the east and mixed oceanic and continental in the west. In addition, isotopic ages indicate that the substrate here preserves older lithosphere with a Re-Os age in the range of 0.6 to 1.8 Ga (Bennett, 2002; Glen, 2005).

Based on a 3D P-wave velocity model, Davies et al. (2015) estimated the lithospheric thickness in east Australia (Fig. 1). According to this model, a large part of the lithosphere beneath the Thomson and Lachlan Orogens exceeds 150 km, where volcanic provinces are not expressed. However, leucitite volcanism is located on thick lithosphere (~125 – 140 km), and basaltic provinces are located on thinner lithosphere (~ 110 km). If primary mafic magmas are generated at the base of the lithosphere, or deeper, it appears that lithospheric thickness is a controlling factor on melt composition.

Among the volcanoes studied here, Dubbo is closest to thicker lithosphere to the west (Fig. 1a). Bingara/Inverell (Central) and Dubbo are both situated to the east of the thick lithosphere zone in areas with a lithospheric thickness < 110 km. However, further to the east, Barrington is located above a small area of thicker lithosphere (110- 125 km). Results of this study are compared to recent data from Buckland (Shea and Foley, 2019), which is located much further north in Queensland, but with a similar spatial relationship to the edge of the thick continental lithosphere: it is close to the step in lithosphere, at a location where the lithosphere is thinner than underneath Barrington. In this study, samples were collected from volcanoes close to the edge of thick lithosphere in New South Wales. The localities at Bingara to Inverell area, Barrington, Ebor are situated in the New England Orogen, whereas Dubbo is on the boundary between the Lachlan Orogen and Gunnedah Basin. Exact localities of studied samples are in the Appendix table 1.

2.2 Previous work on basalts from the sampled localities

In terms of the mode of volcanism, geochemistry and petrography studies in the 1970s divided Cenozoic basaltic volcanism in Australia into three types: (i) central volcanoes, (ii) lava fields and (iii) the much rarer leucitites (Wellman and McDougall, 1974). In this study, the sampled areas at Bingara/Inverell (Central), Dubbo, and Barrington are classified as lava fields, while Buckland is classified as a Central volcano (Johnson et al., 1989). In the following, rock types are used rather than this mixed classification scheme of eruption type and rock type. Previous work on the sampled areas focused on whole-rock chemistry, partly in combination with isotope analysis and xenolith mineralogy and composition (O'Reilly and Griffin, 1987; Skae, 1998; Jessop 2012). In addition, high-pressure petrological experiments have helped to constrain the mantle source environment of the erupted rocks. Fig. 2 shows the Mg# range of whole-rock samples from previous studies, indicating that primitive compositions – which may be expected to carry olivine phenocrysts with little-altered information about their sources – appear to be more common at Barrington, Dubbo and Buckland

than at Bingara/Inverell (Central). A primitive composition can be characterized as having $Mg\# \geq 68$ ($Mg\# = 100 * Mg / (Mg + Fe)$, in terms of molar proportion).

Bingara/Inverell area:

The Bingara to Inverell province was redefined by Vickery et al. (2007) from the old term 'Central' used by Johnson et al. (1989) (In this thesis, to simply the table I used Central or CR to represent samples from Bingara/Inverell area). It consists of three Volcanic Suites: The Middle Eocene-Early Oligocene Maybole Volcanic Suite, the Middle Miocene Langari Hill Volcanic Suite, and the Late Oligocene-Early Miocene Delungra Volcanic Suite. Previous work indicates that the ultra-alkaline lithologies in this area feature very low to moderate potassium, very high thorium and low to high uranium radiometric responses, and strong widespread weathering in many basaltic outcrops (Brown, 2006). In terms of composition, the great majority of the rocks in Central province are alkali basalt and basanite, which is quite similar to mafic rocks from other lava field provinces in eastern Australia (Johnson et al., 1989). According to O'Reilly and Zhang (1995), the rock types in Bingara/Inverell province are composed of 20% basanite, 20% alkali olivine basalt, 23% olivine tholeiite, 3% quartz tholeiite, 20% nepheline hawaiite, and 14% hawaiite. Samples from the study of Vickery et al. (2007) have whole-rock $Mg\#$ ranging from 51.4 to 64.3 and with a median of 58.05 (Fig. 2).

The rocks of a central volcano erupted on Maybole (15 kilometres west of Glencoe village), covering an area that extends from south of the Macintyre River near Doni Hill and north to the Severn River built up the Maybole Volcanic Suite. The outcrop is poor in this area and only one constituent formation with few plugs, dykes, and sills was recognized (Vickery et al. 2007). Undersaturated alkali olivine and transitional basalts are dominant in this unit. A 300-meter sequence of stacked basalts flow was found in the Mount Buckley area (Coenraads, 1994) which includes mantle xenolith-bearing basalts with primary characteristics and was dated at 39.0 ± 0.3 Ma. The latest U-Pb isotope and fission track age of zircon megacryst from the alkali basalts determined an age of 36-38 Ma (Eocene) (Abduriyim et al., 2012). Three samples were collected in the outcrops of this area: One sample was picked up along the Guyra road in Tingha. Two other samples were collected from the outcrops along the Guyra road in Wandsworth area.

The outcrops of Langari Hill Volcanic are two elongated belts extending along the Gwydir Highway from west to the east and only one constituent formation was recognized. They are dominated by basaltic flows of tholeiitic composition. No sample was collected from this area.

The Delungra Volcanic Suite covers the region of Delungra, North Star, Bingara and Inverell. This volcanic suite is composed of four units: Mount Russell Volcanics, Inverell Volcanics, Derra Derra

Volcanics, and Bingara Volcanics. The major Cenozoic volcanic rocks ranges from undersaturated alkaline basalts to quartz and olivine tholeiites. The K-Ar dated age is between 24 Ma and 19 Ma (McDougall and Wilkinson, 1967, Wellman and McDougall, 1974). Two samples were collected in this area: One sample from the outcrops in Benbraggie State Forest along the Killarney Gap road in Pallal, Bingara region that belongs to the Bingara Volcanics unit. Another sample was collected in the outcrop in McIlveen Park lookout, and belongs to the Inverell Volcanics unit, Inverell.

Barrington Tops:

Barrington volcano is located roughly 100 km north-northwest of Newcastle (Bruce, 2011) inside the Barrington Tops National Park. The volcanic field consist of two main basalt sequences: The first one is distributed in the northeast sector along Barrington Tops Forestry road and exposed mainly in the Thunderbolt Lookout in the Polblue region. This basalt sequence was dated as 58.76 ± 0.5 Ma (Sutherland and Fanning 2001). Another one is exposed in the southwestern sector in Sempill Creek and along Stewarts Creek and is dated as 50.96 ± 1.5 Ma with U-Pb isotopes (Sutherland and Fanning 2001). The dominant rocks at Barrington are basaltic, and the major volcanic pile consists of alkaline rocks, including transitional basalt, alkali basalt, basanite and nephelinite. Mantle xenoliths are mainly spinel lherzolite (Johnson et al., 1989). Mantle xenoliths of amphibole-bearing garnet clinopyroxenites and amphibolites are identified in two diatreme vents on the margin of Barrington Tops volcano, adjacent to the township of Gloucester (Wilkinson and Kalocsai, 1974). Previous bulk rock trace element ratios coincide with those of HIMU-associated South Tasman basalts, which feature an amphibole and/or apatite-bearing lithospheric mantle source assemblage (O'Reilly and Zhang, 1995; Sutherland and Fanning, 2001). In addition, on the basis of reconstructed plate migration paths, Sutherland and Fanning (2001) suggested a plume originating in the Tasman rift zone contributed to the basaltic volcanism here. In this study, we have collected five samples in total: Two samples were collected from the outcrops along the Barrington Tops Forest road, one was collected from Polblue Crown Reserve. These three first three samples belong the early erupted basalt sequence. Other two samples belong the later erupted basalt sequence: One was collected from Stewarts Brook Forest, and one was collected from Moonan Brook.

Dubbo:

The Dubbo volcanic is located in the Orana region of New South Wales, extends from Mogriguy in the North to Cowra Trough in the south. The basement of Dubbo volcanic is a Palaeozoic continental crust (Zhang and O'Reilly, 1997). There is a Jurassic aged alkaline magmatic event occurred in Dubbo around 170-220 Ma (Meakin et al., 1999; Spandler and Morris, 2016); later, two magmatic episodes were identified at Dubbo (Morgan et al., 1999). The first one occurred in the Eocene to Lower

Oligocene dated from 43.6 Ma to 36.5 Ma on K-Ar age (Cameron et al. 1999), and the later one in the Miocene (Dulhunty, 1973) and dated at 13.3 ± 1.3 Ma by K-Ar on potassic hawaiites (Wellman and McDougall, 1974), which is the youngest among the locations sampled here. Few outcrops are exposed in the Dubbo volcanic field. The southwestern part of the Dubbo area consists of felsic rocks, while basaltic rocks constitute the northeastern part (Johnson et al., 1989). The Miocene basaltic rocks include olivine tholeiite, basanite, alkali basalt, and K-enriched hawaiite. Primary or primitive basaltic rocks are abundant. Xenoliths are common, and comprise Cr-diopside-bearing lherzolite, wehrlite and pyroxenite. As for Barrington, a plume has been suggested to be involved in generating the volcanism (Zhang and O'Reilly, 1997). Four samples were collected in this area: The first sample was collected in the outcrops along the Goolma road. The second sample was collected in Wongarbon along the Railway lane of Mitchell Highway. The third and the fourth samples were collected in the outcrops of Dubbo and Brocklehurst near Narromine Road, respectively.

Ebor:

The Ebor volcano is situated southeast of Inverell and west of the township of Dorrigo. Along the Great Escarpment it covers an area of about 480 km² with the main lava sequence distributed between Dorrigo and Point Lookout. Around 60% of the surface of the original low-angle shield volcano was eroded. Eocene basaltic rocks are exposed in the west the Ebor Volcano (Askley et al. 1995). Ebor volcano has an age of 19-20 Ma, and lava flows, which are dominated by olivine- and quartz-normative tholeiitic basalts (Vickery et al. 2007), ranging through icelandite to rhyolite, formed at 19.2-19.0 Ma (Ashley et al., 1995). Porphyritic textures in lavas with plagioclase phenocrysts are common (Johnson et al., 1989). Most rocks have microphenocrysts of olivine. A few scattered lherzolite xenoliths occur in some basanites but were suggested to belong to an older Doughboy province; no further compositional information is reported (Ashley et al., 1995), Vickery et al. 2007. Three samples were collected along the Guyra road in Ebor.

Buckland:

Buckland is located in the Central Highlands Region, around 100 km north of the township of Mungallala, Queensland. The dominant eruption of the Buckland shield is exposed in the north-east (Jessop 2012). The shield of Buckland volcano is strongly eroded and the remaining basaltic lava is up to 300 m thick (Skae, 1998). Most flows are almost horizontal. Two eruption episodes during the Cenozoic have been determined for the Buckland volcano: 30.7 ± 0.5 Ma and 27.3 ± 0.8 Ma (Waltenburg, 2006, Jessop 2012). Radially spreading lavas formed the Buckland shield (Johnson et al., 1989) consisting of alkali basalts and hawaiites in the northeast, with intervals of varying amounts of hawaiites and tholeiitic basalts. In the southern part, the flows are composed of

transitional or olivine-tholeiitic basalt and covered by nepheline-hawaiite. More than one hundred intrusive bodies and flow remnants are distributed across the western part of the Buckland province. The prevailing compositions of lava flows are relatively primitive with nephelinite, basanite, alkali basalt, and hawaiite dominating lava compositions. More details about the Buckland samples referenced here are given in Shea and Foley (2019). Shea and Foley (2019) targeted primitive melts (>7.5 wt. % MgO) in Buckland to also elucidate a source assemblage, they found it to be an olivine websterite with accessory apatite, phlogopite and amphibole, which had formed by reacting a carbonatitic metasomatic agent with a spinel lherzolite. The comparison of the New South Wales localities with these Buckland samples allows assessment of the variation of lava and olivine compositions over a much larger area, but at similar distances to the same main lithospheric step.

In summary, samples described in this study cover several volcanic provinces with different basements, lithosphere thickness, and are possibly derived from different hotspot tracks. This widespread sampling is expected to provide comprehensive information and new perspectives on the source assemblages of Cenozoic basaltic volcanism in eastern Australia.

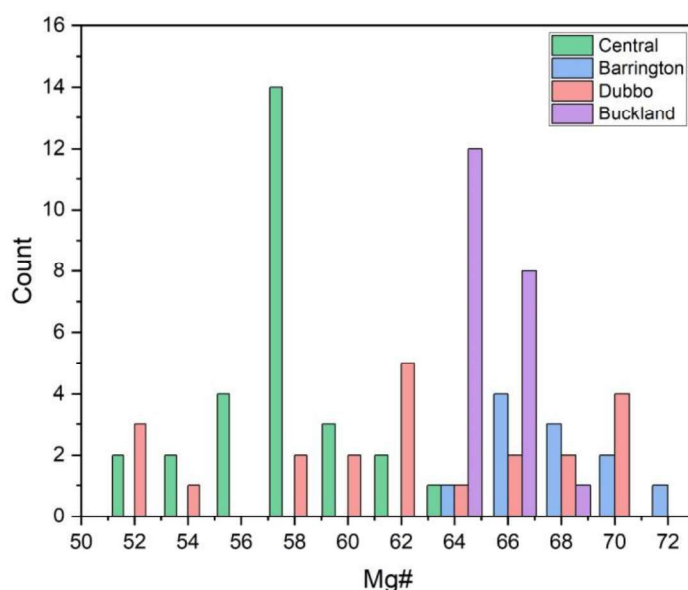


Fig.2 Whole-rock Mg# distribution in sampled locations from previous work. Data sources: Bingara/Inverell (Central): Vickery et al., (2007); Barrington: O'Reilly and Zhang, (1995); Sutherland and Frederick, (2011); Dubbo: O'Reilly and Zhang, (1995); Zhang and O'Reilly, (1997); Buckland: Skae, (1998).

3 Analytical methods

3.1 Whole-rock analysis

Ten samples from Ebor, Dubbo, Bingara/Inverell, Barrington were selected for whole-rock analysis. Weighed sample powders were put into the furnace at 1100 °C overnight and were

weighed again later to calculate loss on ignition (LOI). After this, 1 gram of sample powder was mixed in a crucible with lithium tetraborate flux in a ratio of 10:1. Consequently, the crucibles with sample powders were heated at 1050 °C for at least 25 minutes, later adding in ammonium iodide to increase the viscosity of the sample melt. Afterwards, the new melt mixture was taken out of the furnace, poured onto a metal plate and cooled to a glass disc. The glass disc was used for analysis of major elements with a PANalytical Axios 1 kW X-ray fluorescence (XRF) instrument.

Trace element determination by solution ICP-MS used 0.1 gram of sample powder. Vials were cleaned with HNO₃ and rinsed three times. Afterwards, the vials were cleaned with HCl and rinsed with ultrapure water again and dried for use as sample containers. The weighed sample powder was firstly stabilized by 2% HNO₃ overnight, and later an HNO₃-HF mixture with a ratio of 1:1 was added twice. The above solution was heated at 150 °C overnight and dried out. The samples were then treated with 6N HCl (1:1 HCl) and dried again, after which 2% HNO₃ was added to the solution and dried carefully. Finally, the diluted samples were analysed by an Agilent 7500cs quadrupole ICP-MS at *Macquarie Geoanalytical*, Macquarie University, Sydney. The following standards were placed alternately among samples to track the reproducibility of the analysis: Bir-1, BHVO-2 and BCR-2. BCR-2 was used as the calibration standard (in appendix, table 2 and table 3).

3.2 Element concentrations in olivines

3.2.1 SEM:

Olivines with high Mg# (> 83 in the core or rim) were selected for quantitative analysis with a Phenom XL Benchtop scanning electron microscope (SEM), at the Microscopy Unit of the Faculty of Science and Engineering, Macquarie University, Sydney. The image was taken under 15 kv point mode with BSD defector. The element analysis was measured with EDS detector. To ensure correlation of major and trace element measurements, trace elements were analysed at first by Laser-ICP-MS. Afterwards, major element analysis were carried out by EPMA with the target point adjacent to the laser craters.

3.2.2 EPMA:

Major element compositions of olivines were analysed with a CAMECA SX 100 microprobe at Macquarie University. 15 kV acceleration voltage and 20 nA were applied, with a beam size of 2 µm. Two or three points in each olivine grain were analysed to check for consistency in composition and were accepted if the oxide total lay between 98-101 wt.%. Ten grains in each thin section were measured.

3.2.3 ICP-MS:

Trace element concentrations of olivines were measured using an Agilent 7700x ICP-MS coupled with a Photon Machines Excite Analyte 193nm excimer laser ablation with HelEx II system at Macquarie Geoanalytical (MQGA), Department of Earth and Planetary Sciences, Macquarie University. A beam diameter of 85 μm was applied for most olivines; a beam diameter of 65 μm was used for a few olivines to avoid the contamination from inclusions and cracks, or for small grains. Laser fluence and repetition rate were 5 J/cm^2 and 10 Hz, respectively. All ablations were carried in He carrier gas with a total flow rate of 0.8 l min^{-1} , which is mixed with Ar before introduction to ICP-MS. The operating conditions of ICP-MS were optimised to minimise $^{248}\text{ThO}^+ / ^{232}\text{Th}^+$ oxide formation (< 0.5%), while maintaining maximum sensitivity on Li, Y, and U. Each analysis consists of 120 s background acquisition followed by 60 s ablation and 20 s washout. Dwell times for individual mass scans are 30 ms for the most of the masses; 20 ms for ^{24}Mg , ^{27}Al , ^{29}Si , ^{30}Si , ^{43}Ca , ^{44}Ca ; and 40 ms for ^{67}Zn and ^{93}Nb .

NIST SRM 612 (standard is provided in appendix table 4) was used as the calibration reference material for the drift and yield correction. ^{29}Si was used as an internal standard, which was obtained from EPMA analysis. Accuracy and precision was assessed by measuring the reference materials, NIST SRM 610 and BCR-2G, as unknowns.

The isotopes measured for these analyses were:

^7Li , ^{11}B , ^{23}Na , ^{24}Mg , ^{25}Mg , ^{26}Mg , ^{27}Al , ^{29}Si , ^{30}Si , ^{31}P , ^{43}Ca , ^{44}Ca , ^{45}Sc , ^{47}Ti , ^{49}Ti , ^{51}V , ^{53}Cr , ^{55}Mn , ^{59}Co , ^{60}Ni , ^{62}Ni , ^{63}Cu , ^{66}Zn , ^{67}Zn , ^{69}Ga , ^{88}Sr , ^{89}Y , ^{90}Zr , ^{93}Nb , ^{135}Ba , ^{137}Ba , ^{139}La , ^{140}Ce , ^{157}Gd , ^{172}Yb .

The data reduction was done with the Glitter software package (Griffin, 2008); detection limits are listed in Appendix table 5. The measurement of some isotopes may be affected by isobaric interferences, for example, ^{67}Zn may be interfered by $^{27}\text{Al}^{40}\text{Ar}$. In such cases, the isotopes known to have less interference (Jochum et al., 2012) and higher natural abundances were preferred. After data reduction, some analysis which had abnormally high Al content (e.g. more than 1700 ppm) were assumed to be contaminated by spinel and was abandoned.

4 Results

4.1. Petrography

Table 1 summarizes the petrography of the rock samples. The typical texture is porphyritic with olivine and/or plagioclase being the main phenocrysts. The groundmass is mainly composed of plagioclase and small anhedral olivine grains. There is slight alteration in the samples.

Alkali basalt from Maybole is fine-grained and contains around 20% (in mode) of heavily embayed phenocrysts of olivine that often show zoning. The olivine grains are typically 0.5 mm, up to 1 mm in length. Clinopyroxene is rarely present. The groundmass consists of olivine glomerocrysts and elongated plagioclase.

Basanite from Mount Russell is fine-grained and contains large olivine and pyroxene phenocrysts (up to 2 mm). The groundmass is plagioclase and anhedral olivines. Tholeiite from Dubbo is fine-grained and contains scattered embayed olivines (up to 0.5 mm) less than 5%. The groundmass consists mainly of plagioclase. Alkali basalt from Dubbo (DB-01H) is medium-grained and dominated by elongated plagioclase (up to 1 mm in length), scattered pyroxene and olivine phenocrysts. Olivine phenocrysts are typically less than 0.5 mm and less common than plagioclase. The groundmass is plagioclase and olivine glomerocrysts. Another alkali basalt sample from Dubbo (DB-03F) contains a few but larger olivine grains (up to 2 mm) with zonation. Clinopyroxene is rare. Iddingsite is common as resulted from alteration of olivine. Alkali basalt from Ebor is fine to medium-grained, dominated by plagioclase (up to 1mm) and zoned olivine phenocrysts (up to 1.5 mm). Olivine phenocrysts contain spinel inclusions and fluid inclusions and are often zoned. The matrix is mostly plagioclase. Basanite from Barrington is medium-grained and porphyritic and contains brown alteration and veins. The olivine phenocrysts make up 25-30% and are 0.5 mm in diameter on average and up to 3 mm. Large olivines are commonly embayed and zoned, and often include spinel inclusions. Clinopyroxene is present. The groundmass has a trachytic texture and is composed of plagioclase, and small anhedral olivine grains.

Picrobasalt from Barrington is fine-grained, 15-20% olivine phenocrysts and xenocrysts. Olivine grain is up to 2 mm. zoning in olivine is common. The matrix is mainly anhedral olivine and plagioclase.

Fig. 3 shows representative olivine phenocrysts in thin sections from different locations in New South Wales. Thin sections that contained few or no olivines, or from rocks that had experienced significant alteration, are not shown here and were not used for analyses. Sample 01H from Dubbo is dominated by plagioclase phenocrysts and contains only few olivine phenocrysts. Two other thin

sections from Dubbo, 03F and 04C have more olivine phenocrysts and no plagioclase phenocrysts. Some samples from Bingara/Inverell (Central) have porphyritic textures defined by olivine phenocrysts. Samples from Ebor have few olivine phenocrysts, but large plagioclase phenocrysts. Samples from Barrington are rich in olivine grains (Fig.3a, b), and macrocrystic olivines are common: The grain size can be > 500 μm . Some of them exhibit undulose extinction (Fig. 3b), which is a deformation feature and may indicate xenocrysts from mantle depths. Spinel inclusions are common in olivines (Fig 3.a, c).

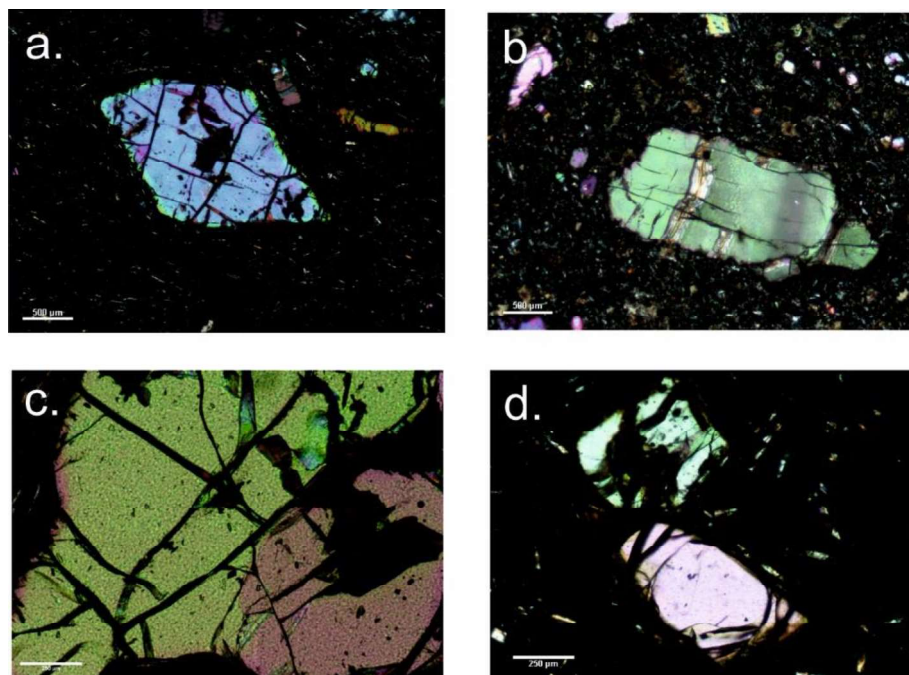


Fig. 3: Representative macrocrystic olivine grains in samples from different locations. a, euhedral olivine with a rim of zonation (DB-23D, Barrington); b, olivine with kink banding, might be xenocryst as the deformation of olivine likely occurred in the mantle (Low et al., 2011)(DB-20B, Barrington); c, spinel inclusion (black) in olivine grains (Barrington, 23D); d, subhedral olivine with spinel inclusion (DB-04C, Dubbo).

Table 1: Petrographic details of analyzed samples

Location	Sample	Rock type	Texture	Phenocrysts	Groundmass	Comments
Mount Russell	CR-11A	Basanite	Porphyritic	Ol	Ol, Plg	Zonation of Ol
Maybole	CR-12A	Alkali basalt	Trachytic	Ol	Ol, Plg, Spl	-
Maybole	CR-13E	Alkali basalt	Trachytic	Ol	Ol, Cpx, Plg	Altered groundmass
Barrington	BR-20B	Picrobasalt	Porphyritic	Ol, Cpx	Ol, Cpx, Plg	Slightly altered
Barrington	BR-22A	Basanite	Porphyritic	Ol, Cpx	Ol, Cpx, Plg	-
Barrington	BR-23D	Basanite	Porphyritic	Ol, Cpx	Ol, Cpx, Plg	Slight alteration, some alteration of Ol to Id
Dubbo	DB-01H	Alkali basalt	porphyritic	Ol, Cpx, Plg	Ol, Cpx, Plg, Spl	Altered groundmass
Dubbo	DB-03F	Basanite	Porphyritic	Ol	Ol, Plg	Alteration of Ol to Id, zonation of Ol
Dubbo	DB-04C	Tholeiite	Porphyritic	Ol	Ol, Plg	-
Ebor	EB-16A	Alkali basalt	Trachytic	Ol, Cpx, Plg	Plg	-

Ol: olivine, Opx: orthopyroxene, Plg: plagioclase, Spl: spinel, Id: iddingsite.

Back-scattered electron (BSE) images of macrocrystic olivines in samples from different locations were obtained when testing for primitive compositions of olivines. Most olivines are homogeneous and a few have a narrow Fe-rich zonation rim (i.e. lighter in BSE images). Plagioclase dominates the groundmass of the sample from Dubbo (Fig. 4a), whereas samples from Bingara/Inverell (Central) (Fig. 4b) and Barrington (Fig. 4c) have intergranular texture composed of clinopyroxene and plagioclase.

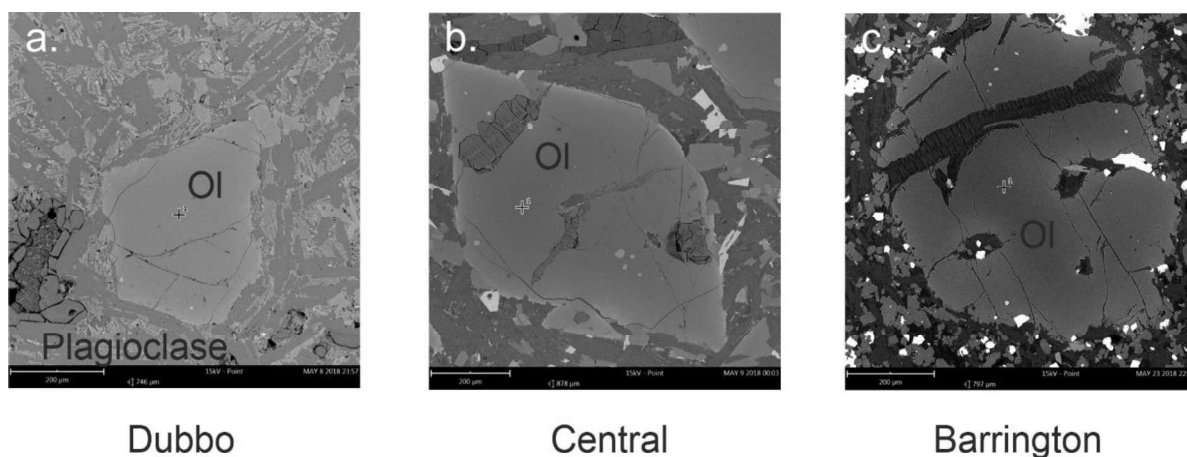


Fig.4 Black-scattered electron image (BSE) displaying olivines (the caption below is the locations), with surrounding spinel, clinopyroxene, and plagioclase in the groundmass.

4.2 Whole-rock analysis

4.2.1 Major elements

Table 2 gives the major and trace element compositions for the bulk rocks. The total alkalis vs. silica (TAS) diagram classifies the samples into four groups (Fig. 5): (i) picobasalt (BR-20B), (ii) alkali basalt (CR-12A, CR-13E, DB-01H, EB-16A), (iii) tholeiitic basalt or tholeiite (DB-04C), and (iv) basanite (CR-11A, BR-22A, BR-23D, DB-03F). In this classification, sample DB-04C from Dubbo is the least alkaline and is classified as tholeiite, sample CR-11A from Bingara/Inverell (Central) is the most alkaline; these two rocks are labelled on Fig.5a. Three samples from Buckland are basanites.

In general, all basaltic samples from New South Wales locations show a systematic trend of decreasing SiO_2 (40-49 wt.%) with increasing Mg# (Fig. 6a), while basanites do not have this kind of trend. CaO abundances in basaltic samples mainly lie in the range of 8.4-9.6 wt % (Fig. 6b), lower than that in basanite which ranges from 8.9 to 10.7 wt.%. Picobasalt from Barrington has high CaO (10.3 wt.%) and the highest MgO content (12.6 wt.%). In contrast, there are no clear correlations

between P_2O_5 (0.32-0.90 wt. %), CaO (8.83-10.73 wt.%) and Mg# in the bulk rocks (Fig. 7), rather the distribution is affected more by rock type. Similarly, there is no clear correlation between Mg# and TiO_2 (1.89-2.59 wt. %) or alkalis ($Na_2O < 4.5$ wt. %, $K_2O < 2.1$ wt. %).

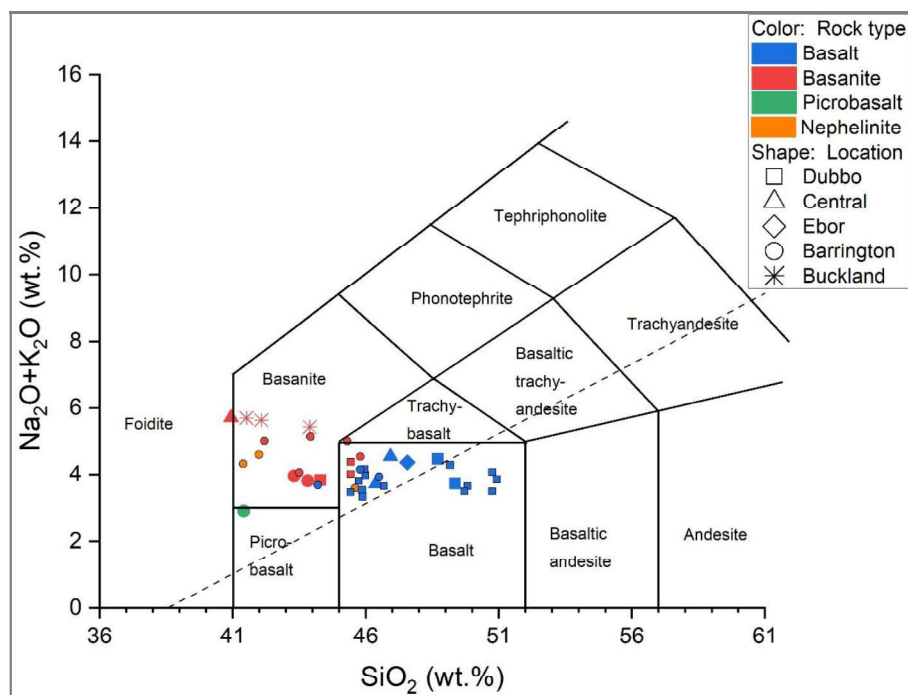


Fig. 5 TAS (Total alkalis vs. silica) classification of sampled whole-rocks. In this and subsequent figures, symbol colours indicate rock types, and shapes indicate localities. Small symbols are from previous studies in the same area: Barrington: O'Reilly and Zhang, (1995; Sutherland and Fanning, (2001); Dubbo: O'Reilly and Zhang, (1995); Zhang and O'Reilly, (1997). The dash line is alkaline (above the line) and subalkaline (below) boundary (Irvine and Baragar, 1971).

The Barrington samples (picrobasalt and basanite) appear to be the most primitive compositions in terms of Mg# (Fig. 6a), whereas Dubbo samples have lower Mg# despite having SiO_2 contents typical for basalts. Samples BR-20B and BR-22A have very low SiO_2 content and the highest MgO and CaO, and high P_2O_5 contents as well. In contrast, two basalt samples from Dubbo have both low MgO and CaO content, except sample DB-03F (basanite). In general, the Barrington basanites and picrobasalt have the highest CaO (9.8-10.7 wt%). In Fig. 6b, there is no indication for an olivine control line as is frequently seen in volcanic series that include picrites and basalts: the picrobasalts have high CaO and relatively low MgO. This is consistent with fractionation having proceeded beyond olivine fractionation to a lower Mg# where clinopyroxene and plagioclase dominate the fractionation trends.

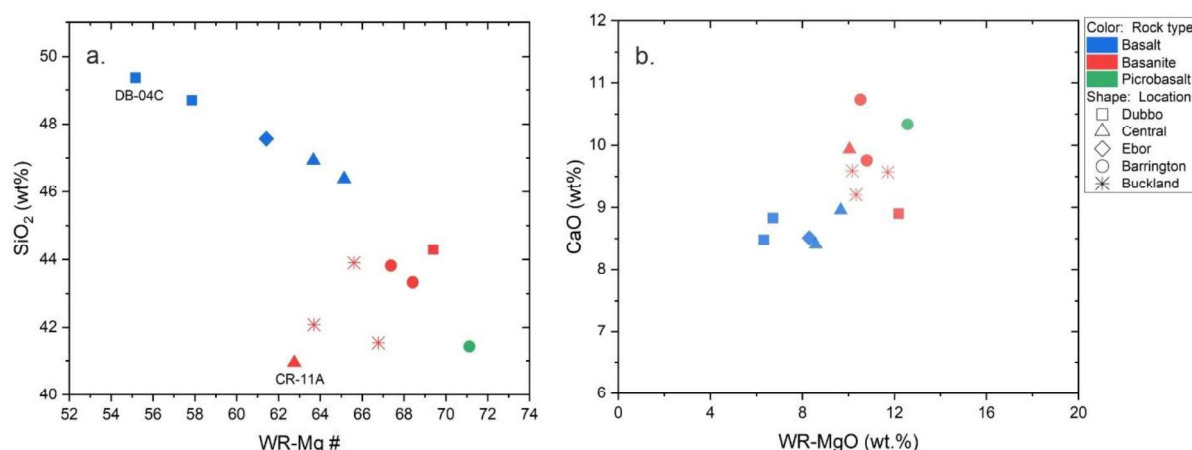


Fig. 6 Bivariate diagrams of whole-rock (WR) compositions from different locations. a. Mg# vs SiO_2 of rock samples from NSW and Buckland; b. Correlation of CaO and MgO of bulk rocks.

Samples from Bingara/Inverell (Central) have compositions intermediate between Dubbo and Barrington (Fig. 7), except CR-11A which has the lowest SiO_2 (40.94 wt.%) and highest P_2O_5 contents (1.46 wt.%) of all the samples. DB-04C has the lowest K_2O content, and all other samples have similar contents (ranging from 1.0 to 2.2 wt.%). Interestingly, in terms of Na_2O and P_2O_5 , all the basalts have similar concentrations despite different Mg#, while in basanite samples, both Na_2O and P_2O_5 decrease with increasing Mg#. MnO concentrations increase with Mg# in basalts and decrease with Mg# in basanites. In general, the distinctive compositional trends in basalts and basanites from this study suggest that these two types of rocks behave differently during magma evolution. Since the same mafic phenocryst phases are involved in fractionation, this may indicate differences in source mineralogy and distinct parental melt compositions.

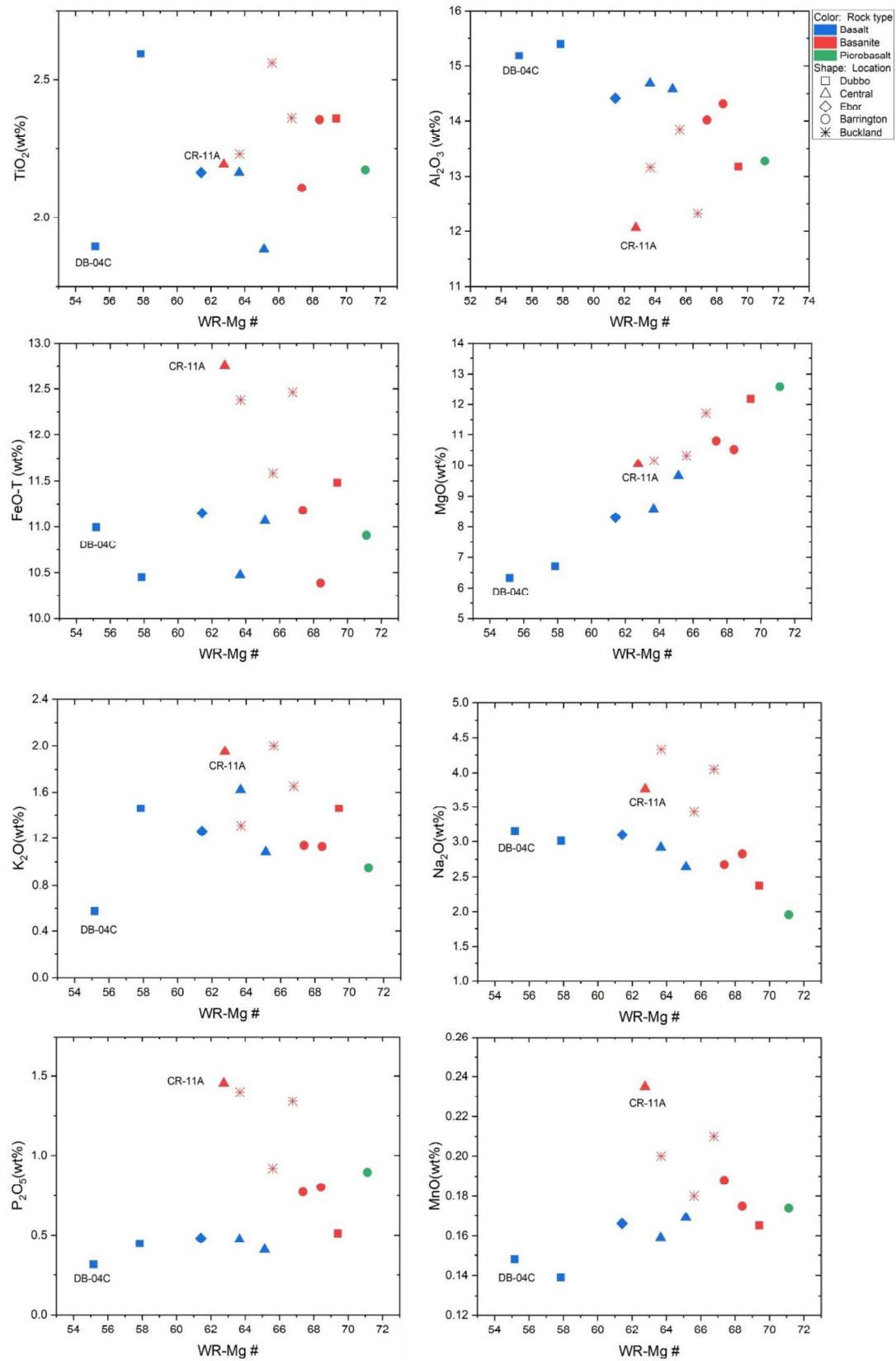


Fig. 7 Selected major and minor elements against Mg# of bulk rocks from different locations

Table 2: Whole-rock data

Location	Dubbo				Bingara/Inverell area(Central)				Ebor		Barrington		Buckland			
Rock type	Basalt	Basalt	Basalt	Basalt	Basalt	Basalt	Basalt	Basalt	Basalt	Picrobasalt	Basalt	Basalt	Basalt	Basalt	Basalt	
Sample No.	DB-01H	DB-03F	DB-04C	CR-11A	CR-12A	CR-13E	EB-16A	BR-20B	BR-22A	BR-23D	BK-75115	BK-75116	BK-75119			
Whole-rock major elements (wt. %)																
SiO ₂	48.69	44.29	49.35	40.94	46.39	46.93	47.56	41.42	43.31	43.82	41.52	43.901	42.08			
TiO ₂	2.59	2.36	1.90	2.19	1.89	2.16	2.16	2.17	2.35	2.11	2.36	2.56	2.23			
Al ₂ O ₃	15.40	13.18	15.19	12.06	14.58	14.69	14.42	13.28	14.32	14.02	12.33	13.85	13.16			
Fe ₂ O ₃	11.62	12.76	12.22	14.17	12.30	11.64	12.39	12.13	11.55	12.43	13.85	12.87	13.76			
MnO	0.14	0.17	0.15	0.24	0.17	0.16	0.17	0.17	0.18	0.19	0.21	0.18	0.2			
MgO	6.71	12.18	6.33	10.05	9.66	8.58	8.30	12.57	10.52	10.80	11.71	10.33	10.16			
CaO	8.83	8.90	8.48	9.93	8.95	8.40	8.51	10.34	10.73	9.76	9.57	9.2	9.59			
Na ₂ O	3.01	2.38	3.16	3.76	2.64	2.92	3.10	1.96	2.83	2.67	4.05	3.43	4.33			
K ₂ O	1.46	1.46	0.58	1.95	1.08	1.62	1.26	0.95	1.13	1.14	1.65	2	1.31			
P ₂ O ₅	0.45	0.51	0.32	1.46	0.41	0.47	0.48	0.90	0.80	0.77	1.34	0.92	1.4			
LOI	1.35	2.16	2.92	3.23	2.33	2.97	1.82	4.41	2.26	2.50	1.11	0.93	1.58			
Total	100.25	100.34	100.57	99.98	100.40	100.54	100.17	100.27	99.98	100.19	99.74	100.17	99.8			
Mg#	57.86	69.41	55.17	62.75	65.14	63.67	61.42	71.13	68.42	67.37	66.77	65.61	63.7			
Whole-rock trace elements (ppm)																
Li	5.24	6.63	4.13	9.99	5.91	5.82	6.11	5.50	5.41	5.74	7.15	6.93	5.92			
Be	2.03	1.76	1.87	3.93	1.55	2.00	1.82	2.50	2.31	2.36	2.13	3.21	3.05			
Sc	24.4	22.1	24.3	11.4	24.1	21.4	24.5	29.1	25.9	28.6	24.9	18.1	22.0			
Ti	16681	14029	12539	11275	11863	13362	13702	14838	13330	14439	13177	13843	15864			
V	210	182	184	114	182	172	191	218	199	220	207	150	192			
Cr	112	316	209	167	266	216	212	384	369	238	226	289	207			
Mn	1054	1183	1146	1453	1258	1165	1273	1385	1228	1287	1413	1431	1348			
Co	102	105	104	72	105	72	89	89	81	106	87	93	102			
Ni	117	336	179	222	217	165	169	356	321	200	217	300	239			
Cu	48.4	80	69	38.9	73	65	69	78	72	81	79	57	71			
Zn	112	94	111	132	94	92	102	100	88	86	98	121	114			

(Continued)

Ga	20.0	16.8	20.4	19.3	16.6	17.0	18.0	18.0	16.0	17.2	17.3	18.8	20.2
Rb	18.1	28.7	12.8	27.7	23.6	38.9	22.7	12.7	11.9	13.5	29.1	26.9	38.6
Sr	589	565	443	1386	575	545	512	945	873	943	965	1000	839
Y	26.0	20.5	44.4	34.3	22.5	22.1	25.3	24.9	22.6	24.6	24.0	27.6	26.1
Zr	230	172	167	393	129	166	170	197	180	201	169	309	298
Nb	28.4	45.1	20.2	131.4	30.6	36.9	32.6	75.5	70.8	83.8	61.9	87.1	81.3
Mo	1.22	0.72	1.07	4.00	0.98	1.85	1.33	2.60	2.11	2.08	2.04	5.06	2.80
Cd	0.11	0.06	0.07	0.08	0.08	0.06	0.07	0.10	0.07	0.08	0.08	0.06	0.05
Cs	0.10	0.47	0.51	0.97	0.34	0.87	0.29	0.40	0.36	0.21	0.49	0.39	0.33
Ba	220	341	880	659	203	262	239	395	366	347	406	405	484
La	21.4	27.4	48.1	110	16.7	19.7	20.0	45.3	41.3	36.2	33.5	76.3	60.1
Ce	47.1	52.7	49.4	198	33.1	39.6	40.5	79.7	71.8	70.3	61.7	142	114
Pr	6.3	6.5	12.7	21.8	4.1	4.9	5.1	9.0	8.0	8.4	7.2	16.0	13.1
Nd	26.9	25.2	54.0	79.5	17.3	20.5	21.6	33.0	29.4	31.3	27.3	59.6	48.1
Sm	6.2	5.3	11.8	13.7	4.2	4.9	5.1	6.3	5.7	6.1	5.5	10.6	8.6
Eu	2.06	1.76	3.66	4.02	1.40	1.63	1.67	2.00	1.83	1.97	1.82	3.21	2.65
Tb	0.88	0.72	1.62	1.52	0.65	0.73	0.77	0.80	0.73	0.80	0.74	1.22	1.05
Gd	5.9	4.9	11.6	11.0	4.2	4.8	5.0	5.6	5.1	5.5	5.1	8.7	7.3
Dy	4.6	3.7	8.1	6.7	3.6	3.8	4.2	4.0	3.6	4.1	3.8	5.5	5.0
Ho	0.85	0.68	1.47	1.10	0.70	0.73	0.81	0.80	0.67	0.77	0.72	0.95	0.89
Er	2.21	1.70	3.65	2.58	1.85	1.88	2.13	2.00	1.75	2.06	1.91	2.33	2.27
Yb	1.67	1.25	2.53	1.47	1.49	1.46	1.71	1.50	1.36	1.61	1.48	1.53	1.57
Lu	0.22	0.17	0.34	0.18	0.21	0.20	0.24	0.20	0.19	0.23	0.21	0.20	0.21
Hf	4.67	3.38	3.56	6.92	2.57	3.33	3.35	3.40	3.00	3.57	2.92	5.89	5.83
Ta	1.65	2.41	1.20	6.21	1.51	2.00	1.68	3.40	3.08	4.26	2.97	4.38	4.27
Th	2.01	3.10	1.82	11.14	1.72	2.42	1.98	5.10	4.62	3.56	3.25	7.82	7.17
U	0.56	0.70	0.47	2.64	0.50	0.71	0.57	1.40	1.20	0.94	0.85	2.03	1.82

4.2.2 Trace elements

Fig. 8 and Fig. 9 display trace elements ordered by increasing compatibility of all samples from New South Wales and Buckland normalized to primitive mantle (Sun and McDonough, 1989). Most samples share the same ocean island basalt (OIB)-like pattern (Sun and McDonough, 1989) of incompatible element enrichment. All basalts and basanite samples are characterized by depletion of K, Ti and heavy rare earth elements (REEs), and enrichment in Zr and Nb (Fig. 9). In general, samples from the same location have quite similar levels of element enrichment, except samples CR-11A (basanite) and CR-12A (alkali basalt) from Bingara/Inverell (Central), which have the highest and lowest enrichment, respectively, in all incompatible elements. On the other hand, basanites generally have higher incompatible elements than picrobasalts and basalts (Fig. 9).

From the perspective of location (Fig. 8), samples from Buckland have higher enrichment than samples from Barrington and Dubbo, and compared to Barrington, Dubbo rocks have relatively low enrichment, which may indicate that higher contents of incompatible elements are characteristic of the most primitive magmas, or that the mineral assemblages in the source differ. Sample DB-04C from Dubbo has the highest enrichment in Ba, which may be attributable to alteration, since the abundances of all other elements of each sample display the similar patterns. DB-04C also has the least enrichment in K and P: These generally low contents of incompatible elements may be due to differences in the parental magmas and thus the source assemblages. This would mean the Barrington source is different from Dubbo. In the Bingara/Inverell area, basanite from the Mount Russell Volcano is significantly enriched in all trace elements relative to basalts from the Maybole Volcano, except for Ti which has similar concentrations.

Sample DB-04C from Dubbo is strongly depleted in Rb and K and has the highest Ba abundance, resulting in high Ba/Rb and Ba/Nb ratios. This feature might be caused by post-magmatic processes, a weathering feature (Price et al., 1991; Zhang and O'Reilly, 1997), which is also supported by the negative Ce anomaly in the REE pattern. However, this alteration mainly affects the REEs in whole-rock, or within plagioclase, whereas Ni, Cr, and Mn are mainly concentrated in olivine and not affected by alteration processes. Therefore, sample DB-04C can still be used to interpret the source lithology, if the focus is on the minor and trace elements in its olivines, e.g. Ni, Mn, Cr, Ti, and Ca.

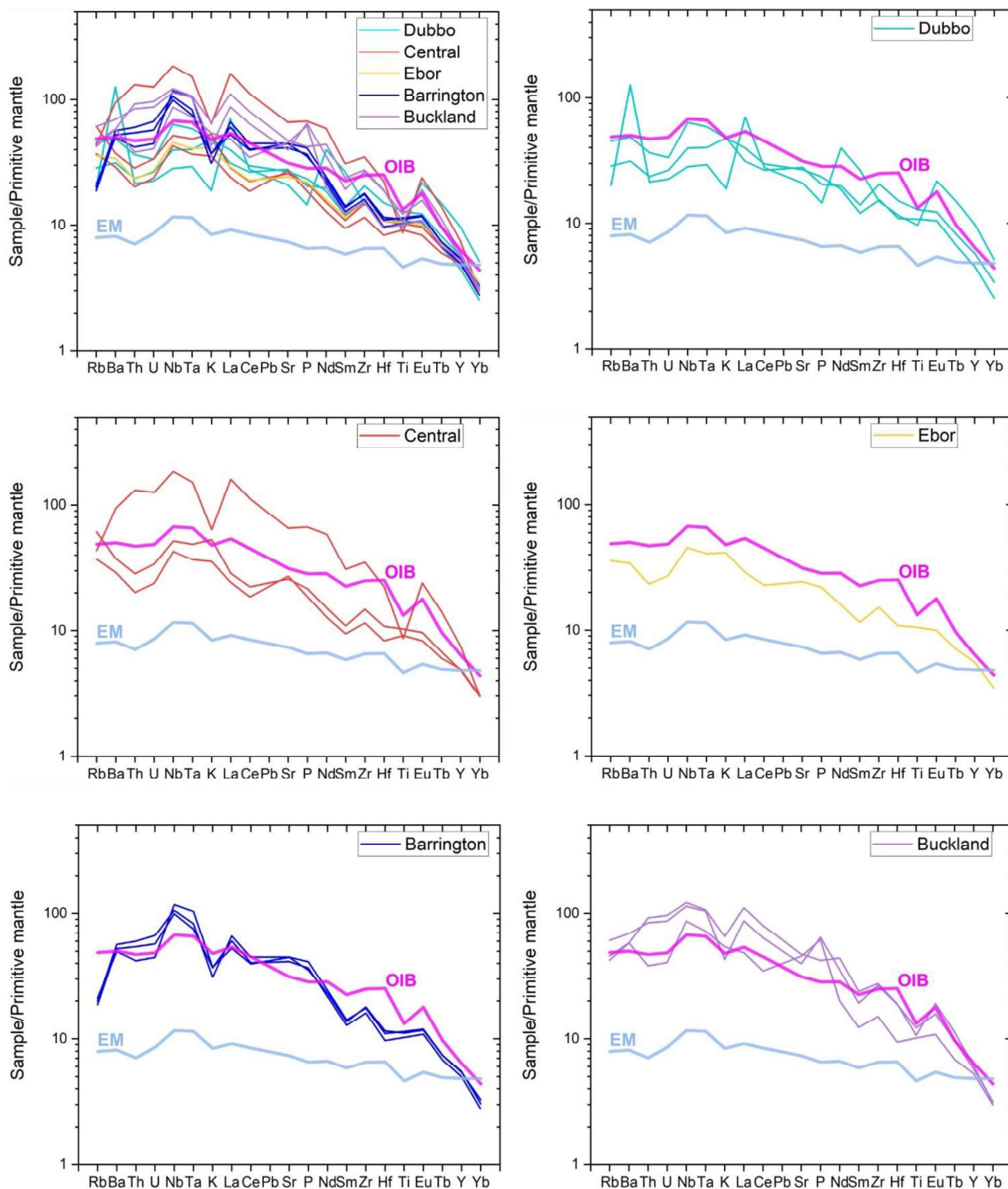


Fig. 8 Incompatible elements pattern normalized to PM based on location. a. is the summary of all locations, b-f are diagrams of each location. OIB indicates oceanic basalt (Sobolev et al., 2005), and EM indicates Enriched mantle (Schmidt and Poli, 1998).

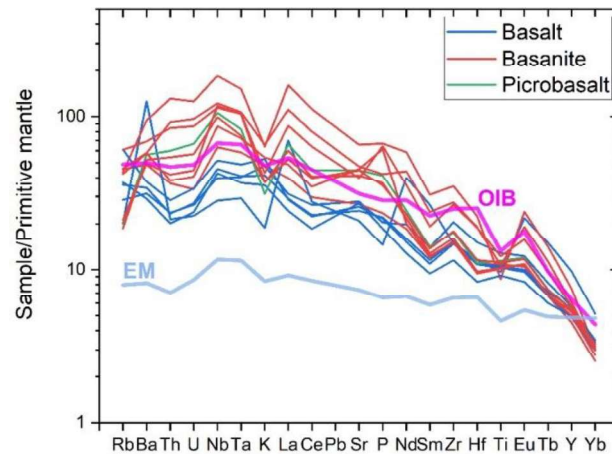


Fig. 9: Incompatible elements pattern normalized to PM based on rock type. OIB indicates oceanic basalt (Sobolev et al., 2005), and EM indicates Enriched mantle (Schmidt and Poli, 1998).

4.3 Analysis of olivine compositions

Representative olivine analyses are listed in Table 3 and the full dataset is provided in Appendix table 6. Plots showing the inter-element relationships in olivines and between olivines and whole-rocks are given in Fig. 10-13.

4.3.1 Characteristics and correlation of major elements in whole-rocks and olivines

In some samples, olivines are zoned with high Mg concentration in the core and high Fe concentration in the rim (see Fig. 4). In this case, the Mg# decreases from more than 85 in the core to as low as 71 in the rim. For tracing the original source mineralogy, only the most primitive olivines are of interest, therefore only core analyses are considered. Furthermore, the dataset is incomplete for rims because they are too thin for accurate LA-ICP-MS analysis of many trace elements.

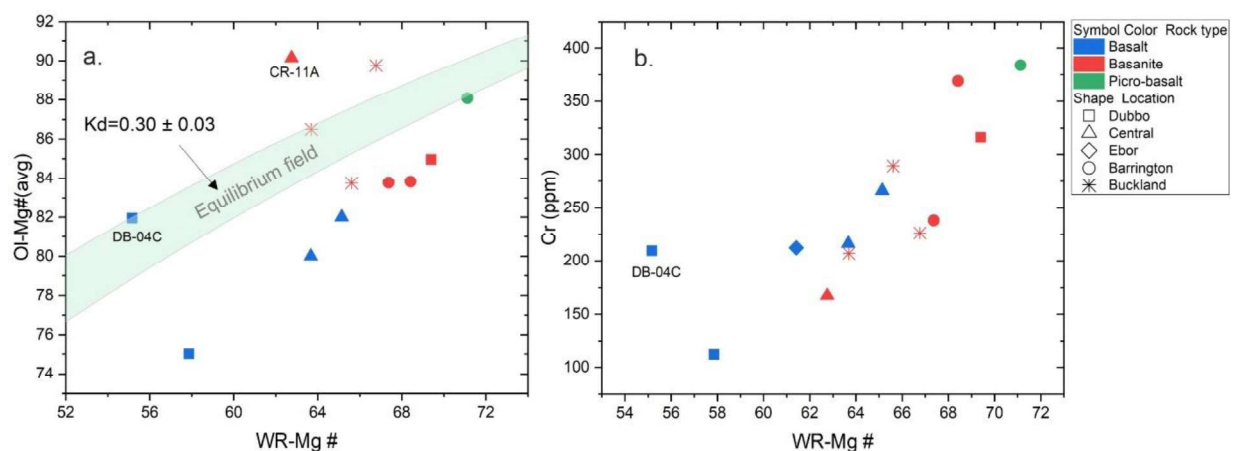


Fig. 10 a. Rhodes diagram of olivine Mg# vs whole-rock Mg#, the green field is equilibrium field; b. Mg# vs Cr of whole-rocks

Figure 10 displays the correlation between the composition of olivine phenocrysts and whole-rock samples. The left panel shows the average Mg# of olivine (mostly represented by primitive olivine

cores) plotted against the corresponding whole-rock sample. For samples from New South Wales, there is a general positive trend, except for samples DB-04C from Dubbo and CR-11A from Bingara/Inverell (Central). These two unexpectedly Mg-rich olivines might be mantle xenocrysts, or phenocrysts from a more primitive magma batch.

The green shaded olivine-liquid equilibrium field in Fig. 10a delineates the field for expected Mg# of olivine phenocrysts equilibrated with coexisting liquids based on data from tholeiitic basalts (Roeder and Emslie, 1970), with K_D ranging from 0.27 to 0.33. In this study, there are one tholeiitic sample from Dubbo, one picobasalt sample from Barrington, and one basanite sample from Buckland that fit this trend, despite their relatively low Mg#. The position above this field for two basanite samples (one from Bingara/Inverell (Central) and one from Buckland volcano) might indicate mantle xenocrysts. All other olivine phenocrysts in basaltic and basanitic samples lie below this equilibrium field, although all but one Dubbo sample are offset by similar amounts (Mg# of 5-10 lower in whole-rock than expected for equilibrium), which probably reflects fractionation of the groundmass after crystallization of the olivines.

Fig. 10b displays the variation of Cr concentration in olivine versus Mg# of the whole-rock samples. In general, all samples from New South Wales and Buckland have a positive correlation: although tholeiitic sample DB-04C from Dubbo lies off the main trend to higher Cr contents, confirming its position in the equilibrium field. Sample DB-01H from Dubbo has the lowest Cr concentration, and the primitive picobasalt sample BR-20B from Barrington has the highest Cr concentration in olivine.

4.3.2 Characteristics of minor and trace elements (EPMA data)

Many first-row transition elements in olivine were analyzed (Sc, Ti, Cr, Mn, Zn, Co, etc), but here only those commonly used to identify source assemblages are discussed. EPMA analyses of samples from Ebor are shown here as well, however, since they are not so primitive, they were not analyzed by ICP-MS.

Table 3 Representative compositions of olivines in samples from Dubbo and Barrington

Location	Dubbo				Barrington						
Rock type	Basanite	Basalt	Picrobasalt			Basanite					
Sample No.	DB-03F	DB-04C	BR-20A	BR-20B	BR-20C	BR-22A	BR-23D-1	BR-23D-2	BR-23D-3	BR-23D-4	
	Major elements (wt.%)										
MgO	48.98	43.16	45.95	49.73	45.07	45.01	45.46	44.35	44.78	45.13	
Al ₂ O ₃	0.03	0.05	0.07	0.02	0.03	0.04	0.06	0.05	0.05	0.06	
SiO ₂	40.95	38.13	39.5	40.38	39.63	39.47	38.63	38.83	39.44	37.97	
CaO	0.10	0.20	0.21	0.06	0.16	0.24	0.24	0.21	0.22	0.22	
Cr ₂ O ₃	0.03	0.04	0.04	0.01	0.02	0.03	0.03	0.02	0.03	0.03	
MnO	0.12	0.19	0.17	0.15	0.21	0.21	0.21	0.22	0.2	0.21	
FeO	9.10	15.71	12.27	9.70	14.09	14.14	15.47	15.85	14.92	15.29	
NiO	0.39	0.32	0.27	0.37	0.27	0.22	0.21	0.19	0.22	0.21	
Total	99.70	97.80	98.47	100.42	99.47	99.33	100.31	99.73	99.85	99.12	
Mg#	90.56	83.04	86.97	90.14	85.08	85.02	83.97	83.3	84.25	84.03	
	Trace elements (ppm)										
Li	2.2	2.2	2.1	2.6	3.3	4.1	2.3	6.8	2.5	3.0	
B	4.4	4.7	2.5	8.9	3.3	4.1	4.0	6.0	6.9	4.8	
Na	97	62	105	28.8	108	85.5	97	82.8	108	103	
Al	152	204	304	85	95	217	261	278	263	269	
P	62	158	129	56	92	142	77	88	74	71	
Ca	579	1386	1371	398	588	1482	1236	1845	1564	1521	
Sc	3.84	5.09	5.39	3.52	4.62	5.77	4.87	5.65	5.81	5.3	
Ti	22.1	76	85.1	27.9	27.3	94.1	69	91.5	76.4	89.1	
V	4.80	6.88	5.74	2.73	3.12	4.97	7.02	7.45	7.14	7.17	
Cr	190	260	216	63	127	135	209	97	208	210	
Mn	1124	1653	1373	1179	1596	1699	1611	2823	1741	1764	
Co	148	193	163	152	146	167	179	187	188	184	

(Continue)

Location		Dubbo			Barrington							
Rock type		Basanite	Basalt		Picrobasalt			Basanite				
Sample No.		DB-03F	DB-04C		BR-20A	BR-20B	BR-20C	BR-22A	BR-23D-1	BR-23D-2	BR-23D-3	BR-23D-4
Co		148	193		163	152	146	167	179	187	188	184
Ni		3094	2449		2086	3079	2400	1766	1866	1048	1757	1672
Cu		1.60	1.84		2.34	2.19	2.63	0.70	2.18	0.62	4.57	1.91
Zn		76	155		109	69	133	150	124	218	151	145
Ga		0.102	0.209		0.186	0.077	0.096	0.173	0.215	0.288	0.193	0.216
Sr		0.709	0.939		0.026	0.017	0.009	0.022	0.008	0.257	0.089	0.011
Y		0.056	0.137		0.089	0.033	0.042	0.129	0.085	0.237	0.116	0.104
Zr		0.201	4.02		0.066	0.063	0.287	0.561	0.165	0.960	0.052	0.822
Nb		0.006	0.012		<0.0012	0.148	0.013	0.004	0.001	0.021	0.014	0.001
Ba		<0.0147	0.045		0.028	0.02	<0.020	<0.014	<0.0124	0.025	0.326	0.059
La		0.002	0.02		<0.0014	<0.00190	<0.0013	0.003	<0.00120	0.007	0.005	0.003
Ce		0.002	0.056		<0.0012	0.002	0.001	0.002	0.018	0.007	0.071	<0.001
Gd		<0.0065	0.022		0.013	<0.0080	0.013	0.016	<0.0086	<0.010	<0.006	0.017
Yb		0.017	0.035		0.05	0.017	0.014	0.042	0.015	0.067	0.028	0.025

4.3.2.1 Minor elements: Nickel and Manganese (EPMA data)

Olivines in picrobasalt from Barrington (BR-20B and BR-20C) and basanites from Dubbo and Bingara/Inverell (Central) have the highest Ni concentrations and Mg# (Fig. 11a). At lower Mg#, the pattern splays out, with olivine in tholeiitic basalt from Dubbo having high Ni concentrations compared to olivine in alkali basalts from Buckland, followed by basanite from Barrington, which has the lowest Ni abundance. Ni abundance in olivine from Ebor is similar to that of alkali basalt from Buckland and basanite from Barrington.

Mn composition plotted against Mg# defines a negative slope for all samples (Fig. 11b), but again with a pattern of wider variation at Mg# < 84. Picrobasalts always have slightly higher Mn contents than other rock types at the same Mg#. The Mn contents in olivines of basalts from Buckland are higher than olivines of basalt from Dubbo and Ebor at intermediate to low Mg#. Olivines in the basanites from Dubbo and Bingara/Inverell (Central) carry the lowest Mn content at the highest Mg#.

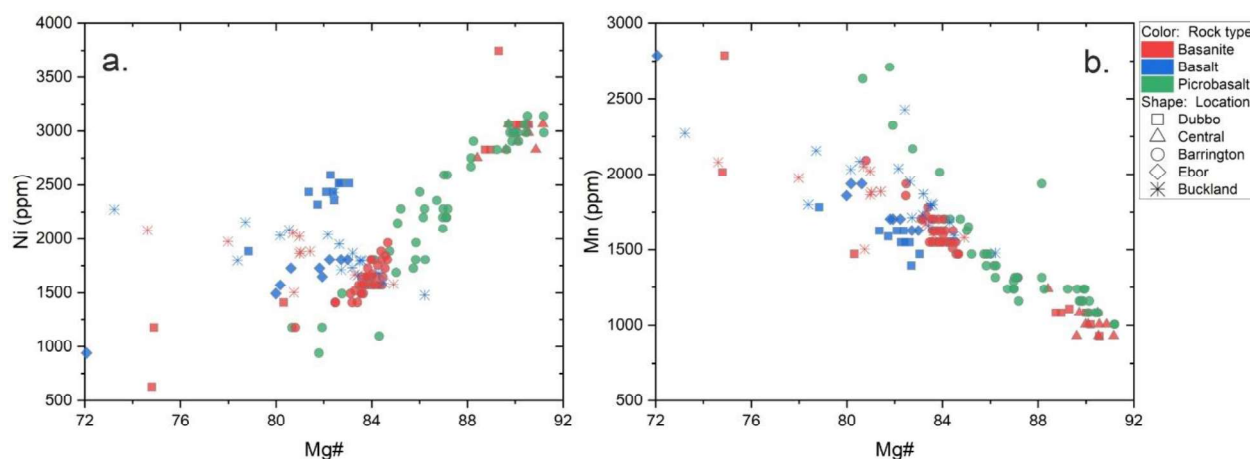


Fig 11: Minor element abundances in olivine and correlation with Mg# from EPMA. a. Ni concentration variation with Mg# in olivines; b. Mn concentration variation with Mg#.

4.3.2.2 Trace elements in olivines (LA-ICP-MS data)

Minor and trace element concentrations in olivines are shown in Figs. 12-14. Since the abundance of rare earth elements (REE) are very low (< 0.25 ppm), and similar in phenocrysts and xenocrysts, the analytical results are not plotted here.

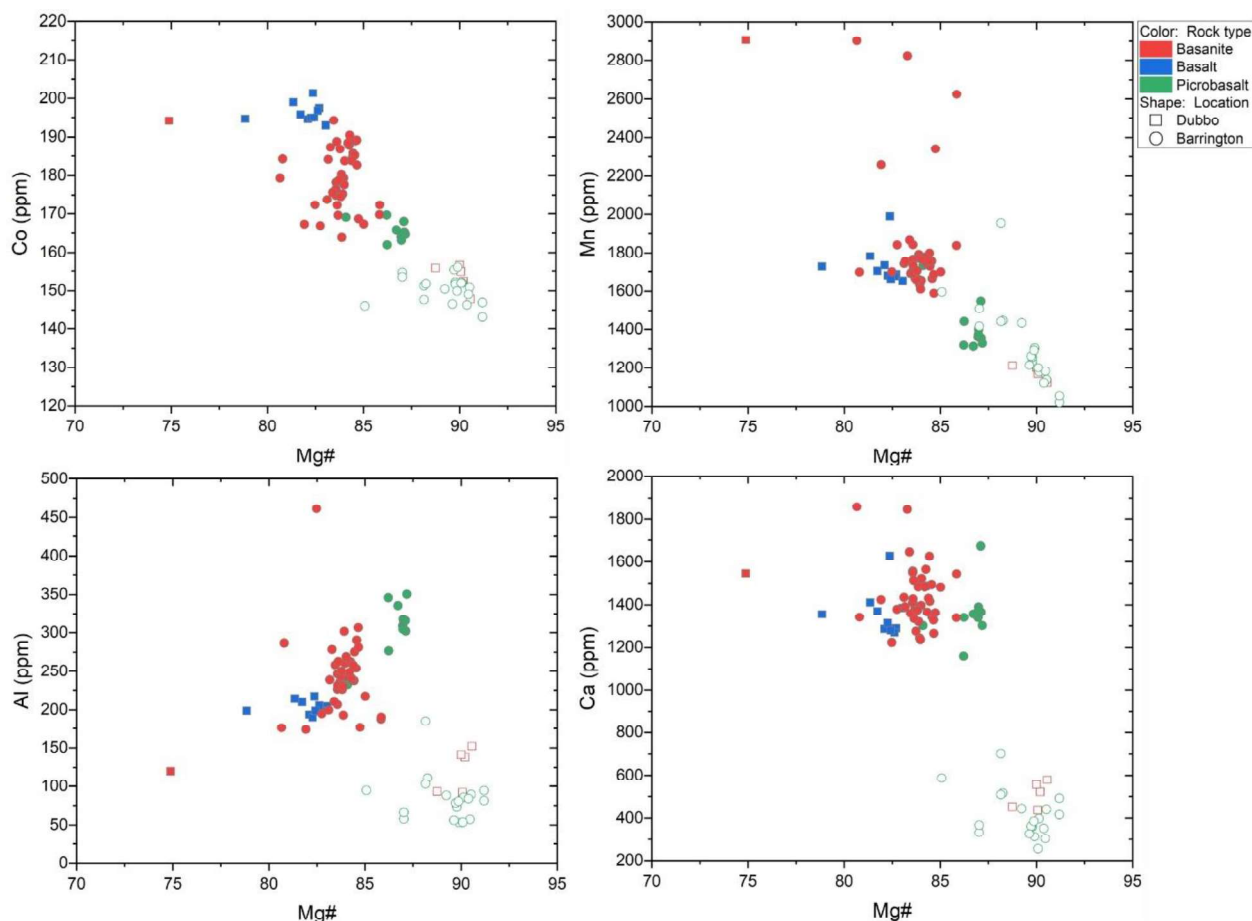


Fig. 12 Minor elements plotted against Mg# in olivines from Dubbo and Barrington (Filled symbols=phenocrysts, open symbols=xenocrysts).

Both Co and Mn show negative correlations with Mg# (Fig. 12) and are enriched in phenocrysts (160-200 ppm for Co, and 1250-3000 ppm for Mn) relative to xenocrysts (140-160 ppm for Co, and 1000-1500 ppm for Mn mostly). In addition, Al and Ca in olivines are distinct for phenocrysts and xenocrysts from all locations but are not strongly correlated with Mg#. The content of Al in olivines from the picrobasalts have the highest abundances with a value around 350 ppm.

Alkali and alkaline earth elements in olivine (Fig. 13) have wide ranges, with Li ranging between 1.5 and 8 ppm, and Na ranging between 10-120 ppm. Na in olivine of basalt from Dubbo (DB-04C) has the lowest concentration amongst phenocrysts, and in general, Na in xenocrysts is lower than that in phenocrysts. The alkaline earth elements Sr and Ba are very low (< 1.8 ppm and < 1 ppm, respectively), and have no strong correlation with Mg#. Two outliers from Dubbo are exceptions, with elevated abundances of Sr, whereas most Sr contents are < 0.5 ppm with basanite from Barrington having a slightly wider range. Similarly, Ba content in most samples is < 0.2 ppm, and many olivines in tholeiite from Dubbo and picrobasalt from Barrington are below the detection limit. The few grains with high Ba concentrations are probably contaminated.

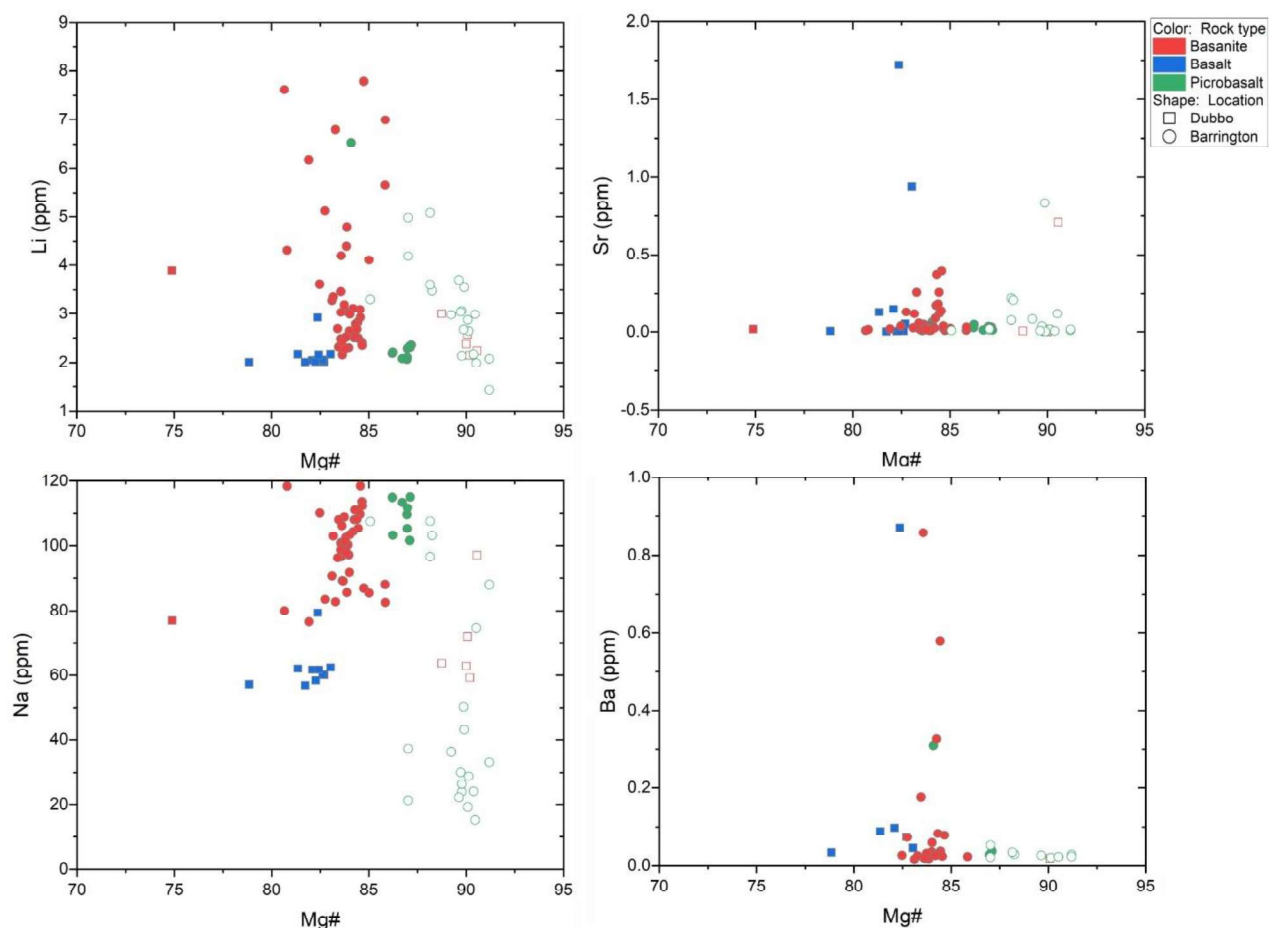


Fig. 13 Alkali and alkaline earth elements against Mg# in olivines from Dubbo and Barrington (Filled symbols=phenocrysts, open symbols=xenocrysts).

First row transition elements (Fig. 14) such as Sc, Ti, V, and Zn are generally enriched in phenocrysts relative to xenocrysts. The abundance of Cu ranges between 0.5 to 4 ppm for both phenocrysts and xenocrysts for basaltic samples from Dubbo and Barrington. In addition, Zn contents in olivine have a clear negative correlation with Mg# and correlated with rock type. In terms of phenocrysts, tholeiitic basalt (DB-04C) is relatively enriched in Zn relative to basanites from Barrington (mostly in the range of 110-150 ppm), and higher than picobasalts from Barrington. Amongst xenocrysts, Zn abundances in olivine in picobasalt from Barrington are similar to xenocrysts in basanites from Dubbo. Both are relatively low, mainly in the range of 60-80 ppm.

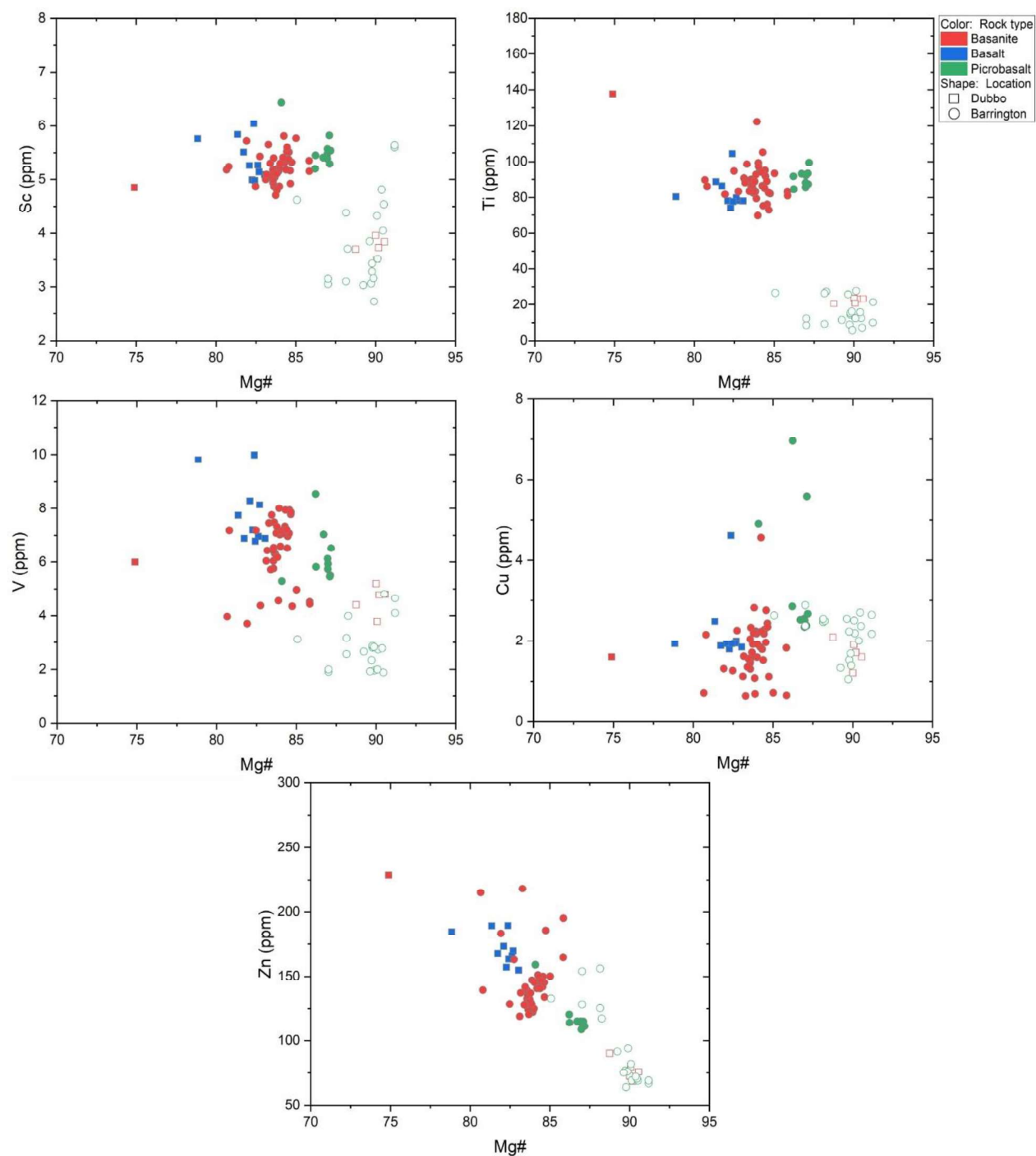


Fig. 14 First row transition elements against Mg# in olivines from Dubbo and Barrington (Filled symbol-phenocryst, open symbol-xenocryst).

5 Discussion

5.1. Distinguishing olivine xenocrysts and phenocrysts

The chemical composition of olivine phenocrysts carries information about the composition of the melt from which they crystallized. For this reason, the most primitive olivine compositions chosen

should reflect the characteristics of the undifferentiated melt. In contrast, xenocrysts originate in a shallower depth than the source of their host magma, representing samples of the lithosphere through which the melt passed (O'Reilly and Zhang, 1995; Veter et al., 2017). These distinct modes of formation result in distinctive trace element characteristics (Fig. 15). In this study, all xenocrysts have low Ca concentrations (< 800 ppm), while all phenocrysts have $\text{Ca} > 1100$ ppm. In terms of Al contents, all xenocrysts have < 160 ppm, whereas Al content in xenocrysts correlates positively with Ca, especially in xenoliths from picrobasalts. Almost all high Mg# (> 84) olivine grains in samples DB-03F, BR-20B, BR-20C are xenocrysts. Based on the EPMA data, olivine grains in CR-11A appear to also be mainly xenocrysts, based on their high Mg# with an average of 90.29, low in Al (< 106 ppm) and Ca (< 643 ppm) contents.

Nickel is another tracer that effectively distinguishes xenocrysts from phenocrysts: Ni concentrations in mantle olivines from many localities and lithologies ranges between 2040 and 3310 ppm (De Hoog et al., 2010). In this study, most xenocrysts have more than 2700 ppm of Ni, while all phenocrysts have less than 2550 ppm Ni. Additionally, xenocrysts have less than 30 ppm of Ti, while all phenocrysts have more than 50 ppm (Fig. 14).

Similar characteristics were identified at Buckland in Queensland (Shea and Foley, 2019), where all phenocrysts have Ca contents > 1000 ppm, and almost all xenocrysts < 840 ppm. Most phenocrysts at Buckland have more than 172 ppm of Al content, less than 40 ppm of Ti, and Ni content ranging from 1402 to 2549 ppm, while xenocrysts have less than 1445 ppm of Al content, more than 65 ppm of Ti, and Ni content ranging from 2214 to 3292 ppm.

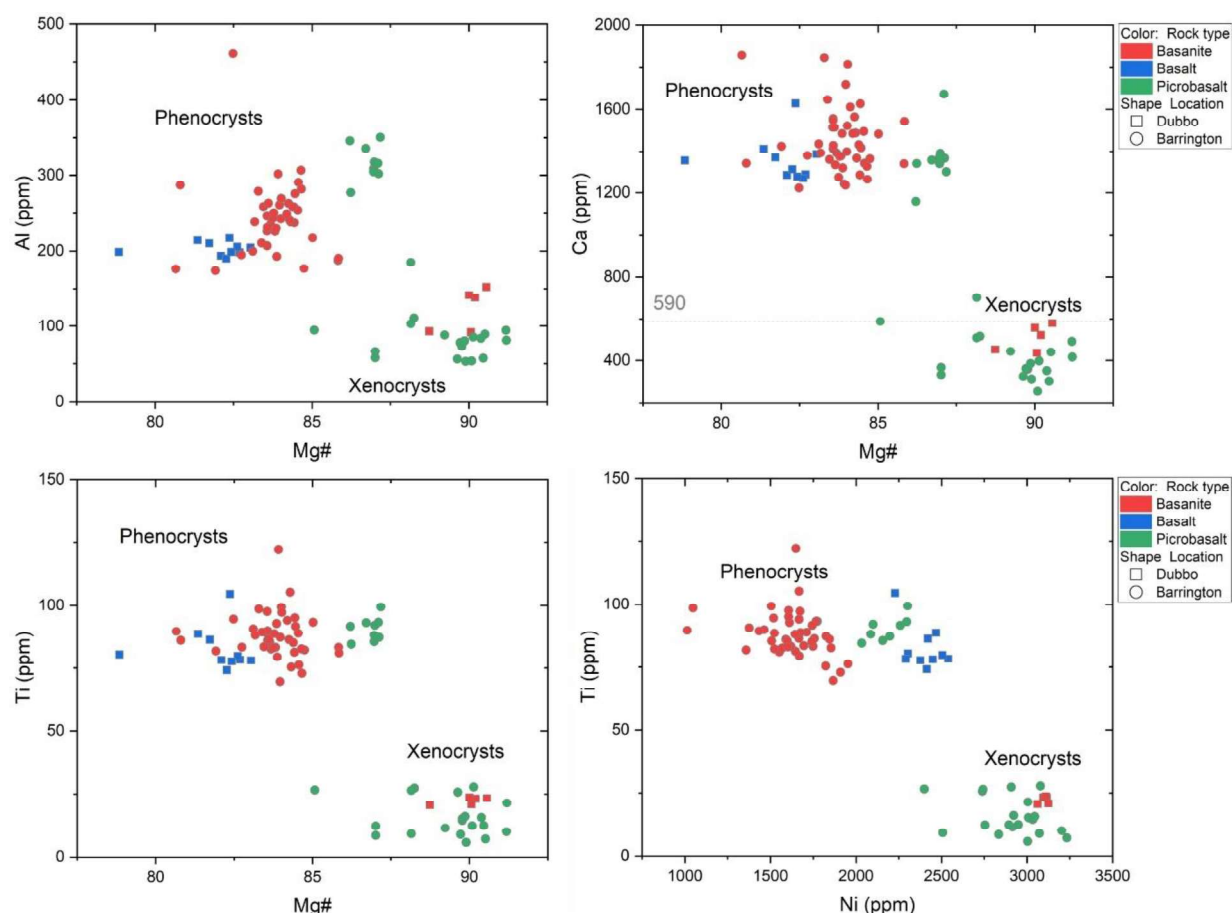


Fig. 15 Distinguishing characteristics of xenocrysts and phenocrysts based on minor and trace elements in olivines.

5.2. Characterisation of the mantle source

5.2.1. Xenocrysts characterize the peridotite facies

Certain elements in olivine xenocrysts are helpful to determine the mineralogy of the peridotite source from which those xenocrysts originate because of their affinities to specific minerals, or because of pressure-dependent partitioning (De Hoog et al., 2010; Bussweiler et al., 2017). For example, Mn and Sc have a strong affinity for garnet compared to spinel: as a result, their abundances in olivine from spinel peridotite are higher than in garnet peridotite. Here, the criteria suggested by (De Hoog et al., 2010) are followed using the distribution of Al vs Mn and Sc vs Zr to identify the source of xenocrysts in our samples (Fig. 16). Although xenocrysts in basanite from Dubbo have higher Al abundances than those in picrobasalt from Barrington, most samples in this study have similar concentrations of Mn (1000-1750 ppm; few samples have higher values up to 3000 ppm) and Al (50-160 ppm), and thus fall in the spinel peridotite field (Fig. 16). The distribution of Sc and Zr is more scattered but confirms the spinel peridotite origin of the olivine xenocrysts.

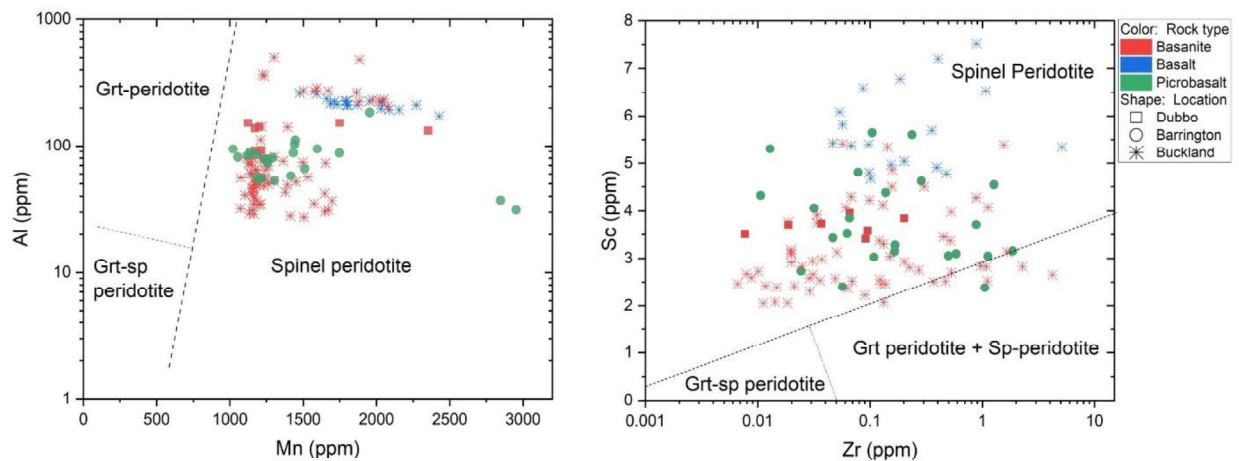


Fig. 16 Identifying peridotite facies based on olivine xenocrysts at Dubbo, Barrington, and Buckland

5.2.2. Source determination based on olivine phenocrysts: Pyroxenite or peridotite?

5.2.2.1. Minor elements: Ni and Fe/Mn

On the basis of olivine phenocryst compositions, previous researchers have used the abundances of the minor elements Ni, Ca, and Mn, and the Fe/Mn ratio to explain the mineralogical characteristics of the source of basalts from different geological settings, such as mid-ocean ridge basalt (MORB) and OIB (Sobolev et al., 2005; Sobolev et al., 2007; Herzberg, 2010). This is mainly based on the assumption that the partitioning of Ni and the ratio of Fe/Mn between olivines and coexisting melts are quite stable and are not subject to temperature and pressure variations (Sobolev et al., 2007; Geng et al., 2019). Instead, the variation in Ni concentration and Fe/Mn ratio in basalt is a function of the bulk composition of the source.

Fe and Mn generally have similar partitioning behaviour during melting of peridotites. The similar behaviour of Mn^{2+} and Fe^{2+} during partial melting dictates that the Fe/Mn ratio is approximately stable (Humayun et al., 2004). Moreover, this ratio depends least on olivine fractionation, and olivine in peridotite has a higher partition coefficient for Fe than for Mn. In this respect, Sobolev et al. (2005; 2007) applied the Fe/Mn ratio in olivine as a parameter to diagnose the difference in parental magma compositions. During the reaction between partial melts of eclogite (recycled basaltic oceanic crust) and peridotite, olivine in the peridotite is replaced by pyroxene to form second-stage olivine-free pyroxenite. Basaltic melt generated from partial melting of this second-stage pyroxenite will have lower Mn/Fe than melts of peridotite, which causes lower Mn/Fe to be inherited and exhibited by olivine phenocrysts that crystallize in these melts (Fig. 17).

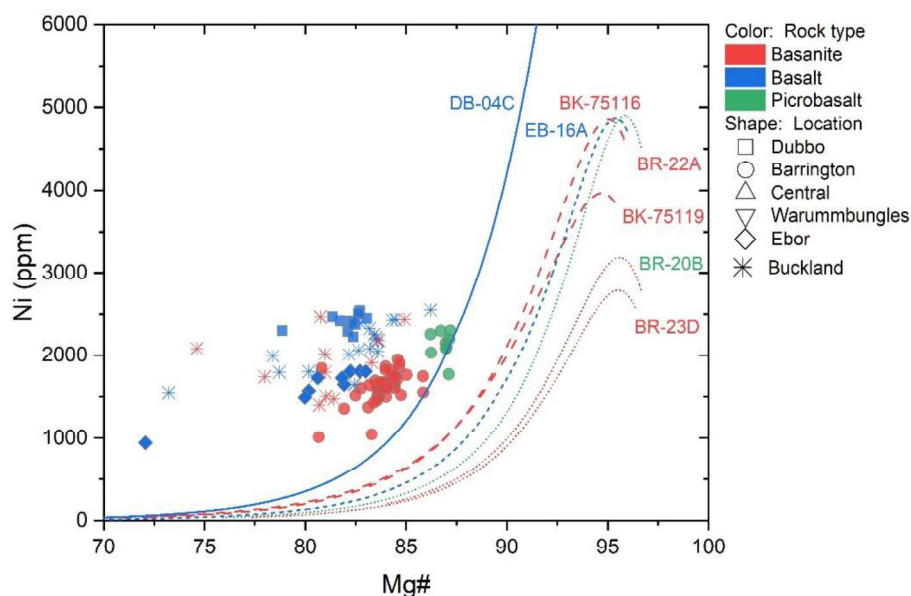


Fig. 17: The curves represent the calculated Ni in olivine with equilibrates with melt based on Primelt3 (Herzberg & Asimow, 2015) from a peridotite source. Rock type is classified by colors; line type represents different locations: solid line-Dubbo, dash line-Buckland, short dot line-Barrington.

Herzberg (2010) proposed a model to predict the evolution of Ni concentrations with Mg# of olivine phenocrysts in basaltic melts derived from a peridotite source (Fig. 17). To assess whether the olivine compositions in the basalts and basanites indicate a peridotite source, here, the whole-rock compositions are used to apply his latest modified model PRIMELT3 (Herzberg and Asimow, 2015) to the New South Wales data. In Fig. 17, it is clear that samples from this study do not match the expected compositions for olivines from a purely peridotite source (shown by the curves in Fig. 17). Ni concentrations in our samples are too high for olivines fractionated from primary partial melts of peridotite alone, which is a composition similar to spinel lherzolite KLB-1 (Walter 1998). Furthermore, since olivine is the first phase to crystallize from the melt, the deviation between samples from this study and the modeled curve could not be caused by fractionation of clinopyroxene or plagioclase (Shea and Foley, 2019), rather, it indicates either peridotite being only partly present in the source or a different source. In terms of whole rock composition, Herzberg (2006) demonstrates the peridotite-source generated basalt from Mauna Kea features a relatively low SiO_2 (<46.9 %), high CaO content ($\geq 10\%$), high MgO content (17.1-19.0%). If the primary magma has low CaO content (less than 9%, for example), and then it is more likely derived from a pyroxenite source than a peridotite source (Herzberg, 2006) due to the residual clinopyroxene. This principle identifies all basalt samples from New South Wales which all have less than 10% CaO and 5-12% MgO, are likely coming from a pyroxenite-dominant source (Fig. 6b) rather than direct melting of peridotite.

Figure 18 displays the variation of Ni/Mg and Mn/Fe from different rocks and potential sources. Olivine from a pyroxenite source should have high Ni/Mg (0.8-2.5) at relatively low Mn/Fe, while olivine from a peridotite source has low Ni/Mg of no more than 0.8 but a range of 1.6-1.9 in Mn/Fe. Samples from this study cover a range of $100 \times \text{Ni/Mg}$ between 0.5-1.1, which is lower than that of Hawaiian OIB, and a range of $100 \times \text{Mn/Fe}$ from 1.2 to 1.8. Basalt samples from Buckland have slightly lower Mn/Fe compared to samples from Dubbo and Barrington. A few basalt samples from Dubbo overlap slightly with a pyroxenite source, and most samples plot below the curve that represents mixing of pyroxenite-derived and peridotite-derived melts (Sobolev et al., 2007). Compared to the Ni/Mg ratio, using the $(\text{Ni} \times \text{Fe})/\text{Mg}$ ratio decreases the effect of olivine fractionation (Sobolev et al., 2007). Therefore, the feature from various geological settings is very clear in the diagram of $(\text{Ni} \times \text{Fe})/\text{Mg}$ against $100 \times \text{Mn/Fe}$. Fig. 18b highlights the difference among samples from Dubbo, Barrington and Buckland, which have similar ranges of Ni/Mg ratio: basalts from Dubbo have consistently the highest $(\text{Ni} \times \text{Fe})/\text{Mg}$, while samples from Barrington have the lowest Mn/Fe, and samples from Buckland have intermediate $(\text{Ni} \times \text{Fe})/\text{Mg}$, and Mn/Fe that just between Hawaii OIB and MORB.

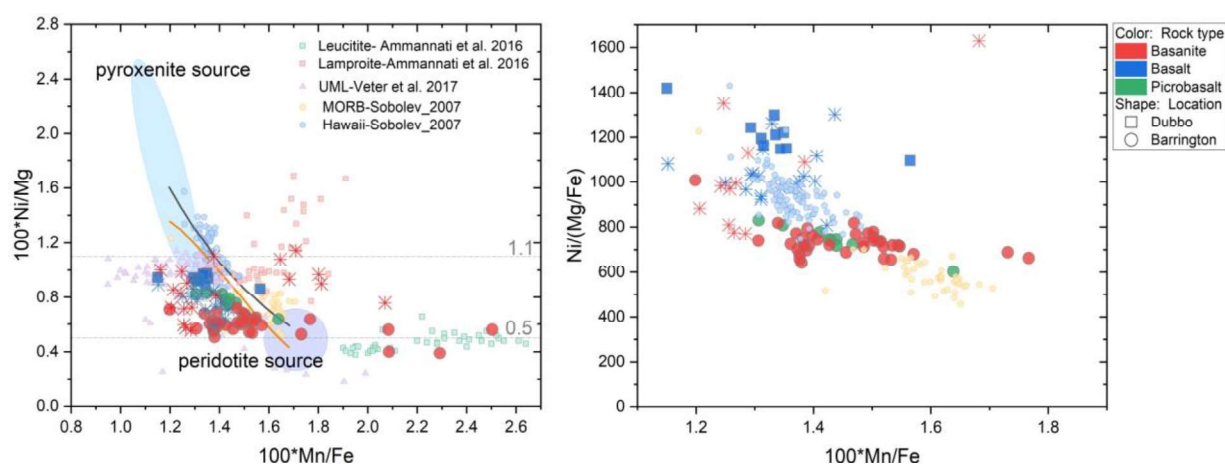


Fig. 18 Diagrams of $100 \times \text{Ni/Mg}$ vs $100 \times \text{Mn/Fe}$ (Fig. a) and $\text{Ni}/(\text{Mg} \times \text{Fe})$ vs $100 \times \text{Mn/Fe}$ (Fig. b). Two curves representing mixtures of pyroxenite-derived and peridotite-derived melts calculated with different Ni partition models ((Sobolev et al., 2007)). The blue oval represents olivine compositions derived from a pyroxenite source, and purple oval represents olivine compositions derived from a peridotite source. Olivines in leucitite and lamproite are from (Ammannati et al., 2016). Olivines in UML (ultramafic lamprophyre) is from (Veter et al., 2017).

All these samples thus appear to come from mixed peridotite-pyroxenite sources rather than a 100% olivine-free pyroxenite source alone. Basaltic samples from Dubbo may have the highest proportion of pyroxenite in the source, followed by Buckland, with the lowest proportion of pyroxenite at Barrington.

If we assume the source is a mixture of peridotite and pyroxenite, then a simple mass balance calculation indicates that 30-70% of pyroxenite is needed for a mixture of pyroxenite and peridotite-derived melt to produce the Ni/Mg vs Mn/Fe of samples from Barrington. Based on Ni and Mn

contents in olivine phenocrysts, (Gurenko et al., 2009) modified the equation of (Sobolev et al., 2008) for the mixing calculation to estimate the proportion of pyroxenite in the mixed source. The equation is based on the partitioning of Ni between olivine and silicate melt (Kinzler et al. 1990), and is written below:

$$X_{py}^m = 6.705 \times \left[Ni \times \frac{FeO}{MgO} \right] / 10000 - 1.332 \times \left[\frac{Mn}{FeO} \right] / 100 + 1.5215$$

Here X_{py}^m represents the fraction of pyroxenite-derived melt. Ni, Mn, FeO and MgO represent their concentrations in olivine, whereby Ni and Mn are given in ppm, while FeO and MgO are in wt.%.

Applying this equation to our samples, an average of 74% of olivine-free pyroxenite-derived melt in the parental magma is needed to account for tholeiitic sample DB-04C from Dubbo, whereas no more than 42% of pyroxenite-derived melt is needed for picrobasalts and basanites from Barrington, and 47% and 63% for basanite from Bingara/Inverell (Central) and alkali basalt from Ebor, respectively. Alkali basalt from Buckland requires less than 67% pyroxenite, while the pyroxenite proportion for Buckland basanites ranges between 28 - 67%. Therefore, in general, alkali basalts need more pyroxenite in the source than basanites.

Although it was assumed that the partitioning of Ni and the ratio of Fe/Mn between olivine and coexisting melts are not affected by temperature and pressure variations (e.g. Fig. 18), other studies advocate that multiple factors could also cause high Ni concentrations in olivine phenocrysts. These include the alkali contents in the melt during crystallization (Foley et al., 2013), the pressure and temperature of mantle source melting, and mantle mineralogy (Ammannati et al., 2016). Herzberg (2010) concluded that Hawaiian tholeiitic lava with Ni-rich olivine phenocrysts might come from a solid-state reaction between recycled crust and mantle peridotite, rather than by the melting of recycled eclogite and peridotite as suggested by Sobolev et al. (2005). Alternatively, melting of peridotite at high temperature and pressure under thick lithosphere may also lead to elevated Ni contents in olivine phenocrysts (Niu et al., 2011; Matzen et al., 2013; Herzberg, 2016; Heinonen and Fusswinkel, 2017; Matzen et al., 2017). Consequently, caution should be taken and a more comprehensive consideration is needed to interpret the source of basalts as a mixed peridotite-pyroxenite lithology based on Fig. 18.

Compared to olivine from basalts and basanites, olivine from other rock types, such as silica-undersaturated leucitites (Fig. 18a), has low Ni but high Mn/Fe compared to olivine from MORB (Ammannati et al., 2016). This high but slightly scattered Mn/Fe ratio (1.8-3.4) was attributed to elevated bulk D_{Fe} relative to D_{Mn} during partial melting of the mantle source. Because Mn/Fe ratio is not affected by olivine fractionation, this feature might require a mineral assemblage in the source

that holds back Ni. In contrast, olivine in silica-saturated lamproites from the same area have high contents of Ni and relatively low Mn/Fe. $D_{Ni}^{Ol/melt}$ calculated for both leucitite and lamproite by (Ammannati et al., 2016) are similar to partition coefficients between olivine and basalt, but much lower than the previously calculated value for ultrapotassic rocks (including olivine from other lamproites (Foley and Jenner, 2004; Foley et al., 2011)). Furthermore, a peridotitic mantle source affected by a CaCO_3 -rich metasomatic agent (i.e. carbonatite) was suggested to be responsible for the minor and trace element features in olivine phenocrysts in leucitite, while lamproite in the same location was attributed to silica-rich melt reacting with the ambient mantle at the expense of olivine (Ammannati et al., 2016). At this point, high Ni/Mg ratio is consistent with the enrichment of orthopyroxene in the source assemblage that was interpreted as pyroxenite source signature. Therefore, olivines in samples from Dubbo and Buckland most possibly indicate a larger contribution from a pyroxenite source than samples from Barrington (Fig. 18b).

Olivine phenocrysts in ultramafic lamprophyres (UML) from Aillik Bay lie to the left side of olivine of Mediterranean lamproite (Fig. 18a). This low Mn/Fe and Ni/Mg feature was suggested to be inherited from phlogopite and carbonate in the source (Veter et al., 2017), given that phlogopite crystallized in the mantle during the earlier episode of lamproite magmatism. This includes phlogopite that could contain a considerable Ni content. For example, phlogopite phenocrysts in Mediterranean lamproites carry 355-1380 ppm Ni (Fritschle et al., 2013). Carbonatitic phlogopite can exhibit low Ni abundances but much higher concentrations of Mn (Reguir et al., 2009). Therefore, the presence of phlogopite in the source may shift the Ni distribution into an area slightly below the Hawaiian OIB field at lower Mn/Fe. In this study, the low Ni/Mg and Mn/Fe olivines in our samples all lie to the left of the modelled mixed peridotite+pyroxenite source, similar to the position of the ultramafic lamprophyres from Aillik Bay. This feature conforms to a plausible phlogopite or carbonatitic contribution in the source.

Moreover, both olivines in OIB and MORB have a narrow distribution in $100 \times \text{Mn/Fe}$ (Fig. 18a), while all olivines in rocks from metasomatized sources have significantly wider ranges in $100 \times \text{Mn/Fe}$. Given that the Fe/Mn ratio depends least on olivine fractionation, the wide range in samples from this study, especially Buckland and Barrington, might support a silica-rich or carbonate-rich metasomatized end-member in the source.

In summary, established tests for peridotite and pyroxenite in the mantle source appear to conclude that the eastern Australian magma sources tend to be a mixture of peridotite and pyroxenite or at least a pyroxenite-dominated lithology, and yet their position on Fig. 18a is offset to lower Mn/Fe compared to these mixing models. Further trace element indicators and a

combination of evidence from olivines with whole-rock analyses are needed to assess the metasomatized end-member in the source.

5.2.3. Other parameters for identifying pyroxenite in the source

5.2.3.1 Zn/Fe vs Mn/Fe

Another useful diagram for the characterisation of source mineralogy is Zn/Fe against Mn/Fe, because fractionation of Mn, Fe, and Zn are not affected by olivine and orthopyroxene during melting (Le Roux et al., 2011). Fractionation of Zn/Fe among olivine, orthopyroxene and melt is equal: the inter-mineral exchange coefficient $K_{D(C/M)}^{Zn/Fe}$ of olivine is similar to that of orthopyroxene with a value between 0.9-1, while both $K_{D(C/M)}^{Zn/Fe}$ of clinopyroxene and garnet are $\ll 1$ (Le Roux et al., 2010). Therefore, Zn/Fe ratio of the magma can only be significantly fractionated by clinopyroxene or garnet. This can thus be used as an indicator to identify clinopyroxene and/or garnet-rich mantle lithologies in the sources of magmas. In this respect, high Zn/Fe in a primitive magma might result from a pyroxenite source enriched in clinopyroxene and garnet. In arc environments, hydrous fluid released from a subducted slab could introduce enrichment of Zn in the mantle source, thus causing a high Zn/Fe ratio (Kamenov et al., 2008), but this is not the case for the samples of this study. Therefore, the Zn/Fe ratio in olivine phenocrysts might also be a good indicator to track the parental magma and would have wider applications for the evolution of the magmas.

In this study, whole-rock compositions (Fig. 19a) indicate that only basalts from Dubbo have high Zn/Fe ratio and lie in the pyroxenite field. In terms of olivine (Fig. 19b), almost all samples from Buckland and tholeiitic samples have high Zn/Fe ratio and lie in the pyroxenite area, while only a few basanitic samples from Barrington have high Zn/Fe: most basanitic and picrobasaltic samples have low Zn/Fe ratio. Both Zn/Fe and Mn/Fe ratios in whole-rocks and olivines of Dubbo stay in the same position, which supports the partitioning behaviour of Zn, Mn, and Fe described above. This signature means that the high Zn/Fe basalts originate either from a clinopyroxene and/or garnet-enriched pyroxenite. On the other hand, this signature confirms the partition behaviour of Zn, Mn, and Fe mentioned above. Samples from Ebor and Bingara/Inverell (Central) are most possibly affected by a peridotite source, this is confirmed by the olivine xenocrysts in sample from the Bingara/Inverell (Central), which have the signature that is similar to xenocrysts from other locations. However, there is no xenocryst in samples from Ebor to confirm this. The inconsistency between whole-rock data and olivines in basanitic samples from Barrington might mean that these samples

have higher proportion of peridotite-derived olivine xenocrysts, rather than meaning that they were derived from partial melting of peridotite. Although the presence of sulphide in the source would affect Cu, Zn, and Ni budgets (Le Roux et al. 2010), no sulphide-bearing xenoliths were previously reported from the sampled areas (O'Reilly & Griffin, 1987). However, in Allyn River which lies 360 km east of Dubbo and 41 km south of Barrington Tops, Powell and O'Reilly (2007) found sulphide (up to 50-80 μm) in melt patches of spinel lherzolite xenoliths. Those sulphides were interpreted as low-temperature recrystallization of a sulphide melt at lithospheric mantle. Nevertheless, the scale of the proposed sulphide melt has not been confirmed. Thus, the possible effect of sulphide in the source region of Barrington cannot be estimated.

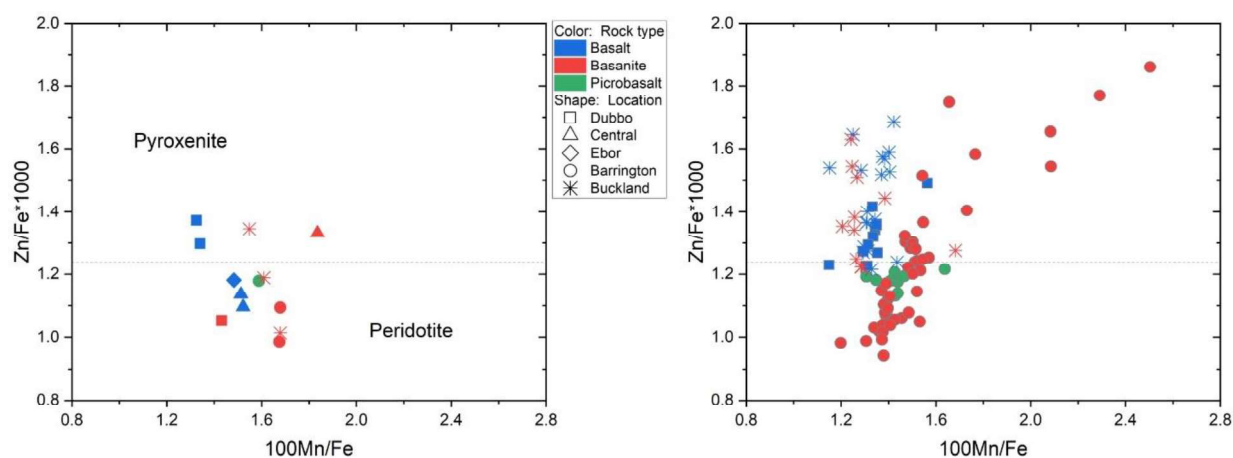


Fig. 19 a. $100 \cdot \text{Mn}/\text{Fe}$ vs $\text{Zn}/\text{Fe} \cdot 1000$ indicating two possible sources for basalts based on whole-rock analysis (a) and olivine (b). The horizontal line divide the diagram into two fields: pyroxenite (top) and peridotite (bottom).

5.2.3.2 FC3MS ($\text{FeO}^{\text{T}}/\text{CaO} - 3 \cdot \text{MgO}/\text{SiO}_2$) parameter

In addition to trace elements in olivine, major elements in whole rocks are also helpful to identify source mineralogy (Yang and Zhou, 2013; Yang et al., 2016; Howarth and Harris, 2017). For example, FC3MS ($\text{FeO}^{\text{T}}/\text{CaO} - 3 \cdot \text{MgO}/\text{SiO}_2$) is a parameter designed to discern pyroxenite from peridotite source generated continental oceanic island basalt-like volcanic rocks (Yang and Zhou, 2013). This parameter is based on a large amount of data from melting experiments on peridotite and pyroxenite and is mainly dependent on the composition of bulk rocks and the degree of melting. Using $\text{FeO}^{\text{T}}/\text{CaO}$ to represent the effect of clinopyroxene and MgO/SiO_2 for the role of olivine and considering the different extent in fractionation of clinopyroxene and olivine during partial melting of peridotite and pyroxenite, magma derived from these two sources would have characteristics reflected in $\text{FeO}^{\text{T}}/\text{CaO}$ and MgO/SiO_2 ratio. Especially, magmas from partial melting of pyroxenite would feature a wide $\text{FeO}^{\text{T}}/\text{CaO}$ ratio with a short range of MgO/SiO_2 ratios and tend to parallel with clinopyroxene. Therefore, FC3MS which combines these two parameters together

can be used to identify the dominant source lithology of pyroxenite or peridotite. Generally, basalt derived from peridotite has a FC3MS value ≤ 0.65 , whereas most garnet-pyroxenite-derived basalts with $\text{MgO} > 7.5\%$ lie above or around the value of 0.65 ± 0.35 . FC3MS enables to identify the dominant pyroxenite source of Continental oceanic island basalt-like volcanic rocks despite their variable MgO contents (Yang and Zhou, 2013). However, this has only been applied in the past to explain basalts, not basanites. In the diagram FC3MS vs MgO (Fig. 20), all basalts from this study (Dubbo and Bingara/Inverell area) lie high enough to indicate a pyroxenite source. In contrast, all basanites and picobasalts lie in the peridotite source area but all lie above 0.3 which is within the uncertainty of FC3MS. Picobasalt has low FC3MS and high MgO which suggests a non-pyroxenite melting mechanism for this magma. The indication that basalts from Dubbo have pyroxenite in their source matches the evidence from $100 \cdot \text{Mn}/\text{Fe}$ vs $1000 \cdot \text{Zn}/\text{Fe}$ based on whole-rock analyses (Fig. 19a). In this figure, all samples from Bingara/Inverell (Central) and Ebor lie in the pyroxenite derived melt area. Since this signature contradicts Fig. 18a slightly, it might mean that those samples are from a mixed source of peridotite and pyroxenite.

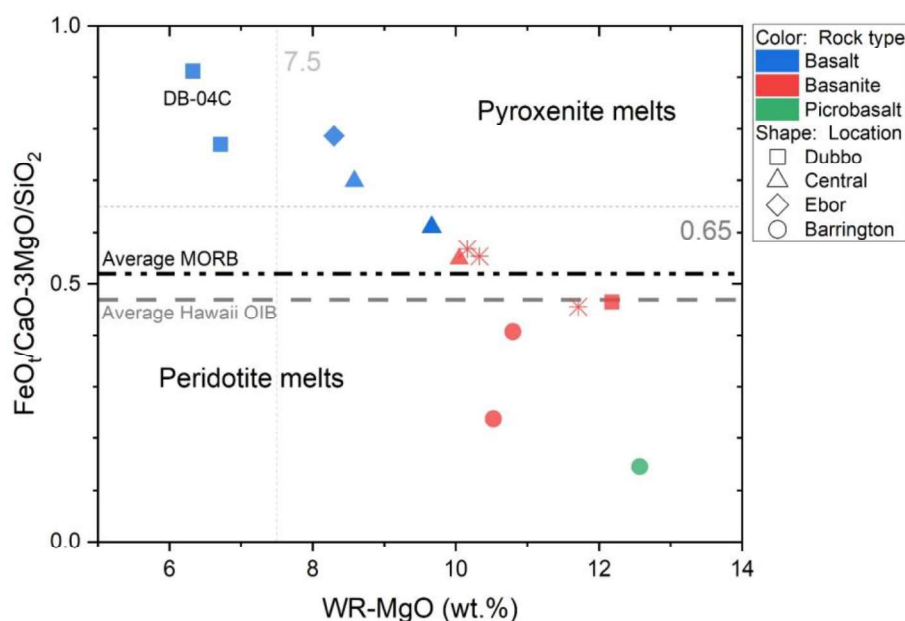


Fig. 20 Source determination based on MgO vs FC3MS of whole-rock composition with average MORB (Schmidt & Poli 1998) and OIB samples (Dasgupta et al. 2009). Here the average Hawaii OIB is lower than Average MORB and lie in the peridotite melts area, might be caused by heterogeneity of samples from Hawaii islands.

5.2.4. Possible influence of continental crustal material based on phenocrysts

Lithium and Zinc enrichment in olivine can indicate the influence of continental crustal material (Foley et al., 2013). Li is strongly enriched in the continental crust; the mantle only holds 1.9 ppm Li that is dominantly hosted by olivine and orthopyroxene (Ryan and Langmuir, 1987). Intercrystalline partitioning of Li is not sensitive to temperature, pressure or bulk composition (Seitz and Woodland,

2000). In different metasomatic processes, Li will partition into different minerals: Li partitions more into clinopyroxene during silicate metasomatism and tends to be concentrated in olivine in carbonatite metasomatism (Su et al. 2014). Therefore, the concentration of Li in olivine is a good tracer for metasomatic processes. Zinc is sequestered dominantly in olivine in mantle rocks, because of the higher partition coefficient for Zn in olivine compared to other minerals in basaltic and mantle rocks. According (De Hoog et al., 2010), olivine is the major host for both Li and Zn in the mantle, with 80% and 75% of the mantle budget, respectively.

Fig. 21a shows the distribution of Li and Zn from different rock samples. In this figure, four features can be recognized: Samples from this study have very low Li (2-8 ppm) but significant Zn (109-227 ppm) concentrations. These are all much lower than in leucitites and lamproites from the Mediterranean, which show extremely high concentrations of Li and Zn thought to be derived from continental material in the source (Foley et al., 2013; Prelević et al., 2013). Olivine samples from UML have low concentrations of both Li and Zn (Veter et al., 2017). These are thought to be near-primary melts of carbonated mantle at high pressures (4-7 GPa) in a rift environment with no involvement of recycled crust (Tappe et al., 2006).

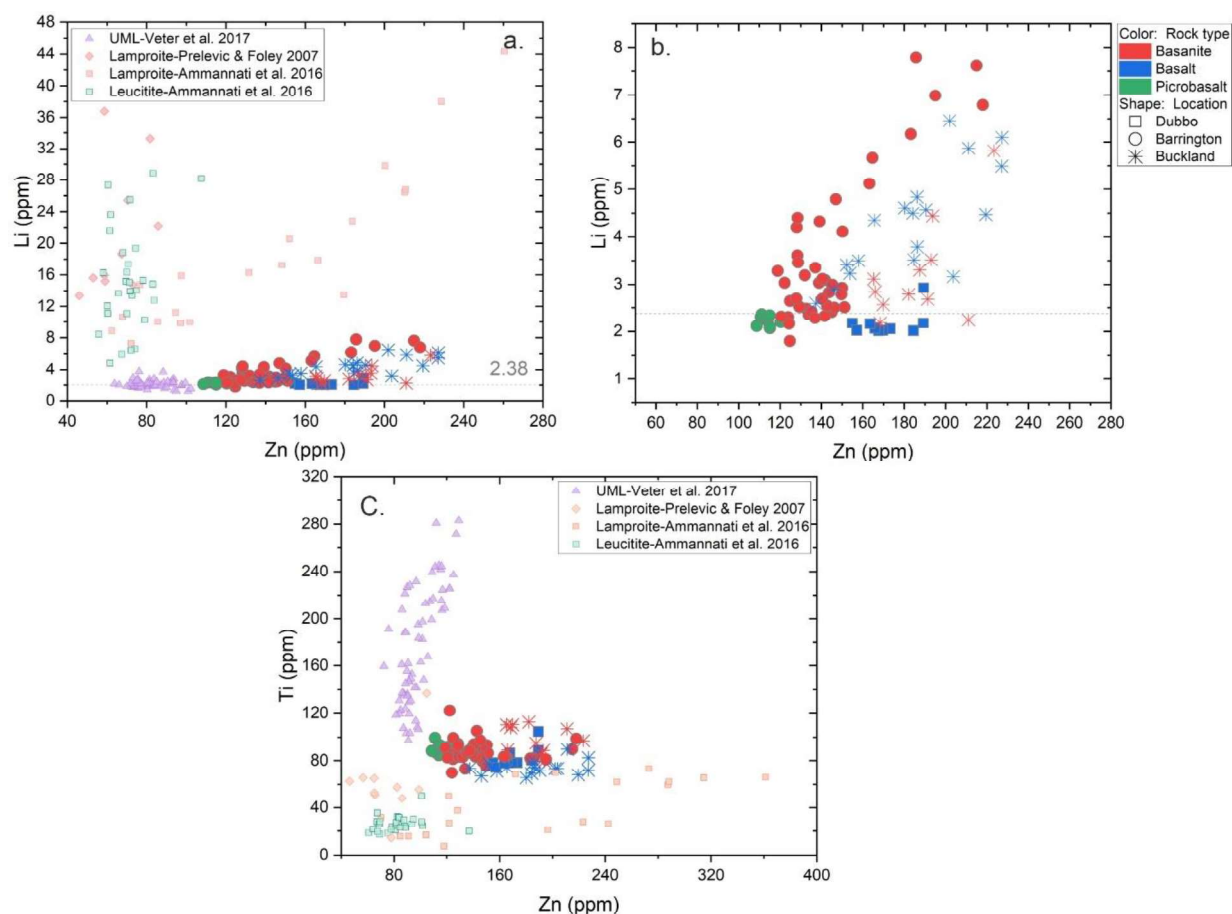


Fig. 21 Relationship between Zn and Li (a), close-up of Zn vs Li in olivines from this study (b), Zn vs Ti (c). In the first two figures, the dashed line represents the upper limit of Li in olivine xenoliths from mantle (2.38 ppm). (De Hoog et al., 2010).

Fig. 21b is the close-up of the lower part of the Li-Zn distribution diagram. Olivines in picrobasalts from Barrington have the lowest Li and Zn concentration, and those in basanites from both Barrington and Buckland have variably enriched Li and Zn content. In the samples from Buckland, a rock type-related correlation exists in Li concentration: olivines in alkali basalts generally have higher concentrations of Li than olivines in basanites. The highest Li concentrations in olivine xenocrysts from different locations is 2.38 ppm (De Hoog et al. 2010), while most phenocrysts in samples from this study are higher than that value, except sample DB-04C from Dubbo.

Fig. 21c shows the variation of Ti with Zn. Ti concentrations in olivine from this study range from 60 to 120 ppm. Both Ti and Zn are concentrated in a small range. Basalt and lamproite have low Ti but high Zn, and generally, the former has slightly higher abundances of Ti compared to the latter. Ti is often enriched by various types of metasomatism, such as Fe-Ti-metasomatism in kimberlitic olivines (Vetter et al., 2017), and especially beneath cratonic areas (Eaton et al., 2009).

In summary, some samples from Dubbo and Barrington have slight enrichment in Li as is also seen at Buckland, but most olivines have no more than 4 ppm Li. The partition coefficient for Li between olivine and melt determined by experiments at upper mantle conditions (3-14 GPa, 1600-1900 °C) lies in the range 0.21-0.56 (Taura et al., 1998) and is higher than that for orthopyroxene and clinopyroxene (0.1-0.25) (Blundy and Wood, 1994). Therefore, enrichment of Li in phenocrystic olivine indicates that the melts were derived from a Li-rich source, since Li would partition more into the melt than into all mineral phases. In addition, when phlogopite is present in the source, it will preferably take up Li with respect to olivine, orthopyroxene or clinopyroxene (Seitz and Woodland, 2000).

Zinc has a similar ionic radius to Mg and is mainly hosted by olivine in mantle peridotites (De Hoog et al., 2010). As for other first-row transition elements (FRTes), partitioning of Zn is susceptible to changes in mineralogy and major element composition. However, there are only few studies of the partitioning of Zn in mantle rocks. $D_{Zn}^{Ol/lq}$ determined by Kohn and Schofield (1994) at 1 bar, 1150-1400 °C in a Fe-free system ranges from 0.77 to 1. The partitioning behaviour of Zn^{2+} and Mn^{2+} are affected more by melt composition than temperature; highly polymerized melts have high partition coefficients (up to 4.5 for Zn^{2+} and 3.0 for Mn^{2+}). Le Roux et al. (2011) determined an average partition coefficient of 1.04 ± 0.12 at 1.5-2 GPa, 1300-1500 °C. Therefore, the variation of Zn in basanite from Barrington might result from magma evolution, while the difference between samples from Barrington, Dubbo and Buckland might indicate mineralogical diversity in the source.

The range of Li in olivine from equilibrated un-metasomatized peridotites is restricted to 1 to 2 ppm, and the partitioning of Li is not sensitive to pressure, temperature and bulk composition (Seitz and Woodland, 2000), while olivine from metasomatized peridotite commonly has elevated Li content that may result from disequilibrium redistribution. In this study, all our samples have Li contents higher than the range for olivine from un-metasomatized peridotite. The correlated increase of Li with Zn at low Ti concentrations shown in Fig. 20c may indicate the involvement of recycled continental crust (Foley et al., 2013). Therefore, the elevated Li in olivines of our samples (Barrington, Buckland) might indicate that the host basalts are derived from a metasomatized pyroxene-rich source. However, picrobasalt from Barrington and tholeiitic basalt from Dubbo do not show this signature, and their source has probably been least affected by metasomatism.

5.2.5. Indicators and identification of metasomatism in the source

5.2.5.1 Possible metasomatism signature in olivines

Ca and Ti are not only useful in distinguishing phenocrystic from xenocrystic olivine, but also in identifying the type of melt that causes metasomatism (Foley et al., 2013). For igneous olivines, contrasting trends in the variation of Ti against Ca are caused by melting of different sources (Fig. 22 a,b): low Ca (<500 ppm) and Ti (<50 ppm) is typical for unmetasomatized mantle olivine. Olivines in ugandite from a Ti-rich silica-poor metasomatic source in the East African Rift show characteristically high Ti at low Ca concentration.

A coupled increase of Ca and Ti is characteristic for within plate volcanism or rift-related continental rocks, here shown by two trends: ultramafic lamprophyres from the edge of the Labrador Sea rift (Veter et al., 2017), and a lower Ti trend composed of samples from this study (65-114 ppm in Ti and 1000-2000 ppm in Ca) and the Canary Islands. Low Ti but high Ca is characteristic of Mediterranean leucitites derived from a metasomatically CaCO_3 -enriched peridotitic mantle, whereas low-Ca olivines in Mediterranean lamproites were suggested to have crystalized from high-Si and low-Ca magmas from mantle metasomatized by a silicate melt (Ammannati et al., 2016). Compared to these, samples from this study have moderate abundances of Ti and Ca. Samples from the Canary Islands (Gurenko et al., 2009) shown in Fig. 22a have correlated Ti and Ca concentrations that are higher than olivines from this study. The carbonatitic metasomatism was evidenced by the presence of phlogopite and high whole-rock $\text{CaO}/\text{Al}_2\text{O}_3$ ($\gg 1$; Neumann et al., 1999), and inclusions of carbonate droplets in spinel peridotite xenoliths (Frezzotti et al., 2002). Basaltic magmas from Lanzarote, the easternmost island of the Canary Islands, were suggested to originate from

heterogeneous mantle that had been affected by carbonate metasomatism (Gómez-Ulla et al., 2018). Olivines in the Lanzarote basaltic magmas have scattered Ca concentrations ranging from 178-2700 ppm with a median of 1650 ppm (Gómez-Ulla et al., 2017), which is a similar concentration range to our samples. Therefore, this distribution is reminiscent of carbonatitic metasomatism, but further supporting evidence is needed.

Ca abundances in olivine largely depend on MgO content and melt composition; the partitioning of Ca is not sensitive to oxygen fugacity or temperature (Libourel, 1999). For example, 15% Na₂O in the melt can significantly increase the amount of Ca concentration in olivine, 6 times higher than for Na₂O-free melts. Furthermore, enrichment of Ca in olivine may correlate with Ca content and undersaturation of silica in the coexisting melt. Therefore, the Ca contents in our samples might indicate a silica-undersaturated agent that is enriched in calcium and/or alkalis. Although the Ca content in olivine can be affected by alkalis in the melt, it is not affected by Ti concentration in the melt (Libourel, 1999). Of possible relevance here is that although the lithosphere is thicker at Barrington and Buckland than Dubbo, and they are located closer to the cratonic lithosphere edge, the Ti contents in olivines are quite constant across all locations.

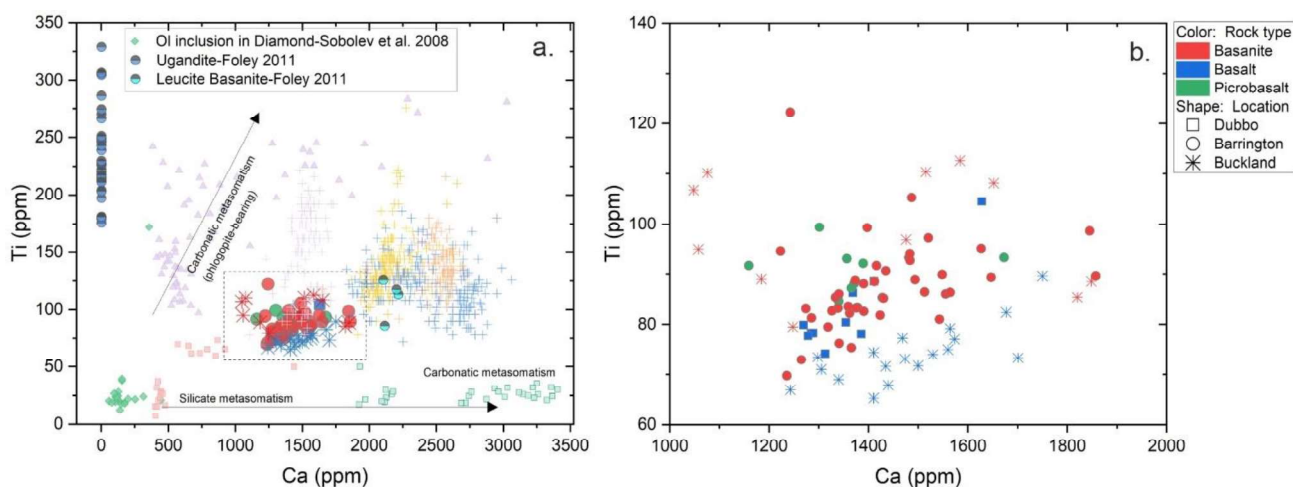


Fig. 22 a: Ca vs Ti in olivines. Crosses indicate samples from Canary Islands (Gurenko et al., 2009). Orange-La Palma; yellow-Tenerife, light purple-El Hierro, blue-La Gomera.) Triangles-lamprophyre ((Veter et al., 2017)). Pink square-lamproite, green square-leucitite (Ammannati et al., 2016). The area in the box are samples from this study. b. Closeup of Ca vs Ti in olivines of samples from this study (the box in fig. a).

5.2.5.2 Possible signature of metasomatism in whole-rock compositions

The effects of carbonatite metasomatism should be detectable in the bulk rock compositions in addition to appearing as signatures in the trace element patterns of olivines.

Zr and Hf are two incompatible elements with similar geochemical behaviour. They have similar partition coefficients for the major mantle minerals and the Zr/Hf ratio of basalts from different

geological settings varies over a fairly small range between 33 and 40 (Dupuy et al., 1992). The elevated Zr/Hf of undersaturated intraplate basalts usually correlates with carbonatite involvement, so that this ratio can be used as an indicator for metasomatism caused by carbonate-rich fluids. In this case, high Zr/Hf and correspondingly low Ti/Eu may indicate carbonatitic metasomatism (Fig. 23, Shea and Foley, 2019).

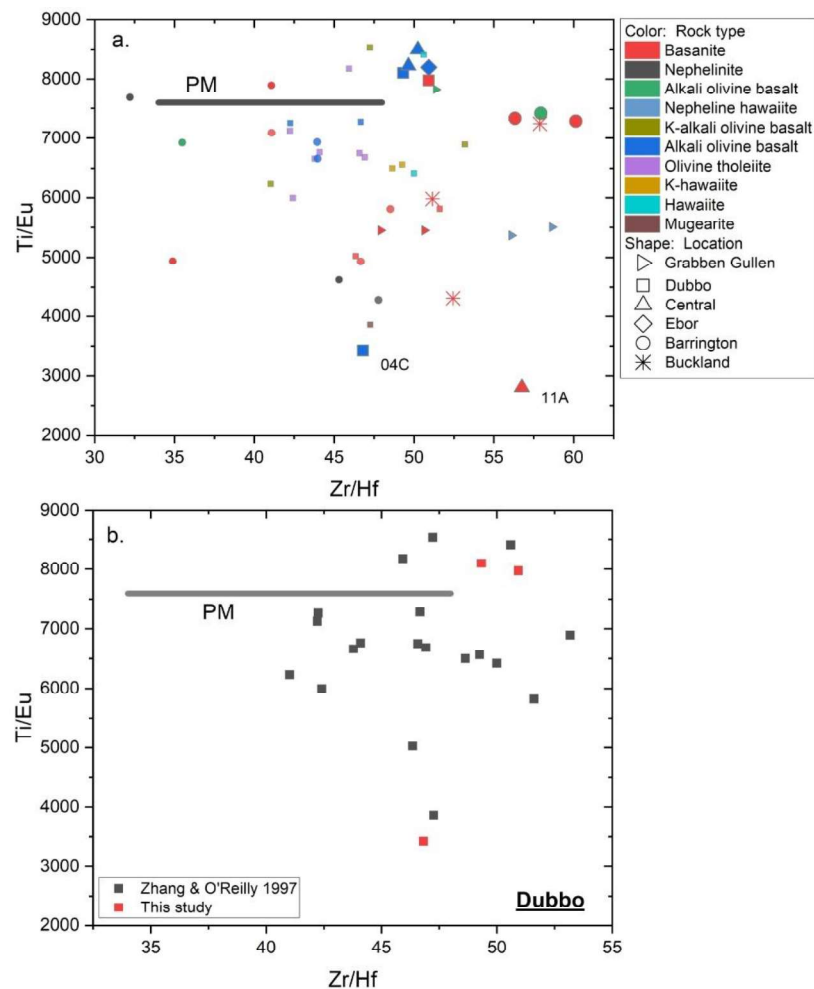


Fig. 23 a. Zr/Hf vs Ti/Eu of bulk rocks (Small symbols are from other researchers: Barrington-O'Reilly and Zhang, 1995, Sutherland and Fanning, 2011); Grabben Gullen-O'Reilly and Zhang, 1995; Dubbo-Zhang and O'Reilly, 1997; b. Zr/Hf vs Ti/Eu of all samples from Dubbo.

Zr/Hf ratios in samples from Buckland, Barrington, and CR-11A from Bingara/Inverell are all higher than the primitive mantle value (fractionates from 34 to 48) (Fig. 23). However, only two basanite samples from Buckland and CR-11A from Bingara/Inverell have markedly low Ti/Eu (lower than the primitive mantle value of 7598). Ti/Eu has a stronger correlation with location than with rock type: most samples from Dubbo in this study have high Ti/Eu ratios that range between 6000 and 8500 (Fig. 23b). In addition, as shown in Fig. 23a, previous results on basanite, alkali olivine basalt, nepheline hawaiiite from Grabben Gullen are mainly concentrated in the range 5366-5502 (O'Reilly and Zhang, 1995). However, samples from Barrington show a larger variation: 4288-7895 and have

scattered Zr/Hf in basanites (35 to 60). Therefore, these three samples might indicate carbonatite metasomatism in the source assemblage of Buckland and Bingara/Inverell area.

The presence of certain minerals can contribute to high Zr/Hf in the whole-rock compositions; one is the presence of residual amphibole in the source. Amphibole has a higher partition coefficient for Hf (1.56) than for Zr (0.08-0.89) (Tiepolo et al., 2007). Thus, it could hold back more Hf in the source and lead to high Zr/Hf in the magma. On the other hand, garnet has a higher partition coefficient for Zr than Hf in basaltic melts (2.12 and 1.22, relatively; (Hauri et al., 1994), while the bulk partition coefficient during melting of spinel lherzolite is $D_{Zr/Hf} < 1$. This is consistent with the xenocrysts evidence that the peridotite source for basaltic samples in this study is spinel lherzolite rather than garnet lherzolite source.

In addition to amphibole, rutile also has a higher partition coefficient for Hf than Zr in basalt melts (4.98 and 3.07, respectively; (Foley et al., 2000), but only if enough rutile remains in the source will Hf be retained, leading to elevated Zr/Hf ratio in the melt. However, this is unlikely in the geological setting of the current study, as rutile is unlikely to be residual in an intraplate environment.

Apatite has been suggested to be a product of carbonate metasomatism of peridotites. The partition coefficient of Zr between apatite and carbonatite is very low (0.008-0.011), while the partition coefficient of Hf between apatite and carbonatite is between 0.004-0.02 (Klemme and Dalpé, 2003). The slightly higher value of Zr than Hf might contribute to the high Zr/Hf of magma if apatite is exhausted.

The Ti/Eu ratio may also be influenced by apatite during carbonatitic metasomatism, because Eu is strongly compatible in apatite, which is highly soluble in carbonate melts (Paster et al., 1974; Green et al., 2000; Dawson and Hinton, 2003). Thus, melting of apatite in the source should lead to a high Eu content in the melt, and consequently low Ti/Eu in basaltic melts derived from an apatite-bearing source caused by carbonate metasomatism.

Since P has very low partition coefficients between olivine, orthopyroxene, garnet and carbonatite liquid, and Ti-bearing minerals such as rutile and ilmenite also have low solubility in these melts (Baker and Wyllie, 1992), high P_2O_5/TiO_2 is taken as an indicator of carbonatitic metasomatism. This is supported by basaltic samples from Lanzarote, Canary Islands (Fig. 24a, b), which are suggested to have been affected by carbonate melts in the source (Gómez-Ulla et al., 2018). In this respect, basanites from Binagra/Inverell area might have experienced a higher degree of carbonatitic metasomatism than Buckland and Barrington. As shown in Fig. 23a, all basanites from this study have higher P_2O_5/TiO_2 (0.22-0.66) than basalts (0.17-0.22), CR-11A from Mount Russell (Bingara/Inverell area) has the highest P_2O_5/TiO_2 ratio and the lowest SiO_2 content. The Dubbo

basalt has the lowest probability of having experienced carbonatitic metasomatism. Moreover, basalt samples from the Hawaiian Islands (Rhodes and Vollinger, 2004) have still lower P_2O_5/TiO_2 , no more than 0.24, and are all lower than values of samples from this study. Basanite samples from the Hawaiian Islands (not plotted) have similarly low ratios. On the other hand, carbonatitic metasomatism in the source of Barrington samples is consistent with previous proposals that metasomatism formed amphibole or apatite in the subcontinental lithospheric mantle (O'Reilly and Zhang, 1995) at Barrington.

Although basalt sample DB-04C from Dubbo has low Ti/Eu, its Zr/Hf ratio is even lower (46.8) and lies in the primitive mantle range (34-48). This might mean that either this basalt came from the deep mantle as a result of melting at high pressure and temperature, and/or it had less carbonatitic component in the source. On the other hand, the P_2O_5 concentration in this Dubbo basalt is very low (Fig. 7) so that it may come from a source assemblage without apatite. Another possibility is high degree melting of pyroxenite in the lower lithospheric mantle that exhausted apatite. All basanite rocks from this study have higher P_2O_5/TiO_2 than basalts, and all basalts from this study have higher Na_2O+K_2O than OIB (Rhodes and Vollinger, 2004; Gómez-Ulla et al., 2018).

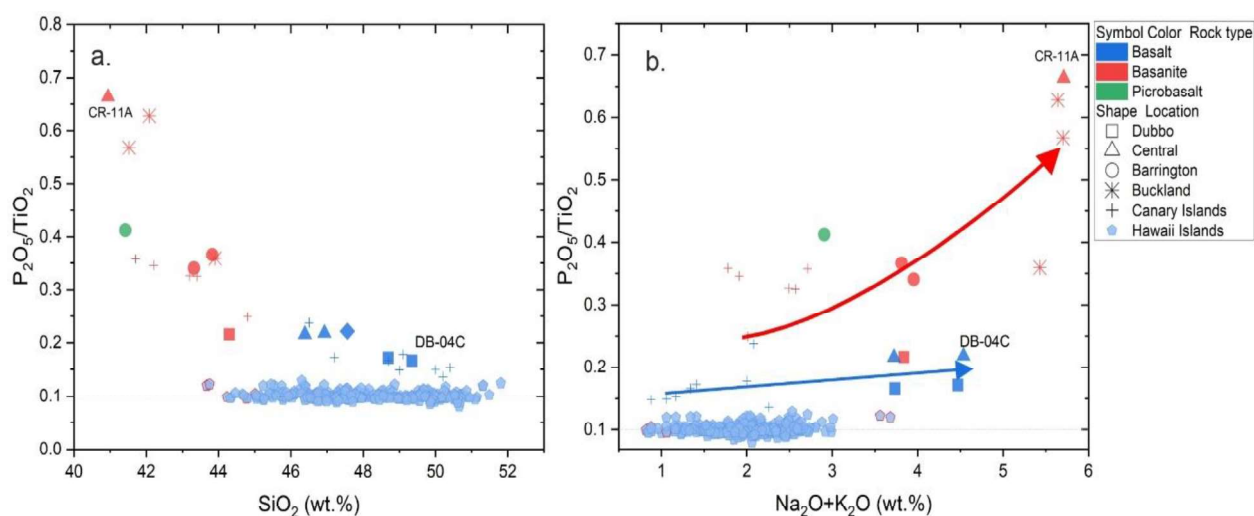


Fig. 24 SiO_2 vs P_2O_5/TiO_2 , (a.) and Na_2O+K_2O vs P_2O_5/TiO_2 (b.) In whole-rock samples. Crosses are basanite (red) and basalt (blue) from Lanzarote, one of the Canary Islands (Gómez-Ulla et al., 2018); Blue pentagons are basalts from the Hawaiian Islands (Rhodes and Vollinger, 2004), some with red rims representing two basanite and three picrobasalt samples.

The Sr/La vs K/Nb diagram (Fig. 25) can be used to distinguish between amphibole and apatite in the source based on their differing partition coefficients for Sr and La (Shea and Foley, 2019), whereas low K/Nb indicates residual phlogopite. This figure indicates that apatite and/or phlogopite may be in the source for all samples, but there is no indication of amphibole. Therefore, apatite rather than amphibole might result from carbonatitic metasomatism at these locations. Furthermore, Sr partitions into calcite more strongly than into apatite ($D_{cal/ap}$ value of 1.22), while

La preferentially partitions into apatite ($D_{\text{cal/ap}}$ value of 0.24) (Dawson and Hinton, 2003). Thus, magma from a source metasomatized by carbonatitic melts should have low Sr/La if calcite retains Sr in the source (Fig. 25), and the low Sr/La might be explained by melting of apatite resulting from carbonatitic metasomatism. This requires apatite to remain in the residue in the source region. Fig. 25 does not support residual amphibole in the source, which might have caused high Zr/Hf in the magma.

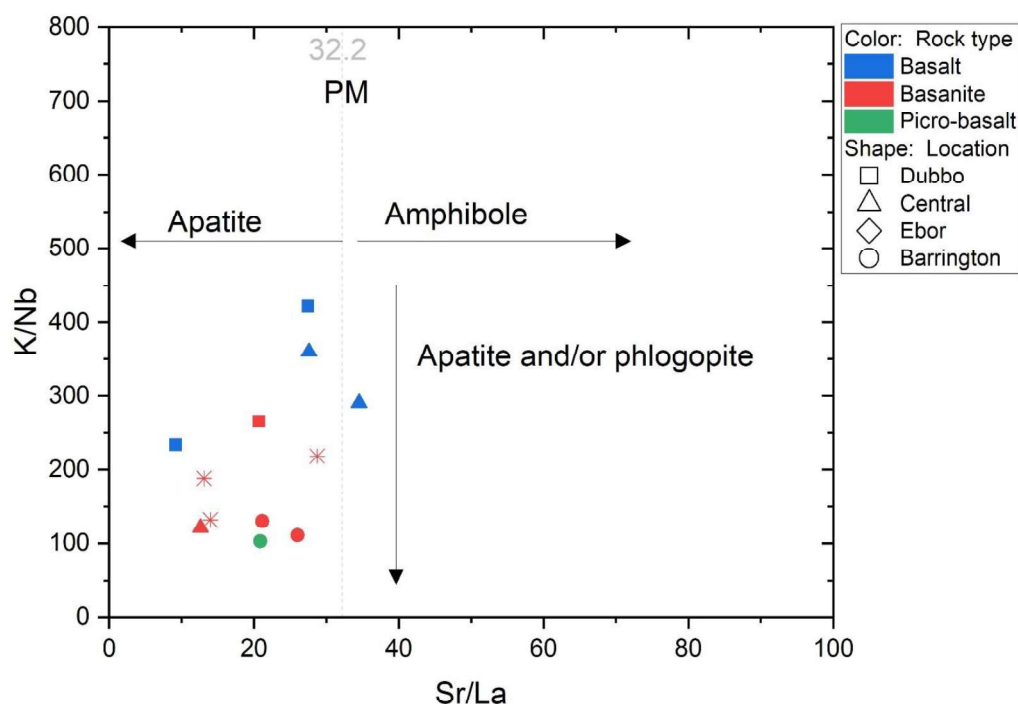


Fig. 25 Sr/La vs K/Nb ratio in whole-rock indicating different OH-bearing minerals resulted from a carbonatitic metasomatism

5.2.6. Redox conditions

Vanadium has different valences that are sensitive to the oxidation state of the magma. Previous research indicates that the controlling factor for partitioning of V between olivine and melt is the oxygen fugacity (Canil, 1997); with increasing oxygen fugacity, the partition coefficient $D^{\text{Ol/liquid}}$ for vanadium decreases because V^{3+} is incorporated in olivine but V^{5+} is not. Since V and Sc have similar geochemical behaviour but only the former is sensitive to oxidation change, V/Sc may be used to trace the oxidation state in the source (Li and Lee, 2004). Figure 26 indicates the distribution of samples from this study and compares them to olivines from peridotite (De Hoog et al., 2010). Almost all samples from this study have a V/Sc value < 3 , which is indicative for oxidised conditions, and might have experienced metasomatism (Foley et al., 2013). However, the V/Sc ratio should be used with caution because Sc and V contents may be affected by amphibole, which has much higher

partition coefficients for Sc and V relative to olivine (Tiepolo et al., 2007). The partition coefficient for Sc and V in amphibole lie in the range 1.62-35 and 1.49-22, respectively. While Sc and V are incompatible in olivine (partition coefficients of 0.23 and 0.09, respectively; (Foley et al., 2013), the partition coefficient for V in clinopyroxene is 1.81 compared to 0.808 for Sc, and the partition coefficient for V in garnet is 1.48 compared to 2.62 for Sc (Hauri et al., 1994). Therefore, if there is abundant clinopyroxene and/or garnet in the source, such as in pyroxenite, V may be fractionated from Sc. Since those samples are most possibly from a mixed pyroxenite and spinel peridotite source, the presence of garnet from garnet peridotite is eliminated. Compared to samples from New South Wales, the high V/Sc of samples from Buckland indicates that alkali basalts from Buckland come from a relatively reduced environment. On the other hand, it implies that the assemblage in the source for Buckland has retained more Sc or has less V abundance in comparison with basanite from Barrington.

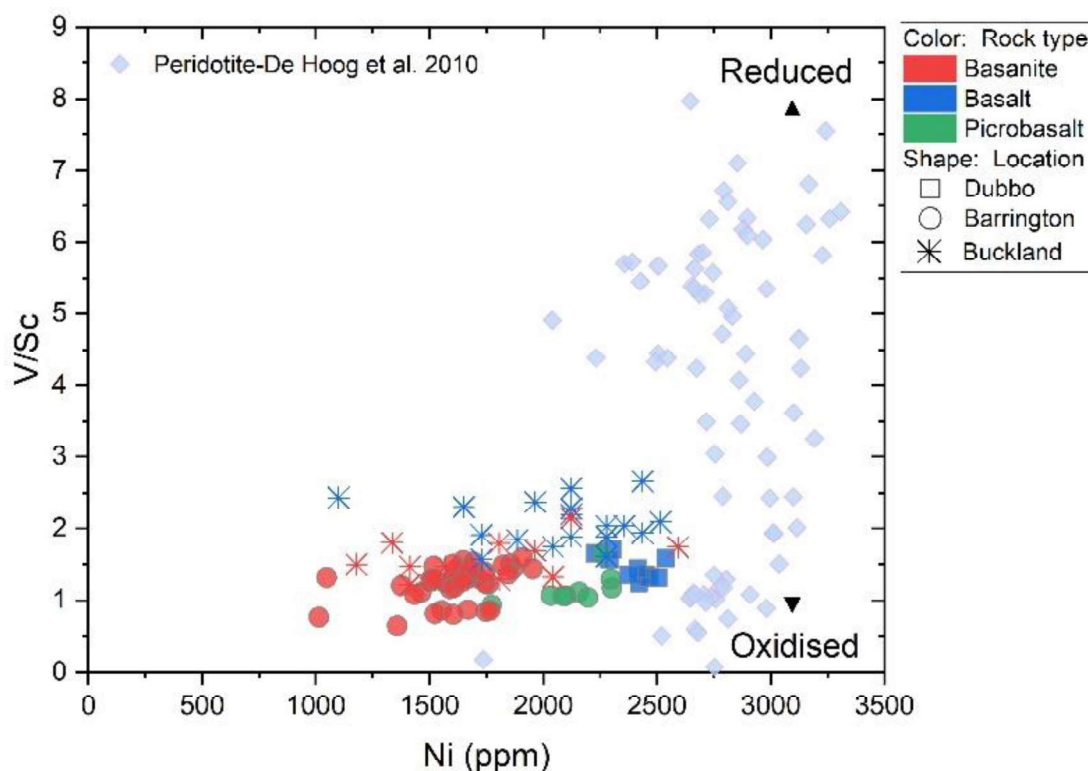


Fig. 26 Ni vs V/Sc in olivine phenocrysts illustrating the redox condition of magma generation.

6 Magmatic processes in the sources of New South Wales Cenozoic basaltic rocks

6.1. Mineralogy of the source assemblages

As discussed above, intraplate basaltic samples such as tholeiite from Dubbo, basanite from Bingara/Inverell, alkali basalt and basanite from Buckland, are most likely derived by melting of a mixed pyroxenite and spinel-peridotite source assemblage, with calculated proportions of pyroxenite of 60-74%, rather than from a purely peridotite source. In the source of Barrington, only ~42% of pyroxenite is needed. Furthermore, mixed pyroxenite and peridotite alone cannot explain all the characteristics of olivine and the geochemistry of the whole rocks. On the other hand, although samples from Buckland lie in a different Orogen, the alkali basalts and basanites there have a lot in common with samples from New South Wales: both localities seem to have experienced carbonatite modification. This indicates that similar magmatic processes may have affected the mantle throughout eastern Australia, which should include other Cenozoic basaltic provinces that are yet to be studied.

Spinel lherzolite xenoliths from western Victoria have been interpreted to have interacted with CO₂-rich fluids, replacing primary pyroxenes and spinel with amphibole \pm mica \pm apatite (O'Reilly and Griffin, 1988). Characteristically, amphibole-rich peridotite is enriched in LREE, Zr, Ta, and high K/Rb, while mica-rich peridotite is enriched in K, Rb, Ba, Ta, Ti, low K/Rb. Apatite contributes to elevated total REE, Sr, U and Th. Therefore, the enriched LREE, Zr, Ta of bulk samples from Buckland and Barrington may indicate a contribution of amphibole in the source.

Taken together, these features indicate that wide expanses of the mantle below eastern Australian have experienced carbonatitic metasomatism to the east of, and close to where, the lithosphere decreases in thickness. Olivine xenocrysts in these samples are derived from spinel peridotite and constrain the generation depth of the basaltic melts to be within the spinel peridotite zone.

6.2. The possible role of a mantle plume based on whole-rock and olivine phenocryst analysis

A mantle plume was suggested to be the trigger for melting to produce the Cenozoic volcanics in eastern Australia (O'Reilly and Zhang, 1995; Sutherland and Fanning, 2011; Davies et al., 2015). However, indicative elements such as Ni, Mn, and Cr have controversial multiple interpretations: they can be used to indicate the mineralogy of the source but cannot tell directly whether the melts

come from a mantle plume. O'Reilly and Zhang(1995) suggested that Dubbo olivine tholeiites, similar to the Dubbo tholeiitic basalt sample DB-04C in this study, originated from either a metasomatized source within the lithosphere or from mixing of OIB-like and metasomatized SCLM components. This conclusion was based on positive trends between $^{87}\text{Sr}/^{86}\text{Sr}$ and Rb/Sr , $^{143}\text{Nd}/^{144}\text{Nd}$ and Sm/Nd , and negative trends between $^{87}\text{Sr}/^{86}\text{Sr}$ and Sr/La , Sr/Nb . In our samples, the low CaO in the bulk composition (< 10.74 wt%), and incompatible trace element distribution patterns are quite similar to Hawaiian OIB (McDonough & Sun 1989), especially for samples from Dubbo, Bingara/Inverell, and Buckland. Moreover, the minor and trace elements Ni, Ca, Cr, and Mn all have similar abundances to phenocrysts in basalts from the Canary Islands (Gurenko et al., 2009) which originate from an OIB source. This OIB-like source is attributable to a plume, which was thus suggested to be the dominant source component for basalts from the main lava-field basalts in New South Wales and the Victorian Newer Basalts by (O'Reilly and Zhang, 1995).

However, although trace elements in olivine phenocrysts of tholeiitic basalt from Dubbo and other basalt provinces support a pyroxenite-associated source, the origin of the pyroxenite needs to be considered carefully. Reaction between recycled subducted slabs with peridotite in the mantle wedge above the subducting slab can also produce pyroxenite (Sekine and Wyllie, 1983; Förster et al., 2019). These pyroxenites may tend to have a greater variety of minerals, especially where they are formed by reaction with carbonate melts (Shea and Foley, 2019). Since tholeiite DB-04C from Dubbo shows indications of pyroxenite, as well as many features which are not consistent with those of Barrington or Buckland, the pyroxenite source of DB-04C from Dubbo may come from a plume source similar to Hawaiian basalts. This is supported by $^{87}\text{Sr}/^{86}\text{Sr}$ and Zr/Nb ratios (Zhang and O'Reilly, 1997), which are different from Barrington and Buckland. Since trace element abundances in olivine and whole-rock data between Barrington and Buckland are similar, and indicate a pyroxenite-associated source, it might mean that the type and formation of pyroxenite in two locations are similar: a pyroxenite source that was originally peridotite from subcontinental lithospheric mantle but altered by carbonate melt.

Heating by the mantle plume combined with the thinner lithosphere might have promoted melting at Dubbo, resulting in high degree melting of pyroxenite unaffected or only little affected by carbonatitic metasomatism, which is supported by the high calculated ratio of pyroxenite/peridotite but restricted geochemical signature for carbonatite metasomatism. This is consistent with volatile-bearing minerals being unstable at high temperature (Zhang and O'Reilly, 1997). This high degree melting process also dilutes the minor and trace element concentrations of the initial magma, such as P and Sr (Fig. 4). The relatively low Ni content in olivine of basalt from Dubbo compared to olivine in Hawaiian basalt might be caused by the retention of olivine in the

peridotite part of the source. Given that this sample is on the Ni-Mg# equilibrium zone in Fig. 8, this may also be a result of extensive melting of pyroxenite, which should have lower Mg# than peridotite. Thus, the usual assumption that primary melts have Mg# > 90 would not apply.

6.3. Magmatic processes leading to metasomatism of the lithosphere

The reaction between carbonatite and spinel peridotite in the sub-lithospheric mantle produces olivine and clinopyroxene at the expense of orthopyroxene and is accompanied by the crystallization of apatite, amphibole, and phlogopite (Yaxley et al., 1991; Yaxley and Green, 1998). Olivine produced by this reaction holds back Ni in the source. Partial melting of an apatite-bearing assemblage contributes to low Ti/Eu and high P_2O_5/TiO_2 in the magmas.

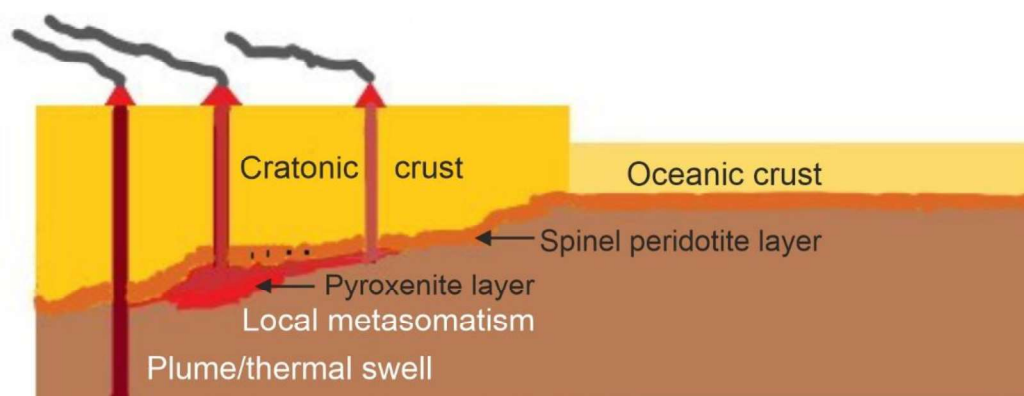


Fig. 27 Schematic cross section of basaltic magmatism in eastern Australia. The red area is the possible source of carbonate-rich melts. The carbonatitic melts migrate east that passed by the sampled location (local metasomatism), like Buckland and Mount Russell from Central (the middle right volcano), and to the shallow lithosphere area (like Barrington) which has experienced relatively less carbonatitic metasomatism. While Dubbo is mainly affected by plume but less by carbonatitic metasomatism (the most left). The black points in the spinel peridotite layer represent xenocrysts obtained in the basalts.

Upwelling of mantle beneath the lithosphere could facilitate the formation of basaltic rocks if the solidus of peridotite was depressed by the presence of volatiles, e.g. H_2O and CO_2 . Therefore, when the deep carbonate melt moves through the source at near-solidus temperatures around 1.5-2 GPa, it would react with the surrounding lherzolite to form clinopyroxene, forsterite + CO_2 at the expense of enstatite (Yaxley and Green, 1998). P_2O_5 -bearing carbonatite melt reacting further with primary olivine and clinopyroxene would form secondary orthopyroxene and apatite (Yaxley et al. 1991). H_2O in the carbonatite melt would cause the formation of hydrous phases such as amphibole and/or phlogopite during partial melting of lherzolite (Green 2005). Therefore, the consequent lithology

would consist of olivine + clinopyroxene + orthopyroxene + apatite \pm amphibole \pm phlogopite. Erupted basalts and basanites derived from this pyroxenite record this process. Furthermore, the carbonatitic features in whole rock and olivine phenocryst chemistry indicate the depth of magma generation. Basanite from Barrington requires less than 42% olivine-free pyroxenite in the source as discussed previously, which is lower than that calculated for Bingara to Inverell to Bingara area (Central) and Ebor. Although that calculation is based on olivine free-pyroxenite, the mixing of olivine-free pyroxenite and surrounding lherzolite can be seen as the equivalent of new pyroxenite described above in terms of silicate phases. Thus, the estimation on basanite from Barrington indicates a shallow generation depth relative to basanite and basalt from in the Inverell to Bingara area, and Ebor volcanic fields. The absence of an amphibole signature in samples of Barrington might suggest that the residence of amphibole is deeper. Basanite from Mount Russell (Central) has the strongest carbonatitic signature which indicates a deeper source region dominated more by the newly formed pyroxenite. This carbonatitic metasomatism is evidenced by the apatite in hawaiite from Bingara Volcanics in the same area (Vickery et al. 2007). Basanite and alkali basalt samples that have similar features as samples from New South Wales demonstrate a similar generation mechanism (Shea and Foley, 2019).

This process is accompanied by enrichment of LILE and P in the bulk composition (Yaxley et al., 1991). as a result, the basalts from this carbonatitic metasomatized source have low Ti/Eu ratio that trend towards carbonatitic melt. Moreover, the presence of clinopyroxene also explains the high FC3MS ratio, Zn/Fe ratio of bulk rock compositions and olivine phenocrysts discussed in previous sections, because it can significantly fractionate Zn/Fe with a partition coefficient value < 1 , thus causing elevation of Zn/Fe in the magma. On the other hand, this carbonatitic metasomatism happened close to the transition depth between spinel to garnet peridotites (at 1.8-2 GPa, around 1200 °C) (Klemme and O'Neill, 2000), but there, garnet in the pyroxenite may control the abundances of minor and trace elements that are characteristically associated with garnet.

Furthermore, as proposed by Shea and Foley (2019) for the basaltic volcanism of Buckland, the carbonatite metasomatism could occur at the craton edge (Fig. 27). According to this study, carbonatitic metasomatism may have occurred over a large area of eastern Australia, from the step of thick lithosphere to shallower regions in the east. The source of carbonate melt may come from the leftover of ancient subduction zone, as suggested for some locations (O'Reilly and Zhang, 1995), or from incipient melting at high pressures beneath the cratonic lithosphere in conditions that are known to produce carbonate-rich melts (Foley and Fischer, 2017).

The abundance and mineralogy of volatile-bearing mantle xenoliths in basaltic rocks varies from region to region, and the best-described localities are in western Victoria (Griffin et al., 1988; Yaxley

et al., 1991; Norman, 1998; O'Reilly and Griffin, 2000), which have secondary amphibole and apatite (Johnson et al., 1989). Xenoliths of spinel lherzolite and spinel pyroxenite from Bullenmerri and Gnotuk maars, southwestern Victoria, containing up to 3 vol% of high pressure trapped CO₂-rich fluids (Andersen et al., 1984) have also been described. Other scattered xenoliths with veins of amphibole ± mica ± apatite occur at Chudleigh and Atherton volcanic provinces in northern Queensland (more than 1500 km away north of Dubbo). In eastern Australia at Kiama (130 km south of Sydney), the original Cr-diopside rocks were extensively replaced by amphibole/apatite-series rocks (O'Reilly and Griffin, 1987). A spinel lherzolite with signs of carbonatite metasomatism has been described from Allyn River (Powell and O'Reilly, 2007), which lies 360 km east of Dubbo and 41 km south of Barrington Tops. Mantle xenoliths of amphibole-bearing garnet clinopyroxenite are recorded on the margin of Barrington Tops Volcanics (Wilkinson and Kalocsai, 1974; Sutherland et al., 1998). All these volatile-bearing mantle xenoliths are from thin lithospheric provinces (< 50 km) along the coastal line (Fishwick et al., 2008). However, no amphibole-apatite xenoliths have been reported in Buckland, Dubbo, Ebor, despite the evidence presented here for the presence of these minerals in the source.

7 Conclusions

Based on the reserved Ni concentration, the Ni/Mg vs Mn/Fe ratio, Zn/Fe vs Mn/Fe ratio in olivines, and FC3Ms vs MgO whole rock sample, tholeiite DB-04C from Dubbo appears to originate from a plume-type pyroxenite-bearing source that has experienced little or no carbonatitic metasomatism. Alkali basalt from Dubbo also comes from a pyroxenite-associated source based on whole-rock data. Xenocrysts in alkali basalt from Dubbo and Barrington all come from a spinel-peridotite source, thus basalts from these Volcanics at least originated from the spinel-peridotite stability region. In other areas such as Barrington, there are geochemical signs for pyroxenite in the source, but these pyroxenites originate from metasomatic reaction between peridotite and a migrating carbonatitic melt, and not from pyroxenite caused by melting of recycled eclogite in a plume source as is the case for tholeiite from Dubbo. High P₂O₅/TiO₂ and Zr/Hf at low Ti/Eu in whole-rocks indicate that the basanite (CR-11A) from Mount Russell (Bingara/Inverell area) has experienced the highest degree of carbonatitic metasomatism in the source of all studied samples. Basalts from Ebor might come from mixed source peridotite and pyroxenite based on current Zn/Fe versus Mn/Fe ratio, and FC3Ms value in the whole-rock analysis. The source of basanites from Barrington also includes pyroxenite originating from carbonatitic metasomatism and appears to have residual apatite in the

source. Similar to the case of Barrington, alkali basalts and especially basanites from Buckland come from a source assemblage with pyroxenite that contains pyroxene, apatite and/or amphibole.

Intensive carbonatitic metasomatism occurred throughout eastern Australia, with all known localities beneath thin lithosphere that borders the extensive thick lithosphere of central Australia, stretching from North Queensland, Buckland, to Bingara/Inverell, Barrington, and Western Victoria (Fig. 1a,b). Although Dubbo is close to the edge of the thick lithosphere, the action of the plume beneath this area might have hindered the infusion of carbonate melt or have diluted and dispersed the geochemical features of carbonatite metasomatism. For the same reason, it is no surprise that there is no sign of carbonatitic metasomatism reported from Cenozoic volcanoes located in the intervals of thick lithosphere which are suggested to belong to the longest hotspot track. At Buckland, however, the previous interpretation of a plume is now thought to be explained by carbonatite metasomatism in this study. Carbonate-rich melts might originate beneath the thick lithosphere but become absorbed in this lithosphere (Fig. 27) or migrated toward the edge and shallow areas. This process explains the extensive existence of cryptical metasomatism in eastern Australia.

8 Appendix

Table 1-sample locations in the field trip

Sample Code	Volcanic Province	Latitude	Longitude	Location
18N01	Goolma/Dubbo	-32.3830	149.4903	Gulgong
18N02	Dubbo	-32.3588	148.7897	Wongarbon
18N03	Dubbo	-32.2363	148.5798	Dubbo
18N04	Dubbo	-32.1632	148.6139	Brocklehurst
18N06	Warumbungles	-31.2810	149.0988	Coonabarabran
18N07	Warumbungles	-31.2708	149.0789	Coonabarabran
18N08	Warumbungles	-31.4490	149.0243	Tooraweenah
18N09	Warumbungles	-31.4054	149.0542	Gowang
18N10	Bingara Volcanics	-29.9037	150.4873	Pallal
18N11	Mount Russell Volcanics	-29.7796	151.0782	Inverell
18N12	Maybole Volcanics	-29.9311	151.2480	Tingha
18N13	Maybole Volcanics	-29.9267	151.3667	Wandsworth
18N14	Maybole Volcanics	-29.9804	151.4588	Wandsworth
18N15	Ebor	-30.4061	152.3023	West of Ebor
18N16	Ebor	-30.4119	152.3441	Ebor
18N17	Ebor	-30.3721	152.3700	Ebor
18N20	Barrington	-31.8981	151.5787	Barrington Tops
18N21	Barrington	-31.9403	151.4575	Barrington Tops
18N22	Barrington	-31.9552	151.4264	Polblue Crown Reserve
18N23	Barrington	-31.9330	151.3467	Stewarts Brook Forest
18N24	Barrington	-31.9283	151.3424	Moonan Brook

Table 2- XRF analysis standard

Sample	BHVO-2		GeoReM	
	Mean	SD	Mean	SD
SiO ₂	49.5	0.8	49.3	0.1
TiO ₂	2.4	0.7	2.79	0.02
Al ₂ O ₃	14.1	0.8	13.6	0.1
Fe ₂ O ₃	12.3	0.4	11.3	0.1
MnO	0.175	0.002	0.17	0.03
MgO	7.8	0.9	3.60	0.02
CaO	11.8	0.7	7.13	0.08
Na ₂ O	2.17	0.15	2.40	0.10
K ₂ O	0.43	0.19	0.51	0.02
P ₂ O ₅	0.23	0.10	0.29	0.02

Table3 Solution ICP-MS standard

Sample	BCR-2		GeoReM	BHVO-2		GeoReM
	Mean	SD		Mean	SD	
Li	7.81	0.05	7.9	4.47	0.05	4.8
Be	2.55	0.03	2.7	1.47	0.01	1.0
Sc	33.4	0.1	33.9	35.4	0.2	32
Ti	13367	8	13595	17850	196	16300
V	394	3	396	330	3	317
Cr	16.6	0.3	16.7	242	1	280
Mn	1477	23	1520	1361	8	
Co	35.8	0.4	36	45.8	0.5	45
Ni	13.3	0.1	13	135	2	119
Cu	27.6	0.3	27	158.2	0.8	127
Zn	123.4	0.1	125	106.3	0.8	103
Ga	20.4	0.1	21	20.80	0.03	22
Rb	46.3	0.8	46	9.41	0.01	9.1
Sr	326.1	0.5	329	381.7	0.6	396
Y	37.9	0.5	38	27.4	0.2	26
Zr	192	3	192	175.5	0.8	172
Nb	12.8	0.1	13	18.5	0.1	18
Mo	250	4	252	3.6	0.1	4.0
Cd	0.394	0.004	0.4	0.093	0.001	0.1
Cs	1.21	0.02	1.2	0.107	0.001	0.1
Ba	672	3	659	127.6	0.4	131
La	25.3	0.2	25	14.97	0.003	15
Ce	52.3	0.4	52	35.7	0.4	38
Pr	6.9	0.1	6.8	5.03	0.02	5.4
Nd	28.2	0.4	28	22.92	0.02	25
Sm	6.6	0.1	6.6	5.81	0.01	6.1
Eu	2.06	0.02	2.0	1.899	0.004	2.1
Tb	1.08	0.02	1.1	0.897	0.005	0.9
Gd	6.8	0.1	6.8	5.87	0.01	6.2
Dy	6.3	0.1	6.3	4.89	0.02	5.3
Ho	1.32	0.02	1.3	0.94	0.01	1.0
Er	3.70	0.05	3.7	2.43	0.03	2.5
Yb	3.3	0.1	3.3	1.84	0.01	2.0
Lu	0.48	0.01	0.5	0.254	0.0005	0.3
Hf	4.7	0.1	4.8	3.93	0.03	4.4
Ta	0.75	0.02	0.8	1.04	0.01	1.1
Th	6.2	0.1	6.1	1.15	0.01	1.2
U	1.71	0.03	1.7	0.381	0.005	0.4

Table 4: LA-ICP-MS data for NIST612 and BCR-2G compared to GeoReM preferred values.

Method	LA-ICP-MS							
Sample	NIST612		GeoReM*		BCR-2G		GeoReM	
	n=36	1 σ		1 σ	n=39	1 σ		1 σ
Li (ppm)	40.4	1.4	40.2	1.3	9.4	0.4	9	1
V	38.9	1.0	38.8	1.2	429	13	425	18
Cr	36.5	1.0	36.4	1.5	15.6	0.9	17	2
Mn	38.8	0.5	38.7	0.9	1581	53	1550	70
Co	35.5	0.4	35.5	1	38.5	1.0	38	2
Cu	37.8	0.8	37.8	1.5	17.8	0.6	21	5
Zn	39.1	0.8	39.1	1.7	174	10	125	5
Ga	36.9	0.4	36.9	1.5	38.8	6.5	23	0.1
Sr	78.6	2.1	78.4	0.2	330	10	342	4
Y	38.4	1.0	38.8	1.4	31.9	1.2	35	3
Zr	38.0	1.0	37.9	1.2	174	8	184	15
Nb	39.0	0.9	38.9	2.1	12.2	0.4	12.5	1
Ba	39.4	1.3	39.3	0.9	666	20	683	7
La	36.1	1.0	36	0.7	24.2	0.8	24.7	0.3
Ce	38.5	1.1	38.4	0.7	51.1	1.7	53.3	0.5
Gd	37.4	1.1	37.3	0.9	6.4	0.2	6.71	0.07
Yb	39.3	1.1	39.2	0.9	3.3	0.1	3.39	0.03

GeoReM are preferred values

Table 5-Detection limit of LA-ICP-MS

Element	Mean	Median
⁷ Li	0.029	0.016
¹¹ B	0.125	0.071
²³ Na	0.396	0.239
²⁷ Al	0.084	0.050
³¹ P	0.946	0.565
⁴³ Ca	14.883	9.120
⁴⁴ Ca	8.210	4.800
⁴⁵ Sc	0.028	0.016
⁴⁷ Ti	0.081	0.050
⁴⁹ Ti	0.114	0.071
⁵¹ V	0.019	0.012
⁵³ Cr	0.168	0.097
⁵⁵ Mn	0.047	0.027
⁵⁹ Co	0.009	0.004
⁶⁰ Ni	0.036	0.015
⁶² Ni	0.325	0.180
⁶³ Cu	0.024	0.013
⁶⁶ Zn	0.066	0.038
⁶⁷ Zn	0.208	0.118
⁶⁹ Ga	0.005	0.003
⁸⁸ Sr	0.003	0.002
⁸⁹ Y	0.002	0.001
⁹⁰ Zr	0.005	0.003
⁹³ Nb	0.002	0.001
¹³⁵ Ba	0.024	0.017
¹³⁷ Ba	0.015	0.010
¹³⁹ La	0.002	0.001
¹⁴⁰ Ce	0.002	0.001
¹⁵⁷ Gd	0.012	0.007
¹⁷² Yb	0.008	0.005

Chapter 2

Table 6-Major elements in olivines (DB-Dubbo, CR-Central, BR-Barrington, EB-Ebor)

Name	MgO (wt%)	Al ₂ O ₃	SiO ₂	CaO	Cr ₂ O ₃	MnO	FeO	NiO	Total	Mg#
DB-03F-1	48.98	0.03	40.95	0.10	0.03	0.12	9.10	0.39	99.70	90.56
DB-03F-2	41.46	0.04	38.82	0.10	0.00	0.19	18.12	0.18	98.91	80.31
DB-03F-3	48.89	0.03	40.81	0.11	0.02	0.13	9.47	0.39	99.85	90.20
DB-03F-4	48.25	0.02	40.42	0.07	0.01	0.14	10.30	0.48	99.69	89.31
DB-03F-5	47.67	0.03	40.44	0.10	0.02	0.14	10.54	0.36	99.30	88.97
DB-03F-6	48.34	0.03	40.65	0.10	0.02	0.14	9.57	0.38	99.23	90.00
DB-03F-7	48.47	0.01	40.62	0.07	0.01	0.14	9.53	0.39	99.24	90.07
DB-03F-9	37.28	0.02	37.98	0.11	0.00	0.26	22.39	0.08	98.12	74.80
DB-03F-10	37.10	0.02	37.95	0.28	0.00	0.36	22.18	0.15	98.04	74.89
DB-03F-11	47.63	0.02	40.37	0.08	0.01	0.14	10.77	0.36	99.38	88.74
DB-04C-1	43.16	0.05	38.13	0.20	0.04	0.19	15.71	0.32	97.80	83.04
DB-04C-2	40.37	0.04	37.97	0.20	0.04	0.23	19.31	0.24	98.40	78.84
DB-04C-3	42.71	0.04	38.24	0.19	0.04	0.21	16.60	0.31	98.34	82.10
DB-04C-4	42.86	0.06	38.15	0.20	0.04	0.21	16.35	0.31	98.18	82.37
DB-04C-5	43.11	0.05	38.79	0.20	0.04	0.18	16.08	0.32	98.77	82.70
DB-04C-6	42.54	0.04	38.88	0.21	0.04	0.21	16.96	0.30	99.16	81.73
DB-04C-7	42.10	0.04	39.01	0.21	0.04	0.21	17.20	0.31	99.12	81.35
DB-04C-8	43.07	0.04	38.95	0.20	0.04	0.20	16.15	0.32	98.97	82.62
DB-04C-9	42.93	0.04	38.78	0.21	0.03	0.20	16.49	0.33	99.01	82.27
DB-04C-10	42.78	0.03	38.51	0.21	0.05	0.20	16.26	0.30	98.34	82.43
CR-11A-1	48.49	0.02	40.33	0.06	0.01	0.14	9.90	0.39	99.34	89.72
CR-11A-2	49.26	0.02	40.39	0.07	0.00	0.13	8.83	0.36	99.06	90.86
CR-11A-3	48.59	0.02	40.19	0.07	0.01	0.13	9.64	0.38	99.03	89.99
CR-11A-4	49.92	0.03	40.60	0.07	0.01	0.12	8.63	0.39	99.77	91.16
CR-11A-6	49.14	0.02	40.43	0.05	0.01	0.13	9.13	0.38	99.29	90.56
CR-11A-7	48.64	0.01	40.08	0.04	0.00	0.12	10.05	0.36	99.30	89.61
CR-11A-8	49.15	0.02	40.43	0.06	0.01	0.14	9.21	0.38	99.40	90.49
CR-11A-9	47.52	0.01	40.05	0.09	0.01	0.16	11.10	0.35	99.29	88.41
CR-11A-10	48.99	0.01	40.38	0.03	0.00	0.12	9.14	0.39	99.06	90.53
CR-11A-11	48.65	0.01	40.29	0.06	0.01	0.13	9.54	0.37	99.06	90.09
BR-20B-1	49.73	0.02	40.38	0.06	0.01	0.15	9.70	0.37	100.42	90.14
BR-20B-2	48.33	0.02	40.51	0.06	0.01	0.25	11.58	0.34	101.10	88.15
BR-20B-3	48.73	0.03	40.39	0.09	0.02	0.16	11.56	0.37	101.35	88.26
BR-20B-4	47.53	0.01	40.18	0.06	0.01	0.17	12.64	0.33	100.93	87.02
BR-20B-5	43.74	0.01	39.46	0.06	0.00	0.35	17.36	0.12	101.10	81.79
BR-20B-6	50.22	0.02	40.94	0.08	0.03	0.14	9.38	0.40	101.21	90.52
BR-20B-7	49.63	0.02	40.85	0.06	0.00	0.15	10.07	0.38	101.16	89.78
BR-20B-8	47.46	0.03	40.34	0.09	0.02	0.17	12.47	0.33	100.91	87.15
BR-20B-9	46.14	0.03	39.93	0.15	0.02	0.19	14.27	0.29	101.02	85.22
BR-20B-10	48.96	0.03	40.66	0.08	0.01	0.16	10.53	0.36	100.79	89.23
BR-20B-11	49.53	0.03	40.78	0.06	0.01	0.15	10.11	0.39	101.06	89.73
BR-20B-12	49.90	0.02	40.61	0.06	0.01	0.16	9.99	0.38	101.13	89.90

(Continued)

Name	MgO	Al ₂ O ₃	SiO ₂	CaO	Cr ₂ O ₃	MnO	FeO	NiO	Total	Mg#
BR-20B-13	49.84	0.01	40.68	0.06	0.01	0.16	9.93	0.38	101.07	89.95
BR-20B-14	47.02	0.01	39.99	0.09	0.01	0.18	13.47	0.28	101.05	86.15
BR-20B-15	49.91	0.02	40.70	0.07	0.01	0.15	10.03	0.37	101.26	89.87
BR-20B-16	46.86	0.06	40.04	0.22	0.03	0.19	13.59	0.31	101.30	86.01
BR-20A-1	45.52	0.07	39.25	0.18	0.03	0.17	12.98	0.29	98.49	86.21
BR-20A-2	45.58	0.06	39.43	0.23	0.03	0.18	12.97	0.23	98.71	86.23
BR-20A-3	45.97	0.06	39.50	0.20	0.04	0.16	12.28	0.28	98.49	86.97
BR-20A-4	45.98	0.07	39.61	0.21	0.03	0.17	12.11	0.28	98.46	87.13
BR-20A-5	46.25	0.07	39.52	0.20	0.03	0.15	12.12	0.29	98.63	87.18
BR-20A-6	46.02	0.08	39.61	0.20	0.04	0.16	12.27	0.29	98.67	86.99
BR-20A-8	45.95	0.07	39.50	0.21	0.04	0.17	12.27	0.27	98.47	86.97
BR-20A-10	45.89	0.07	39.48	0.20	0.03	0.16	12.53	0.30	98.65	86.72
BR-20A-11	45.09	0.06	39.32	0.25	0.03	0.19	13.37	0.22	98.53	85.74
BR-20A-12	46.08	0.07	39.57	0.21	0.04	0.17	12.16	0.28	98.58	87.11
BR-20C-3	49.98	0.03	40.66	0.08	0.02	0.13	8.61	0.40	99.91	91.19
BR-20C-4	48.71	0.01	40.35	0.06	0.01	0.16	10.04	0.36	99.70	89.64
BR-20C-5	44.51	0.01	39.40	0.18	0.00	0.22	14.77	0.14	99.23	84.31
BR-20C-6	49.20	0.02	40.46	0.05	0.00	0.14	9.25	0.38	99.50	90.46
BR-20C-7	47.46	0.03	40.40	0.10	0.02	0.17	11.37	0.35	99.90	88.15
BR-20C-8	45.07	0.03	39.63	0.16	0.02	0.21	14.09	0.27	99.47	85.08
BR-20C-9	44.45	0.06	39.41	0.21	0.03	0.22	14.98	0.23	99.59	84.10
BR-20C-10	49.16	0.01	40.56	0.05	0.01	0.14	9.64	0.38	99.95	90.09
BR-20C-11	49.81	0.02	40.68	0.07	0.03	0.13	8.57	0.38	99.69	91.20
BR-20C-12	49.42	0.03	40.42	0.06	0.01	0.14	9.37	0.39	99.84	90.39
BR-22A 2-1	45.51	0.04	39.66	0.22	0.03	0.18	13.39	0.23	99.26	85.83
BR-22A 3-1	44.54	0.05	38.93	0.23	0.02	0.26	15.26	0.20	99.49	83.88
BR-22A 4-1	45.90	0.05	39.43	0.21	0.03	0.19	13.49	0.25	99.55	85.85
BR-22A 5	45.01	0.04	39.47	0.24	0.03	0.21	14.14	0.22	99.33	85.02
BR-22A 6-1	45.03	0.04	39.33	0.22	0.03	0.22	14.45	0.24	99.56	84.74
BR-22A 7-1	43.33	0.04	38.96	0.22	0.02	0.28	16.10	0.19	99.14	82.75
BR-22A 8-1	41.91	0.04	38.79	0.26	0.02	0.34	17.91	0.15	99.42	80.66
BR-22A-9	42.67	0.04	38.98	0.28	0.02	0.30	16.79	0.15	99.22	81.92
BR-23D-1-1	45.19	0.07	38.40	0.20	0.03	0.20	15.44	0.21	99.74	83.92
BR-23D-1-2	45.545	0.055	37.91	0.205	0.025	0.195	14.98	0.23	99.15	84.42
BR-23D-1-3	44.83	0.06	37.87	0.24	0.03	0.22	16.24	0.19	99.68	83.11
BR-23D-1-4	44.1	0.04	37.49	0.24	0.03	0.24	16.72	0.18	99.04	82.46
BR-23D-1-5	44.19	0.04	37.94	0.24	0.02	0.25	16.73	0.18	99.59	82.48
BR-23D-1-6	45.46	0.06	38.63	0.24	0.03	0.21	15.47	0.21	100.31	83.97
BR-23D-1-7	44.97	0.07	38.69	0.24	0.02	0.21	15.76	0.19	100.15	83.57
BR-23D-1-8	45.56	0.05	37.82	0.2	0.03	0.2	15.46	0.23	99.55	84.01
BR-23D-1-9	45.09	0.06	37.46	0.24	0.03	0.22	15.72	0.19	99.01	83.64
BR-23D-1-10	44.94	0.05	37.35	0.22	0.03	0.21	15.62	0.2	98.62	83.68
BR-23D-2-1	44.35	0.05	38.83	0.21	0.02	0.22	15.85	0.19	99.73	83.30

Chapter 2

(Continued)

Name	MgO	Al ₂ O ₃	SiO ₂	CaO	Cr ₂ O ₃	MnO	FeO	NiO	Total	Mg#
BR-23D-2-2	44.55	0.06	37.86	0.22	0.03	0.2	15.61	0.21	98.74	83.57
BR-23D-2-3	44.54	0.06	38.58	0.25	0.04	0.2	15.6	0.2	99.47	83.58
BR-23D-2-4	44.5	0.03	38.45	0.24	0.03	0.22	15.61	0.19	99.27	83.56
BR-23D-2-5	44.51	0.04	38.21	0.26	0.02	0.22	15.6	0.19	99.05	83.57
BR-23D-2-6	44.85	0.04	38.06	0.22	0.03	0.2	15.43	0.21	99.04	83.82
BR-23D-2-7	44.18	0.04	38.68	0.26	0.02	0.23	15.68	0.18	99.27	83.40
BR-23D-2-8	44.67	0.04	38.91	0.22	0.04	0.21	15.33	0.21	99.63	83.86
BR-23D-2-9	44.6	0.05	38.62	0.21	0.03	0.2	15.43	0.2	99.34	83.75
BR-23D-2-10	44.74	0.05	38.8	0.22	0.04	0.22	15.38	0.22	99.67	83.83
BR-23D-3-1	44.78	0.05	39.44	0.22	0.03	0.20	14.92	0.22	99.85	84.25
BR-23D-3-2	44.83	0.07	39.27	0.20	0.03	0.19	14.58	0.24	99.39	84.57
BR-23D-3-1	44.86	0.04	39.51	0.24	0.03	0.21	14.74	0.2	99.83	84.44
BR-23D-3-4	44.52	0.05	39.37	0.22	0.03	0.21	14.98	0.2	99.58	84.12
BR-23D-3-5	44.92	0.06	39.44	0.21	0.03	0.19	14.52	0.23	99.60	84.65
BR-23D-3-6	44.83	0.05	39.44	0.22	0.03	0.2	14.86	0.2	99.83	84.32
BR-23D-3-7	44.75	0.04	39.45	0.22	0.03	0.2	14.68	0.21	99.58	84.46
BR-23D-3-8	44.48	0.06	39.33	0.23	0.02	0.20	14.78	0.20	99.28	84.29
BR-23D-3-9	44.88	0.04	39.37	0.21	0.03	0.2	14.62	0.22	99.57	84.55
BR-23D-3-10	44.57	0.06	39.52	0.22	0.03	0.2	14.91	0.21	99.72	84.20
BR-23D-4-1	45.13	0.06	37.97	0.22	0.03	0.21	15.29	0.21	99.12	84.03
BR-23D-4-2	45.62	0.05	38.48	0.2	0.04	0.2	15.04	0.24	99.87	84.39
BR-23D-4-3	45.36	0.04	38.4	0.24	0.03	0.22	15.36	0.2	99.85	84.04
BR-23D-4-4	44.91	0.03	38.24	0.22	0.03	0.2	15.87	0.2	99.70	83.46
BR-23D-4-5	45.42	0.05	38.59	0.21	0.02	0.2	15.45	0.23	100.17	83.98
BR-23D-4-6	45.57	0.06	38.46	0.19	0.04	0.19	14.71	0.25	99.47	84.67
BR-23D-4-7	45.11	0.05	38.22	0.23	0.03	0.21	15.76	0.2	99.81	83.61
BR-23D-4-8	45.19	0.06	38.36	0.22	0.03	0.21	15.59	0.21	99.87	83.79
BR-23D-4-9	43.04	0.04	37.24	0.24	0.02	0.27	18.23	0.15	99.23	80.80
BR-23D-4-10	44.79	0.05	37.85	0.23	0.03	0.22	16.15	0.18	99.50	83.18
EB-16A-1	43.77	0.05	39.16	0.25	0.04	0.22	17.21	0.21	100.91	81.93
EB-16A-2	44.07	0.06	39.38	0.25	0.04	0.22	16.97	0.23	101.22	82.24
EB-16A-3	42.54	0.33	38.96	0.26	0.04	0.25	18.75	0.20	101.33	80.18
EB-16A-4	44.70	0.05	39.55	0.22	0.04	0.21	16.65	0.23	101.65	82.72
EB-16A-5	43.18	0.26	38.93	0.22	0.04	0.25	18.50	0.22	101.60	80.62
EB-16A-6-core	44.84	0.04	39.59	0.25	0.03	0.21	16.38	0.23	101.57	82.99
EB-16A-6-rim	42.53	0.05	38.88	0.25	0.03	0.24	18.97	0.19	101.14	79.99
EB-16A-7-core	43.87	0.05	39.21	0.26	0.05	0.22	17.38	0.22	101.26	81.82
EB-16A-7-rim(new)	37.04	0.04	37.86	0.37	0.01	0.36	25.59	0.12	101.39	72.07

Table 7-Trace elements in olivine-Samples from Dubbo (Unit: ppm)

Name	03F-1	03F-2	03F-3	03F-6	03F-7	03F-9	03F-10	03F-11	04C-1	04C-2	04C-3	04C-4	04C-5	04C-6	04C-7	04C-8	04C-9	04C-10
⁷ Li	2.24	3.31	2.15	2.38	2.57	3.51	3.89	3.00	2.17	2.01	2.05	2.92	2.02	2.01	2.17	2.06	2.02	2.16
¹¹ B	4.44	4.07	4.40	4.60	4.64	4.00	3.66	4.27	4.72	5.55	4.47	3.95	4.46	5.61	5.83	4.31	4.50	3.98
²³ Na	97	71	59	63	72	83	77	64	62	57	62	79	60	57	62	60	58	62
²⁷ Al	152	152	138	141	92	132	120	93	204	199	194	217	198	210	214	206	190	199
³¹ P	62.3	78.2	29.6	34.0	202.6	113	114	89	158	140	135	399	127	147	211	149	98	146
⁴⁸ Ca	579	655	521	556	437	779	1545	452	1386	1355	1285	1628	1289	1369	1411	1270	1313	1278
⁴⁴ Ca	672	734	623	669	553	867	1609	545	1505	1349	1373	1733	1285	1399	1434	1303	1298	1300
⁴⁸ Sc	3.84	3.58	3.73	3.96	3.51	3.41	4.85	3.70	5.09	5.76	5.26	6.04	5.14	5.51	5.84	5.27	4.99	4.98
⁴⁷ Ti	22.1	96.1	22.7	24.3	20.5	138.7	133.6	20.9	75.7	78.0	74.2	100.3	73.0	82.4	84.5	77.4	70.8	76.2
⁴⁹ Ti	23.3	101.5	23.2	23.7	20.9	144.1	137.7	20.6	78.1	80.4	78.2	104.5	78.3	86.3	88.6	79.9	74.2	77.7
⁵¹ V	4.80	7.10	4.78	5.20	3.78	6.76	5.99	4.40	6.88	9.81	8.28	9.99	8.13	6.88	7.74	6.96	7.20	6.78
⁵³ Cr	190	14	101	111	78	12	13	74	260	261	251	289	261	264	266	260	250	258
⁵⁵ Mn	1124	1748	1170	1200	1168	2353	2906	1212	1653	1726	1734	1989	1686	1704	1782	1676	1680	1662
⁵⁸ Co	148	234	152	157	155	216	194	156	193	195	195	201	197	196	199	197	195	195
⁶⁰ Ni	3094	1514	3116	3109	3125	718	1161	3062	2449	2303	2291	2228	2539	2421	2467	2505	2414	2377
⁶⁵ Ni	3087	1528	3078	3157	3133	730	1167	3058	2458	2311	2287	2266	2550	2425	2486	2528	2429	2394
⁶³ Cu	1.60	2.51	1.71	1.20	1.90	2.52	1.60	2.09	1.84	1.93	1.93	4.62	1.99	1.88	2.48	1.94	1.79	1.93
⁶⁶ Zn	76	153	68	73	80	210	229	90	155	185	173	189	170	168	189	166	157	164
⁶⁷ Zn	72	150	65	69	78	205	223	89	150	174	166	180	162	163	185	159	152	158
⁶⁹ Ga	0.102	0.141	0.092	0.121	0.093	0.178	0.161	0.128	0.209	0.198	0.185	0.338	0.211	0.191	0.238	0.178	0.173	0.181
⁸⁸ Sr	0.709	0.010	<0.008	0.002	0.019	0.013	0.019	0.006	0.939	0.007	0.149	1.720	0.052	0.004	0.129	0.006	0.006	0.008
⁸⁹ Y	0.056	0.049	0.042	0.055	0.048	0.156	0.343	0.041	0.137	0.123	0.154	0.604	0.212	0.123	0.247	0.116	0.127	0.122
⁹⁰ Zr	0.201	0.095	0.037	0.066	0.008	0.092	0.090	0.019	4.020	0.077	2.530	7.110	1.196	0.166	0.094	0.070	0.068	0.846
⁹³ Nb	0.006	0.004	<0.005	0.005	0.005	0.001	0.002	0.004	0.012	<0.00	0.008	0.063	0.007	<0.00	<0.00	<0.00	<0.00	0.001
¹³⁵ Ba	<0.015	0.069	<0.012	<0.010	0.018	<0.014	<0.012	<0.013	0.045	0.034	0.098	0.870	0.074	<0.03	0.089	<0.01	<0.01	<0.013
¹³⁷ Ba	0.049	<0.011	0.014	<0.007	0.020	0.013	<0.006	<0.008	0.062	0.013	0.088	1.010	0.075	<0.02	0.090	<0.01	0.021	<0.007
¹³⁹ La	0.002	0.002	0.003	0.002	<0.001	<0.001	0.001	<0.001	0.020	<0.00	0.011	0.240	0.024	<0.00	0.031	<0.00	<0.00	0.002
¹⁴⁰ Ce	0.002	0.002	0.003	0.012	<0.001	0.007	0.003	<0.001	0.056	<0.00	0.017	0.254	0.013	0.004	0.032	0.002	<0.00	<0.001
¹⁵⁷ Gd	<0.007	0.012	<0.006	<0.006	0.008	0.016	0.014	<0.006	0.022	<0.01	0.008	0.046	<0.00	<0.01	<0.01	<0.00	0.017	<0.007
¹⁷² Yb	0.017	0.011	0.033	0.026	0.016	0.025	0.107	0.018	0.035	0.026	0.037	0.100	0.045	0.052	0.052	0.023	0.021	0.023

Name	208-01	208-02	208-03	208-4-center	208-4-rim	208-5-center	208-5-rim	208-6	208-7-1	208-7-2	208-10	208-11	208-12	208-15	20A-1	20A-2	20A-3	20A-4
7Li	2.64	5.08	3.48	4.19	4.98	6.46	4.79	1.99	2.14	3.06	2.98	3.04	3.55	2.67	2.19	2.21	2.07	2.31
11B	8.90	8.07	7.36	7.93	10.19	6.79	6.48	6.82	7.13	6.62	6.67	6.06	6.21	5.79	2.66	2.36	2.67	7.86
23Na	29	97	103	21	37	36	37	75	24	26	36	30	43	50	115	103	110	115
27Al	85	185	111	58	66	31	37	89	78	73	88	78	53	81	346	277	309	302
31P	56	104	200	68	95	56	53	162	46	107	53	58	54	56	116	120	118	147
43Ca	398	702	516	333	368	387	384	441	359	361	444	363	312	386	1159	1340	1339	1366
44Ca	431	731	602	396	488	417	431	568	442	441	475	442	403	487	1234	1392	1421	1399
48Sc	3.52	3.10	3.71	3.05	3.15	2.38	2.40	4.54	3.28	3.43	3.03	3.06	2.73	3.16	5.20	5.45	5.47	5.29
47Ti	27.9	11.0	26.8	8.9	14.0	122.7	60.7	7.5	14.4	14.9	11.2	9.4	6.0	16.3	88.8	80.0	82.0	84.3
48Ti	27.8	9.1	27.3	8.5	12.3	132.2	63.5	7.1	14.4	15.2	11.4	8.8	5.7	16.1	91.7	84.6	85.6	87.3
51V	2.73	2.56	3.99	1.91	2.00	1.47	1.42	4.81	2.81	2.87	2.66	2.34	1.96	2.83	8.54	5.82	6.12	5.51
53Cr	63	127	146	54	54	4.12	6.53	197	60	64	91	66	95	104	231	208	213	180
55Mn	1179	1954	1446	1415	1510	2953	2847	1137	1234	1256	1433	1261	1304	1292	1318	1440	1361	1355
59Co	152	151	152	155	154	156	162	151	152	152	150	155	156	150	170	162	164	165
60Ni	3079	2508	2908	2835	2754	1035	1216	3233	3033	3008	2915	3073	3004	2923	2259	2034	2156	2197
64Ni	3143	2547	2992	2860	2774	1062	1225	3271	3092	3058	2956	3113	3048	2959	2281	2075	2192	2246
65Cu	2.19	2.46	2.49	2.88	2.37	0.33	1.50	2.36	1.52	2.23	1.33	1.05	1.39	1.68	2.85	6.96	2.55	5.59
67Zn	69	156	117	128	154	194	184	69	64	77	92	77	94	76	120	114	115	111
68Zn	65	147	113	120	152	187	173	63	60	74	85	74	87	75	118	111	111	107
69Ga	0.077	0.183	0.096	0.077	0.101	0.035	0.044	0.052	0.056	0.070	0.059	0.081	0.047	0.063	0.231	0.213	0.212	0.190
88Sr	0.017	0.220	0.208	0.012	0.020	0.004	0.010	0.119	0.012	0.004	0.083	0.037	0.003	0.833	0.028	0.048	0.018	0.031
89Y	0.033	0.076	0.067	0.039	0.080	0.037	0.048	0.044	0.033	0.033	0.039	0.027	0.043	0.043	0.083	0.079	0.091	0.092
90Zr	0.063	0.586	0.883	1.126	0.166	1.051	0.057	1.271	0.167	0.047	0.109	0.499	0.024	1.870	0.789	0.063	0.065	0.051
93Nb	0.148	0.268	0.021	0.011	0.008	0.145	0.021	0.054	0.014	0.010	0.012	0.007	0.006	0.012	0.002	0.008	0.004	0.001
135Ba	0.020	<0.015	0.029	0.021	0.052	<0.016	<0.013	0.022	<0.017	<0.014	<0.022	<0.018	<0.021	<0.018	<0.021	<0.020	<0.024	<0.021
137Ba	<0.012	0.038	<0.011	0.015	<0.036	<0.010	<0.008	0.011	0.017	<0.011	<0.007	<0.013	<0.012	0.015	<0.011	<0.013	<0.011	<0.010
139La	<0.002	0.007	0.032	0.006	<0.003	0.002	0.002	0.005	0.007	0.001	<0.001	0.002	<0.001	0.012	<0.001	0.001	<0.002	0.005
140Ce	0.002	0.017	0.053	0.007	0.010	0.002	0.004	0.005	0.003	0.002	0.003	0.002	<0.001	0.006	<0.002	0.003	0.002	<0.001
157Gd	<0.008	0.014	<0.007	<0.007	<0.020	<0.007	<0.007	0.009	<0.008	<0.008	<0.007	<0.008	0.009	<0.009	<0.009	<0.008	<0.010	<0.009
172Yb	0.017	0.033	0.026	0.022	<0.017	0.009	0.015	0.021	0.019	0.013	0.019	0.018	0.022	0.009	0.009	0.017	0.023	0.027

(Continued)-Trace elements in olivine-Samples from Barrington (Unit: ppm)

Name	20A-5	20A-6	20A-8	20A-10	20A-12	20C-3	20C-4	20C-5	20C-6	20C-7	20C-8	20C-9	20C-10	20C-11	20C-12	22A-2	22A-3	22A-4	22A-5
⁷ Li	2.36	2.29	2.11	2.08	2.34	1.43	3.69	2.76	2.99	3.60	3.30	6.53	2.87	2.08	2.17	5.66	4.79	6.99	4.11
¹¹ B	2.57	2.61	2.47	2.64	2.29	3.32	3.42	3.61	2.99	3.28	3.29	3.08	3.15	2.95	3.26	3.97	3.97	4.01	4.11
²³ Na	125	112	105	113	102	33	22	25	15	108	108	188	19	88	24	88	86	83	86
²⁷ Al	350	317	304	336	316	94	56	88	57	103	95	232	54	81	84	188	193	190	217
³¹ P	237	169	129	141	140	93	72	94	55	166	92	649	42	147	68	116	111	104	142
⁴³ Ca	1302	1390	1371	1357	1673	492	325	435	304	510	588	1301	256	416	352	1339	1319	1543	1482
⁴⁴ Ca	1362	1455	1536	1360	1691	561	379	485	365	590	627	1322	352	486	407	1389	1377	1580	1508
⁴⁵ Sc	5.54	5.57	5.39	5.41	5.82	5.60	3.85	5.30	4.05	4.38	4.62	6.42	4.32	5.64	4.81	5.35	5.21	5.15	5.77
⁴⁷ Ti	95.2	90.0	85.1	88.9	89.9	9.9	24.5	16.5	12.5	26.3	27.3	92.8	13.8	21.8	16.0	78.6	80.2	80.9	94.1
⁴⁹ Ti	99.4	92.2	88.1	93.1	93.3	9.9	25.8	16.7	12.4	26.5	26.6	95.0	12.3	21.5	15.7	83.2	79.5	81.0	93.3
⁵¹ V	6.52	5.93	5.74	7.03	5.46	4.65	1.93	2.42	1.88	3.17	3.12	5.29	2.00	4.10	2.78	4.51	4.55	4.43	4.97
⁵³ Cr	224	221	216	221	203	161	40	26	40	98	127	176	46	200	77	156	135	135	135
⁵⁵ Mn	1329	1398	1373	1313	1548	1020	1215	1747	1182	1441	1596	1732	1201	1055	1121	1839	1792	2625	1699
⁵⁹ Co	165	165	163	166	168	147	147	194	149	148	146	169	152	143	146	170	164	172	167
⁶⁰ Ni	2301	2100	2086	2297	1774	3202	2739	981	2949	2742	2400	1971	2894	3005	3045	1749	1669	1553	1766
⁶² Ni	2339	2120	2113	2333	1806	3164	2705	976	2906	2711	2366	1957	2874	2960	2980	1781	1696	1562	1782
⁶³ Cu	2.67	2.50	2.34	2.52	2.38	2.64	2.54	3.78	2.70	2.54	2.63	4.91	2.50	2.17	2.00	1.82	0.67	0.64	0.70
⁶⁶ Zn	111	114	109	115	115	67	75	75	70	125	133	159	82	69	72	165	147	195	150
⁶⁷ Zn	105	112	107	109	113	64	71	72	66	117	128	155	77	63	66	157	143	187	148
⁶⁹ Ga	0.216	0.195	0.186	0.213	0.218	0.050	0.053	0.061	0.044	0.075	0.096	0.194	0.052	0.067	0.051	0.142	0.153	0.151	0.173
⁸⁸ Sr	0.013	0.036	0.026	0.012	0.021	0.011	0.008	0.007	<0.002	0.076	0.009	0.066	<0.002	0.017	0.007	0.011	0.022	0.032	0.022
⁸⁹ Y	0.093	0.100	0.089	0.089	0.110	0.025	0.025	0.017	0.025	0.059	0.042	0.117	0.024	0.041	0.034	0.096	0.152	0.218	0.129
⁹⁰ Zr	0.068	0.067	0.066	0.131	0.059	0.236	0.066	0.013	0.032	0.138	0.287	0.257	0.011	0.105	0.078	0.068	0.058	0.090	0.561
⁹³ Nb	0.001	0.005	<0.001	0.003	0.003	0.075	0.008	0.029	0.007	<0.004	0.013	0.013	0.005	0.021	0.010	<0.001	0.002	0.001	0.004
¹³⁵ Ba	<0.025	<0.025	0.028	<0.021	0.037	0.028	0.026	<0.020	<0.019	0.034	<0.020	0.309	<0.021	0.023	<0.022	<0.012	0.028	0.023	<0.014
¹³⁷ Ba	<0.012	<0.001	<0.011	<0.014	0.014	0.012	<0.012	<0.012	<0.011	0.027	<0.010	0.366	<0.014	0.027	0.012	<0.008	0.010	<0.010	0.250
¹³⁹ La	<0.002	<0.002	<0.001	<0.002	0.002	0.002	<0.001	0.002	0.001	0.003	<0.001	<0.002	<0.002	<0.001	<0.001	<0.001	<0.001	0.002	0.003
¹⁴⁰ Ce	<0.002	0.005	<0.001	<0.002	<0.002	0.002	<0.001	<0.001	0.002	0.006	0.001	0.008	<0.001	0.007	0.002	0.001	0.002	0.007	0.002
¹⁵⁷ Gd	<0.010	0.022	0.013	<0.008	<0.008	<0.008	<0.009	0.016	<0.009	0.010	0.013	<0.009	<0.009	<0.009	<0.009	0.005	0.008	0.008	0.016
¹⁷² Yb	0.033	0.019	0.050	0.046	0.015	0.016	0.016	0.006	0.016	0.014	0.014	0.042	0.018	0.016	<0.007	0.023	0.035	0.054	0.042

(Continued)

Name	22A-6	22A-7	22A-8	22A-9	23D-1-1	23D-1-2	23D-1-3	23D-1-5	23D-1-6	23D-1-7	23D-1-8	23D-1-9	23D-1-10	23D-2-1	23D-2-2	23D-2-3
⁷ Li	7.79	5.12	7.62	6.17	3.03	1.80	3.28	3.61	2.30	2.48	2.64	2.16	2.31	6.79	3.46	4.20
¹¹ B	3.98	3.81	4.03	3.80	4.59	4.45	4.14	3.76	3.96	4.52	4.74	3.96	4.13	5.97	4.75	4.69
²³ Na	87	84	80	76	100	97	91	110	97	101	92	89	89	83	97	100
²⁷ Al	177	195	176	174	302	258	200	461	261	246	243	229	235	278	226	231
³¹ P	128	103	126	112	135	68	113	169	77	102	120	86	69	88	81	113
⁴³ Ca	1362	1379	1858	1424	1243	1286	1435	1223	1236	1556	1397	1334	1391	1845	1412	1428
⁴⁴ Ca	1454	1407	1826	1554	1238	1267	1430	1278	1218	1542	1389	1367	1396	1821	1438	1427
⁴⁵ Sc	5.32	5.43	5.18	5.72	5.15	4.86	5.00	4.87	4.87	5.18	5.21	4.87	5.04	5.65	4.94	4.99
⁴⁷ Ti	79.1	83.3	88.9	83.9	116.5	78.3	88.5	93.3	69.1	85.6	97.9	85.5	82.0	91.5	84.8	81.1
⁴⁹ Ti	82.3	83.3	89.7	81.8	122.2	81.3	90.7	94.6	69.7	86.0	99.3	85.4	82.6	98.6	88.5	85.3
⁵¹ V	4.34	4.37	3.96	3.70	8.00	6.87	6.04	7.18	7.02	6.04	6.59	6.31	6.29	7.45	6.42	6.54
⁵³ Cr	135	138	58	113	195	198	165	265	209	183	171	181	188	97	193	202
⁵⁵ Mn	2340	1842	2903	2258	1633	1616	1742	1698	1611	1706	1654	1681	1666	2823	1766	1730
⁵⁹ Co	169	167	179	167	175	173	174	172	179	175	178	172	170	187	176	178
⁶⁰ Ni	1524	1604	1014	1358	1649	1646	1375	1518	1866	1590	1505	1508	1569	1048	1523	1598
⁶² Ni	1518	1621	1029	1370	1642	1641	1376	1519	1861	1581	1511	1514	1572	1053	1537	1606
⁶³ Cu	1.12	2.25	0.70	1.31	2.24	1.73	1.12	1.26	2.18	2.04	1.59	1.57	1.71	0.62	1.47	1.30
⁶⁶ Zn	186	163	215	183	122	125	119	128	124	133	125	124	121	218	129	128
⁶⁷ Zn	183	159	209	179	120	123	114	125	119	132	125	120	118	212	126	124
⁶⁹ Ga	0.175	0.156	0.167	0.166	0.240	0.182	0.158	0.308	0.215	0.173	0.160	0.157	0.162	0.288	0.182	0.186
⁸⁸ Sr	0.010	0.130	0.010	0.019	0.041	0.018	0.026	0.039	0.008	0.011	0.017	0.050	0.015	0.257	0.016	0.009
⁸⁹ Y	0.134	0.093	0.210	0.136	0.084	0.088	0.127	0.110	0.085	0.112	0.098	0.103	0.092	0.237	0.090	0.103
⁹⁰ Zr	0.114	0.339	0.044	0.056	0.485	0.522	4.490	3.810	0.165	0.046	0.069	0.109	0.072	0.960	0.908	0.079
⁹³ Nb	0.002	0.006	0.009	0.002	0.005	0.001	0.009	0.016	0.001	<0.002	<0.002	<0.001	<0.001	0.021	0.002	0.001
¹³⁵ Ba	<0.012	0.073	<0.012	<0.012	<0.021	<0.016	0.016	0.026	<0.012	<0.028	0.035	<0.019	0.018	0.025	<0.014	<0.018
¹³⁷ Ba	<0.007	0.058	<0.006	<0.008	0.017	<0.012	<0.011	0.032	<0.008	<0.017	<0.017	<0.0106	<0.0113	0.017	0.038	<0.012
¹³⁹ La	0.002	0.007	<0.001	<0.001	<0.002	<0.001	0.004	0.005	<0.001	<0.002	<0.003	<0.001	0.001	0.007	0.001	<0.001
¹⁴⁰ Ce	0.001	0.010	0.004	<0.001	0.002	0.002	0.011	0.012	0.018	<0.002	0.048	<0.001	0.002	0.007	0.003	<0.001
¹⁵⁷ Gd	0.021	<0.005	<0.006	<0.006	<0.008	<0.007	0.022	0.015	<0.009	<0.013	0.027	0.008	0.006	<0.010	0.011	<0.008
¹⁷² Yb	0.032	0.032	0.057	0.035	0.024	0.030	0.023	0.029	0.015	<0.018	0.049	0.034	0.018	0.067	0.028	0.034

(Continued)

Name	23D-2-5	23D-2-6	23D-2-7	23D-2-8	23D-2-9	23D-3-1	23D-3-2	23D-3-3	23D-3-5	23D-3-6	23D-3-7	23D-3-8	23D-3-9	23D-3-10	23D-4-1	23D-4-2
⁷ Li	3.03	2.52	2.69	4.40	3.19	2.51	2.92	2.82	2.41	2.78	2.50	2.54	3.09	3.11	2.99	2.68
¹¹ B	4.40	4.78	4.72	4.70	4.24	6.94	6.31	6.16	5.71	5.70	6.19	5.76	5.47	5.38	4.81	4.73
²³ Na	99	102	96	98	109	108	118	111	114	203	105	111	110	104	103	108
²⁷ Al	207	226	210	230	243	263	290	238	307	238	275	241	254	249	269	258
³¹ P	91	63	96	92	106	74	102	95	89	71	55	106	92	86	71	91
⁴³ Ca	1548	1376	1647	1484	1274	1564	1341	1627	1327	1366	1417	1487	1494	1483	1521	1431
⁴⁴ Ca	1581	1391	1712	1495	1311	1607	1472	1772	1403	1441	1526	1596	1537	1621	1566	1515
⁴⁵ Sc	5.17	4.80	5.30	5.12	4.71	5.81	5.51	5.52	5.16	5.33	5.60	5.31	5.38	5.41	5.30	5.18
⁴⁷ Ti	86.2	79.5	85.8	86.4	79.1	76.4	68.7	84.6	73.9	68.6	82.9	95.6	82.0	87.4	89.1	79.3
⁴⁹ Ti	89.9	83.3	89.4	92.8	83.2	86.4	76.2	95.1	82.7	75.4	91.7	105.3	88.9	94.0	97.2	85.2
⁵¹ V	5.76	6.17	5.72	7.21	7.08	7.14	7.93	6.52	7.77	7.93	6.96	7.32	7.07	7.07	7.17	7.21
⁵³ Cr	181	199	181	211	172	208	229	190	256	205	218	190	207	196	210	214
⁵⁵ Mn	1843	1661	1867	1770	1659	1742	1665	1799	1685	1735	1728	1745	1755	1778	1764	1756
⁵⁹ Co	176	174	176	180	179	188	189	185	189	189	186	190	185	188	184	184
⁶⁰ Ni	1463	1620	1434	1612	1602	1757	1954	1607	1855	1823	1745	1668	1712	1667	1672	1743
⁶² Ni	1489	1633	1448	1634	1613	1752	1938	1596	1847	1815	1738	1668	1716	1669	1683	1750
⁶³ Cu	1.45	2.82	1.35	1.08	1.91	4.57	2.75	2.18	2.43	1.79	2.28	2.23	1.96	1.84	1.91	1.52
⁶⁶ Zn	139	129	128	129	132	151	150	144	145	150	146	143	142	140	145	140
⁶⁷ Zn	135	125	127	124	125	142	139	134	138	139	137	132	131	130	138	131
⁶⁹ Ga	0.180	0.156	0.178	0.181	0.185	0.193	0.229	0.177	0.205	0.219	0.225	0.183	0.179	0.180	0.216	0.191
⁸⁸ Sr	0.029	0.031	0.056	0.025	0.027	0.089	0.393	0.257	0.026	0.371	0.121	0.174	0.138	0.025	0.011	0.183
⁸⁹ Y	0.130	0.090	0.122	0.100	0.082	0.116	0.089	0.101	0.091	0.087	0.095	0.109	0.103	0.106	0.104	0.092
⁹⁰ Zr	4.160	0.086	0.440	0.269	0.604	0.052	0.417	0.094	0.148	2.040	0.052	0.158	1.009	0.068	0.822	0.052
⁹³ Nb	0.002	0.003	0.007	0.018	0.012	0.014	0.011	0.001	0.002	0.010	<0.001	0.002	0.004	0.001	0.001	0.007
¹³⁵ Ba	0.857	<0.018	<0.017	0.017	0.031	0.326	<0.016	0.579	<0.014	0.083	0.037	0.030	0.024	0.026	0.059	<0.015
¹³⁷ Ba	<0.012	<0.011	<0.011	0.035	<0.010	<0.008	0.015	0.078	0.227	0.297	<0.008	0.045	0.054	0.020	0.015	0.014
¹³⁹ La	0.005	<0.001	<0.001	0.003	0.002	0.005	0.001	<0.001	0.003	0.001	0.001	0.004	0.007	<0.001	0.003	<0.001
¹⁴⁰ Ce	0.011	0.002	<0.001	<0.001	<0.001	0.071	0.003	0.005	0.002	0.021	0.002	0.011	0.007	0.008	<0.001	0.001
¹⁵⁷ Gd	0.007	0.019	0.013	0.010	<0.007	<0.006	<0.005	0.009	<0.007	<0.006	<0.005	0.010	0.009	0.014	0.017	0.012
¹⁷² Yb	0.028	0.014	0.207	0.029	0.030	0.028	0.033	0.026	0.022	0.158	0.030	0.027	0.043	0.029	0.025	0.037

(Continued)

Name	23D-4-4	23D-4-6	23D-4-7	23D-4-8	23D-4-9	23D-4-10
⁷ Li	2.32	2.35	2.42	2.28	4.32	3.35
¹¹ B	4.55	5.02	4.38	4.33	4.62	4.36
²³ Na	108	112	106	101	118	103
²⁷ Al	258	281	263	250	287	239
³¹ P	80	65	107	88	145	78
⁴³ Ca	1360	1265	1513	1374	1341	1391
⁴⁴ Ca	1456	1355	1558	1506	1446	1488
⁴⁵ Sc	5.06	4.92	5.40	5.10	5.24	5.09
⁴⁷ Ti	77.6	68.3	80.9	83.7	82.3	82.0
⁴⁹ Ti	83.5	72.9	86.5	88.8	86.0	88.1
⁵¹ V	7.75	7.85	7.48	7.31	7.18	6.43
⁵³ Cr	221	207	226	211	224	190
⁵⁵ Mn	1691	1589	1692	1705	1698	1754
⁵⁹ Co	194	183	189	187	184	184
⁶⁰ Ni	1695	1909	1666	1676	1845	1643
⁶² Ni	1700	1908	1667	1682	1841	1643
⁶³ Cu	1.56	2.34	2.32	2.20	2.15	1.61
⁶⁶ Zn	142	134	135	137	139	137
⁶⁷ Zn	135	127	126	129	131	130
⁶⁹ Ga	0.179	0.209	0.207	0.168	0.238	0.174
⁸⁸ Sr	0.018	0.038	0.013	0.016	0.016	0.118
⁸⁹ Y	0.093	0.097	0.091	0.085	0.115	0.100
⁹⁰ Zr	0.547	3.320	0.069	0.049	7.470	0.203
⁹³ Nb	0.002	0.005	0.002	0.002	0.009	0.003
¹³⁵ Ba	0.176	0.078	0.019	<0.017	<0.014	<0.013
¹³⁷ Ba	0.030	0.013	0.539	0.020	1.080	<0.008
¹³⁹ La	<0.001	0.006	<0.001	<0.001	<0.001	<0.001
¹⁴⁰ Ce	0.001	0.015	0.001	0.002	0.017	<0.001
¹⁵⁷ Gd	<0.007	0.013	<0.006	0.006	0.008	0.020
¹⁷² Yb	0.032	0.029	0.022	0.024	0.041	0.015

Chapter 3 The effect of C-O-H fluids on partial melting of eclogite and lherzolite under moderately oxidizing and reducing conditions

1 Introduction

Partial melting of the Earth's mantle is one of the most important processes on Earth and the other terrestrial planets, and ultimately leads to the generation of a large variety of volcanic and plutonic rocks in the Earth's crust. Melting occurs when the solidus of mantle rocks is crossed, but the exact location of the solidus and the melting reactions of the various mantle rocks during partial melting have been a matter of debate for several decades (e.g., Kushiro et al., 1968; Green, 1976; Kawamoto and Holloway, 1997; Green, 1990; Kushiro, 2001; Longhi, 2002; Conceição and Green, 2004; Kessel et al., 2005; Dasgupta and Hirschmann, 2006; Grove et al., 2006; Dasgupta et al., 2007; Foley et al., 2009; Till et al., 2012; Green, 2015). Whilst it is well known that the solidus depends on temperature, pressure, and chemical compositions, the role of fluids on the solidus and the melt compositions of partial melts is still not well constrained.

The most important fluid components in the Earth's mantle are within the system C-O-H, and consequently the nature of fluid species is controlled by redox conditions, i.e. the oxygen fugacity (f_{O_2}). For example, at oxidizing conditions, a C-O-H fluid is mainly composed of CO_2 and H_2O , and their presence can significantly decrease the solidus of peridotite and eclogite (Eggler, 1976; Wyllie and Huang, 1976; Wallace and Green, 1988; Green et al., 1998; Dasgupta and Hirschmann, 2006; Foley et al., 2009) relative to anhydrous melting (Falloon et al. 1988; Jaques and Green, 1980; Spandler et al. 2007). In contrast, at reducing conditions, the C-O-H fluid is dominated by CH_4 and H_2O (Taylor, 1985; Matveev et al., 1997; Frost and McCammon, 2008; Foley, 2010), and the presence of CH_4 in the fluid decreases the activity of H_2O , which leads to a higher solidus temperature. However, oxidation of reduced fluids, e.g. when reduced fluid ascends within the mantle, will increase the activity of H_2O , which lowers the solidus, and will result in melting, the so-called "hydrous redox melting" (Taylor, 1985; Rohrbach and Schmidt 2011, Taylor and Green, 1988; Foley, 2010).

The global average fugacity of MORB is around -0.41 ± 0.43 relative to FMQ buffer (Bézos and Humler, 2005), and the top of upper mantle has an oxygen fugacity of $FMQ \pm 2$ (Frost and McCammon, 2008). Redox conditions change from moderately oxidizing conditions in the uppermost mantle (around the fayalite-magnetite-quartz equilibrium - FMQ) to much more reducing conditions with increasing depth (Ballhaus 1993, Woodland and Koch 2003; Frost and McCammon 2008; Yaxley et al. 2012; Stagno et al. 2013). At higher pressures, this potentially leads to conditions close to metal saturation (Ballhaus 1995; O'Neill et al., 2003; Frost et al., 2004; Rohrbach et al., 2007). Despite this general trend, it seems also important to consider Earth's mantle, at least the lithospheric mantle, as a heterogeneous mixture of material of different compositions,

ranging from fertile peridotite to subducted oceanic crust. Furthermore, there is a lot evidence that many mantle rocks have experienced different degrees of melt extraction, and were or were not subjected to metasomatic overprinting (Yaxley et al., 1998; Ishimaru et al., 2006; O'Driscoll et al., 2015). Whenever such mantle reservoirs are entrained in regimes of different redox state, redox reactions must occur that either consume melt by redox freezing (Rohrbach and Schmidt, 2011) or induce melting via hydrous or carbonatitic redox melting (Taylor and Green, 1988; Foley, 2010; Rohrbach and Schmidt, 2011). To cover the whole spectrum of redox conditions at which melting might occur in Earth's mantle, melting needs to be studied experimentally under oxidizing and reducing conditions in peridotitic and eclogitic systems.

For a long time, the redox state of Earth's uppermost mantle was considered to be at relatively constant fO_2 and close to present day values since ~3.8 Ga (Canil 1997, Delano 2001, Li and Lee, 2004). However, recent fO_2 calculations for Archean and Proterozoic basalts imply that Earth's mantle experienced a secular variation in redox state (Aulbach et al., 2015; Aulbach et al., 2016). Consequently, more data on melting under reducing conditions are needed to better understand magmatism during early stages of Earth's evolution. However, only limited experimental work on partial melting at reduced conditions has been done (Taylor and Green, 1988; Jakobsson and Holloway, 2008; Litasov et al., 2014; Green, 2015), probably due to the fact that it is rather difficult to control fO_2 during experiments under reducing conditions. Taylor and Green (1988) carried out partial melting experiments of a pyrolite-type peridotite with various C-O-H fluids at reducing conditions and at pressures up to 3.5 GPa. However, they do not report the composition of their melts. Jakobsson and Holloway (2008) conducted experiments on partial melting of peridotite with C-O-H fluids at an oxygen fugacity around the iron-wüstite buffer. In their experimental assemblage, the main composition and the buffering assemblage were loaded in graphite/sealed platinum double capsules in which the buffering assemblage (C-O-H fluid + Fe metal wire) was separated from the main composition by a platinum foil. Litasov et al. (2014) used an experimental method with double-capsules consisting of an outer Fe or Mo capsule and an inner Pt capsule, which should allow for better control of oxygen fugacities in the runs, but they do not report fO_2 , neither in the buffer assemblage of the outer capsule nor in the inner capsule. Therefore, the control of fO_2 in their runs remains somewhat unconstrained. The studies on partial melting of peridotite by Green and co-workers (Taylor and Green, 1988; Green, 2015) were performed at relatively low pressure, but the studies at higher pressure and more reduced conditions (Jakobsson and Holloway, 2008; Litasov et al., 2014; Litasov and Shatskiy, 2018) are limited in pressure and temperature range. Moreover, to our knowledge, compositions of partial melts of eclogite at reducing conditions have not been reported yet.

As to the partial melting of eclogite, several studies investigated phase relations of eclogite or peridotite with C-O-H fluids at oxidizing conditions (Dasgupta et al., 2004; Foley et al., 2009), but only Litasov et al. (2011, 2014) has investigated the effects of C-O-H fluids on the melting of eclogite at reducing conditions.

Therefore, we carried out several high-pressure high-temperature experiments to investigate partial melting of both eclogite and peridotite at a range of pressures, temperatures, fluid compositions, and redox compositions. We aim to constrain both the solidus and the partial melt compositions at different redox conditions.

2 Methods

2.1 Starting materials

We performed experiments using two different synthetic starting materials, the starting material for eclogite is similar to the one used by Dasgupta et al. (2004), which is based on an eclogite xenolith from Salter lake crater of Hawaii, and the lherzolite composition is based on a spinel lherzolite (Palme and O'Neill, 2003). Both compositions are given in Table 1. We used carbonates as a source of CaO, Na₂O, and K₂O. These carbonates were dried at 110 °C for 4 hours before preparation. Analytical grade oxides SiO₂, Al₂O₃ and MgO (Alfa Aesar) were first mixed with acetone in an agate mortar, then carbonates were added to the mixture. The resulting mixture was slowly ground under acetone for about 20 minutes, to ensure that the mixture is homogenous. The resulting mixture was fired at 1000 °C overnight to decarbonate. FeO and Mg(OH)₂ as a source for water in oxidizing runs were subsequently added to the previous mixture. The resulting mixture was reground under acetone again until the acetone had evaporated. The final starting material mixtures were always kept in a desiccator.

The starting material of the experiments at oxidizing conditions contained Mg(OH)₂ which released about 5 wt.% H₂O at run conditions.. This is the proportion of fluid used in experiments without oxygen fugacity control (supposed to be oxidized condition). The peridotite melting experiments at reducing conditions contained 3 wt.% Ir in the starting material, with the intention to independently monitor redox conditions of the run (Stagno et al., 2010; Rohrbach and Schmidt, 2011). Furthermore, stearic acid was used as a source for fluids in the reducing peridotite melting experiments. Stearic acid decomposes to H₂O, CH₄ and C at high temperatures (Jakobsson et al., 1986), and this yields 5 wt.% C-O-H fluid in our runs. Note that the eclogite melting runs under reducing conditions did not contain Ir metal.

Table 1. Compositions of starting materials

	Eclogite-5%H ₂ O	Eclogite-5%COH	Lherzolite-5%H ₂ O	Lherzolite-5%COH
SiO ₂	44.2	42.4	43.9	41.78
MgO	11.6	11.3	35.1	33.83
Al ₂ O ₃	11.7	11.2	4.36	4.13
FeO	11.5	11.0	7.58	7.41
CaO	12.0	11.5	3.52	3.36
Na ₂ O	1.49	1.43	0.47	0.32
K ₂ O	0.11	0.10	0.02	0.03
TiO ₂	2.32	2.22	-	
Cr ₂ O ₃	0.09	0.09	-	
MnO	0.13	0.13	-	
NiO		-	0.24	0.22
H ₂ O	4.95		4.88	
COH		5.00		5
C		3.65		3.77
Total	100.0	100.0	100.0	100.0

Eclogite compositions are similar to 66039 B of Dasgupta et al. (2004); Lherzolite after Palme and O'Neill (2003). In addition, 3% Ir is added in the starting material of Lherzolite with 5% COH fluids.

2.2 Experimental and analytical methods

We used various capsule designs in our runs with different redox conditions. For experiments without controlling fO_2 , we used a single Au₈₀Pd₂₀ capsule and alternatively, a Pt capsule at high temperature to prevent capsule melting. The experiments at reducing conditions contained double capsules (Fig. 1), which consisted of an outer capsule (with a lid) made of iron, and an inner capsule that was made of Au₈₀Pd₂₀ or Pt at high temperature. We placed brucite between the outer capsule and inner capsule, and brucite decomposes to MgO and H₂O during the run. The resulting MgO reacts with Fe of outer capsule to form magnesio-wüstite, H₂O partly dissociates at the run conditions and is thus a source for H₂. The permeability of the inner capsule enables the transfer of H₂ between the inner and the outer capsules and this adjusts the fugacity of O₂ of the inner capsule to be equal to the outer capsule. The inner capsule, that contains the starting material, was sealed by welding, while the outer Fe capsule with a Fe lid was cold-welded by compression during the experiment.

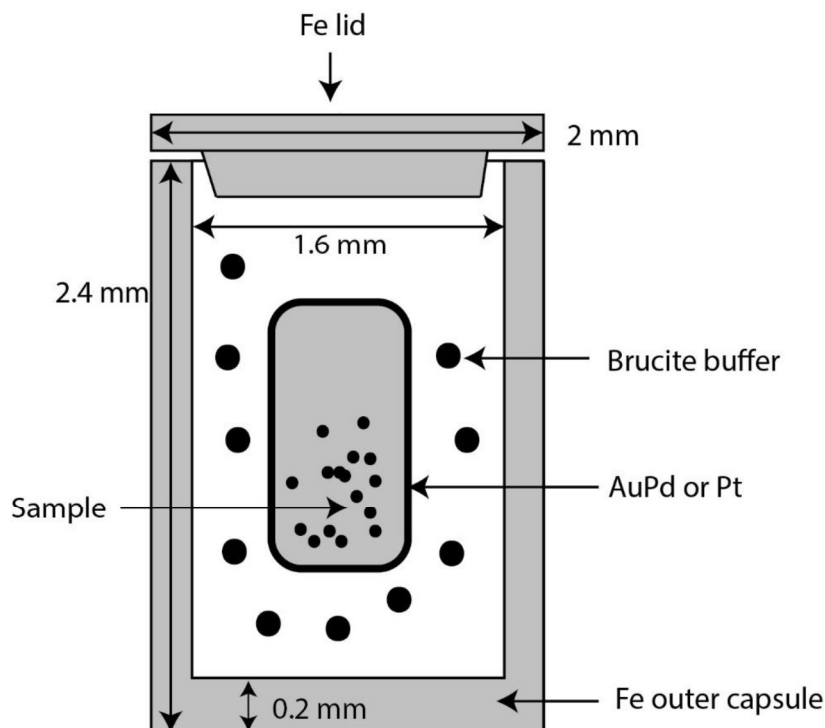


Fig. 1 Schematic diagram of double capsules used in both PC and MA experiments. See text for details.

All experiments were performed with a piston cylinder apparatus (PC) and a 1000-ton Walker-type multi anvil (MA) apparatus at Institute for Mineralogy at Münster University, Germany. The ½ inch PC assembly consisted of an outer talc sleeve, a Duran (Schott GmbH, Germany) glass cylinder, a graphite heater, alumina and/or boron nitride as inner parts. The completed assembly was placed in a pre-stressed pressure vessel with a tungsten-carbide core, using an end load of 3750 psi. The sample pressure was firstly pumped up to about 0.2 GPa, and then the sample was slowly heated up to 200 °C. The pressure and temperature were subsequently increased to the final run pressure and temperature. We used 14/8 assemblies in the multi anvil runs, where the 14 refers to the edge length of the MgO-octahedra (14 mm), and the 8 to the truncated edge length of the tungsten-carbide cubes (8 mm) and either graphite or LaCrO₃ heaters.

Temperature was measured by W₅Re₉₅-W₂₅Re₇₅ thermocouples in both PC and MA experiments. The pressure of piston cylinder runs was calibrated using the quartz-coesite transition (Bose and Ganguly, 1995), and with the MgCr₂O₄ + SiO₂ = MgSiO₃ + Cr₂O₃ reaction to account for friction during the runs (Klemme and O'Neill, 1997). Based on our pressure calibration, reported pressures are accurate within 0.1 GPa. Details of the multi anvil pressure calibration can be found in (Wijbrans et al., 2016). Considering that the buffers used here may be used up in very long experiments (Litasov et al., 2014) and to limit Fe loss into the capsule, almost all of our experiments were run for less

than 12 hours. The experiments were quenched by turning off the power supply. Only undeformed capsules were used and mounted in epoxy resins. The mounts were polished with ethanol, and subsequently carbon coated. Preliminary phase detection was done with a JEOL JSM 6510LA Scanning Electron Microscope (SEM) at Münster University. We carefully checked whether the outer capsule had touched the inner capsule or whether the inner capsule had leaked. Only if the capsules passed this initial evaluation, the run products were further studied. Quantitative major element analyses of all phases were conducted with a JEOL JXA 8900 or a JEOL 8530F microprobe at Münster University. Analytical conditions for minerals were 15 kV accelerating voltage, 15 nA beam current, and counting times of 10 s for peak and 5 s for the background signal, except for Na and K (7 s for peak and 5 s for the background). The beam diameter was 3 μm for crystal analysis. For the analysis of quenched melts, the beam diameter was increased to 15 - 20 μm for larger melt pools and about 6 μm for small pockets of melts between minerals. The beam current was also reduced to 5 nA for such measurements and counting times were monitored regularly and 5 s on the peak and 3 s on the background to minimize alkali element loss and diffusion.

Prior to quantitative analyses, all elements were standardized on matrix matched natural standards (Na, K, Mg, Si, Al, Ca, Fe, Mn) and synthetic (Ti, Cr) reference materials (Table 2). The phi-rho-z correction was applied to all data and the uncertainties on major oxide analyses were in the range to be about 1-2% relative. To monitor accuracy and precision over the course of this study, microanalytical reference materials (Table 2) were analysed, and obtained results match published values within error.

Table 2. Standards used during EMPA analyses

Element	Standard	Mass (%) oxide
Na ₂ O	H_JadeiteST6	15.1
MgO	U_OlivineSanCarlos	49.4
SiO ₂	U_Hypersthene	54.1
Al ₂ O ₃	H_DistheneR8	63.0
K ₂ O	H_SanidineP14	13.0
CaO	H_DiopsideST48	25.9
FeO	U_Fayalite	66.4
TiO ₂	Ast_Rutile	100.0
Cr ₂ O ₃	Ast_Cr ₂ O ₃	100.04
MnO	Ast_Rhodonite	37.7

2.3 Equilibrium and preliminary results

Experimental run conditions and run products are reported in Table 3.

Table 3. Experimental run conditions, calculated fO_2 and phases present in the experiment.

Exp No.	P (GPa)	T (°C)	T (h)	Capsules	fO_2 ($\Delta\log IW$) ¹	fO_2 ($\Delta\log IW$) ²	Phases
L5	2	950	24	AuPd-AuPd			Spl+Ol+Opx+Cpx+Amph
L4	2	1050	24	AuPd-AuPd			Ol+Opx+Cpx+Melt
L3	2	1150	40	AuPd			Ol+Opx+Melt
L2	2	1200	72.6	AuPd			Ol+Opx+Melt
L-CHO-Rd-2-6	1.8	1100	7	Fe-AuPd	-0.77		Ol+Opx+Cpx+Melt
L-CHO-Rd-2-5	1.8	1200	6.3	Fe-AuPd	-0.69	-0.99	Ol+Opx+Cpx+Melt
L-CHO-Rd-2-7	1.8	1250	6	Fe-Pt	-0.37	-0.62	Ol+Opx+Cpx+Melt +C
L-CHO-Rd-6-1	6	1300	6	Fe-AuPd	-0.52		Ol+Opx+Cpx+Grt
L-CHO-Rd-6-4	6	1450	4	Fe-Pt		0.52	Ol+Opx+Cpx+Grt+C
L-CHO-Rd-6-7-4	6	1500	3	Fe-Pt	-0.57	1.35	Ol+Opx+Grt+C
L-CHO-Rd-6-8	6	1600	1	Mo-Pt			Ol+Opx+melt+C
E7	2	800	24	AuPd-AuPd			Spl+Cpx+Rt+Ep+Amph
E6	2	850	24	AuPd-AuPd			Spl+Cpx+Rt+Amph+Melt+Qz
E5	2	950	24	AuPd			Fe-Ti oxide+Cpx+Rt+Amph+Melt
E1	2	1000	46.7	AuPd			Fe-Ti oxide+Cpx+Opx+Amph+Melt
E2	2	1100	48.1 3	AuPd			Fe-Ti oxide+Cpx+Opx+Melt
E-CHO-Rd-2-1	2	950	8	Fe-AuPd	-0.74		Cpx+Opx+Rt+Grt+Melt
E-CHO-Rd-2-4	2	1100	7	Fe-AuPd	-0.61		Cpx+Rt+Grt+Fe-metal+Melt
E-CHO-Rd-2-5	2	1200	6	Fe-AuPd	-0.51		Cpx+Melt
E-CHO-Rd-6-3	6	1400	5	Fe-AuPd	-0.39		Fe-Ti oxide+Cpx(2)+Grt+Fe ₃ C+melt
E-CHO-Rd-6-5	6	1500	4	Fe-Pt	-0.49		Cpx+Grt+Melt+C

From L5 to L2: experiments of lherzolite with 5% H₂O, from L-CHO-Rd-2-6 to L-CHO-Rd-6-8: experiments of lherzolite with 5% COH fluids, from E6 to E2: experiments of eclogite with 5% H₂O, from E-CHO-Rd-2-1 to E-CHO-Rd-6-5: experiments of eclogite with 5% COH fluids. P-pressure, T-temperature, t-run duration, fO_2 -oxygen fugacity. Spl-spinel, Ol-olivine, Opx-orthopyroxene, Cpx-clinopyroxene, Amph-amphibole, C-graphite, Ep-Epidote, Grt-garnet, Rt-rutile, Qz-Quartz, Cpx(2) stands for two kinds of clinopyroxenes formed in different area of capsule that might be affected by thermal gradients. fO_2 ($\Delta\log IW$)¹ and fO_2 ($\Delta\log IW$)² means the fO_2 calculated as fO_2 relative to IW buffer in the outer capsule and inner capsule, respectively.

2.3.1 Attainment of equilibrium

In this study, we only used experiments that show evidence for the attainment of chemical equilibrium. Evidence for the attainment of equilibrium are (1) the presence of large and unzoned phases, (2) subhedral to euhedral shapes of major mineral phases, and (3) homogenous chemical compositions of the same mineral phase in different areas of the capsule (i.e., with a standard deviation of total less than 1.8 % for all solid phases). Note that the quenched melt composition exhibits larger variations, but never more than 4.2 % of the standard deviation. We assume that the larger variations of the quenched melt are due to problems with the analysis of quenched melt, which consists of various proportions of glass and quench crystals. Note also that garnets are frequently zoned, but that we assumed equilibrium was attained if the garnets show large rims of homogenous composition. In addition, because the dynamic transmitting of hydrogen between the outer and inner capsules, the experiments at reducing conditions could only reach approximate equilibrium (Litasov and Shatskiy, 2018).

In addition, we compared temperatures calculated with the two-pyroxene geothermometer (Brey and Köhler, 1990), with our experimental run temperatures. At 1.8 GPa, the calculated temperature of reducing experiments agrees very well with the experimental temperatures (Fig. 2). The runs at oxidizing conditions also agree well. Only the runs L3 and L2 do not, because the geothermometer cannot be used without the presence of clinopyroxene. Similarly, the geothermometer cannot be applied for the reducing experiment at 6 GPa and 1600 °C. We also tried to use the clinopyroxene and garnet geothermometer (Ellis and Green, 1979; Ravna, 2000) but, due to the absence of garnet in the partial melting experiments of eclogite with 5% H₂O and the presence of melt coexisting with garnet in the partial melting experiments of eclogite with 5% COH fluids, these thermometers could be not applied in the runs on partial melting of eclogite.

Table 4 Calculated temperature and Kd in experiments of partial melting of lherzolite

Exp No.	Redox condition	P (GPa)	T _{exp} (°C)	T _{Ca-Opx} (°C)	T-cal-count*	Kd-quenched	Kd-GMB
L4	oxidizing	2	1050	1099 ± 57	3	0.236 ± 0.007	0.495
L3	oxidizing	2	1150	-	-	0.099 ± 0.002	0.24
L2	oxidizing	2	1200	-	-	0.259 ± 0.004	0.41
L-CHO-Rd-2-6	reducing	1.8	1100	1134 ± 34	10	0.215 ± 0.058	0.302
L-CHO-Rd-2-5	reducing	1.8	1200	1204 ± 51	4	0.126 ± 0.012	0.347
L-CHO-Rd-2-7	reducing	1.8	1250	1227 ± 27	5	0.247 ± 0.036	0.340

T-cal-count = counted grains to calculate temperature based on Ca in orthopyroxene. Kd-quenched means Kd was calculated based on direct measured quenched melt composition, while Kd-GMB means Kd was calculated based on the melt composition from graphic mass balance calculation.*

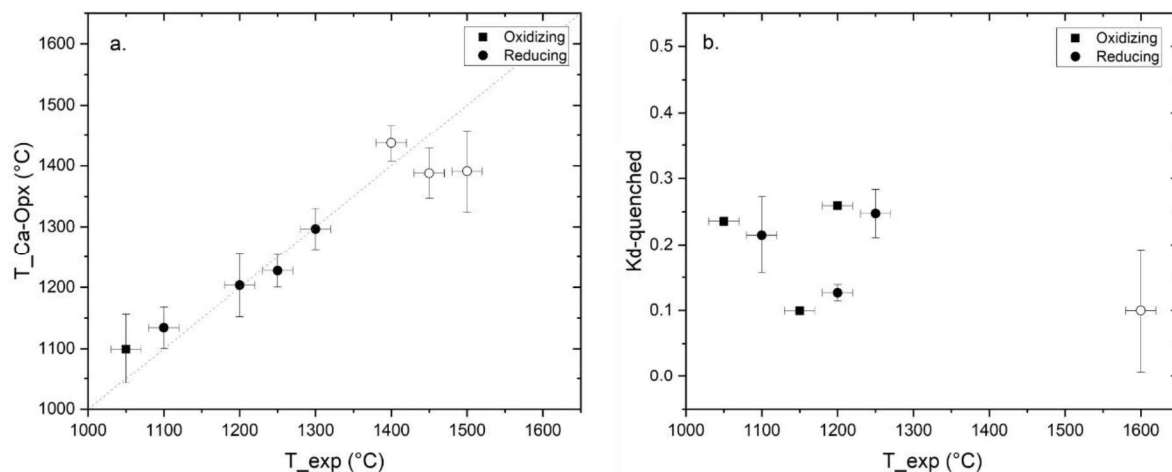


Fig. 2 a: Calculated temperature (T_{Ca-Opx}), (based on Brey and Köhler, 1990) vs experimental run temperatures (T_{exp}) at different redox conditions (Filled squares: oxidizing experiments, filled circles: reducing experiments). b: Calculated Fe-Mg Kd against temperature at different redox conditions and pressures. In both a and b, filled symbols refer to runs at 2 GPa, open symbol representing experiments that were run at 6 GPa.

We also calculated Fe-Mg exchange coefficients (Kd) between olivine and melt for peridotite melting (Tab. 4) to check if equilibrium is attained, which is defined by FeO, MgO in olivine and equilibrated liquid (Roeder and Emslie, 1970):

$$K_d = \frac{X_{FeO}^{Ol} * X_{MgO}^L}{X_{FeO}^L * X_{MgO}^{Ol}}$$

Here, X_{FeO} and X_{MgO} refer to the mole fraction of FeO and MgO, in olivine (Ol) and liquid (L). The experiments at 1.8-2 GPa show that Kd in runs at oxidizing condition ranges from 0.24 to 0.41 and 0.3 to 0.34 from experiments at reducing conditions (Fig. 3). Note that previous values for Kd (Toplis, 2005) range from 0.17 to 0.45 at 1 bar, and Kd is affected by P, T, Na_2O , K_2O , TiO_2 , H_2O , and SiO_2 concentrations (Sack et al., 1987), (Jones, 1988; Wagner and Grove, 1997), H_2O (Toplis, 2005), (Longhi et al., 1978; Ulmer, 1989)(Kushiro and Walter, 1998).

2.3.2 Oxygen fugacity:

We used buffering techniques to control redox conditions during the runs in our reducing experiments as described in the method part of this paper. The calculated fO_2 relative to the IW buffer is provided in Table 3. Since the experiments with 5% H_2O only have intrinsic fO_2 in the capsule, no extra fO_2 calculation has been attempted. Our data show that the oxygen fugacity increases slightly with temperature (Fig. 3). In addition, the oxygen fugacity of the outer capsule is slightly lower (0.25-0.29 log units) than that of the inner capsule. On the other hand, the oxygen fugacity of the Fe-AuPd buffer is slightly higher than the Fe-Pt buffer due to the stronger tendency

of Fe to partition into Pt (Barr et al., 2010). Nevertheless, the difference between inner capsule and outer capsule is less than 1 log unit, which is within the overall uncertainties of $\text{Fe}^{3+}/\Sigma\text{Fe}$ determined in natural garnets with the electron microprobe flank method and Mössbauer spectroscopy (Höfer and Brey, 2007). We also added Ir metal to some experiments to monitor the $f\text{O}_2$ in our runs (Swartzendruber, 1984; Woodland and O'Neill, 1997; Stagno et al., 2010; Rohrbach and Schmidt, 2011). The details of the $f\text{O}_2$ calculation is provided in the Appendix.

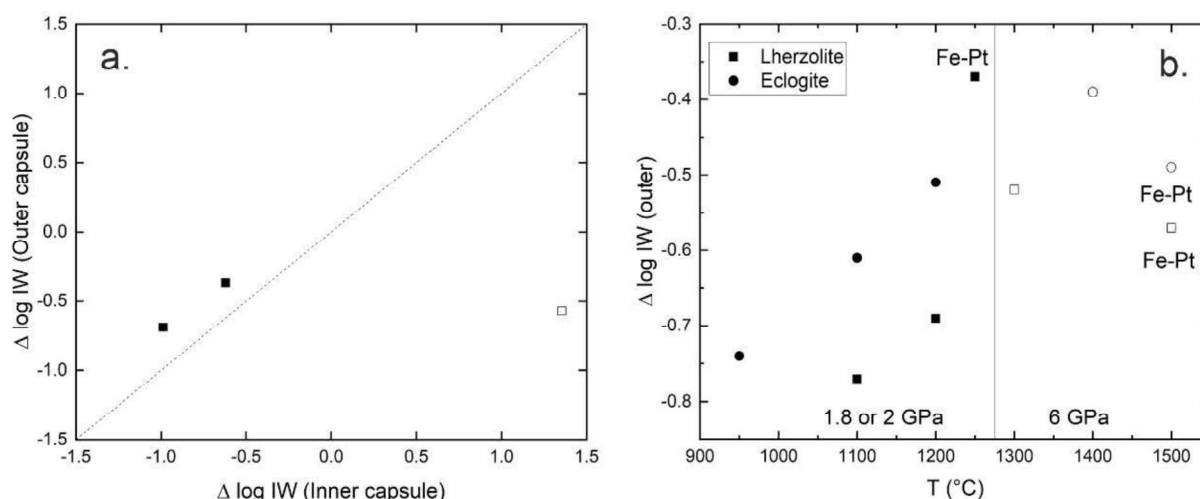


Fig. 3. $f\text{O}_2$ of experiments at reducing conditions. Filled symbols refer to low pressure (1.8-2 GPa), open symbols to high pressure (6 GPa). a: $f\text{O}_2$ of inner capsule and outer capsule. At 6 GPa, the $f\text{O}_2$ is affected by Fe-loss. Thus, there is an obvious shift between the value of inner capsule and outer capsule. b: $f\text{O}_2$ of outer capsule of Fe-AuPd capsules, except the one marked with Fe-Pt, the latter runs employed Fe outer and Pt inner capsules.

2.3.3 Iron loss:

During high-pressure experiments, Fe-loss is an unavoidable issue. Iron loss from the sample to the AuPd capsule is controlled by the Fe activity in Au-Pd-Fe alloy, which depends on $f\text{O}_2$ and temperature at constant pressure (Kawamoto and Hirose, 1994; Balta et al., 2011). Furthermore, the presence of graphite in our runs creates reduced conditions and causes even more Fe-loss to the capsule material. Our experimental results show that Fe-loss to the $\text{Au}_{80}\text{Pd}_{20}$ capsule ranges from 11 to 19 % from the inner side of the inner wall to the outside in reducing experiments.

In our experiments, Fe-loss happened in some high-pressure (6 GPa) experiments with a Pt capsule, i.e. in the reducing partial melting experiments of Lherzolite with 5 % CHO fluid (1450 to 1600 °C at 6 GPa). FeO loss in such experiments is significant and coincides with the formation of graphite. Consequently, almost no FeO content was left in the silicates. Similarly, in some partial melting experiments of eclogite with 5 % C-H-O fluid, (6 GPa, 1500 °C) Fe-loss was significant and resulted in zoned garnet and clinopyroxene and almost no FeO remaining in the melt (0.2 wt.% on

average). Consequently, all our high-pressure experiments at 6 GPa must be considered (more or less) Fe-free system.

2.4 Mass balance calculation:

2.4.1 Mass balance-modal calculation:

It is difficult to determine accurate melt compositions in high-pressure high-temperature experiments with C-O-H fluids (e.g., Takahashi and Kushiro, *Am Mineral*, 68, 859-879, 1983). One of the most serious problems is related to the fact that melts in these experiments do not quench to glasses without some quench modification, which may be due to rapid olivine or pyroxene crystallisation during the quench or due to exsolution of a fluid phase during the quench. Although we aim to maximise the quench rates of our experiments, we observed olivine crystallisation, which we interpret as quench modification. Therefore, we used chemical mass balance calculations to determine phase abundances in each experiment. The mass balance calculations include a weighted least square regression, because the uncertainties of the chemical composition of each phase is not constant, for example, the measurements of Na₂O or K₂O are close to the detection limit with consequently high uncertainties, whilst the uncertainties SiO₂ or MgO analyses are relatively small. The uncertainties are indicated as standard deviation (SD). FeO is another component that needs to be carefully evaluated, because of the aforementioned problem of Fe-loss to the capsule. The best fits were usually achieved when the FeO component was not considered.

For experiments at oxidizing condition, we normalized the melt composition to 100% without considering H₂O. In our experiments at reducing conditions, the volatile phase is a mixture of H₂O and CH₄. Because of low solubilities, CH₄ is not part of our mass balance calculations, but H₂O is a significant component in the melt and in H₂O-bearing phases like amphibole. However, in our experiments at reducing condition, amphibole is not stable.

Therefore, under reducing conditions we considered the involvement of H₂O. The experiments by Berndt et al. (2002), show that the H₂O solubility in basaltic melts increases with pressure, and decreases slightly with decreasing of fO₂ from MnO-Mn₃O₄ to QFM buffer at 0.05-0.2 GPa. Experiments from Hamilton et al. (1964) indicate that the solubility of H₂O in a basaltic melt increased from 3.1 wt% at 0.1 GPa to 9.4 wt% at 0.6 GPa. Given that in the speciation of COH fluids that consists of CH₄, H₂O, H₂ (Holloway and Blank, 1994; Mysen et al., 2009), the mass balance calculations need to consider H₂O in the quenched melt as a component,. Furthermore, the modal

calculations at reducing condition assumes that the dissolved silicate components in the COH fluids is not significant.

Furthermore, to simplify the mass balance calculations and due to the fact that the H₂O solubility in nominally anhydrous minerals is very low (much less than 0.5 %wt.; (Kohn, 1996), the H₂O content of nominally anhydrous minerals was not considered. We used Origin (OriginLab, Inc) to perform the multi-linear regression. To ensure that the calculations are reasonable, the mass balance calculations were compared to SEM images of each run.

2.4.2 Graphic mass balance:

In the run products of the lherzolite melting experiments, olivines tend to have FeO-rich rims which were most likely caused by overgrowth during the quenching of the run (Mysen and Boettcher, 1975a). Therefore, this late Fe-rich overgrowth was part of the melt at run temperature and ignoring the quench modification leads to underestimated Mg# of the melt when only glass is measured (Mysen and Boettcher, 1975a). To reconstruct the original melt composition before the alteration of quenching, we used a graphic mass balance approach for the experiments with the presence of pyroxenes based on the olivine fractionation: First, we normalized the average composition of each phase to 100%. We plotted the compositions of olivine, measured glass composition and nominal bulk composition, i.e of the starting material, in Harker diagrams of MgO, Al₂O₃, and FeO vs. SiO₂. Since the melt is derived from the bulk composition with olivine as the residual phase, the plot of those three components defines the olivine fractionation line (Fig. 4). We then projected the compositions of orthopyroxene and clinopyroxene, which usually lie on either side of the olivine fractionation line. The point where a straight line through the pyroxene compositions intersects the olivine fractionation line represents the composition of the original melt, which has been corrected for olivine growth during the quench. As explained above, conducting graphic mass balance to correct the missing FeO into olivine requires the presence of two pyroxenes.

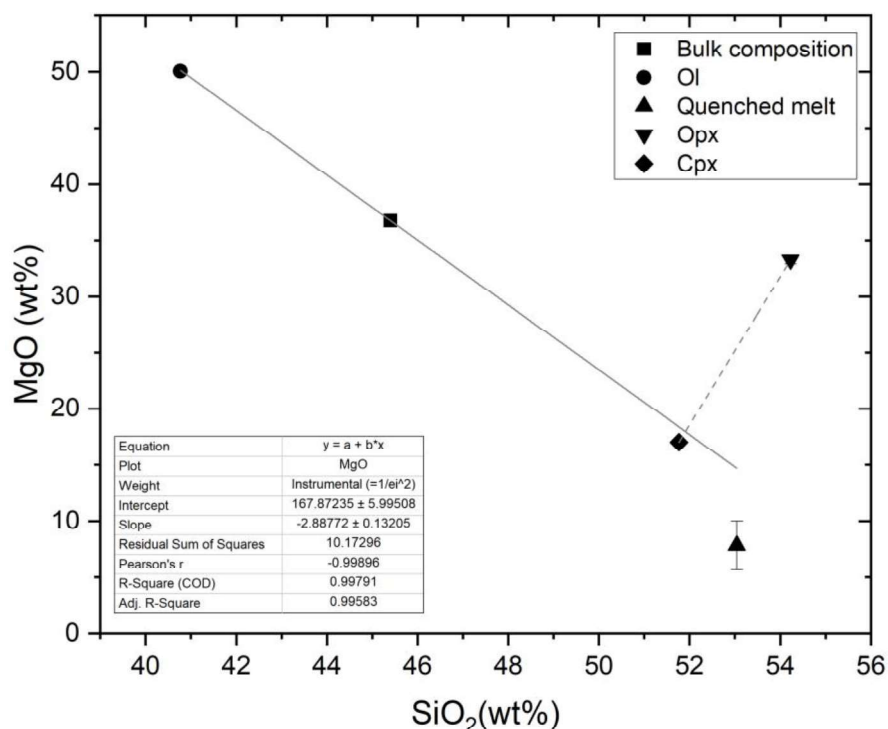


Fig. 4 Graphic mass balance calculations: Symbols represents different phases used in mass balance calculations: The straight line is constructed using the measured olivine composition (Ol) in each run and the bulk composition (black square). The stippled line represents the orthopyroxene (Opx) and clinopyroxene (Cpx) fractionation. The intersection of two lines is the calculated melt composition in this diagram. Note the analyzed quenched melt composition (Quenched melt) deviates significantly from the calculated melt composition due to olivine and pyroxene crystallization during the quenching of the experiments. The parameters of linear fitting based on olivine fractionation is shown in the box in the left bottom.

3 Results and discussion

3.1 C-bearing phases in experiments:

We added stearic acid to the starting material to produce C-O-H fluids via the decomposition reaction $C_{24}H_{36}O_2 = 8CH_4 + H_2O + 10C$ during the runs. Furthermore, at high temperature, when methane decomposes, the chemical reaction equation becomes: $CH_4 = C + 2H_2$. Therefore, in general, the decomposition of stearic acid may be written as: $C_{24}H_{36}O_2 = 18C + 16H_2 + 2H_2O$.

Consequently, the environment of the inner capsule of our runs is a highly reduced environment and our experimental results show that significant amounts of graphite and in one case (run E-CHO-Rd-6-3) also Fe_3C formed. We noted that the amount and grain size of graphite increases with pressure, which may be related to the following reactions: $2FeO + CH_4 = Fe + C + 2H_2O$ and $3FeO + CH_4 = Fe_3C + 3H_2O + 2H_2$, although the mass balance calculations are complicated by the fact that we do not know the exact composition of the fluid phase. Since both CH_4 and C have limited solubilities in solid silicates (Shcheka et al., 2006) and silicate melt (0.2-0.3 wt.%) (Foley, 2010; Mysen et al., 2011; Ardia et al., 2013), we only considered silicates and OH-bearing phases to account for the phases changes with temperature.

3.2 Peridotite melting experiments

3.2.1 Solidi of the mantle lherzolite with C-O-H fluids at different redox conditions:

Our experiments display that the solidus temperature of lherzolite in the presence of C-O-H fluids at reducing conditions is around 1100 °C between 1.8 and 2 GPa, and between 1400 - 1500 °C at 6 GPa (Fig. 5). Since in high-pressure experiments the melt usually does not quench to glass but to an irregular mixture of glass and quench crystals, melt in our runs is identified by textural observations and by chemical composition. Note that the solidus determined in experiments with significant Fe-loss (see above) represent a Fe-free solidus of lherzolite.

We observed that melt quenches to glass in our low pressure runs and in these run we found the solidus for lherzolite with 5 % H₂O which is referred to as at oxidizing conditions in this study, between 950 – 1050 °C at 2 GPa. This value is consistent with the solidus of a pargasite-rich spinel peridotite with 5.7 % H₂O (Millhollen et al., 1974), but higher as the solidus in a H₂O-saturated system (e.g., Katz et al., 2003). In our experiments at reducing conditions, lherzolite with 5 % COH fluid, the solidus temperature is 1100 °C at 1.8 GPa and 1550 °C at 6 GPa and this solidus is parallel to and about 100°C lower than the anhydrous solidus (Katz et al. 2003). Our solidus is substantially higher than the solidus under reducing conditions by Litasov et al. (2014). Our results confirm that the presence of CH₄ in the fluid lowers the solidus compared to the hydrous solidus (Green, 1990), and in fact, that the solidus at reducing conditions is close to the volatile-free solidus. Consequently, all solidi at reducing conditions are at substantially higher temperatures than in oxidizing systems with H₂O, or H₂O+CO₂ fluids. Moreover, all peridotite with various amount of H₂O+CH₄ compositions at low pressure have very similar solidus temperatures, but the solidus increases with decreasing oxygen fugacity. Considering the different experimental peridotite systems, a general trend can be described for the solidus temperatures: peridotite solidus (H₂O + CH₄) > peridotite solidus (H₂O) or peridotite solidus (H₂O + CO₂). As CH₄ solubility in silicate melts is low, it cannot have a direct impact on the solidus of silicate melts but rather large amounts of CH₄ in the fluid lowers the activity of H₂O in the fluid, which in turn causes higher solidus temperatures.

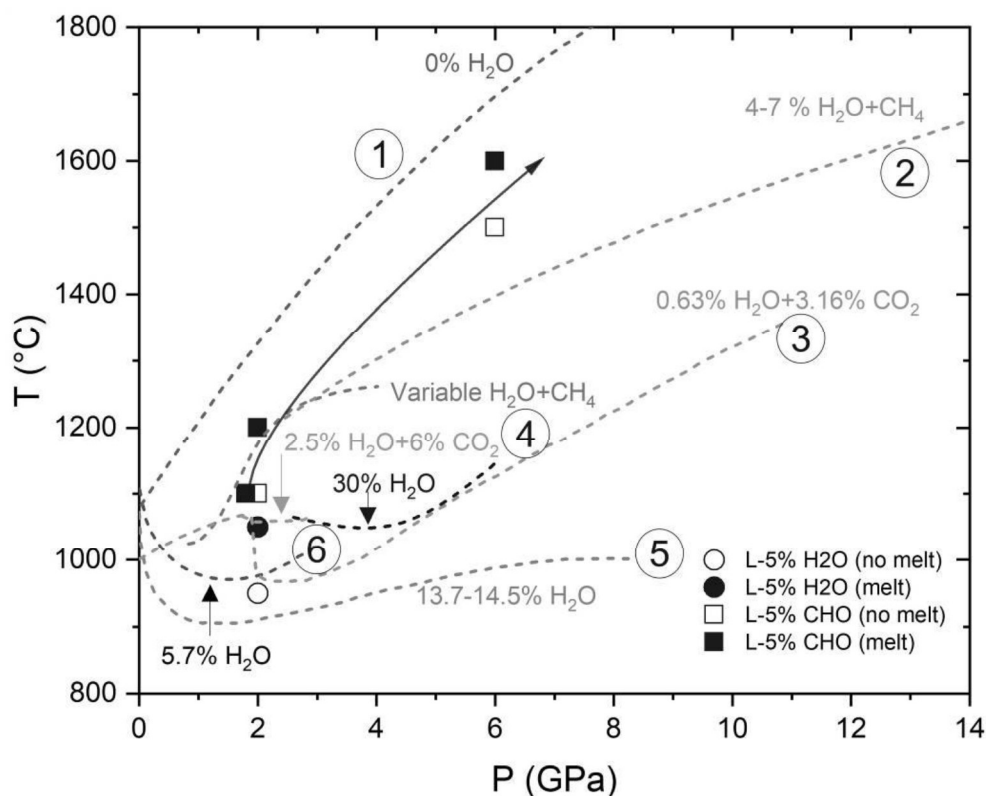


Fig. 5 Peridotite solidi in systems with or without different C-O-H fluids. Our new data are given in circles (oxidized runs) and squares (reducing runs). Open squares or circles = no melt present and solid squares or circles = melt present). Solidi from other studies are marked as numbers in circles together with the amount and kind of fluid used: 1- anhydrous peridotite solidus (Katz et al. 2003); 2- solidus of peridotite with reducing C-O-H fluid (Litasov et al., 2014); 3- solidus of peridotite with oxidizing C-O-H fluid (Foley et al., 2009); 4- solidus of C-O-H-bearing peridotite (Tumati et al. 2012); 5- H₂O-saturated solidus (Katz et al. 2003); 6- solidus of peridotite with 5.7 % H₂O (Millhollen et al. 1974).

3.2.2 Major compositions of all phases in the experiments:

The experimental run products of all experiments are given in Table 3. Olivine and orthopyroxene are the most stable phases, while clinopyroxene is only stable at relatively low temperatures. Fig. 6 displays SEM images of representative experiments at oxidizing conditions and reducing conditions. In general, capsules of experiments at reducing condition have more voids which represents the previous H₂O+CH₄ fluids before the opening of capsule (Fig. 6c). In the experiment at reducing condition at high temperature like 1250 °C, 1.8 GPa, there are formation of graphite (Fig. 6d).

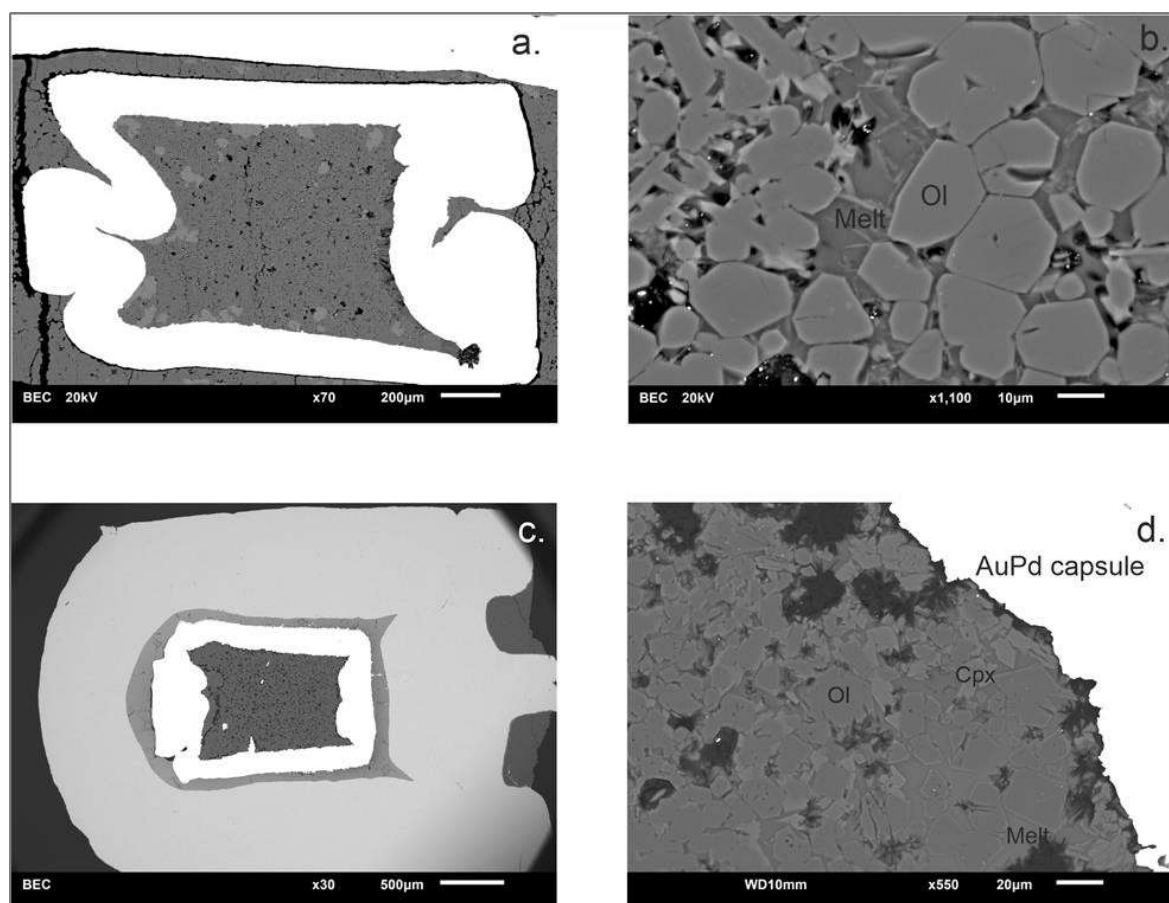


Fig. 6: Back scattered electron images of representative experimental run products at different redox conditions (a,b-oxidizing run, no fO_2 buffer; c,d- $\Delta IW-0.37$). a.-L4: overview of capsule for experiment with 5 % H_2O at 2 GPa, 1050 °C; b.-L4: phases of L4 ; c.-L-CHO-Rd-2-7: overview of capsule for experiment 5 % CHO fluid at 1.8 GPa, 1250 °C. The lighter grey outer capsule is made of Fe, whereas the inner very light capsule is made from Au-Pd alloy; d.- L-CHO-Rd-2-7: phases in L-CHO-Rd-2-7. Abbreviations: Ol-olivine, Cpx-clinopyroxene, melt = quenched melt. The black radial cluster is graphite.

No run above the solidus contains amphibole, which is an important H_2O -bearing phase in lithosphere down to about 85-90 km depths (Green 1990, Flemetakis et al. 2019) and consequently amphibole is only present subsolidus (2 GPa, 950 °C) and at oxidizing conditions. This clearly shows that breakdown of amphibole controls the onset of melting in water-bearing mantle peridotite (Green 1990, Flemetakis et al., 2019), The average major compositions of all run product phases are given in Table 5 (mineral phases) and Table 6 (melts).

3.2.2.1 Al_2O_3 in Orthopyroxene:

Orthopyroxenes in all experiments of peridotite melting experiment with 5% H_2O are enstatite-rich, and the Mg# varies between 90-92 (Table 5). Al_2O_3 in orthopyroxene decreases with temperature at oxidizing conditions (Fig. 7). Although Al_2O_3 concentration in orthopyroxenes has been proposed as a thermometer (Lane and Ganguly, 1980; Sachtleben and Seck, 1981), later work showed the Al_2O_3 concentrated in the orthopyroxene is affected by pressure, temperature and the nature of coexisting fluids. This trend might be related to the continuous melting of clinopyroxene.

However, at reducing conditions, there is no evidence for this trend at low temperatures, probably due to the extended stability of clinopyroxene. At 6 GPa, Al_2O_3 in orthopyroxene has a positive correlation with temperature as garnet is stable, which controls the Al substitution in orthopyroxene (Lane and Ganguly, 1980).

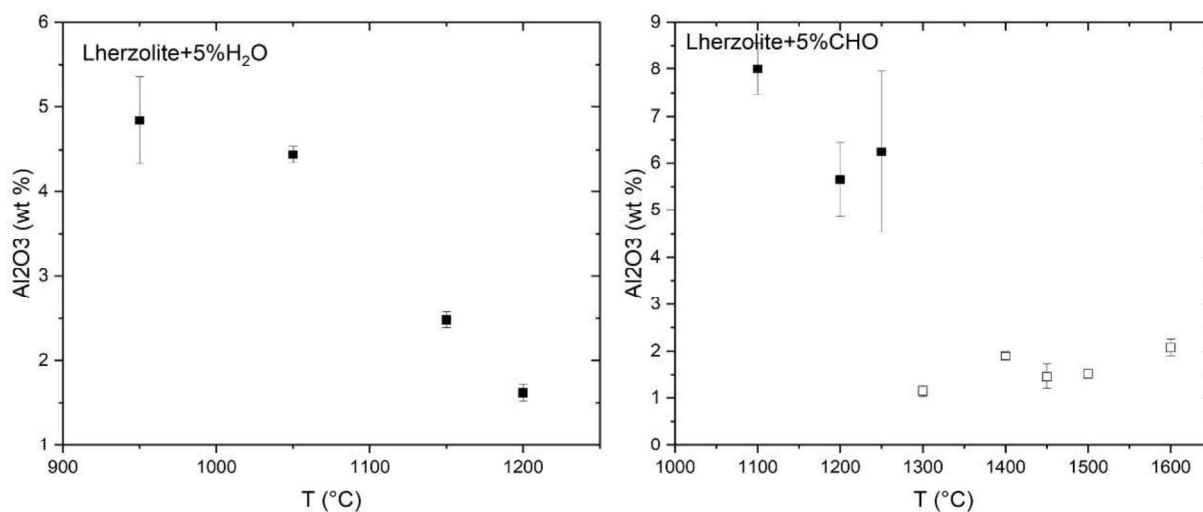


Fig. 7 Al_2O_3 in orthopyroxene plotted against temperature at oxidizing conditions (left diagram) and reducing conditions (right diagram). Filled symbols: 2 or 1.8 GPa (oxidizing or reducing conditions); Open symbols: 6 GPa.

Table 5 Compositions (in wt.%) of mineral phases from partial melting of Iherzolite with different fluids

Exp No.	Phase	n	SiO ₂	Al ₂ O ₃	FeO	MgO	CaO	Na ₂ O	K ₂ O	NiO	Total	Mg#
L5	Spl	6	0.8(9)	2.3(1)	83.1(1)	1.1(1)	0.03(4)	0.04(3)	n.d.*	0.02(2)	87.45(1)	
L5	Ol	3	42.6(2)	0.11(8)	1.8(1)	56.3(4)	0.08(4)	n.d.	0.01(1)	0.54(6)	101.5(6)	98.2(1)
L5	Opx	1	54.0(4)	4.8(5)	5.3(5)	34.1(4)	1.0(4)	0.10(8)	0.03(3)	0.12(3)	99.6(1)	92.0(7)
L5	Cpx	1	51.3	4.24	4.31	16.79	23.35	0.20	0.04	0.07	100.29	87.41
L5	Amph	4	43.4(9)	11.7(3)	5.6(4)	19.8(5)	11.6(2)	1.65(6)	0.9(1)	0.14(3)	94.8(1)	86.3(9)
L4	Ol	7	41.0(6)	0.03(1)	8.7(2)	50.4(2)	0.08(1)	n.d.	0.01(1)	0.39(2)	100.6(3)	91.1(2)
L4	Opx	3	54.1(2)	4.4(1)	6.8(3)	33.2(4)	1.1(2)	0.04(1)	0.01(1)	0.10	99.8(3)	89.7(5)
L4	Cpx	5	51.9(3)	4.1(2)	5.00(3)	17.1(2)	21.7(2)	0.37(3)	0.01(1)	0.07(3)	100.3(3)	85.9(8)
L3	Ol	8	41.8(2)	0.03(1)	5.9(1)	53.0(4)	0.07(2)	0.01(1)	0.01(1)	0.49(4)	101.3(5)	94.1(1)
L3	Opx	8	56.5(3)	2.5(9)	5.5(1)	35.4(2)	0.82(8)	0.01(1)	0.01(1)	0.15(4)	101.0(3)	91.9(2)
L2	Ol	4	40.9(2)	0.02(1)	7.8(4)	51.0(1)	0.09(4)	n.d.	n.d.	n.d.	99.7(3)	92.13(2)
L2	Opx	5	56.9(3)	1.6(1)	5.3(2)	35.2(3)	0.77(4)	0.02(1)	0.01(1)	n.d.	99.8(3)	92.3(3)
L-CHO-Rd-2-6	Ol	3	41.3(4)	0.2(2)	6.6(2)	51.5(1)	0.3(3)	0.01(1)	n.d.	0.05(4)	99.8(4)	93.3(2)
L-CHO-Rd-2-6	Opx	10	54.3(8)	8.0(6)	1.1(4)	35.3(3)	1.3(2)	0.10(5)	0.02(2)	0.02(1)	100.2(4)	98.3(7)
L-CHO-Rd-2-6	Cpx	7	52.9(1)	7.4(1)	1.3(6)	20.6(3)	18.0(2)	0.54(9)	0.03(2)	0.01(1)	100.8(6)	96.6(2)
L-CHO-Rd-2-5	Ol	8	41.0(4)	0.1(3)	9.0(8)	50.0(6)	0.15(2)	n.d.	0.01(1)	0.06(4)	100.2(8)	90.9(8)
L-CHO-Rd-2-5	Opx	4	55.9(6)	5.7(8)	3.6(6)	33.5(8)	1.6(3)	0.06(2)	n.d.	0.02(1)	100.3(8)	94.3(1)
L-CHO-Rd-2-5	Cpx	7	53.0(4)	5.7(7)	2.4(2)	19.1(4)	19.7(3)	0.5(1)	0.02(2)	0.02(2)	100.5(7)	93.4(5)
L-CHO-Rd-2-7	Ol	6	41.7(2)	0.07(1)	5.7(8)	52.6(9)	0.18(2)	0.01(1)	n.d.	0.08(3)	100.3(9)	94.2(8)

(Continued)

Exp No.	Phase	n	SiO ₂	Al ₂ O ₃	FeO	MgO	CaO	Na ₂ O	K ₂ O	NiO	Total	Mg#
L-CHO-Rd-2-7	Opx	5	55.6(1)	6.3(2)	2.4(7)	34.5(9)	1.8(1)	0.08(2)	0.01(1)	0.02(3)	100.6(7)	96.2(1)
L-CHO-Rd-2-7	Cpx-1	5	53.5(5)	5.5(9)	1.4(2)	20.3(3)	18.8(6)	0.47(7)	0.01(1)	0.01(1)	100.1(9)	96.2(6)
L-CHO-Rd-6-1	OI	10	41.5(4)	0.04(3)	7.0(3)	51.7(8)	0.07(4)	0.02(2)	n.d.	n.d.	100.3(9)	92.9(3)
L-CHO-Rd-6-1	Opx	11	58.8(5)	1.1(1)	2.6(9)	36.6(8)	1.1(1)	0.27(6)	0.04(5)	n.d.	100.6(8)	96.1(1)
L-CHO-Rd-6-1	Cpx	5	56.4(3)	3.6(2)	1.2(3)	19.6(4)	17.1(3)	1.9(1)	0.04(1)	n.d.	99.9(4)	96.6(8)
L-CHO-Rd-6-1	Grt	11	43.4(1)	23.6(6)	5.8(3)	23.2(2)	4.2(4)	0.08(7)	0.02(3)	n.d.	100.3(7)	87.6(6)
L-CHO-Rd-6-4	OI	2	42.6(7)	0.03(1)	0.1(3)	57.7(1)	0.09(1)	n.d.	0.01(1)	0.02(2)	100.6(7)	99.9(3)
L-CHO-Rd-6-4	Opx	5	59.2(2)	1.5(3)	0.5(2)	38.0(4)	1.4(2)	0.16(3)	0.01(1)	0.01(1)	100.7(4)	99.3(3)
L-CHO-Rd-6-4	Cpx	5	56.7(2)	1.8(5)	0.10(5)	22.3(3)	19.0(3)	0.75(1)	n.d.	n.d.	100.7(5)	99.8(1)
L-CHO-Rd-6-4	Grt	4	44.8(4)	23.7(6)	0.6(3)	26.2(3)	4.7(1)	0.06(3)	0.01(2)	0.01(1)	100.0(6)	98.7(6)
L-CHO-Rd-6-7-4	OI	8	42.7(4)	0.2(2)	0.2(1)	56.8(6)	0.2(3)	0.05(3)	n.d.	0.02(5)	100.1(6)	99.8(1)
L-CHO-Rd-6-7-4	Opx	12	58.3(7)	1.5(9)	0.7(8)	37.7(8)	1.4(3)	0.18(5)	0.01(1)	0.01(2)	99.9(9)	99.0(1)
L-CHO-Rd-6-7-4	Cpx	3	53.5(2)	7.3(2)	0.09(3)	20.9(3)	16.3(3)	1.0(2)	0.01(1)	n.d.	99.1(3)	99.8(9)
L-CHO-Rd-6-7-4	Grt	10	44.5(8)	23.7(5)	1(1)	26.3(1)	4.0(2)	0.08(3)	n.d.	n.d.	99.8(8)	97.5(2)
L-CHO-Rd-6-8	OI	7	42.6(3)	0.10(1)	0.01(1)	57.5(6)	0.07(1)	n.d.	n.d.	0.01(0)	100.3(6)	99.99(1)
L-CHO-Rd-6-8	Opx	8	58.6(3)	2.1(2)	0.02(2)	38.9(1)	0.76(7)	0.06(2)	0.01(1)	0.02(3)	100.5(7)	99.97(3)
L-CHO-Rd-6-8	Cpx	7	50.4(2)	11.9(2)	0.02(2)	18.1(2)	17.5(2)	1.05(9)	0.01(1)	n.d.	99.0(9)	99.94(7)

runs labeled L (L5 to L2): Iherzolite melting runs with 5 % H₂O (oxidizing) at 2 GPa, runs labelled L-CHO-Rd-2-5 to L-CHO-Rd-2-7: Iherzolite melting runs with 5 % C-O-H (reducing) fluids at 2 GPa, runs labelled L-CHO-Rd-6-1 to E-CHO-Rd-6-9: Iherzolite melting runs with 5 % C-O-H (reducing) fluids at 6 GPa. Numbers in parentheses are the standard deviations using last significant digits. Phase abbreviations: Spl-Spinel, Ol-olivine, Opx-orthopyroxene, Cpx-clinopyroxene, Amph-amphibole, Grt-garnet, Cpx-1 and Cpx-2 mean there are two kind of clinopyroxenes, see text for details. n.d. =not detected. n = number of analyses.

3.2.3 Compositions of melts at different redox condition:

3.2.3.1 Determination of melt composition and classification:

To determine the chemical compositions of our partial melt runs in lherzolite compositions with C-O-H fluid, we used graphic mass balance techniques as described in the section of 2.4.2. As only trace amounts of Na and K are incorporated into olivine crystals, composition of alkalis in the melt is extracted from the direct measurement of quenched melts, not from the graphic mass balance calculations. Furthermore, we compared the difference between the calculated melt based on graphic mass balance and the analyzed quenched melt to verify the approach of graphic mass balance (Tab. 7). In general, after the correction with graphic mass balance, the Al_2O_3 , and FeO, and CaO content of melts are slightly higher than the measured melt compositions, but the MgO contents are significantly higher than the measurements. Considering that graphic mass used in this study corrects mainly quench overgrowth of olivines, with the FeO-rich rim in the olivine there is risk that we might 'over correct' the MgO content in the melt composition. Therefore, the MgO content in the melt composition based on graphic mass balance is higher than the direct measurement of quenched melt which has experienced pyroxenes fractionation. Given this reason, we mainly considered the SiO_2 and FeO components in graphic mass balance calculated melt for later discussions. CaO, Al_2O_3 , and alkali concentrations are based on the direct measurement of melt.

In addition, we calculated the exchange coefficient K_d of Fe^{2+} -Mg between olivine and liquid (Fig. 8) and this provides further strong evidence for the fact that quenching of the melt at high pressures resulted in significant amounts of olivine crystallization during the quenching, and that the mass balance calculations correct successfully for the quench modifications. K_d has no linear correlation with temperature (Fig. 8), because the partitioning of Fe and Mg is strongly dependent on composition, especially from the Mg-content in the melt (Longhi et al., 1978; Ulmer, 1989; Kushiro and Walter, 1998). The large variation of K_d at oxidizing conditions and the small variation at reducing conditions indicates that the melt composition changes significantly with the increasing degree of partial melting.

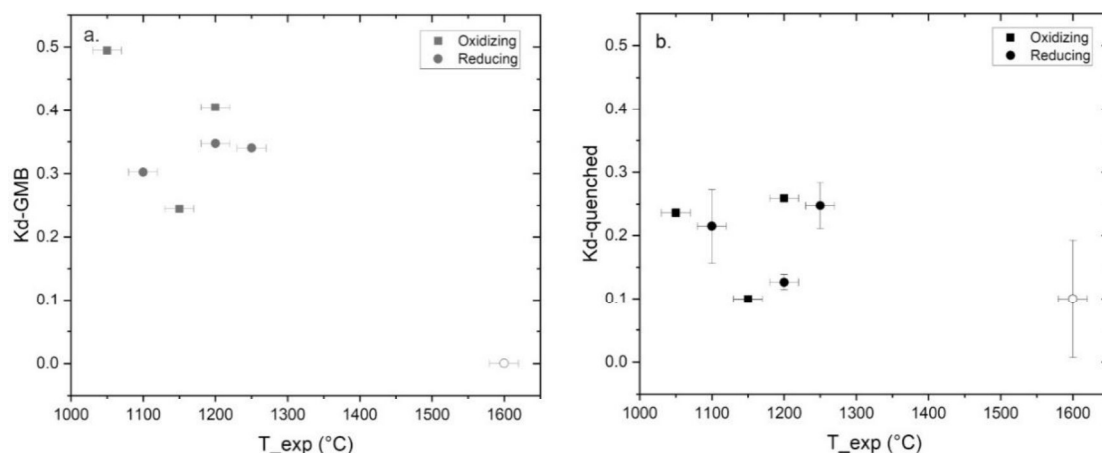


Fig. 8 Kd of melts calculated using graphic mass balance (Kd-GMB) compared to Kd of quenched melt analysed with EMPA methods. Filled square-oxidizing condition (lherzolite + 5% H₂O) at 2 GPa, Filled circles: reducing conditions (lherzolite + 5% COH fluids) at 2 GPa, open circles: reducing conditions at 6 GPa. Kd has no linear correlation with temperature since the partition coefficient between olivine and melt strongly depends on composition.

The melt compositions of our lherzolite partial melting runs are plotted in the total alkalis vs. silica (TAS) diagram (Fig. 9). The melts at lower temperatures in our oxidizing experiments are basaltic and become basaltic andesitic with increasing temperature, but all melts from more reducing runs, are basaltic andesite, except the one at 6 GPa (L-CHO-Rd-6-8) which is basaltic.

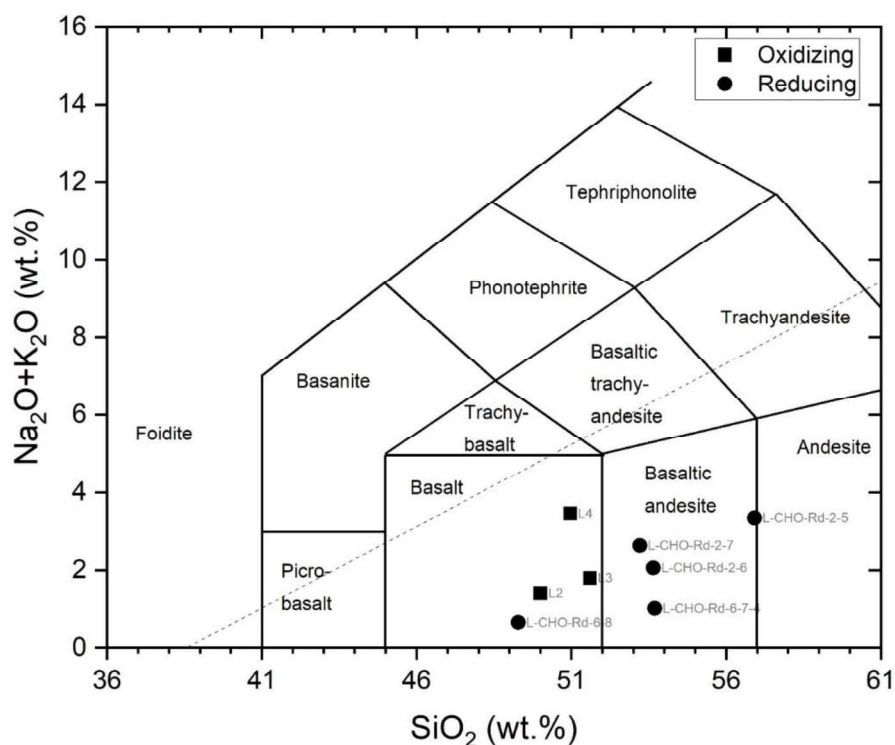


Fig. 9 Melt compositions (Except L2 and L3, the melt composition of other experiments are based on graphic mass balance) of partial melting runs of lherzolite (lower) with different fluids. The run name with 'COH-Rd' refer to the system of eclogite/lherzolite with 5% COH fluids at reducing conditions, otherwise it refers to eclogite/lherzolite runs with 5% H₂O at oxidizing conditions. The number follows 'COH-Rd' indicates pressure of experiments: i.e. 2 actually means 1.8 GPa (here used 2 to keep the name clear) at 6 means 6 GPa.

Table 6 Melt composition from graphic mass balance and measurement from EPMA.

T/°C	Exp No.	SiO ₂	Al ₂ O ₃	FeO	MgO	CaO	Na ₂ O	K ₂ O	NiO	Total	Mg#
Mass balance*											
1050	L4	51.0	15.3	5.8	16.5	8.0	2.38	1.08	0.02	100.00	83.58
1100	L-CHO-Rd-2-6	53.7	11.7	7.3	17.2	8.1	1.62	0.45	0.01	100.00	80.87
1200	L-CHO-Rd-2-5	56.9	10.7	7.0	13.5	8.5	2.83	0.52	0.03	100.00	77.54
1250	L-CHO-Rd-2-7	53.2	12.1	5.4	17.0	9.6	2.19	0.46	0.05	100.00	84.79
1500	L-CHO-Rd-6-7-4	-	-	-	-	-	-	-	-	-	-
1600	L-CHO-Rd-6-8	49.29	10.12	15.43	16.19	8.23	0.52	0.14	0.09	100.00	65.15
Quenched melt											
1050	L4	53.0(9)	19.8(1)	5.3(7)	7.8(2)	10.5(1)	2.4(3)	1.1(2)	0.02(2)	100.0(9)	72.5(5)
1150	L3	51.6(2)	13.8(7)	11.1(8)	10.1(2)	11.2(5)	1.4(1)	0.8(2)	0.03(3)	100.0(7)	61.9(2)
1200	L2	50.0(9)	11.9(3)	9.9(3)	16.6(7)	10.1(8)	0.6(1)	0.8(1)	0.06(4)	100.0(9)	75.0(7)
1100	L-CHO-Rd-2-6	54.6(2)	19.0(2)	4.9(2)	10.9(4)	8.7(9)	1.6(6)	0.44(6)	0.01(2)	100.0(9)	79.9(1)
1200	L-CHO-Rd-2-5	52.4(6)	22.8(7)	6.2(5)	4.4(9)	11.1(2)	2.6(3)	0.47(7)	0.02(3)	100.0(9)	55.7(5)
1250	L-CHO-Rd-2-7	54.4(1)	18.2(1)	4.4(6)	10.8(3)	9.5(2)	2.2(3)	0.46(7)	0.05(4)	100.0(7)	81.3(4)
1500	L-CHO-Rd-6-7-4	53.7(5)	7.7(3)	0.2(1)	21.9(7)	15.6(5)	1.0(3)	0.02(2)	n.d.	100.0(7)	99.6(3)
1600	L-CHO-Rd-6-8	51.4(3)	8.5(5)	0.07(4)	33.3(2)	6.0(6)	0.5(2)	0.14(6)	0.09(3)	100.0(6)	99.9(8)

All melts compositions are normalized to 100% from direct measurement, the values of Na₂O, K₂O, NiO in mass balance calculation are derived from direct measurements.

3.2.3.2 Mineral and melt compositions

At oxidizing conditions, Al_2O_3 in melts decreases with temperature from 15 wt.% to 9 wt.% and increases slightly at higher temperature (Fig. 10). At oxidizing conditions, the subsolidus phase assemblage consists of amphibole, clinopyroxene, orthopyroxene and olivine. Melting occurs somewhere between 950 °C and 1050 °C and goes along with the disappearance of amphibole. Clinopyroxene is melted out at higher temperatures of around 1100 °C, while Al_2O_3 in orthopyroxene decreases with temperature. At reducing conditions, Al_2O_3 in all phases decreases with temperature and then increases slightly. Since there is no disappearance or appearance of any phase, this kind of change indicates that the modal amount of one of the phases has changed. At 6 GPa, Al_2O_3 in all phases does not vary systematically with temperature.

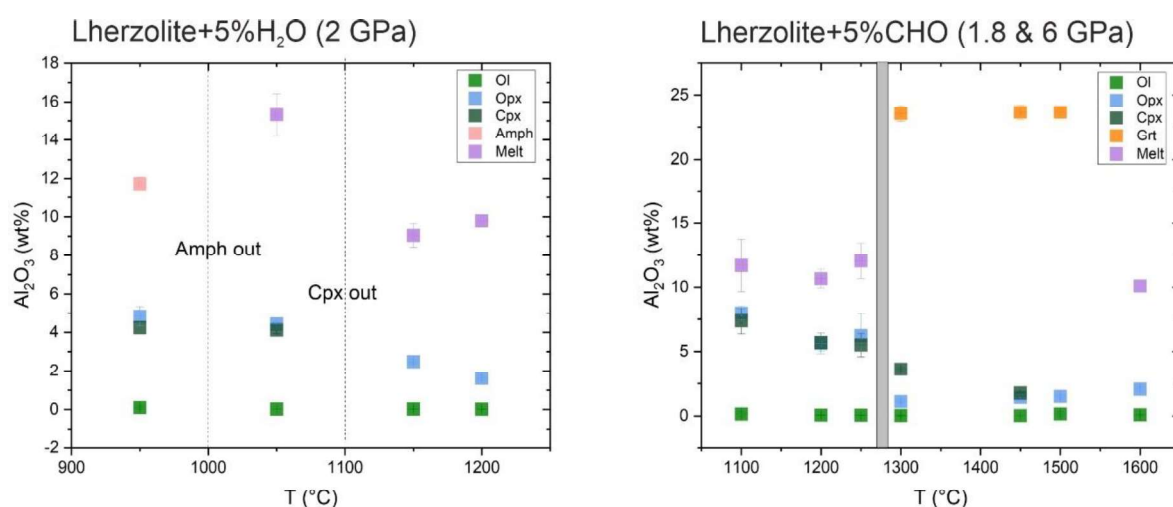


Fig.10 Al_2O_3 in minerals and melts plotted against T in Lherzolite melting runs at different redox conditions. The melt compositions are from graphic mass balance calculations.

We further examine the melt compositions in our runs, and we find that Na_2O in the melt varies between 0.5-2.7 wt% at oxidizing and reducing conditions (Fig. 11). K_2O in the melts at oxidizing conditions range from 0.8 to 1.1 wt%, while K_2O in melts at reducing conditions is quite constant around 0.5 wt %. At oxidizing conditions, Na_2O decreases with temperature and degree of melting increased, and the Na_2O content in clinopyroxene increases slightly with temperature before clinopyroxene is melted out.

At reducing conditions, Na_2O of melts is similar in all runs and does not significantly vary with temperature. At 6 GPa, Na_2O in the melt is very low at around 0.5 wt.%.

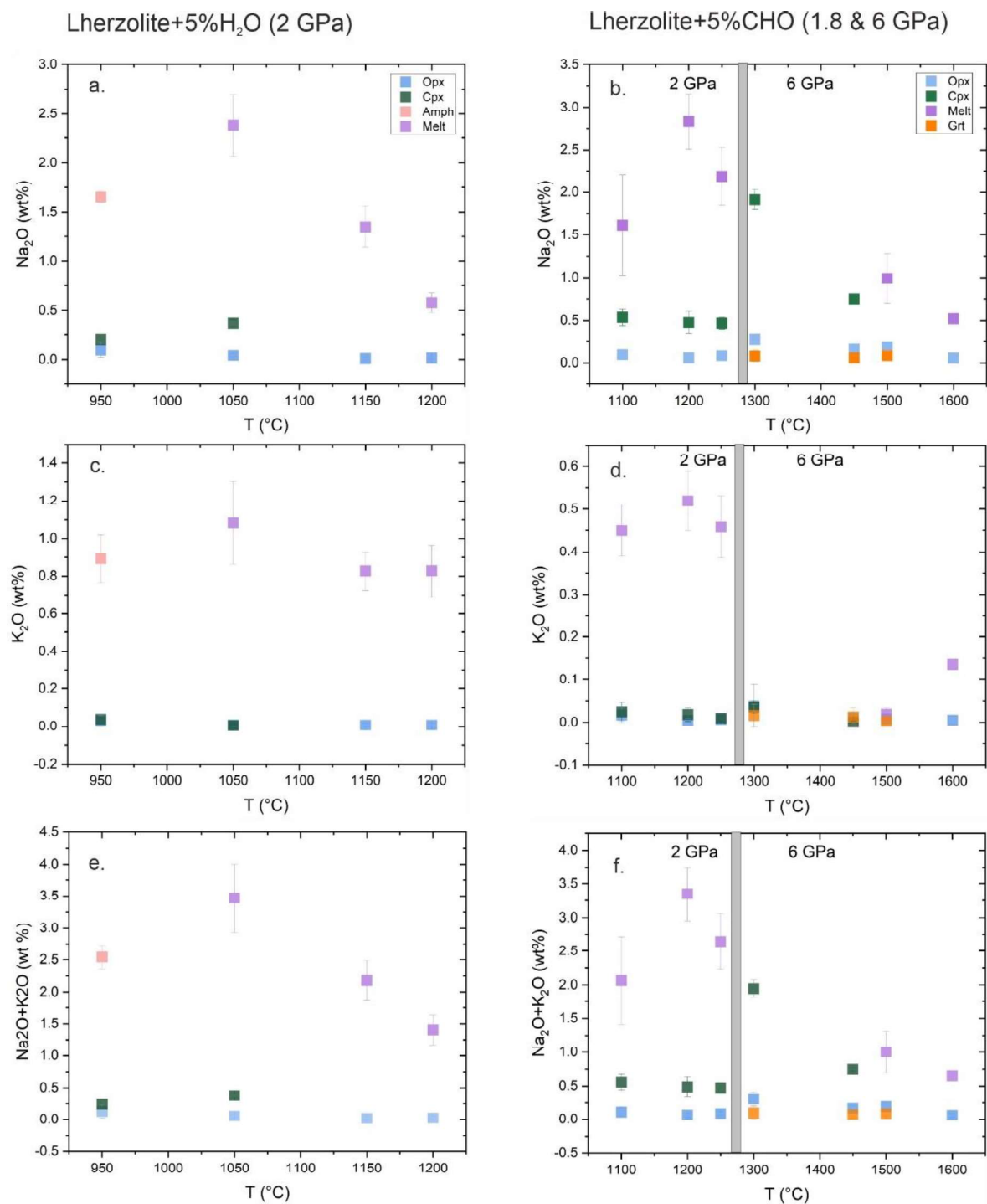


Fig. 11 Na_2O and K_2O of melts and minerals plotted vs temperature in our lherzolite partial melting runs at different redox conditions. The melt compositions are derived from graphic mass balance calculations. The left panel (a, c, e) represent partial melting of lherzolite with 5% H_2O at 2 GPa, the right panel (b, d, f) shows melts from lherzolite partial melting runs with reducing 5% C–O–H fluid at 2 (left side of d and f & 6 GPa (right side of d and f). Phases are represented by different colors; symbols without error bars indicate that the uncertainty is smaller than the size of the symbol.

Comparing the experiments at different redox conditions at a similar degree of melting, i.e. 2 GPa, 1050°C at oxidizing condition (ca. 21% degree of melting based on mass balance calculations) and 1.8 GPa, 1250 °C at reducing conditions (ca. 15% degree of melting based on mass balance calculation), the melt at oxidizing conditions has 21% Al_2O_3 , 8.0% CaO and 3.5% $\text{Na}_2\text{O}+\text{K}_2\text{O}$, while the melt at reducing conditions is more refractory with 15% Al_2O_3 , 9.6% CaO and 2.65% $\text{Na}_2\text{O}+\text{K}_2\text{O}$.

For lherzolite melting experiments, another useful parameter is the Mg number ($\text{Mg\#} = 100 \text{ Mg}/(\text{Mg}+\text{Fe})$). In this study, the Mg numbers of all mineral phases are higher than that of co-existing melts. At oxidizing conditions, olivine has the highest Mg#, higher than 95, and then followed by orthopyroxene, and the lowest is clinopyroxene. On the contrary, in our reducing experiments and at lower temperatures orthopyroxene has the highest Mg# (Fig. 12), followed by clinopyroxene, and olivine. Mg# of melts produced at oxidizing conditions decrease from 84 to 75 with increasing temperature, which goes together with increasing degree of melting. Similarly, at reducing conditions the Mg# of the melt decreases from 81 to 78 (Table 6) as temperature increases from 1100 to 1200°C. The small variation in Mg# relative to the case of partial melting at oxidizing condition is due to the low degree of melting (12-15%) at reducing experiments. At 1250 °C Mg# of melt is 85, higher than the Mg# of melt at 1200 °C, so as the Mg# in other phases. This is probably due to the Fe-loss to the Pt capsule at high temperature, as suggested by Green (1976); Falloon and Green (1987) in previous experiments. The small variation of Mg# of melts at reducing condition illustrates the relative low variation in degree of melting comparing the same temperature range at oxidizing condition.

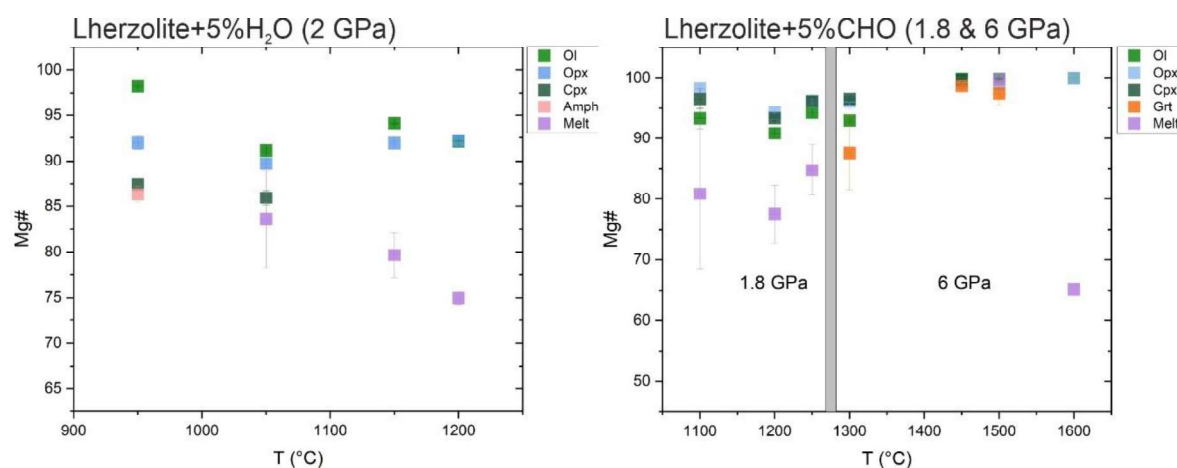


Fig. 12 Mg# of minerals and melts of the experiments at different redox condition. The melt composition here is from graphic mass balance calculation and is given in Table 6.

3.2.3.3 Mineral and melt modes in the lherzolite melting experiments

Here we present calculated mineral and melt modes of our lherzolite melting experiments. Fig. 13 shows calculated modes of the lherzolite melting experiments. At oxidizing conditions, clinopyroxene is only stable at low temperatures, i.e. 1050 °C (Fig. 13). With increasing temperature, the stability field of orthopyroxene increases and the olivine stability field increases. The modal amounts of melt do not change much between 1050 and 1200 °C. In the reducing experiments, clinopyroxene is stable over a wide range of temperatures, i.e. between 1100 and 1250 °C. As a result, the modes of each phase do not change much with increasing temperature. However, the stability field of orthopyroxene increases which is correlated with the expanded stability of clinopyroxene.

At reducing conditions and 6 GPa, garnet is stable from 1400 °C until 1500 °C, and clinopyroxene is stable up to 1450 °C. The stability field of orthopyroxene increases with increasing temperature at the expense of olivine stability field. At the high temperature as 1600 °C, orthopyroxene has the largest stability field. Therefore, our data shows that the stability field of orthopyroxene in our reducing lherzolite melting experiments expands over a broad temperature range, even if the stability field of garnet has been increased, but not at higher temperature. The stability field of graphite was not shown here, but our data shows that graphite rods observed in our runs grow larger with increasing temperature.

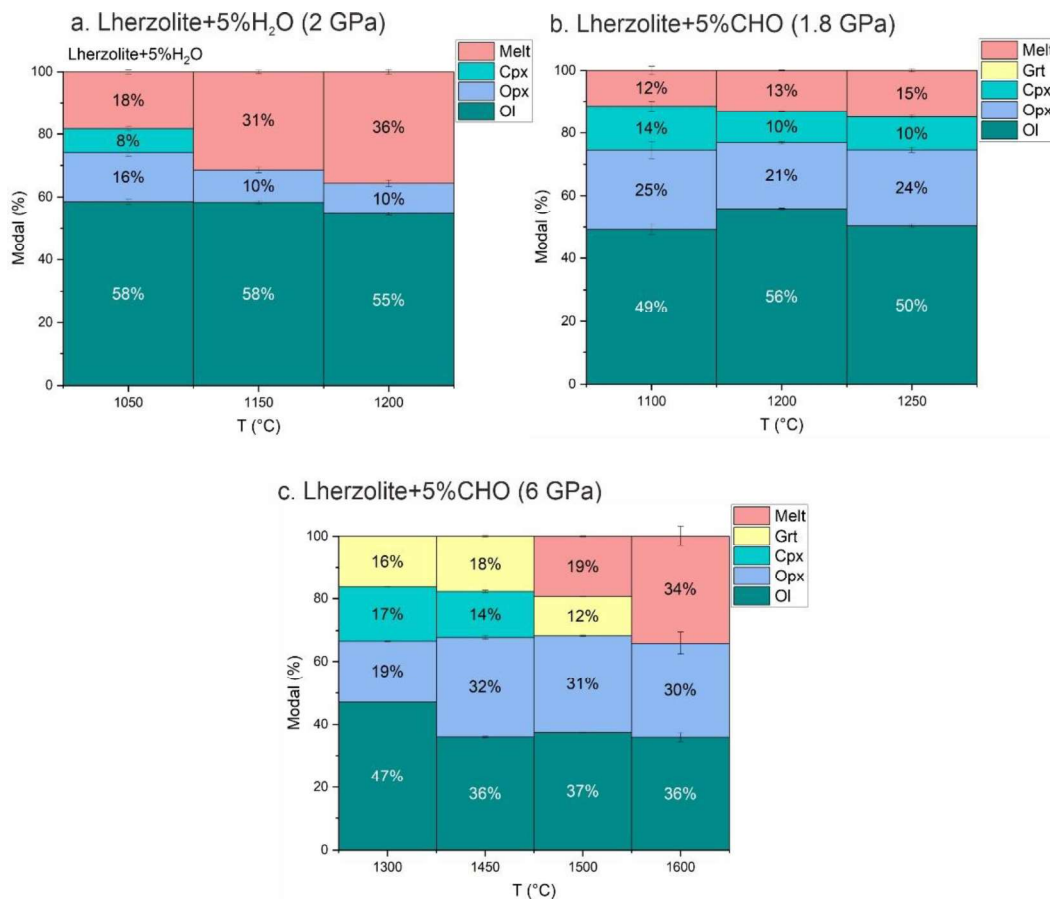


Fig. 13 Mineral and melt modes of melting experiments of lherzolite, both at oxidizing and reducing conditions. At oxidizing condition, as the increase of temperature, clinopyroxene disappears at the temperature lower than 1150 °C, and the modal of melt increases at the expense of shrinking proportion of orthopyroxene.

If we compare melt compositions at reducing conditions to those at oxidizing conditions, melting at reducing conditions begins at much higher temperatures. At reducing conditions, the modal amount of melt increases from 12% to 15% as temperature increases from 1100 to 1250 °C, while the modal amount of melt at oxidizing conditions increases from 21% to 29% at temperatures between 1050 and 1200 °C. The slightly increased melt productivity at oxidizing conditions may be caused by higher stability of clinopyroxene at reducing conditions. The partial melting experiment of lherzolite (c) at 6 GPa and 1600 °C is slightly peculiar, as mass balance calculations result in 34% melt (Fig. 13). However, in the SEM image of this particular run, the quenched melt occupies more than half of the capsule. As the experiment has been polished and the SEM image shows only a cross section of the run product, we believe the mass balance calculation is more accurate.

3.2.3.4 Melting reactions in the experiments

Based on mass balance results presented in the last section, we proposed the following melting reactions (Walter et al., 1995):

At oxidizing conditions:

- 2 GPa, 1050°C → 1200°C:
 $0.43 \text{ Cpx} + 0.34 \text{ OPx} + 0.21 \text{ Ol} \rightarrow 1.00 \text{ Melt}$

The number in front of each phase represents the modal proportions of this phase. As temperature increases from 1050 °C to 1200 °C, the reaction above indicates that the net increase of melt is caused by the consumption of orthopyroxene, olivine, and clinopyroxene. On the other hand, clinopyroxene is only stable at the temperature below 1050 °C. This is consistent with the partial melting of primitive peridotite with $F = 14.6\%$ (Grove et al., 2006) at 2 GPa, that clinopyroxene, orthopyroxene, and olivine are present in a wide temperature range of 850 -1100 °C.

While at reducing conditions:

- 1.8 GPa, 1100°C → 1200°C:
 $2.59 \text{ Opx} + 2.53 \text{ Cpx} \rightarrow 4.12 \text{ Ol} + 1.00 \text{ Melt}$
- 6 GPa, 1450°C → 1500°C:
 $0.74 \text{ Cpx} + 0.05 \text{ Opx} + 0.29 \text{ Grt} \rightarrow 0.08 \text{ Ol} + 1.00 \text{ Melt}$

Therefore, at 1.8 GPa, with temperature increasing from 1100 °C to 1200 °C the stability field of olivine expands at the expense of orthopyroxene and clinopyroxene. While at 6 GPa, clinopyroxene disappeared between 1450 °C and 1500 °C, formation of melt and olivine are at expense of clinopyroxene, orthopyroxene and garnet.

3.2.3.5 Our experimental melt compositions compared to those from the literature

The measured melt compositions and melt compositions calculated from graphic mass balance are given in Table 6 and plotted in Fig. 14. We show the variations of our melt compositions at different pressures, and compare our data to those of previous studies on peridotite melting with various amounts of fluids at different redox conditions (Green, 1976; Gupta et al., 1987; Hirose and Kawamoto, 1995; Grove et al., 2006; Jakobsson and Holloway, 2008; Litasov et al., 2014).

At 1 GPa, high H₂O content causes the melt to be Qz-normative with a low solidus temperature, and with increasing temperatures, the composition of melts moves to olivine normative compositions. Our experiments at 1.8 GPa show that the melt composition is Qz-normative at

reducing conditions, while melts at oxidizing conditions are olivine-normative, which coincides with a higher degree of melting of those experiments. This scenario is different to results from previous studies at 1 GPa (Hirose and Kawamoto, 1995) which is probably due to different degree of partial melting. At 5-12.5 GPa (Figure was not shown here), the available data is from experiments at reducing conditions, and most of results from previous study are very olivine-normative (Jakobsson and Holloway, 2008; Litasov et al., 2014), while the experiments from our study are the least olivine-normative. The differences may be caused by the difference of bulk composition, the measurement of melt, the fluid composition, but perhaps also by different pressures. It is well known that the melt composition moves in olivine-normative direction with pressure, and this has also been observed in experiments on the melting of phlogopite harzburgite (Foley, 1993), where the MgO content of melts increased with increasing pressure.

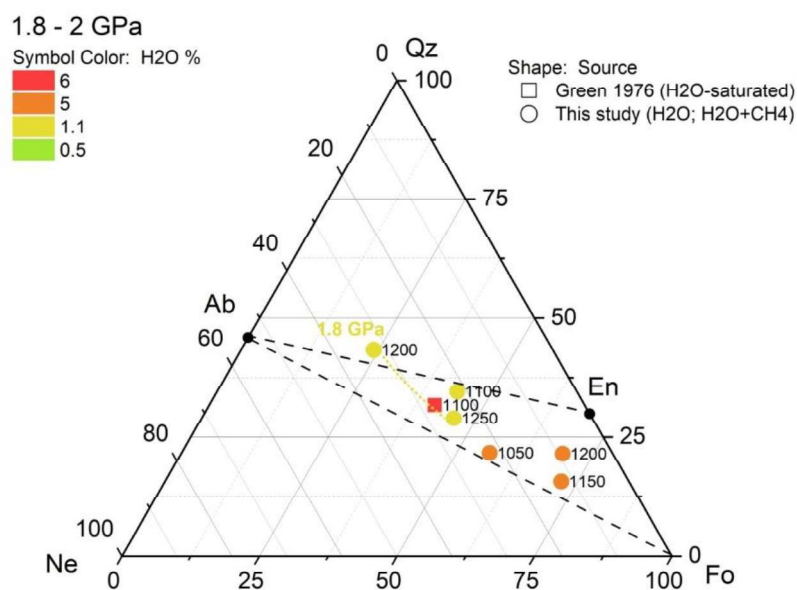
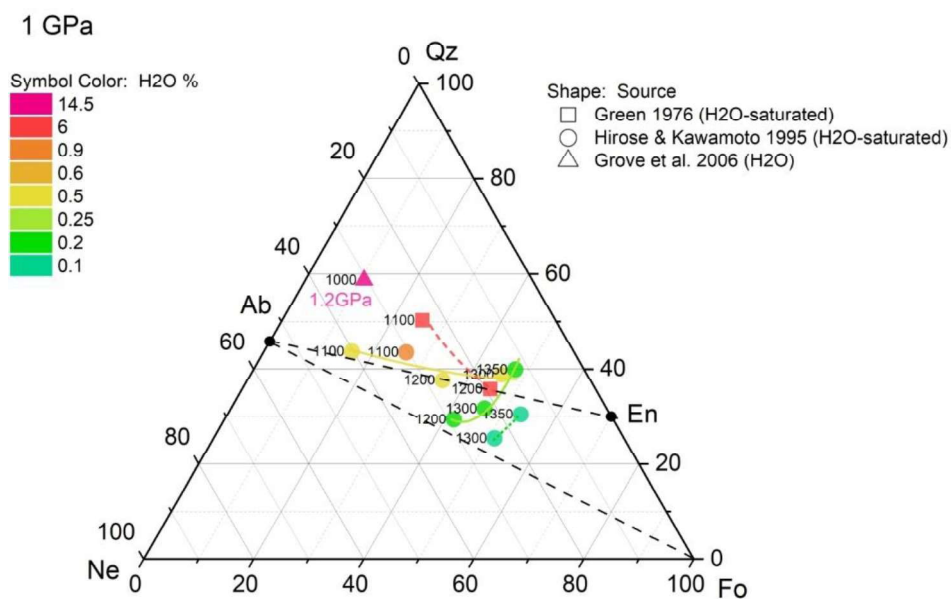


Fig. 14 Melts from partial melting of peridotite with different fluid contents in the system nepheline-forsterite-quartz projected from clinopyroxene at different pressure. Qz-quartz, Ne-nepheline, Fo-forsterite (Mg_2SiO_4), Ab-albite, En-enstatite.

3.3 Eclogite melting experiments

3.3.1 Solidi of eclogite with C-O-H fluids at high pressures and temperatures:

The solidus of eclogite with reducing C-O-H fluid was studied previously (Kessel et al., 2005; Litasov et al., 2014; Brovarone et al., 2018; Martin and Hermann, 2018). Fig. 15 shows the position of eclogite solidi from the literature together with our new data. We find that the solidus of eclogite with 5% H₂O remains not very well constrained, but in our experiments, we find evidence for melt at 850 °C and 2 GPa. Our data at reducing conditions show that the solidus is between 900 and 950 °C at 2 GPa, between 1400 and 1500 °C at 6 GPa. Similar to our results in peridotite with C-O-H fluid system, the solidus of eclogite with reduced fluids is also parallel to, and only slightly lower than the anhydrous solidus (Yasuda et al., 1994), and also much higher than the solidus determined by Litasov et al (2014). As shown in Fig. 15, our solidus of eclogite with H₂O+CH₄ is at higher temperatures than the solidus with CO₂, and even 300°C higher than the H₂O-saturated solidus eclogite (Lambert & Wyllie et al. 1972). Overall, the solidus of eclogite with reducing C-O-H fluids is also lower than that of lherzolite with the same amount C-O-H fluid. The remarkable difference in solidus positions between this study and the one from Litasov et al. (2014) may be caused by bulk composition or fO₂. As the bulk composition used in this study and the one from Dasgupta et al. (2004) are almost identical, the only difference is fluid composition. Dasgupta et al. (2004) used 5% CO₂ fluid, while we used 5% H₂O+CH₄ in our reducing runs. The bend of solidus curve of Dasgupta et al. (2004) is caused by the decomposition of dolomite. Our data in conjunction with the Dasgupta et al. (2004) data indicates that, when partial melting of eclogite from a CO₂-rich oxidizing environment moves into a region of the mantle with more reducing conditions (Rohrbach and Schmidt, 2011), the melts will freeze as the solidus under reducing conditions is much higher. If only reducing C-O-H-rich fluids are present in the mantle, fluids under oxidizing conditions will cause partial melting but the same amount of fluid under reducing conditions will not.

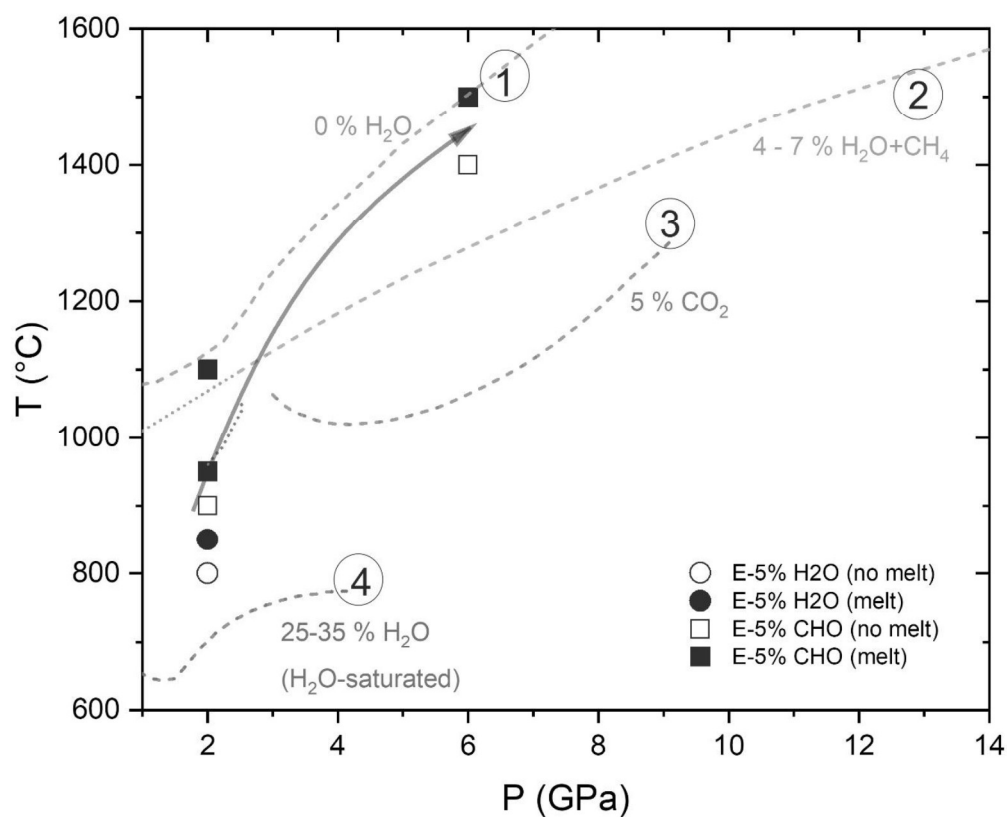


Fig. 15 Solidi of eclogite with or without different C-O-H fluids. Our new data are given in small circles (oxidized runs) and squares (reducing runs). Open squares or circles = no melt present; solid squares or circles = melt present). Solidi from other studies are marked as numbers in large circles together with the amount and kind of fluid used: 1-Anhydrous solidus of mid-ocean ridge basalt (Yasuda et al. 1994); 2-solidus of eclogite with reducing fluid ((Litasov et al., 2014)); 3-solidus of carbonated eclogite (Dasgupta et al., 2004); 4-solidus of H₂O saturated quartz eclogite (Lambert and Wyllie et al. 1972).

3.3.2 Major element compositions of minerals and melts:

The experimental conditions for our eclogite melting runs are given in Table 3. The average mineral compositions (with uncertainties) from our partial melting experiments of eclogite are provided below (Table 7).

Table 7 Compositions (in wt.%) of mineral phases from partial melting of eclogite with different fluids.

9	Phase	n	SiO ₂	TiO ₂	Al ₂ O ₃	Cr ₂ O ₃	FeO	MnO	MgO	CaO	Na ₂ O	K ₂ O	Total	Mg#
E7	Spl	6	0.06(2)	0.19(14)	0.91(68)	0.01(1)	87.52(103)	0.03(01)	0.04(03)	0.11(06)	0.01(02)	0.01(01)	88.88(55)	
E7	Cpx	9	52.83(16)	0.63(86)	5.97(228)	0.02(01)	2.94(105)	0.17(07)	17.85(384)	17.5(495)	0.66(25)	0.04(03)	98.61(99)	90.94(460)
E7	Rt	4	1.35(4)	92.29(6)	0.58(07)	0.29(03)	4.30(01)	0.02(01)	0.07(05)	0.84(18)	0.06(03)	0.01(01)	99.82(38)	
E7	Ep	8	38.33(3)	0.51(08)	24.76(41)	0.06(04)	9.14(23)	0.18(02)	1.04(27)	22.99(42)	0.04(04)	0.01(01)	97.05(34)	
E7	Amph	8	46.79(17)	1.21(48)	14.21(144)	0.09(05)	6.72(126)	0.16(03)	15.09(120)	12.00(28)	1.56(13)	0.15(03)	97.96(48)	79.97(383)
E6	Cpx	4	49.9(4)	1.4(3)	6.9(5)	0.05(2)	6.0(1)	0.19(1)	12.6(6)	22.9(7)	0.48(8)	0.02(1)	100.4(8)	79.0(4)
E6	Spl	6	0.2(2)	13.0(2)	1.7(8)	0.03(2)	73.6(2)	0.13(3)	1.7(4)	0.27(7)	0.02(2)	n.d.	90.6(7)	
E6	Rt	5	1.6(2)	88.9(3)	0.9(4)	0.24(4)	4.5(3)	0.02(2)	0.4(4)	1.1(5)	0.03(4)	0.01(1)	97.5(5)	
E6	Amph	7	44.0(9)	1.2(2)	14.2(6)	0.07(3)	9.7(1)	0.18(3)	13.9(6)	11.7(3)	1.7(1)	0.18(3)	96.9(6)	71.8(3)
E6	Qtz*	1	90.16	0.77	4.93	n.d.	0.62	n.d.	n.d.	2.65	0.87	n.d.	100.00	
E5	Cpx	7	49.1(5)	1.3(6)	9.5(8)	0.10(3)	5.1(8)	0.18(2)	12.7(6)	21.0(1)	1.0(2)	0.03(1)	99.9(8)	81.5(3)
E5	Fe-Ti oxide	7	0.3(3)	20.0(3)	2.1(2)	0.1	68.2(3)	0.05(4)	0.8(9)	0.24(2)	0.01(1)	n.d.	91.78(9)	
E5	Amph	16	45.0(8)	1.0(4)	14.3(6)	0.07(3)	5.5(5)	0.17(3)	17.5(6)	11.3(4)	1.81(8)	0.20(3)	96.8(8)	85.0(12)
E1	Cpx	6	46.8(6)	1.3(2)	10.2(6)	0.10(3)	8.7(3)	0.16(2)	12.0(3)	18.9(6)	0.91(1)	0.02(2)	99.2(6)	71.1(1)
E1	Opx	5	49.7(5)	0.44(5)	9.2(3)	0.09(2)	14.3(4)	0.24(3)	24.3(6)	1.5(2)	0.15(4)	0.03(2)	99.9(6)	75.3(9)
E1	Fe-Ti oxide	8	0.10(3)	23.0(3)	2.7(6)	0.44(8)	64.2(4)	0.09(3)	2.54(5)	0.19(8)	n.d.	n.d.	93.3(8)	
E1	Amph	12	41.5(4)	2.0(4)	15.1(2)	0.12(3)	10.4(2)	0.14(5)	14.4(2)	10.4(2)	2.5(1)	0.27(3)	96.8(5)	71.3(6)
E2	Cpx	11	47.0(4)	0.8(2)	8.6(3)	0.12(3)	7.8(2)	0.15(6)	13.8(2)	19.7(4)	0.9(7)	0.02(2)	98.8(6)	75.9(6)
E2	Opx	13	50.6(4)	0.27(7)	7.9(2)	0.10(4)	9.3(2)	0.20(5)	29.9(4)	1.2(1)	0.07(4)	0.01(1)	99.5(7)	85.2(4)
E2	Fe-Ti oxide	12	0.04(2)	16.9(5)	3.5(1)	0.8(1)	67.3(5)	0.07(4)	3.4(1)	0.10(4)	n.d.	n.d.	92.0(5)	
E-CHO-Rd- 2-1	Cpx	6	51.9(9)	1.7(3)	11.1(7)	0.14(3)	3.6(2)	0.14(3)	11.8(9)	17.6(9)	1.7(2)	0.07(2)	99.7(9)	85.5(7)
E-CHO-Rd- 2-1	Opx	4	54.4(9)	0.7(3)	5.9(1)	0.11(3)	10.5(5)	0.16(3)	27.5(8)	0.7(4)	0.06(3)	0.02(1)	100.1(8)	82.3(7)
E-CHO-Rd- 2-1	Rt	2	3.9(3)	92.3(1)	1.7(3)	0.25(3)	0.35(1)	n.d.	0.42(2)	1.0(1)	n.d.	n.d.	100.0(3)	68.3(2)
E-CHO-Rd- 2-1	Amph	4	45.1(7)	2.6(3)	15.4(7)	0.05(3)	8.5(2)	0.13(1)	12.9(1)	10.2(3)	2.2(2)	0.25(3)	97.3(7)	73.0(6)

(Continued)

E-CHO-Rd-2-1	Grt	5	38.9(5)	1.8(4)	20.9(3)	0.07(2)	19.5(9)	0.43(8)	9.3(9)	8.7(4)	0.05(3)	0.03(3)	99.7(9)	45.9(3)
E-CHO-Rd-2-4	Cpx	13	51.8(1)	2.5(3)	9.4(7)	0.10(4)	5.3(1)	0.12(3)	12.5(9)	16.1(1)	1.9(1)	0.10(9)	99.8(9)	80.9(3)
E-CHO-Rd-2-4	Rt	1	2.54	94.55	1.19	0.14	0.45	0.00	0.21	0.98	0.00	0.00	100.05	45.44
E-CHO-Rd-2-4	Grt	4	41.4(2)	2.0(4)	20.8(1)	0.11(4)	15.3(4)	0.31(8)	12.8(3)	7.4(1)	0.22(2)	0.01(1)	100.3(8)	60.0(7)
E-CHO-Rd-2-4	Fe metal*	6	1.6(1)	0.14(6)	0.2(3)	0.01(1)	126.1(3)	0.01(2)	0.4(5)	0.2(1)	0.02(2)	0.01(1)	128.7(5)	
E-CHO-Rd-2-5	Cpx	5	50.3(3)	1.9(2)	9.0(8)	0.15(1)	4.7(4)	0.14(3)	15.8(7)	17.2(7)	1.0(4)	0.03(2)	100.0(7)	85.8(2)
E-CHO-Rd-2-5	Opx	2	50.7(7)	1.2(5)	7.7(4)	0.14(5)	7.6(4)	0.17(1)	27.4(2)	4.5(3)	0.2(1)	0.01(1)	99.6(7)	86.5(8)
E-CHO-Rd-2-5	Amph	8	41.0(9)	4.3(5)	17.3(1)	0.02(2)	11.0(1)	0.14(4)	10.7(2)	9.5(8)	2.1(2)	0.24(6)	96.2(8)	63.5(9)
E-CHO-Rd-6-3	Cpx-1	6	54.4(3)	2.0(3)	5.7(8)	0.08(8)	5.7(9)	0.09(2)	12.6(3)	16.5(4)	3.5(4)	0.06(2)	100.6(9)	79.8(5)
E-CHO-Rd-6-3	Cpx-2	6	53.7(2)	0.62(9)	3.6(3)	0.06(3)	10.1(4)	0.07(2)	12.9(1)	17.9(2)	2.0(1)	0.04(2)	100.7(9)	69.5(2)
E-CHO-Rd-6-3	Grt	6	40.4(2)	2.2(2)	21.1(2)	0.14(3)	15.5(1)	0.29(3)	11.8(5)	9.0(4)	0.29(5)	0.01(1)	100.7(5)	57.6(3)
E-CHO-Rd-6-3	Fe-Ti oxide	4	3.3(3)	51.1(3)	1.0(3)	0.05(3)	33.4(2)	0.17(4)	7.8(6)	1.5(8)	n.d.	n.d.	98.2(8)	
E-CHO-Rd-6-3	Fe ₃ C rich melt	5	0.01	0.03	0.01	0.03	116.63	0.02	0.02	0.01	0.04	0.02	116.83	
E-CHO-Rd-6-3	Cpx	6	54.4(2)	1.0(2)	8.2(8)	0.08(2)	1.9(4)	0.06(2)	14.3(5)	18.3(4)	2.6(2)	0.02(1)	100.7(8)	93.2(1)
E-CHO-Rd-6-5	Grt	7	43.0(7)	1.1(2)	23.5(6)	0.17(4)	3.6(3)	0.21(5)	18.6(2)	10.8(3)	0.11(3)	0.01(1)	101.1(7)	90.2(1)

From E6 to E2: eclogite melting runs with 5 % H₂O at 2 GPa, from E-CHO-Rd-2-1 to E-CHO-Rd-2-4: eclogite melting runs with 5 % C-O-H fluids at 2 GPa, from E-CHO-Rd-6-3 to E-CHO-Rd-6-5: eclogite melting runs with 5 % C-O-H fluids at 6 GPa. Numbers in parentheses are the standard deviation based on the last digits. Phase abbreviations: Cpx-clinopyroxene, Spl-Spinel, Rt-rutile, Amph-amphibole, Qz-quartz, Opx-orthopyroxene, Grt-garnet, Cpx-1 and Cpx-2 mean there are two kind of clinopyroxenes. Qz* in E5 was detected in SEM not EPMA. n.d.* means not detected, n = number of analyses. Fe-metal and Fe₃C melt were measured by EPMA where Fe metal is expressed as FeO, and thus totals exceeds 100%.

3.3.2.1 Compositional variations of minerals and melts at different redox conditions

At oxidizing conditions, amphibole and melt (10-18 wt.%) contain the highest Al_2O_3 concentrations; Al_2O_3 in melt is variable (Fig. 16) and it decreases with SiO_2 in clinopyroxene and orthopyroxene. At reducing conditions, Al_2O_3 is negatively correlated with SiO_2 in the melt, clinopyroxene, and orthopyroxene. Therefore, it might suggest that the distribution of Al_2O_3 depends on the composition and the proportion of pyroxenes which dissolve into the melt with increasing of temperature. The high Al_2O_3 of orthopyroxene is suggested to be due to the bulk composition which has 12.25 wt% Al_2O_3 and which is higher than many metamorphic eclogite compositions, however naturally found orthopyroxene-bearing eclogite can be MgO-rich (10-15 wt%) and high have high concentration of Al_2O_3 as well (Nakamura, 2003).

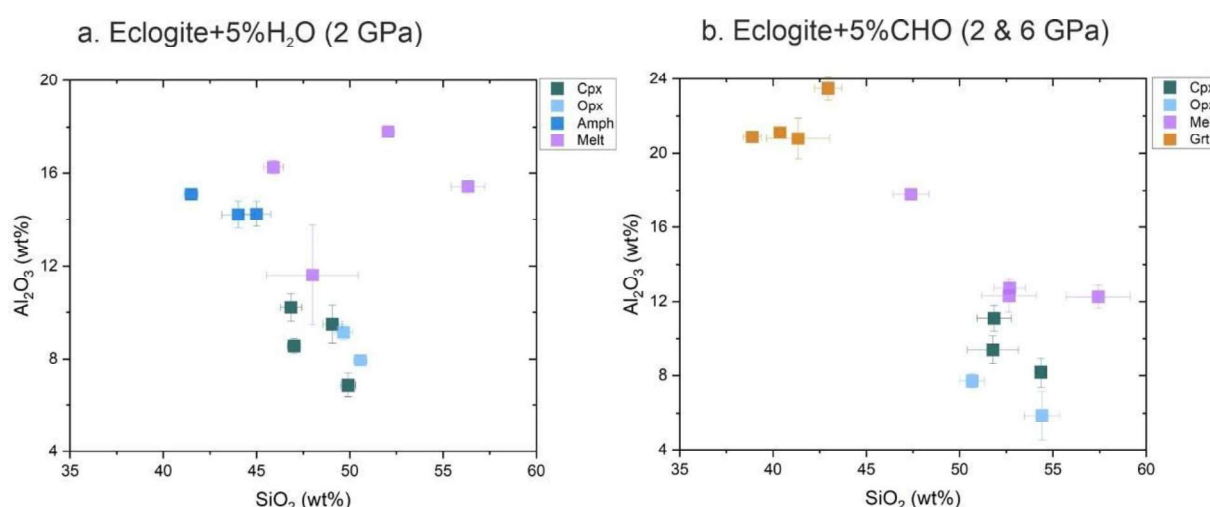


Fig. 16 Al_2O_3 in minerals and melts plotted against SiO_2 in eclogite melting runs at different redox conditions. The minerals and melt compositions are given in Table 7 and Table 8, respectively.

The variation of Na_2O and K_2O with temperature is plotted in Fig. 17 (a-f). At oxidizing conditions, Na_2O in amphibole, clinopyroxene, and melt increases with temperature. K_2O contents in amphibole and melt increase with temperature as well. At 1100 °C amphibole breaks down but neither Na_2O or K_2O in melt are significantly affected and Na_2O and K_2O in clinopyroxene and orthopyroxene (at high temperature) are quite constant. At reducing conditions, however, the main Na-bearing phase amphibole is absent in all runs, and consequently the Na_2O contents in clinopyroxene and melt increase with temperature. While the K_2O content of melts increases with temperature below 1200 °C, it decreases at $T > 1200$ °C because of high degrees of melting. At 1200 °C both clinopyroxene and orthopyroxene contain low amounts of K_2O (Table 7) at reducing conditions. At 6 GPa, clinopyroxene contains about Na_2O (~2.6 wt.%), so that clinopyroxene contains much higher amounts of Na_2O than the melt. Na_2O in garnet is very low (< 0.2 wt.%) at all pressures and increases only slightly with temperature (Table 7).

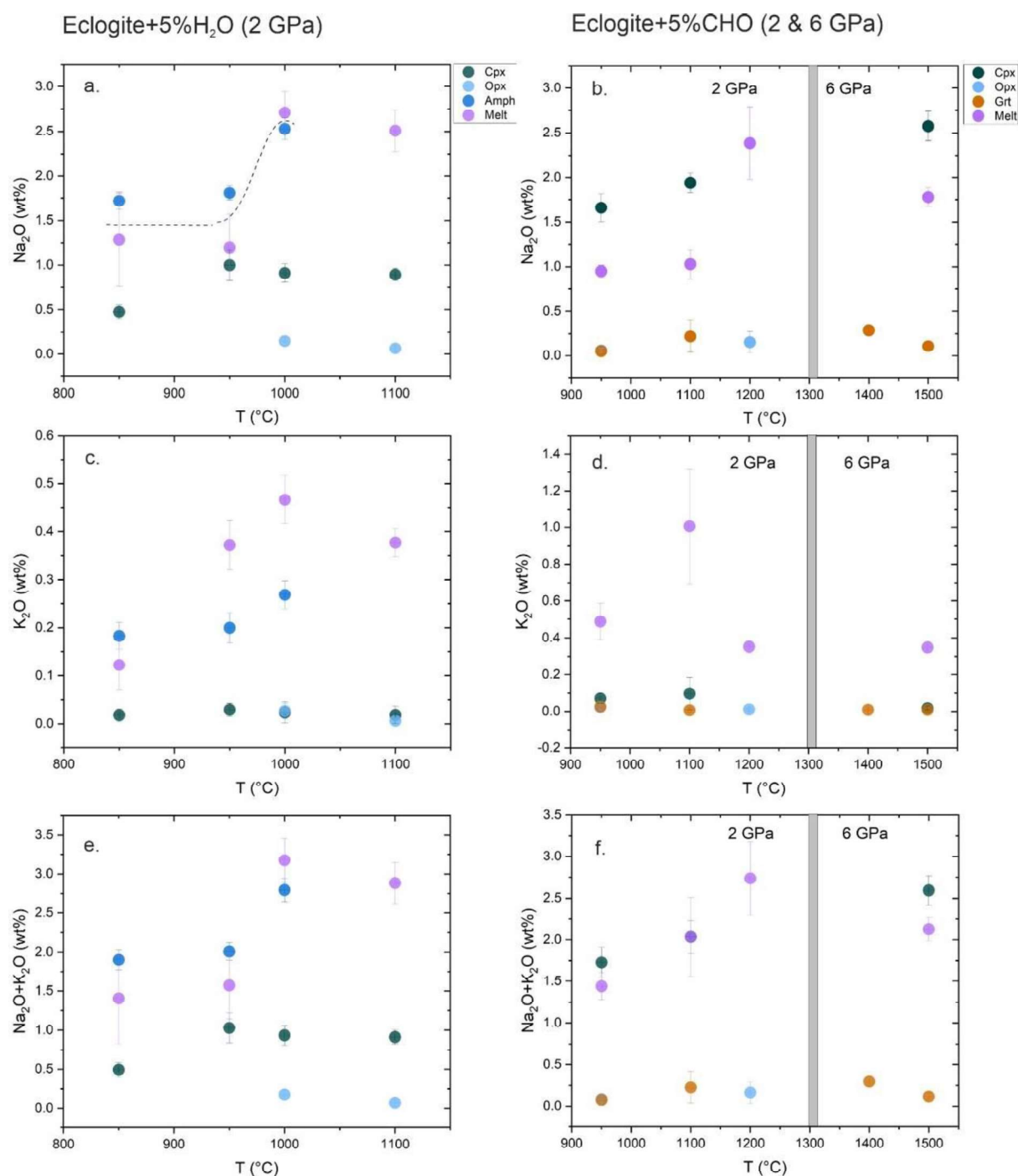


Fig. 17 Na₂O and K₂O plotted against in our partial melting experiments of eclogite. The melt compositions are given in Table 7. The left panel (a, c, e) are melts from (oxidizing) eclogite melting runs with 5% H₂O at 2 GPa, the right panel (b, d, f) are melts from (reducing) eclogite melting runs with 5% C–O–H fluid at 2 (left part of the diagram) and 6 GPa (right part of the diagram). Phases are indicated by different colors; symbols without error means the error is smaller than the size of the symbol. Dashed line in fig. 17 a indicates the variation in Na₂O of amphibole.

Fig. 18 displays the changing modes of each phase with temperature and at different redox conditions. Note that the subsolidus runs are not included in this diagram, as small grain sizes of

the minerals made mass balance calculations difficult. It is obvious that the modal amount of melt varies with temperature. At oxidizing conditions (Fig. 18a), amphibole is present at 950°C and 2 GPa. Orthopyroxene is formed at high temperature at the expense of Fe-Ti oxide and amphibole. This is somewhat surprising as orthopyroxene is not common in natural eclogite rocks. However, Paoli et al. (2012) found biotite- and orthopyroxene-bearing eclogites that were rich in MgO (10-15%), which is only slightly higher than the MgO content of typical average MORB (7.58 % of MgO)(Hofmann, 1988). In our study, the bulk composition in our eclogite melting runs contains about 11 wt.% MgO (Table 8). Therefore, the presence of orthopyroxene might be caused by the high MgO content of the bulk composition. The Fe-Ti oxides in our runs are stable over a wide temperature range. Garnet is not stable at 2 GPa at oxidizing conditions, but at reducing conditions garnet is stable at 2 GPa and 950-1200 °C. The disappearance of garnet before clinopyroxene has been reported in the CMAS-H₂O system (Asahara and Ohtani 2001), especially with 5% H₂O and 4 GPa. At reducing conditions amphibole is not stable in our runs, probably since the water activity in these runs is too low to stabilize the hydrous mineral amphibole.

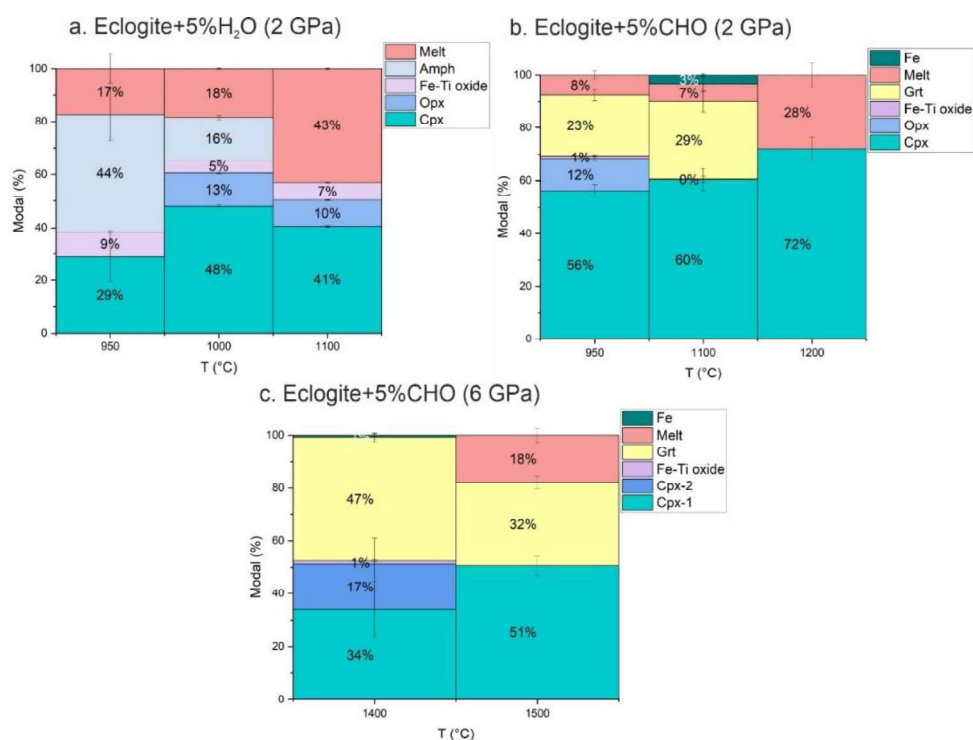


Fig. 18 Modal amounts of all phases of our partial melting of eclogite experiments with fluids at different redox conditions and temperatures. The modes were calculated using mass balance (see text for details). The proportion of each phase is marked as the number in the figure and the colors represent the different phases. Note that at 6 GPa, there are two kinds of clinopyroxene. One Clinopyroxene is higher than another in terms of TiO₂, Al₂O₃ but lower in FeO. These two kinds of clinopyroxenes distribute in different areas in the capsule, might be result from thermal gradient. Stability field of garnet from partial melting of eclogite expands at reducing conditions, while the stability of amphibole shrinks.

In summary, if we compare runs at identical temperatures and pressures, there is generally much less melt at reducing conditions than at oxidizing conditions, and Fe-Ti oxides are also much less

abundant at reducing conditions than at oxidizing conditions. At reducing conditions, the modal amount of clinopyroxene increases with temperature and at high temperature, clinopyroxene is the only stable mineral phase in equilibrium with melt.

3.3.3 Melting reactions of the partial melting of eclogite experiments:

Similar to the case of partial melting of lherzolite, based on the mass balance calculation on the proportion of each phase, we can draw some melting reactions from changes of phases:

At oxidizing conditions:

- From 950°C to 1000°C at 2 GPa:
 $4 \text{ Fe-Ti oxide} + 28 \text{ Amph} \rightarrow 19 \text{ Cpx} + 13 \text{ Opx} + 1 \text{ Melt}$
- From 1000°C to 1100°C at 2 GPa:
 $0.30 \text{ Cpx} + 0.12 \text{ Opx} + 0.66 \text{ Amph} \rightarrow 0.08 \text{ Fe-Ti oxide} + 1.00 \text{ Melt}$

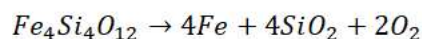
Therefore, at 2 GPa, 1000 °C H₂O-bearing eclogite system, high-Al orthopyroxene forms at the expense of amphibole and a small contribution of Fe-Ti oxide. Amphibole proportion decreases from 44% to 16 % but is not completely consumed. At the same time, the proportion of clinopyroxene increases from 29 % to 48 %. With temperature increasing to 1100 °C, amphibole is consumed, the amount of high-Al orthopyroxene decreases and the proportion of clinopyroxene drops as well with the increase of melt content.

At reducing conditions:

- From 950°C to 1100°C at 2 GPa:
 $12 \text{ Opx} + 1 \text{ Fe-Ti oxide} + 1 \text{ melt} \rightarrow 4 \text{ Cpx} + 7 \text{ Grt} + 3 \text{ Fe}$
- From 1100°C to 1200°C at 2 GPa:
 $0.01 \text{ Rt} + 1.44 \text{ Grt} + \mathbf{0.17 \text{ Fe}} \rightarrow 0.45 \text{ Cpx} + 1.00 \text{ Melt}$
- From 1400°C to 1500°C at 6 GPa:
 $1.75 \text{ Cpx-1} + 1.05 \text{ Cpx-2} + 0.82 \text{ Grt} + 0.07 \text{ Fe-Ti oxide} + \mathbf{0.02 \text{ Fe}_3\text{C}} \rightarrow 2.72 \text{ Cpx} + 1.00 \text{ Melt}$

Therefore, at 2 GPa, from 950 °C to 1100 °C, under reducing conditions, garnet forms in our runs at the expense of orthopyroxene, Fe-Ti oxide and melt. Therefore, this melting reaction suggests that garnet could be a peritectic product at reducing condition. From 1100 °C to 1200 °C, garnet is not stable anymore, and the only solid phase is clinopyroxene. Similarly, at 6 GPa, with the increase of temperature the stability field of garnet decreases, and Fe-Ti oxide is reacted out with the increasing temperature.

At reducing conditions, the product of partial melting of eclogite is garnet, rather than amphibole. It might be suggested as a peritectic product, since melt is consumed for the formation of garnet at high temperature. On the other hand, since there is presence of pure Fe as well in the experiment of 2 GPa, 1100 °C, the disappearance of garnet might also be a result of redox reaction. In the experiments of (O'Neill et al., 1993), Fe²⁺ bearing garnet was in equilibrium with metallic Fe and SiO₂:



Therefore, the presence of garnet at 2 GPa is caused by the fO_2 set in the experiment, rather than by the C–O–H fluid itself. In addition, at 6 GPa subsolidus conditions, there is Fe₃C presents which may point to more reducing conditions. In partial melting of eclogite at reducing condition there is no amphibole stable, probably resulting from the low aH_2O because of higher CH₄/H₂O ratio compared to experiments at oxidizing conditions. The crystallization of amphibole is controlled by H₂O content (Maksimov and Seismology, 2009), oxygen fugacity ($\Delta NiNiO$ -0.1 to +3, (Barclay and Carmichael, 2004)) and alkali content (Bonechi et al., 2017).

3.3.4 Melt compositions of partial melting experiments of eclogite

The melt compositions of the partial melting of eclogite experiments are given in Table 8. Fig. 19 depicts the melt compositions in a TAS diagram. Most melt compositions lie in the range of basaltic andesite and andesite field, especially at reducing condition. Almost all basaltic melts lie in low-K series not calc-alkaline basalts.

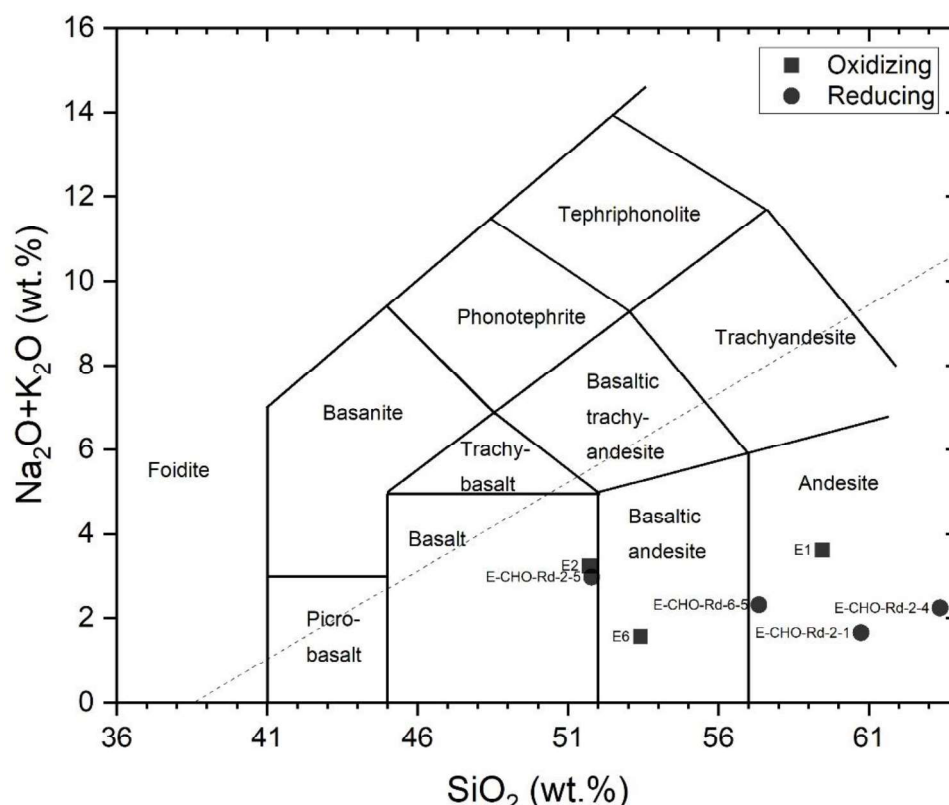


Fig. 19 Total alkali ($\text{Na}_2\text{O}+\text{K}_2\text{O}$) plotted against silica (TAS) to show melts compositions of partial melting runs of eclogite with different fluids. A run number of e.g., 'COH-Rd' refers to an eclogite with 5% COH fluids at reducing conditions, otherwise (e.g. E2) it refers to eclogite with 5% H_2O at oxidizing conditions. The dashed line in the diagram is the Irvine boundary line separating alkalic rocks (above) from subalkalic rocks (below).

When we compare our experimentally derived melt compositions with experimental silicate and/or carbonate melts from eclogite between 3.5-8.5 GPa, 1100 -1400 °C (Dasgupta et al., 2004; Kiseeva et al., 2012), and also melt compositions from the only available experiments of eclogite melting at reducing conditions (Litasov et al., 2014), we find that at 2 GPa, the composition of melts at both reducing and oxidizing conditions evolve from low $\text{MgO}+\text{FeO}$ to high $\text{MgO}+\text{FeO}$. Melt compositions at oxidizing conditions are generally more alkaline than those at reducing condition. At 6 GPa, the melt has lowest $\text{MgO}+\text{FeO}$ and $\text{Na}_2\text{O}+\text{K}_2\text{O}$, but highest CaO contents.

The melt composition from different studies include this study evolve in $\text{MgO}+\text{FeO}$ direction with increasing temperature. Melts from carbonated eclogite evolves from Ca-rich carbonatitic at low temperatures to SiO_2 -rich melts at high temperatures, due to the increasing contribution of clinopyroxene and garnet to the melt composition (Litasov and Ohtani, 2010; Kiseeva et al., 2013). However, melts from this study, regardless of the fluid composition, are not carbonatitic but are enriched in $\text{Mg}+\text{Fe}$ but relatively poor in Ca , compared to melts from carbonated eclogite. This is

because carbonates have lower melting temperatures than silicate minerals, and thus contribute more to the melt composition. The starting material used in this study is similar to the one used by Dasgupta et al. (2004), with only the fluid composition being different: We used 5% H₂O and 5% CH₄+H₂O in this study, but Dasgupta et al. used 5% CO₂ in the starting material. At 2 GPa and 950 °C, we observe melts in our reducing runs with 5% H₂O and CHO fluid. However, Dasgupta et al. (2004) did not report melt in experiments at identical P and T, which support the fact that H₂O is more effective in decreasing the solidus of eclogite than CO₂ is (Schmidt and Poli, 1998; Kessel et al., 2005; Kiseeva et al., 2012).

Table 8 Melt compositions of eclogite with H₂O and C-O-H fluids.

Exp No.	E6	E5	E1	E2	E-CHO- Rd-2-1	E-CHO-Rd- 2-4	E-CHO-Rd- 2-5	E-CHO-Rd- 6-5
n	3	7	5	9	4	6	7	7
SiO ₂	48.0(2)	56.3(9)	52.1(3)	45.9(5)	52.7(1)	57.4(2)	47(1)	59.5(8)
TiO ₂	0.9(2)	1.0(6)	1.0(2)	1.7(2)	1.5(3)	1.6(2)	3.1(2)	2.4(1)
Al ₂ O ₃	11.6(3)	15.4(3)	17.8(2)	16.3(3)	12.3(9)	12.3(6)	17.8(3)	11.23(2)
Cr ₂ O ₃	0.05(4)	0.01(2)	0.02(3)	0.02(2)	0.05(3)	0.08(6)	0.03(3)	0.04(4)
FeO	5.4(1)	2.3(9)	4.3(7)	7.2(4)	1.2(2)	2.7(5)	6.3(6)	0.13(1)
MnO	0.14(7)	0.07(5)	0.09(3)	0.12(6)	0.08(3)	0.03(2)	0.09(5)	0.02(2)
MgO	10.2(2)	2.2(9)	2.6(8)	6.1(5)	7.4(1)	5.5(8)	6.2(1)	5.1(4)
CaO	12.2(1)	5.7(5)	6.5(3)	8.5(1)	10.1(2)	9.1(1)	7.9(8)	8.6(4)
Na ₂ O	1.3(5)	1.2(4)	2.7(2)	2.5(2)	0.95(6)	1.0(2)	2.4(4)	1.3(6)
K ₂ O	0.12(5)	0.37(5)	0.47(5)	0.4(3)	0.5(1)	1.0(3)	0.35(3)	0.30(8)
Total	89.9(4)	84.6(9)	87.6(8)	88.8(6)	86.7(9)	90.6(8)	91.5(8)	88.6(8)
Mg#	77.0(5)	62.6(1)	51.3(4)	60.1(1)	91(1)	78.6(3)	63.4(2)	98.4(2)

From E6 to E2: eclogite melting experiments with 5 % H₂O at 2 GPa, from E-CHO-Rd-2-1 to E-CHO-Rd-2-4: eclogite melting experiments e with 5 % COH fluids at 2 GPa, from E-CHO-Rd-6-3 to E-CHO-Rd-6-5: eclogite melting experiments with 5 % C-O-H fluids at 6 GPa. Numbers in parentheses are the standard deviation based on the last digits. n=number of analyses

4 Implications:

4.1 Reducing fluids in the Earth's mantle

Overall, there is scant information about melting relations in reduced mantle compositions. Moreover, there is also little known about the solubility of reduced C-O-H volatiles in silicate melts, and indeed there is also little known about the speciation of C-O-H fluids that are dissolve in reduced silicate melts. Experimental evidence shows that the solubility of CH₄ in silicate melts is very low (Mysen et al., 2009): Silicate melts in the simple system Na₂O-SiO₂ can incorporate about 0.2% - 0.5% CH₄ at pressure of 1-1.5 GPa and 1400 °C. The dominant species for CH₄ in silicate melt is CH₄ but other C-H complexes such as C_xH_y (e.g., C₂H₆ or C₃H₆) have also been suggested (Benedetti et al., 1999; Kadik et al., 2004; Sokol et al., 2009), but it appears that Si-O-CH₃ bonding complex is of minor importance. This indicates that CH₄ plays a limited role in the depolymerization of silicate melt. On the other hand, the solubility of CH₄ in magma increases with dissolved H₂O content and decreasing fO₂, but the overall solubility of CH₄ in magma does not extend 0.6 wt%. (Ardia et al., 2013).

However, CH₄+H₂O bearing fluid inclusions were found in ophiolitic dunite (Liu and Fei, 2006) and it was suggested that these inclusions represent fluids from the ancient asthenospheric mantle (Liu and Fei, 2006). In addition, other CH₄-bearing fluid inclusions in the mantle wedge are presumed to have originated from devolatilization of subducting lithosphere (Song et al., 2009). The same authors suggested that the oceanic lithosphere may, therefore, be a large CH₄ reservoir that can produce reducing fluids in subduction zones. They proposed that CH₄-rich fluids from subducting slab (around ΔFMQ-5 or ΔIW-1) interact with an oxidized mantle wedge (around ΔFMQ-1). Consequently, H₂O and CO₂ are produced, which lower the solidus of the wedge peridotite and this may trigger arc magmatism.

4.2 Mantle melting and water recycling under reducing conditions in the Archaean

It is well known that the early Earth's redox conditions was much more reducing than the modern earth (Arculus and Delano, 1980; Trail et al., 2011). However, it is still under debate if the redox conditions of the Earth's mantle changed since the accretion of Earth. Whilst most researchers believe that the fO₂ of the mantle has not changed significantly (Delano, 2001) for the last 3800 Ma. Recent evidence (Aulbach and Stagno, 2016) suggests that the early Archaean Earth's mantle was significantly more reducing than today's mantle, implying that the Archaean mantle had, at least partially, equilibrated with the atmosphere. If the Archaean mantle was indeed much more reducing than today's mantle, then mantle melting relationships are controlled by melting reactions and the

solidus presented in this study. Our data show that the solidus with small amounts of C-H-O fluids under reducing conditions are close to the dry solidus so that small amounts of fluid do not promote melting in the Archaean as they would do in today's mantle. This is significant as our experiments define the solidus of Archaean Earth's mantle.

Our experiments indicate that at reducing conditions (at $fO_2 = \Delta IW-0.8$), the production of basaltic melt from lherzolite is very low indeed, as the presence of CH_4 significantly decreases the water activity and thus suppresses the melting production. Furthermore, our experiments show that the melt compositions are more olivine-normative at reducing conditions, regardless of temperature or pressure. As the Archaean mantle was probably significantly hotter than the modern mantle (Nisbet et al., 1993), we propose that partial melting of normal dry or fluid-bearing reduced Archaean mantle was unlikely or limited but melting of reducing subducted slab eclogite was likely (see further discussion below). In order to explain large melting event that lead to the eruption of Archaean komatiites temperature jets or exceptionally hot plumes in the Archaean mantle are needed (Sun, 1987). If the Archaean mantle was indeed as reducing as our experiments, our data shows that even large amounts of reducing C-O-H fluids in the Archaean mantle do not suppress the solidus by more than 100°C and therefore wet-melting in the Archaean (Scaillet et al., 1998; Prouteau et al., 1999; Laurie and Stevens, 2012) nevertheless requires an excess-heat of a few hundred degrees.

Furthermore, our experiments show that, garnet is stabilized in the slab under reducing conditions and at relatively low temperatures and at shallow depth (i.e. 2 GPa and 950-1100 °C, 6 GPa and 1400-1500 °C). Consequently, melting of the slab in an Archaean mantle with high modes of garnet must have resulted in a strong garnet signature, very similar to the trace element signature observed in Archaean tonalite-trondhjemite-granodiorite gneisses (Smithies and Champion, 2000; Huang et al., 2013).

Our experiments may also be useful to constrain the water cycles during subduction in a reducing Archaean mantle. Our experiments show that the stability of amphibole in lherzolite is much lower under reducing conditions compared to more oxidizing conditions (see results sections above). As amphibole is one of the most important water carriers in modern subduction zones, we can speculate that the lack of amphibole in Archaean subducting slabs may hinder the deep subduction of water, and consequently this may lead to direct melting of the subducting eclogite (Rapp et al., 1991; Rapp et al., 2003; Laurie and Stevens, 2012) and not melting of hydrous peridotite in modern subduction zone settings (e.g. Tatsumi and Eggins 1995).

4.3 Melting in the deep reducing mantle?

Our experiments show that the solidus of eclogite and lherzolite under reducing conditions is significantly higher than at oxidizing conditions, and rather close to the anhydrous solidus as indicated in previous sections. Thus, at reducing conditions, CH₄-rich fluids in the deep mantle will hinder melting of lherzolite and expand the stability field of clinopyroxene to higher temperatures. However, the solidus of eclogite under reducing conditions is still substantially lower than the solidus of reduced lherzolitic mantle.

Our experiments confirm that amphibole plays an important role in retaining and releasing water in the lithosphere (Green 1990). However, in our experiments, amphibole only coexists with melts in the partial melting of eclogite experiments. For partial melting of lherzolite, amphibole only exists at subsolidus condition and the breakdown of amphibole significantly contributes to the partial melting of lherzolite. If we consider the solidus of lherzolite and eclogite, a reduction within the mantle would suppress melting and freeze the subsolidus assemblage to a lower oxidation stage (Green 1990), when there's an obvious redox condition contrast (Yaxley and Green, 1998; Foley 2010), and under reducing condition amphibole would not be stable. This is consistent with the lack of amphibole at reducing condition with increase of pressure in previous experiments (Taylor and Green 1988). This process could occur in the deep subductions or ancient subducted oceanic lithosphere (Yaxley and Green, 1998).

4.4 Melting under reducing conditions on other terrestrial planets

As our experiments were done in chemical compositions close to Earth's mantle, we cannot directly apply our results to melting processes on Mars or Mercury because of the compositional difference of the mantle. However, our experiments could also be useful in interpreting melting processes on other terrestrial planets in our solar system. It is well known that the redox conditions constrain the solidus of the mantle of Mars and Mercury (Zolotov, 2011; Zolotov et al., 2013), both of which have much more reducing mantles (Wadhwa, 2008; Malavergne et al., 2014). The oxidation state of basalts from Mars is slightly lower than the Earth (Karner et al. 2006; Renggli et al. 2019) and the basaltic SNC meteorites (subalkaline) from Mars are indicative of mixing between two sources with different fO_2 : one source is relatively reduced (\sim QFM-4 or IW) and incompatible-element depleted, and another is relatively oxidized (\sim QFM-1) and incompatible-element enriched (Taylor and McLennan, 2009). If there was water present during the formation of Martian mantle, it might have a correlation with oxygen fugacity (Herd 2003). The H₂O content of bulk Mars has been estimated to lie between 62 and 298 ppm (Filiberto and Schwenzer, 2018), but it is well known that on Mars methane is episodically produced from an unknown source or mechanism (Webster et al.

2015). Whilst low temperature aqueous alteration of olivine-bearing rocks is one of the possible mechanisms for the generation of CH₄ on Mars (Oze and Sharma 2005), other mechanisms include water-rock reactions, biological activity and exogenous sources from meteorites (Etiope et al. 2013). In any case, the subsurface release of CH₄ which may be associated with H₂O, seems to support the presence of subsurface H₂O in local region of Mars (Filiberto and Schwenzer, 2018).

5 Conclusions

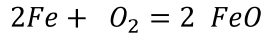
We present experimental results on the solidus of eclogite and lherzolite with C-O-H fluids under reducing and oxidizing conditions. Our data indicates that:

- Under reducing conditions, both the solidi of eclogite and lherzolite with C-O-H fluids are subparallel to and about 200° lower than the anhydrous solidi, and 100 °C higher than those of oxidizing conditions.
- The subsolidus mineralogy of eclogite and lherzolite depends on fO_2 : Higher fO_2 and consequently high H₂O activity leads to the presence of amphibole in the eclogite but at reducing conditions no amphibole is present. Lower fO_2 favors also the stability of garnet in subsolidus eclogite but also as a residual phase during partial melting of eclogite. As the solidus is lower at reducing conditions, residual clinopyroxene is much more stable under reducing conditions than under oxidizing conditions.
- The melt compositions derived from partial melting of lherzolite and eclogite critically depend on the water activity: Partial melting of lherzolite with oxidizing, water-rich fluids forms a basaltic melt while partial melting of lherzolite with reducing C-O-H fluids generates a more silica-rich primary basaltic andesite melt. Furthermore, partial melting of lherzolite with reducing C-O-H fluids generates melts that are rather quartz normative than olivine normative.

6 Appendix-Calculation of fO_2 :

Calculation of fO_2 of inner capsule is based on the approach in Rohrbach & Schmidt (2011).

Buffer in the outer capsule is based on equation below (Mann et al. 2009):



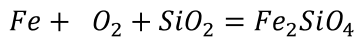
$$\Delta IW = \log f_{O_2}^{exp} - \log f_{O_2}^{IW}$$

$$\Delta IW = 2 \log \left[\frac{X_{FeO}^{fp}}{X_{Fe}^{metal}} \right] + \frac{2(11,000 + 0.011P)(1 - X_{FeO}^{fp})^2}{RT \ln 10}$$

fO_2 relative IW buffer was firstly calculated based on QFI buffer, then converted to ΔIW .

Here it is the steps:

1. $\Delta \log fO_2$ [QFI]:



$$\Delta \log fO_2 [QFI] = 2 \log a_{Fe}^{Ol} - 2 \log a_{Fe}^{Metal} - \log a_{SiO_2}$$

- a. $\log a_{Fe}^{Ol}$:

$$a_{Fe}^{Ol} = a_{Fe}^{Fa} = X_{Fe}^{Ol} \cdot \gamma_{Fe}^{Ol}$$

$$RT \ln(\gamma_{Fe}^{Ol}) = W_{Fe-Mg}^{Ol} (1 - X_{Fe}^{Ol})^2$$

$$\text{Or } \gamma_{Fe}^{Ol} = \exp(W_{Fe-Mg}^{Ol} (1 - X_{Fe}^{Ol})^2 / RT)$$

Margules interaction parameters W is expressed as:

$$W_G = W_U - TW_S + PW_V$$

(W is in J, T is in K, P in bar)

For olivine, W_s is/can be neglected in this study, according previous studies. (Frost 2013)

W_U and W_V were taken from Frost 2013b. Thus, the equation above can be rewritten as:

$$W_G = 2000 + 0.01P$$

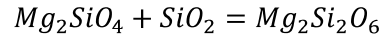
- b. $\log a_{Fe}^{Metal}$:

$$a_{Fe}^{Metal} = a_{Fe}^{Metal} = X_{Fe}^{Metal} \cdot \gamma_{Fe}^{Metal}$$

For metal alloy, based on Ir sensor, according Fe-Ir ratio calculating the activity of Fe metal in the sample. $\gamma_{Fe}^{Metal} = \dots$

c. $\text{Log } a_{\text{SiO}_2}$:

Activity of SiO_2 is calculated from the equilibrium:



$$\log a_{\text{SiO}_2} = \log a_{\text{en}}^{\text{opx}} - \log a_{\text{fo}}^{\text{ol}} - \log K$$

i. $\log a_{\text{en}}^{\text{opx}}$:

$$a_{\text{en}}^{\text{opx}} = X_{\text{Mg}}^{\text{M1}} \cdot X_{\text{Mg}}^{\text{M2}}$$

$$X_{\text{Mg}}^{\text{M1}} = \frac{N_{\text{Mg}}}{N_{\text{Mg}} + N_{\text{Fe}}} \left(1 - \frac{1}{2} (N_{\text{Al}} + N_{\text{Cr}}) - N_{\text{Ti}} \right)$$

$$X_{\text{Mg}}^{\text{M2}} = \frac{N_{\text{Mg}}}{N_{\text{Mg}} + N_{\text{Fe}}} (1 - N_{\text{Ca}} - N_{\text{Na}} - N_{\text{Mn}})$$

ii. $\log a_{\text{fo}}^{\text{ol}}$:

$$\gamma_{\text{Mg}}^{\text{ol}} = \exp(W_{\text{Fe-Mg}}^{\text{ol}} (1 - X_{\text{Mg}}^{\text{ol}})^2 / RT)$$

iii. $\log K$:

$$\Delta G^\theta = -RT \ln K$$

$$\text{Or } \log K = -\frac{\Delta G^\theta}{RT \ln 10}$$

Where ΔG^θ is from Perple_X.

Where ΔG^θ is from Perple_X, from HP database (Holland & Powell, 2011).

Chapter 4 Summary and Conclusions

In this thesis, I present results from two studies that both aim to help our understanding of processes that occur in the Earth's mantle. The Earth's mantle can be studied by various geological and geophysical methods, ranging from seismology, geodynamic modelling, magmatic studies to geochemistry or petrology. Here I use a combination of geochemical and petrological methods to study processes in the Earth's mantle. The first study (Chapter 2) investigates basaltic and similar melts from eastern Australia, which are known to form by partial melting of the Earth's mantle. However, as the degree of melting, and the exact chemical and mineralogical composition of the Earth's mantle below Eastern Australia is not well known, the study of olivine phenocrysts from these basalts can help to explore the source composition of these basalts and the melting and evolution of these basalts. This is a so-called "backward approach", as this study uses melting products, i.e. basalts, to unravel melting processes in the mantle. The second study (Chapter 3) is an experimental study, which uses high-pressure high-temperature experiments to simulate melting of the Earth's mantle. These experiments are so-called "forward approach" experiments, as in this study we investigate melting of the mantle rocks directly.

Chapter 2 aims to provide information about the origin of natural Cenozoic basalt samples on the edge of the thick lithosphere of Australia. To do this, I analysed olivine phenocrysts from the basalts and studied the correlation of several trace and minor elements, e.g. Mn/Fe and Ni/Mg, and trace element concentrations of Ni, Ca, Ti, Zn and Li with whole rock compositions. The results indicate that the tholeiite from Dubbo in Eastern Australia originates from a plume-type pyroxenite-bearing source that has experienced little or no carbonatitic metasomatism. The alkali basalts from Dubbo also come from a pyroxenite-bearing mantle source. Basanites from Barrington, Eastern Australia, however, originate from a pyroxenite-bearing source that was probably formed by metasomatic interaction of peridotite and a migrating carbonate melt, and I propose that the lavas from Buckland, Eastern Australia, come from an identical source. While basalts from Ebor may originate from a mixed peridotite and pyroxenite source, the source for basanites from Mount Russell has experienced the highest degree of carbonatitic metasomatism. These results indicate that intensive carbonatitic metasomatism occurred throughout Eastern Australia, which is fueled by the carbonate-rich melts beneath the thick lithosphere migrating towards the edge and shallow areas.

The trace and minor element concentrations in olivine xenocrysts indicate that these xenocrysts originate from spinel peridotite rather than garnet peridotite and that the source for those Cenozoic basalts are most likely spinel peridotite. These results are in good agreement with V/Sc ratio of the

whole rock which also indicate melting in the spinel lherzolite stability field (Lee et al., 2005). Furthermore, the V/Sc ratio also indicates rather oxidizing redox conditions for the source of these basalts (FMQ=0), which is indeed much oxidizing than the cratonic lithosphere (FMQ=-2.8), and the MORB source (FMQ=-1) (Foley, 2010). These results agree well with the proposed metasomatism by carbonatite melts, which require oxidizing conditions to be stable.

The second part of this thesis (Chapter 3) investigates melting of the mantle, which is not oxidising and where carbonate melts cannot be stable. In this "forward approach" study, I simulated partial melting of the Earth's mantle using high-pressure high-temperature experiments. I specifically explored the role of redox conditions on the solidus and the chemical composition of partial melts at a range of pressures and temperatures. Furthermore, I studied melting of both lherzolite peridotite and a garnet-clinopyroxene-rich eclogite. In summary, the experimental results show that the solidus depends critically on the composition of the fluids.

(1) At reducing conditions, both the solidi of eclogite and lherzolite with C-O-H fluids are subparallel but about 200°C lower than the respective anhydrous solidi.

(2) The mineralogy of eclogite and lherzolite also depends on fO_2 . Higher fO_2 and higher H_2O activity leads to the presence of amphibole in the eclogite, which is not stable in eclogite under reducing conditions. The breakdown of amphibole in eclogite leads to high melt productivity at the solidus, whilst melting reactions are quite different at reducing conditions. Furthermore, garnet is only stable as a residual phase during melting of eclogite at low fO_2 .

In lherzolitic mantle compositions, the stability field of clinopyroxene is much larger at reducing conditions compared to oxidizing conditions. As clinopyroxene dominates the melting reactions at low degrees of partial melting, the solidus of reducing lherzolite peridotite is at much lower temperatures than the solidus at oxidizing conditions.

(3) The melt compositions in my partial melting experiments of both eclogite and lherzolite critically depend on the water activity. Partial melting of lherzolite with only H_2O forms a basaltic melt, which is similar to the melts observed in Chapter 2. However, partial melting of lherzolite with reducing C-O-H fluids forms a more SiO_2 -rich basaltic andesite melt. The melts from experiments on the partial melting of eclogite from basaltic andesite to andesitic with increasing degree of partial melting.

Although the two different studies were performed independently in Münster and in Sydney, the results are quite complementary. The experimentally produced melts at oxidizing conditions and at 2 GPa are rather similar to the basalts from South-Eastern Australia, which further supports the

information from trace and minor elements from the study of the olivine phenocrysts from Eastern Australia. Furthermore, my experiments show nicely that melts from a reducing environment, especially those with an fO_2 slightly less than IW (or FMQ-4), do not agree with melt compositions of the Australian basalts.

Chapter 5 References

- Adam, J., 1990. The geochemistry and experimental petrology of sodic alkaline basalts from Oatlands, Tasmania. *Journal of Petrology* 31, 1201-1223.
- Aeolus Lee, C.-T., Leeman, W.P., Canil, D., Li, Z.-X.A., 2005. Similar V/Sc systematics in MORB and arc basalts: implications for the oxygen fugacities of their mantle source regions. *Journal of Petrology* 46, 2313-2336.
- Agee, C.B., Draper, D.S., 2004. Experimental constraints on the origin of Martian meteorites and the composition of the Martian mantle. *Earth and Planetary Science Letters* 224, 415-429.
- Ammannati, E., Jacob, D.E., Avanzinelli, R., Foley, S.F., Conticelli, S., 2016. Low Ni olivine in silica-undersaturated ultrapotassic igneous rocks as evidence for carbonate metasomatism in the mantle. *Earth and Planetary Science Letters* 444, 64-74.
- Andersen, T., O'Reilly, S.Y., Griffin, W.L., 1984. The trapped fluid phase in upper mantle xenoliths from Victoria, Australia: implications for mantle metasomatism, *Contributions to Mineralogy and Petrology* 88, 72-85.
- Anderson, J.D., Jacobson, R.A., Lau, E.L., Moore, W.B., Schubert, G., 2001. Io's gravity field and interior structure. *Journal of Geophysical Research: Planets* 106, 32963-32969.
- Arculus, R., Delano, J.W., 1980. Implications for the primitive atmosphere of the oxidation state of Earth's upper mantle. *Nature* 288, 72-74.
- Ardia, P., Hirschmann, M., Withers, A., Stanley, B., 2013. Solubility of CH₄ in a synthetic basaltic melt, with applications to atmosphere–magma ocean–core partitioning of volatiles and to the evolution of the Martian atmosphere. *Geochimica et Cosmochimica Acta* 114, 52-71.
- Asahara, Y., Ohtani, E., 2001. Melting relations of the hydrous primitive mantle in the CMAS–H₂O system at high pressures and temperatures, and implications for generation of komatiites. *Physics of the Earth and Planetary Interiors* 125, 31-44.
- Ashley, P., Duncan, R., Feebrey, C., 1995. Ebor volcano and Crescent Complex, northeastern New South Wales: age and geological development. *Australian Journal of Earth Sciences* 42, 471-480.
- Aulbach, S., Gerdes, A., Viljoen, K.S., 2016. Formation of diamondiferous kyanite–eclogite in a subduction mélange. *Geochimica et Cosmochimica Acta* 179, 156-176.
- Aulbach, S., Stagno, V., 2016. Evidence for a reducing Archean ambient mantle and its effects on the carbon cycle. *Geology* 44, 751-754.
- Aulbach, S., Viljoen, K.S., 2015. Eclogite xenoliths from the Lace kimberlite, Kaapvaal craton: from convecting mantle source to palaeo-ocean floor and back. *Earth and Planetary Science Letters* 431, 274-286.
- Baker, M.B., Wyllie, P.J., 1992. High-pressure apatite solubility in carbonate-rich liquids: implications for mantle metasomatism. *Geochimica et Cosmochimica Acta* 56, 3409-3422.
- Ballhaus, C., 1993. Redox states of lithospheric and asthenospheric upper mantle. *Contributions to Mineralogy and Petrology*, 114(3), 331-348.
- Ballhaus, C., 1995. Is the upper mantle metal-saturated? *Earth and Planetary Science Letters* 132, 75-86.
- Balta, J.B., Beckett, J.R., Asimow, P.D., 2011. Thermodynamic properties of alloys of gold-74/palladium-26 with variable amounts of iron and the use of Au-Pd-Fe alloys as containers for experimental petrology. *American Mineralogist* 96, 1467-1474.
- Barclay, J., Carmichael, I.E., 2004. A hornblende basalt from western Mexico: water-saturated phase relations constrain a pressure–temperature window of eruptibility. *Journal of Petrology* 45, 485-506.
- Barr, J.A., Grove, T.L., 2010. AuPdFe ternary solution model and applications to understanding the fO₂ of

- hydrous, high-pressure experiments. *Contributions to Mineralogy and Petrology* 160, 631-643.
- Beattie, P., Ford, C., Russell, D., 1991. Partition coefficients for olivine-melt and orthopyroxene-melt systems. *Contributions to Mineralogy and Petrology* 109, 212-224.
- Benedetti, L.R., Nguyen, J.H., Caldwell, W.A., Liu, H., Kruger, M., Jeanloz, R., 1999. Dissociation of CH₄ at high pressures and temperatures: diamond formation in giant planet interiors? *Science* 286, 100-102.
- Bennett, V., 2002. Combined Osmium isotopic and seismic evidence for orphaned early Proterozoic mantle beneath Phanerozoic crust in the New England Fold Belt, eastern Australia, Geological Society of Australia Abstracts. Geological Society of Australia; 1999, pp. 100-100.
- Bertka, C.M., Holloway, J.R., 1994. Anhydrous partial melting of an iron-rich mantle I: subsolidus phase assemblages and partial melting phase relations at 10 to 30 kbar. *Contributions to Mineralogy and Petrology* 115, 313-322.
- Betts, P., Giles, D., Lister, G., Frick, L., 2002. Evolution of the Australian lithosphere. *Australian Journal of Earth Sciences* 49, 661-695.
- Bézos, A., Humler, E., 2005. The Fe³⁺/ΣFe ratios of MORB glasses and their implications for mantle melting. *Geochimica et Cosmochimica Acta* 69, 711-725.
- Blundy, J., Wood, B., 1994. Prediction of crystal–melt partition coefficients from elastic moduli. *Nature* 372, 452.
- Boettcher, A., Mysen, B., Modreski, P., 1973. Phase relationships in natural and synthetic peridotite-H₂O and peridotite-H₂O-CO₂ systems at high pressures, International Kimberlite Conference: Extended Abstracts, pp. 35-38.
- Boettcher, A., Mysen, B.O., Modreski, P., 1975. Melting in the mantle: Phase relationships in natural and synthetic peridotite-H₂O and peridotite-H₂O-CO₂ systems at high pressures, *Physics and Chemistry of the Earth*. Elsevier, pp. 855-867.
- Bonechi, B., Perinelli, C., Gaeta, M., Tecchiato, V., Granati, S.F., 2017. Experimental constraints on amphibole stability in primitive alkaline and calc-alkaline magmas. *Periodico di Mineralogia* 86, 231-245.
- Bose, K., Ganguly, J., 1995. Quartz-coesite transition revisited: Reversed experimental determination at 500-1200 °C and retrieved thermochemical properties. *American Mineralogist* 80, 231-238.
- Braden, S., Stopar, J., Robinson, M., Lawrence, S., Van Der Bogert, C., Hiesinger, H., 2014. Evidence for basaltic volcanism on the Moon within the past 100 million years. *Nature Geoscience* 7, 787.
- Brett, R., 1984. Chemical equilibration of the Earth's core and upper mantle. *Geochimica et Cosmochimica Acta* 48, 1183-1188.
- Brey, G., 1978. Origin of olivine melilitites—chemical and experimental constraints. *Journal of Volcanology and Geothermal Research* 3, 61-88.
- Brey, G., Köhler, T., 1990. Geothermobarometry in four-phase lherzolites II. New thermobarometers, and practical assessment of existing thermobarometers. *Journal of Petrology* 31, 1353-1378.
- Brovarone, A.V., Chu, X., Martin, L., Ague, J.J., Monie, P., Groppo, C., Martinez, I., Chaduteau, C., 2018. Intra-slab COH fluid fluxes evidenced by fluid-mediated decarbonation of lawsonite eclogite-facies altered oceanic metabasalts. *Lithos* 304, 211-229.
- Bultitude, R., Green, D., 1971. Experimental study of crystal-liquid relationships at high pressures in olivine nephelinite and basanite compositions. *Journal of Petrology* 12, 121-147.
- Burgisser, A., Scaillet, B., 2007. Redox evolution of a degassing magma rising to the surface. *Nature* 445, 194.
- Bussweiler, Y., Brey, G., Pearson, D., Stachel, T., Stern, R., Hardman, M., Kjarsgaard, B., Jackson, S., 2017. The aluminum-in-olivine thermometer for mantle peridotites—Experimental versus empirical calibration and potential applications. *Lithos* 272, 301-314.
- Canil, D., 1997. Vanadium partitioning and the oxidation state of Archaean komatiite magmas. *Nature* 389,

842.

- Canil, D., 2002. Vanadium in peridotites, mantle redox and tectonic environments: Archean to present. *Earth and Planetary Science Letters* 195, 75-90.
- Canil, D., O'Neill, H.S.C., Pearson, D., Rudnick, R.L., McDonough, W.F., Carswell, D., 1994. Ferric iron in peridotites and mantle oxidation states. *Earth and Planetary Science* 123, 205-220.
- Cohen, B., Vasconcelos, P., Knesel, K., 2007. $^{40}\text{Ar}/^{39}\text{Ar}$ constraints on the timing of Oligocene intraplate volcanism in southeast Queensland. *Australian Journal of Earth Sciences* 54, 105-125.
- Cohen, B.E., Knesel, K.M., Vasconcelos, P.M., Schellart, W.P., 2013. Tracking the Australian plate motion through the Cenozoic: Constraints from $^{40}\text{Ar}/^{39}\text{Ar}$ geochronology. *Tectonics* 32, 1371-1383.
- Conceição, R., Green, D., 2004. Derivation of potassic (shoshonitic) magmas by decompression melting of phlogopite+ pargasite lherzolite. *Lithos* 72, 209-229.
- Cundari, A., 1973. Petrology of the leucite-bearing lavas in New South Wales. *Journal of the Geological Society of Australia* 20, 465-492.
- Dasgupta, R., Hirschmann, M.M., 2006. Melting in the Earth's deep upper mantle caused by carbon dioxide. *Nature* 440, 659-662.
- Dasgupta, R., Hirschmann, M.M., Smith, N.D., 2007. Partial melting experiments of peridotite+ CO_2 at 3 GPa and genesis of alkalic ocean island basalts. *Journal of Petrology* 48, 2093-2124.
- Dasgupta, R., Hirschmann, M.M., Withers, A.C., 2004. Deep global cycling of carbon constrained by the solidus of anhydrous, carbonated eclogite under upper mantle conditions. *Earth and Planetary Science Letters* 227, 73-85.
- Davies, D., Rawlinson, N., Iaffaldano, G., Campbell, I., 2015. Lithospheric controls on magma composition along Earth's longest continental hotspot track. *Nature* 525, 511-514.
- Dawson, J., Hinton, R., 2003. Trace-element content and partitioning in calcite, dolomite and apatite in carbonatite, Phalaborwa, South Africa. *Mineralogical Magazine* 67, 921-930.
- De Hoog, J.C., Gall, L., Cornell, D.H., 2010. Trace-element geochemistry of mantle olivine and application to mantle petrogenesis and geothermobarometry. *Chemical Geology* 270, 196-215.
- De Paoli, M., Clarke, G.L., Daczko, N.R., 2012. Mineral equilibria modeling of the granulite-eclogite transition: effects of whole-rock composition on metamorphic facies type-assemblages. *Journal of Petrology* 53, 949-970.
- Delano, J.W., 2001. Redox History of the Earth's Interior since ~3900 Ma: Implications for Prebiotic Molecules. *Origins of Life and Evolution of the Biosphere* 31, 311-341.
- Dixon, J.E., Clague, D.A., 2001. Volatiles in basaltic glasses from Loihi Seamount, Hawaii: Evidence for a relatively dry plume component. *Journal of Petrology* 42, 627-654.
- Dulhunty, J., 1973. Potassium-argon basalt ages and their significance in the Macquarie Valley. *Journal and Proceedings of the Royal Society of New South Wales* 106, 104-110.
- Dupuy, C., Liotard, J., Dostal, J., 1992. Zr/Hf fractionation in intraplate basaltic rocks: carbonate metasomatism in the mantle source. *Geochimica et Cosmochimica Acta* 56, 2417-2423.
- Eaton, D.W., Darbyshire, F., Evans, R.L., Grütter, H., Jones, A.G., Yuan, X., 2009. The elusive lithosphere–asthenosphere boundary (LAB) beneath cratons. *Lithos* 109, 1-22.
- Eggler, D.H., 1976. Does CO_2 cause partial melting in the low-velocity layer of the mantle? *Geology* 4, 69-72.
- Ellis, D., Green, D., 1979. An experimental study of the effect of Ca upon garnet-clinopyroxene Fe-Mg exchange equilibria. *Contributions to Mineralogy and Petrology* 71, 13-22.
- Etiopie, G., Sherwood Lollar, B., 2013. Abiotic methane on Earth. *Reviews of Geophysics* 51, 276-299.
- Falloon, T., Green, D., 1987. Anhydrous partial melting of MORB pyrolite and other peridotite compositions

- at 10 kbar: implications for the origin of primitive MORB glasses. *Mineralogy and Petrology* 37, 181-219.
- Falloon, T.J., Green, D.H., Danyushevsky, L.V., Faul, U.H., 1999. Peridotite melting at 1.0 and 1.5 GPa: an experimental evaluation of techniques using diamond aggregates and mineral mixes for determination of near-solidus melts. *Journal of Petrology* 40, 1343-1375.
- Falloon, T.J., Green, D.H., Hatton, C., Harris, K., 1988. Anhydrous partial melting of a fertile and depleted peridotite from 2 to 30 kb and application to basalt petrogenesis. *Journal of Petrology* 29, 1257-1282.
- Filiberto, J., Schwenzer, S.P., 2018. Volatiles in the Martian crust. Elsevier Press, Amsterdam, 214.
- Filiberto, J., Treiman, A., Le, L., 2008. Crystallization experiments on a Gusev Adirondack basalt composition. *Meteoritics & Planetary Science* 43, 1137-1146.
- Fishwick, S., Heintz, M., Kennett, B., Reading, A., Yoshizawa, K., 2008. Steps in lithospheric thickness within eastern Australia, evidence from surface wave tomography. *Tectonics* 27 (4). 1-17.
- Flemetakis, S., Klemme, S., Rohrbach, A., Stracke, A., Berndt, J., 2019. Discerning the Mineralogy of Metasomatized Mantle Sources by Halogen Partitioning Experiments: A Novel Approach, AGU Fall Meeting 2019. AGU.
- Foley, S., 1992. Vein-plus-wall-rock melting mechanisms in the lithosphere and the origin of potassic alkaline magmas. *Lithos* 28, 435-453.
- Foley, S., Musselwhite, D., Van der Laan, S., 1999. Melt compositions from ultramafic vein assemblages in the lithospheric mantle: a comparison of cratonic and non-cratonic settings, International Kimberlite Conference (7th: 1998). Red Roof Design, pp. 238-246.
- Foley, S., Yaxley, G., Rosenthal, A., Buhre, S., Kiseeva, E., Rapp, R., Jacob, D., 2009. The composition of near-solidus melts of peridotite in the presence of CO₂ and H₂O between 40 and 60 kbar. *Lithos* 112, 274-283.
- Foley, S.F., 1993. An experimental study of olivine lamproite: first results from the diamond stability field. *Geochimica et Cosmochimica Acta* 57, 483-489.
- Foley, S.F., 2010. A reappraisal of redox melting in the Earth's mantle as a function of tectonic setting and time. *Journal of Petrology* 52, 1363-1391.
- Foley, S.F., Barth, M.G., Jenner, G.A., 2000. Rutile/melt partition coefficients for trace elements and an assessment of the influence of rutile on the trace element characteristics of subduction zone magmas. *Geochimica et Cosmochimica Acta* 64, 933-938.
- Foley, S.F., Fischer, T.P., 2017. An essential role for continental rifts and lithosphere in the deep carbon cycle. *Nature Geoscience* 10, 897.
- Foley, S.F., Jacob, D.E., O'Neill, H.S.C., 2011. Trace element variations in olivine phenocrysts from Ugandan potassic rocks as clues to the chemical characteristics of parental magmas. *Contributions to Mineralogy and Petrology* 162, 1-20.
- Foley, S.F., Jenner, G.A., 2004. Trace element partitioning in lamproitic magmas—the Gaussberg olivine leucitite. *Lithos* 75, 19-38.
- Foley, S.F., Prelevic, D., Rehfeldt, T., Jacob, D.E., 2013. Minor and trace elements in olivines as probes into early igneous and mantle melting processes. *Earth and Planetary Science Letters* 363, 181-191.
- Förster, M.W., Foley, S.F., Marschall, H.R., Alard, O., Buhre, S., 2019. Melting of sediments in the deep mantle produces saline fluid inclusions in diamonds. *Science Advances* 5.5 2620.
- Frey, F., Green, D., Roy, S., 1978. Integrated models of basalt petrogenesis: a study of quartz tholeiites to olivine melilitites from south eastern Australia utilizing geochemical and experimental petrological data. *Journal of Petrology* 19, 463-513.
- Frey, F.A., Green, D.H., 1974. The mineralogy, geochemistry and origin of Iherzolite inclusions in Victorian basanites. *Geochimica et Cosmochimica Acta* 38, 1023-1059.
- Frezzotti, M.L., Andersen, T., Neumann, E.-R., Simonsen, S.L., 2002. Carbonatite melt–CO₂ fluid inclusions in

- mantle xenoliths from Tenerife, Canary Islands: a story of trapping, immiscibility and fluid–rock interaction in the upper mantle. *Lithos* 64, 77-96.
- Fritschle, T., Prelević, D., Foley, S.F., Jacob, D.E., 2013. Petrological characterization of the mantle source of Mediterranean lamproites: indications from major and trace elements of phlogopite. *Chemical Geology* 353, 267-279.
- Frost, B.R., 1991. Introduction to oxygen fugacity and its petrologic importance. *Reviews in Mineralogy and Geochemistry* 25, 1-9.
- Frost, C.D., Frost, B.R., Kirkwood, R., Chamberlain, K.R., 2006. The tonalite–trondhjemite–granodiorite (TTG) to granodiorite–granite (GG) transition in the late Archean plutonic rocks of the central Wyoming Province. *Canadian Journal of Earth Sciences* 43, 1419-1444.
- Frost, D.J., Liebske, C., Langenhorst, F., McCammon, C.A., Trønnes, R.G., Rubie, D.C., 2004. Experimental evidence for the existence of iron-rich metal in the Earth's lower mantle. *Nature* 428, 409-412.
- Frost, D.J., McCammon, C.A., 2008. The redox state of Earth's mantle. *Annu. Rev. Earth Planet. Sci.* 36, 389-420.
- Gaillard, F., Scaillet, B., Pichavant, M., Iacono-Marziano, G., 2015. The redox geodynamics linking basalts and their mantle sources through space and time. *Chemical Geology* 418, 217-233.
- Geng, X., Foley, S.F., Liu, Y., Wang, Z., Hu, Z., Zhou, L., 2019. Thermal-chemical conditions of the North China Mesozoic lithospheric mantle and implication for the lithospheric thinning of cratons. *Earth and Planetary Science Letters* 516, 1-11.
- Girnis, A., Bulatov, V., Brey, G., 2011. Formation of primary kimberlite melts—constraints from experiments at 6–12 GPa and variable CO₂/H₂O. *Lithos* 127, 401-413.
- Glen, R., 2005. The Tasmanides of eastern Australia. Geological Society, London, Special Publication, geological society of London, 246, 23-96.
- Glen, R., Korsch, R., Hegarty, R., Saeed, A., Djomani, Y.P., Costelloe, R., Belousova, E., 2013. Geodynamic significance of the boundary between the Thomson Orogen and the Lachlan Orogen, northwestern New South Wales and implications for Tasmanide tectonics. *Australian Journal of Earth Sciences* 60, 371-412.
- Gómez-Ulla, A., Sigmarsson, O., Gudfinnsson, G.H., 2017. Trace element systematics of olivine from historical eruptions of Lanzarote, Canary Islands: Constraints on mantle source and melting mode. *Chemical Geology* 449, 99-111.
- Gómez-Ulla, A., Sigmarsson, O., Huertas, M.J., Devidal, J.-L., Ancochea, E., 2018. The historical basanite-alkali basalt-tholeiite suite at Lanzarote, Canary Islands: Carbonated melts of heterogeneous mantle source? *Chemical Geology* 494, 56-68.
- Greeley, R., Spudis, P.D., 1981. Volcanism on mars. *Reviews of Geophysics* 19, 13-41.
- Green, D., 1973. Experimental melting studies on a model upper mantle composition at high pressure under water-saturated and water-undersaturated conditions. *Earth and Planetary Science Letters* 19, 37-53.
- Green, D., 1990. The role of oxidation-reduction and CHO fluids in determining melting conditions and magma compositions in the upper mantle. *Journal of Earth System Science* 99, 153-165.
- Green, D., Falloon, T., Taylor, W., 1987. Mantle-derived magmas-roles of variable source peridotite and variable CHO fluid compositions. *Magmatic Processes: Pysicochemical Principles*, The geochemical Society, Special Publication 1, 139-154.
- Green, D., O'Hara, M., 1971. Composition of basaltic magmas as indicators of conditions of origin: application to oceanic volcanism. *Philosophical Transactions of the Royal Society of London. Series A: Mathematical, Physical Sciences* 268, 707-725.
- Green, D., O'Hara, M.J., Mathematical, Sciences, P., 1971. Composition of basaltic magmas as indicators of conditions of origin: application to oceanic volcanism. *Philosophical Transactions for the Royal Society*

- of London. Series A, Mathematical and Physical Sciences 707-725.
- Green, D., Ringwood, A., 1967. The genesis of basaltic magmas. *Contributions to Mineralogy and Petrology* 15, 103-190.
- Green, D., Ringwood, A.E., 1970. Mineralogy of peridotitic compositions under upper mantle conditions. *Physics of the Earth and Planetary Interiors* 3, 359-371.
- Green, D.H., 1976. Experimental testing of "equilibrium" partial melting of peridotite under water-saturated, high-pressure conditions. *The Canadian Mineralogist* 14, 255-268.
- Green, D.H., 2015. Experimental petrology of peridotites, including effects of water and carbon on melting in the Earth's upper mantle. *Physics and Chemistry of Minerals* 42, 95-122.
- Green, D.H., Falloon, T.J., Structure, Evolution, 1998. Pyrolite: a Ringwood concept and its current expression. *The Earth's Mantle. Composition, Structure and Evolution* 311-378.
- Green, D.H., Hibberson, W.O., Kovács, I., Rosenthal, A., 2010. Water and its influence on the lithosphere-aesthenosphere boundary. *Nature* 467, 448-451.
- Green, T., Blundy, J., Adam, J., Yaxley, G., 2000. SIMS determination of trace element partition coefficients between garnet, clinopyroxene and hydrous basaltic liquids at 2–7.5 GPa and 1080–1200 °C. *Lithos* 53, 165-187.
- Griffin, W., 2008. GLITTER: data reduction software for laser ablation ICP-MS. *Laser Ablation ICP-MS in the Earth Sciences: Current practices and outstanding issues*, 308-311.
- Griffin, W., O'Reilly, S.Y., Stabel, A., 1988. Mantle metasomatism beneath western Victoria, Australia: II. Isotopic geochemistry of Cr-diopside lherzolites and Al-augite pyroxenites. *Geochimica et Cosmochimica Acta* 52, 449-459.
- Grotzinger, J.P., 2013. Analysis of surface materials by the Curiosity Mars rover. *Science* 341, 1457.
- Grove, T., Parman, S.W., 2004. Thermal evolution of the Earth as recorded by komatiites. *Earth and Planetary Science Letters* 219, 173-187.
- Grove, T.L., Chatterjee, N., Parman, S.W., Médard, E., 2006. The influence of H₂O on mantle wedge melting. *Earth and Planetary Science Letters* 1-2, 74-89.
- Gupta, A.K., Green, D.H., Taylor, W.R., 1987. The liquidus surface of the system forsterite-nepheline-silica at 28 kb. *American Journal of Science* 287, 560-565.
- Gurenko, A.A., Sobolev, A.V., Hoernle, K.A., Hauff, F., Schmincke, H.-U., 2009. Enriched, HIMU-type peridotite and depleted recycled pyroxenite in the Canary plume: a mixed-up mantle. *Earth and Planetary Science Letters* 277, 514-524.
- Halliday, A.N., 2008. A young Moon-forming giant impact at 70–110 million years accompanied by late-stage mixing, core formation and degassing of the Earth. *Philosophical Transactions of the Royal Society A: Mathematical, Physical and Engineering Sciences* 366, 4163-4181.
- Hauri, E.H., Wagner, T.P., Grove, T.L., 1994. Experimental and natural partitioning of Th, U, Pb and other trace elements between garnet, clinopyroxene and basaltic melts. *Chemical Geology* 117, 149-166.
- Heinonen, J.S., Fusswinkel, T., 2017. High Ni and low Mn/Fe in olivine phenocrysts of the Karoo meimechites do not reflect pyroxenitic mantle sources. *Chemical Geology* 467, 134-142.
- Herzberg, C., 2006. Petrology and thermal structure of the Hawaiian plume from Mauna Kea volcano. *Nature* 444, 605.
- Herzberg, C., 2010. Identification of source lithology in the Hawaiian and Canary Islands: Implications for origins. *Journal of Petrology* 52, 113-146.
- Herzberg, C., 2016. Petrological evidence from komatiites for an early Earth carbon and water cycle. *Journal of Petrology* 57, 2271-2288.

- Herzberg, C., Asimow, P., 2015. PRIMELT 3 MEGA. XLSM software for primary magma calculation: peridotite primary magma MgO contents from the liquidus to the solidus. *Geochemistry, Geophysics, Geosystems* 16, 563-578.
- Hirose, K., 1997. Partial melt compositions of carbonated peridotite at 3 GPa and role of CO₂ in alkali - basalt magma generation. *Geophysical Research Letters* 24, 2837-2840.
- Hirose, K., 1997a. Melting experiments on Iherzolite KLB-1 under hydrous conditions and generation of high-magnesian andesitic melts. *Geology* 25, 42-44.
- Hirose, K., 1997b. Partial melt compositions of carbonated peridotite at 3 GPa and role of CO₂ in alkali - basalt magma generation. *Geophysical Research Letters* 24, 2837-2840.
- Hirose, K., Kawamoto, T., 1995. Hydrous partial melting of Iherzolite at 1 GPa: the effect of H₂O on the genesis of basaltic magmas. *Earth and Planetary Science Letters* 133, 463-473.
- Hirschmann, M.M., Kogiso, T., Baker, M.B., Stolper, E.M., 2003. Alkalic magmas generated by partial melting of garnet pyroxenite. *Geology* 31, 481-484.
- Höfer, H.E., Brey, G.P., 2007. The iron oxidation state of garnet by electron microprobe: Its determination with the flank method combined with major-element analysis. *American Mineralogist* 92, 873-885.
- Hofmann, A.W., 1988. Chemical differentiation of the Earth: the relationship between mantle, continental crust, and oceanic crust. *Earth and Planetary Science Letters* 90, 297-314.
- Holland, T., Powell, R., 2011. An improved and extended internally consistent thermodynamic dataset for phases of petrological interest, involving a new equation of state for solids. *Journal of Metamorphic Geology* 29, 333-383.
- Holloway, J.R., Blank, J.G., 1994. Application of experimental results to COH species in natural melts. *Reviews in mineralogy* 30, 187-187.
- Howarth, G.H., Harris, C., 2017. Discriminating between pyroxenite and peridotite sources for continental flood basalts (CFB) in southern Africa using olivine chemistry. *Earth and Planetary Science Letters* 475, 143-151.
- Huang, H., Polat, A., Fryer, B.J., 2013. Origin of Archean tonalite-trondhjemite-granodiorite (TTG) suites and granites in the Fiskensæset region, southern West Greenland: implications for continental growth. *Gondwana Research* 23, 452-470.
- Humayun, M., Qin, L., Norman, M.D., 2004. Geochemical evidence for excess iron in the mantle beneath Hawaii. *Science* 306, 91-94.
- Ishimaru, S., Arai, S., Ishida, Y., Shirasaka, M., Okrugin, V.M., 2006. Melting and multi-stage metasomatism in the mantle wedge beneath a frontal arc inferred from highly depleted peridotite xenoliths from the Avacha volcano, southern Kamchatka. *Journal of Petrology* 48, 395-433.
- Jaeger, W.L., Turtle, E.P., Keszthelyi, L.P., Radebaugh, J., McEwen, A.S., Pappalardo, R., 2003. Orogenic tectonism on Io, 108 (E8).
- Jakobsson, S., Holloway, J.R., 1986. Crystal—Liquid experiments in the presence of a COH fluid buffered by graphite+ iron+ wustite: experimental method and near-liquidus relations in basanite. *Journal of Volcanology and Geothermal Research* 29, 265-291.
- Jakobsson, S., Holloway, J.R., 2008. Mantle melting in equilibrium with an Iron—Wüstite—Graphite buffered COH-fluid. *Contributions to Mineralogy and Petrology* 155, 247-256.
- Jamieson, J.C., Lawson, A., Nachtrieb, N., 1959. New Device for Obtaining X - Ray Diffraction Patterns from Substances Exposed to High Pressure. *Review of Scientific Instruments* 30, 1016-1019.
- Jaques, A.L., Foley, S.F., 2018. Insights into the petrogenesis of the West Kimberley lamproites from trace elements in olivine. *Mineralogy and Petrology*, 1-19.
- Jessop, K., 2012. Intrusions, dykes, plugs and flows of the Buckland Tertiary Basalt Province, Central

Queensland. Msc thesis, Macquarie University.

- Jochum, K.P., Scholz, D., Stoll, B., Weis, U., Wilson, S.A., Yang, Q., Schwalb, A., Börner, N., Jacob, D.E., Andreae, M.O., 2012. Accurate trace element analysis of speleothems and biogenic calcium carbonates by LA-ICP-MS. *Chemical Geology* 318, 31-44.
- Johnson, R.W., Johnson, R.W., Knutson, J., Taylor, S.R., 1989. Intraplate volcanism: in eastern Australia and New Zealand. Cambridge University Press.
- Jones, J., 1988. Partitioning of Mg and Fe between olivine and liquids of lunar compositions: the roles of composition, pressure and Ti speciation, Lunar and Planetary Science Conference.
- Kadik, A., 1997. Evolution of Earth's redox state during upwelling of carbon-bearing mantle. *Physics of the Earth and Planetary Interiors* 100, 157-166.
- Kadik, A., Pineau, F., Litvin, Y., Jendrzewski, N., Martinez, I., Javoy, M., 2004. Formation of carbon and hydrogen species in magmas at low oxygen fugacity. *Journal of Petrology* 45, 1297-1310.
- Kasting, J.F., Egger, D.H., Raeburn, S.P., 1993. Mantle redox evolution and the oxidation state of the Archean atmosphere. *The Journal of Geology* 101, 245-257.
- Katz, R.F., Spiegelman, M., Langmuir, C.H., 2003. A new parameterization of hydrous mantle melting. *Geochemistry, Geophysics, Geosystems* 4 (9), 19.
- Kawamoto, T., Hirose, K., 1994. Au-Pd sample containers for melting experiments on iron and water bearing systems. *European Journal of Mineralogy* 6, 381-386.
- Kawamoto, T., Holloway, J.R., 1997. Melting temperature and partial melt chemistry of H₂O-saturated mantle peridotite to 11 gigapascals. *Science* 276, 240-243.
- Kessel, R., Pettker, T., Fumagalli, P., 2015. Melting of metasomatized peridotite at 4–6 GPa and up to 1200 C: an experimental approach. *Contributions to mineralogy and petrology* 169, 37.
- Kessel, R., Ulmer, P., Pettker, T., Schmidt, M., Thompson, A., 2005. The water basalt system at 4 to 6 GPa: Phase relations and second critical endpoint in a K-free eclogite at 700 to 1400° C. *Earth and Planetary Science Letters* 237, 873-892.
- Kinzler, R.J., Grove, T.L., Recca, S.I., 1990. An experimental study on the effect of temperature and melt composition on the partitioning of nickel between olivine and silicate melt. *Geochimica et Cosmochimica Acta* 54, 1255-1265.
- Kiseeva, E.S., Litasov, K.D., Yaxley, G.M., Ohtani, E., Kamenetsky, V.S., 2013. Melting and phase relations of carbonated eclogite at 9–21 GPa and the petrogenesis of alkali-rich melts in the deep mantle. *Journal of Petrology* 54, 1555-1583.
- Kiseeva, E.S., Yaxley, G.M., Hermann, J., Litasov, K.D., Rosenthal, A., Kamenetsky, V.S., 2012. An experimental study of carbonated eclogite at 3· 5–5· 5 GPa—implications for silicate and carbonate metasomatism in the cratonic mantle. *Journal of Petrology* 53, 727-759.
- Klemme, S., Blundy, J.D., Wood, B.J., 2002. Experimental constraints on major and trace element partitioning during partial melting of eclogite. *Geochimica et Cosmochimica Acta* 66, 3109-3123.
- Klemme, S., Dalpé, C., 2003. Trace-element partitioning between apatite and carbonatite melt. *American Mineralogist* 88, 639-646.
- Klemme, S., O'Neill, H.S., 1997. The reaction $\text{MgCr}_2\text{O}_4 + \text{SiO}_2 = \text{Cr}_2\text{O}_3 + \text{MgSiO}_3$ and the free energy of formation of magnesiochromite (MgCr_2O_4). *Contributions to Mineralogy and Petrology* 130, 59-65.
- Kushiro, I., 2001. Partial melting experiments on peridotite and origin of mid-ocean ridge basalt. *Annual Review of Earth and Planetary Sciences* 29, 71-107.
- Klemme, S., O'Neill, H.S., 2000. The near-solidus transition from garnet lherzolite to spinel lherzolite. *Contributions to Mineralogy and Petrology* 138, 237-248.
- Klemme, S., Van der Laan, S., Foley, S.F., Günther, D., 1995. Experimentally determined trace and minor

- element partitioning between clinopyroxene and carbonatite melt under upper mantle conditions. *Earth and Planetary Science Letters* 133, 439-448.
- Kogiso, T., Hirschmann, M.M., Frost, D.J., 2003. High-pressure partial melting of garnet pyroxenite: possible mafic lithologies in the source of ocean island basalts. *Earth and Planetary Science Letters* 216, 603-617.
- Kohn, S.C., 1996. Solubility of H₂O in nominally anhydrous mantle minerals using 1H MAS NMR. *American Mineralogist* 81, 1523-1526.
- Kohn, S.C., Schofield, P.F., 1994. The importance of melt composition in controlling trace-element behaviour: an experimental study of Mn and Zn partitioning between forsterite and silicate melts. *Chemical Geology* 117, 73-87.
- Kushiro, I., 2001. Partial melting experiments on peridotite and origin of mid-ocean ridge basalt. *Annual Review of Earth and Planetary Sciences* 29, 71-107.
- Kushiro, I., Syono, Y., Akimoto, S.i., 1968. Melting of a peridotite nodule at high pressures and high water pressures. *Journal of Geophysical Research* 73, 6023-6029.
- Kushiro, I., Walter, M.J., 1998. Mg-Fe partitioning between olivine and mafic-ultramafic melts. *Geophysical Research Letters* 25, 2337-2340.
- Lane, D.L., Ganguly, J., 1980. Al₂O₃ solubility in orthopyroxene in the system MgO - Al₂O₃-SiO₂: A reevaluation, and mantle geotherm. *Journal of Geophysical Research: Solid Earth* 85, 6963-6972.
- Lassiter, J.C., Hauri, E., 1998. Osmium-isotope variations in Hawaiian lavas: evidence for recycled oceanic lithosphere in the Hawaiian plume. *Earth and Planetary Science Letters* 164, 483-496.
- Laurie, A., Stevens, G., 2012. Water-present eclogite melting to produce Earth's early felsic crust. *Chemical Geology* 314, 83-95.
- Le Roux, V., Dasgupta, R., Lee, C.-T., 2011. Mineralogical heterogeneities in the Earth's mantle: constraints from Mn, Co, Ni and Zn partitioning during partial melting. *Earth and Planetary Science Letters* 307, 395-408.
- Le Roux, V., Lee, C.-T., Turner, S., 2010. Zn/Fe systematics in mafic and ultramafic systems: Implications for detecting major element heterogeneities in the Earth's mantle. *Geochimica et Cosmochimica Acta* 74, 2779-2796.
- Li, Z.-X.A., Lee, C.-T.A., 2004. The constancy of upper mantle fO₂ through time inferred from V/Sc ratios in basalts. *Earth and Planetary Science Letters* 228, 483-493.
- Libourel, G., 1999. Systematics of calcium partitioning between olivine and silicate melt: implications for melt structure and calcium content of magmatic olivines. *Contributions to Mineralogy and Petrology* 136, 63-80.
- Litasov, K., 2011. Physicochemical conditions for melting in the Earth's mantle containing a C-O-H fluid (from experimental data). *Russian Geology and Geophysics* 52, 475-492.
- Litasov, K., Ohtani, E., 2010. The solidus of carbonated eclogite in the system CaO-Al₂O₃-MgO-SiO₂-Na₂O-CO₂ to 32 GPa and carbonatite liquid in the deep mantle. *Earth and Planetary Science Letters* 295, 115-126.
- Litasov, K.D., Shatskiy, A., 2018. Carbon-bearing magmas in the Earth's deep interior, *Magmas Under Pressure*. Elsevier, pp. 43-82.
- Litasov, K.D., Shatskiy, A., Ohtani, E., 2014. Melting and subsolidus phase relations in peridotite and eclogite systems with reduced C O H fluid at 3–16 GPa. *Earth and Planetary Science Letters* 391, 87-99.
- Liu, W., Fei, P.X., 2006. Methane-rich fluid inclusions from ophiolitic dunite and post-collisional mafic-ultramafic intrusion: the mantle dynamics underneath the Palaeo-Asian Ocean through to the post-collisional period. *Earth and Planetary Science Letters* 242, 286-301.
- Liu, Y., Gao, S., Kelemen, P.B., Xu, W., 2008. Recycled crust controls contrasting source compositions of

- Mesozoic and Cenozoic basalts in the North China Craton. *Geochimica et Cosmochimica Acta* 72, 2349-2376.
- Longhi, J., 2002. Some phase equilibrium systematics of lherzolite melting: I. Geochemistry, Geophysics, Geosystems 3, 1-33.
- Longhi, J., Walker, D., Hays, J.F., 1978. The distribution of Fe and Mg between olivine and lunar basaltic liquids. *Geochimica et Cosmochimica Acta* 42, 1545-1558.
- Maksimov, A.P. J., 2009. The influence of water on the temperature of amphibole stability in melts. *Journal of Volcanology and Seismology* 3, 27-33.
- Malavergne, V., Cordier, P., Righter, K., Brunet, F., Zanda, B., Addad, A., Smith, T., Bureau, H., Surblé, S., Raepsaet, C., 2014. How Mercury can be the most reduced terrestrial planet and still store iron in its mantle. *Earth and Planetary Science Letters* 394, 186-197.
- Martin, L.A., Hermann, J., 2018. Experimental phase relations in altered oceanic crust: implications for carbon recycling at subduction zones. *Journal of Petrology* 59, 299-320.
- Matveev, S., Ballhaus, C., Fricke, K., Truckenbrodt, J., Ziegenben, D., 1997. Volatiles in the Earth's mantle: I. Synthesis of CHO fluids at 1273 K and 2.4 GPa. *Geochimica et Cosmochimica Acta* 61, 3081-3088.
- Matzen, A.K., Baker, M.B., Beckett, J.R., Stolper, E.M., 2013. The temperature and pressure dependence of nickel partitioning between olivine and silicate melt. *Journal of Petrology* 54, 2521-2545.
- Matzen, A.K., Wood, B.J., Baker, M.B., Stolper, E.M., 2017. The roles of pyroxenite and peridotite in the mantle sources of oceanic basalts. *Nature Geoscience* 10, 530.
- McDougall, I., Wilkinson, J., 1967. Potassium - argon dates on some Cainozoic volcanic rocks from northeastern New South Wales. *Journal of the Geological Society of Australia* 14, 225-233.
- McKenzie, D., O'Nions, R.K., 1995. The source regions of ocean island basalts. *Journal of Petrology* 36, 133-159.
- McKenzie, D., Stracke, A., Blichert-Toft, J., Albarède, F., Grönvold, K., O'Nions, R.K., 2004. Source enrichment processes responsible for isotopic anomalies in oceanic island basalts. *Geochimica et Cosmochimica Acta* 68, 2699-2724.
- Mibe, K., Kanzaki, M., Kawamoto, T., Matsukage, K.N., Fei, Y., Ono, S., 2007. Second critical endpoint in the peridotite-H₂O system. *Journal of Geophysical Research: Solid Earth* 112 (B3). 8
- Millhollen, G., Irving, A., Wyllie, P., 1974. Melting interval of peridotite with 5.7 per cent water to 30 kilobars. *The Journal of Geology* 82, 575-587.
- Montelli, R., Nolet, G., Dahlen, F., Masters, G., 2006. A catalogue of deep mantle plumes: New results from finite - frequency tomography. *Geochemistry, Geophysics, Geosystems* 7. 69
- Morgan, J.W., Anders, E., 1979. Chemical composition of Mars. *Geochimica et Cosmochimica Acta* 43, 1601-1610.
- Mysen, B.O., Boettcher, A., 1975a. Melting of a hydrous mantle: II. Geochemistry of crystals and liquids formed by anatexis of mantle peridotite at high pressures and high temperatures as a function of controlled activities of water, hydrogen, and carbon dioxide. *Journal of Petrology* 16, 549-593.
- Mysen, B.O., Boettcher, A.J., 1975b. Melting of a hydrous mantle: I. Phase relations of natural peridotite at high pressures and temperatures with controlled activities of water, carbon dioxide, and hydrogen. *Journal of Petrology* 16, 520-548.
- Mysen, B.O., Fogel, M.L., Morrill, P.L., Cody, G.D., 2009. Solution behavior of reduced COH volatiles in silicate melts at high pressure and temperature. *Geochimica et Cosmochimica Acta* 73, 1696-1710.
- Mysen, B.O., Kumamoto, K., Cody, G.D., Fogel, M.L., 2011. Solubility and solution mechanisms of C-O-H

- volatiles in silicate melt with variable redox conditions and melt composition at upper mantle temperatures and pressures. *Geochimica et Cosmochimica Acta* 75, 6183-6199.
- Mysen, B.O., Virgo, D., Popp, R.K., Bertka, C.M., 1998. The role of H₂O in Martian magmatic systems. *American Mineralogist* 83, 942-946.
- Nakamura, D., 2003. Stability of phengite and biotite in eclogites and characteristics of biotite- or orthopyroxene-bearing eclogites. *Contributions to Mineralogy and Petrology* 145, 550-567.
- Neumann, E.-R., Wulff-Pedersen, E., Simonsen, S., Pearson, N., Martí, J., Mitjavila, J., 1999. Evidence for fractional crystallization of periodically refilled magma chambers in Tenerife, Canary Islands. *Journal of Petrology* 40, 1089-1123.
- Nisbet, E., Cheadle, M., Arndt, N., Bickle, M., 1993. Constraining the potential temperature of the Archaean mantle: a review of the evidence from komatiites. *Lithos* 30, 291-307.
- Niu, Y., Wilson, M., Humphreys, E.R., O'Hara, M.J., 2011. The origin of intra-plate ocean island basalts (OIB): the lid effect and its geodynamic implications. *Journal of Petrology* 52, 1443-1468.
- Norman, M.D., 1998. Melting and metasomatism in the continental lithosphere: laser ablation ICPMS analysis of minerals in spinel lherzolites from eastern Australia. *Contributions to Mineralogy and Petrology* 130, 240-255.
- O'Neill, C., Moresi, L., Lenardic, A., Cooper, C., 2003. Inferences on Australia's heat flow and thermal structure from mantle convection modelling results. *Speical papers-geological society of America*, 169-184.
- O'Driscoll, B., Walker, R.J., Day, J.M., Ash, R.D., Daly, J.S., 2015. Generations of melt extraction, melt–rock interaction and high-temperature metasomatism preserved in peridotites of the ~ 497 Ma Leka Ophiolite Complex, Norway. *Journal of Petrology* 56, 1797-1828.
- O'Hara, M., 1965. Primary magmas and the origin of basalts. *Scottish Journal of Geology* 1, 19-40.
- O'Reilly, S., Griffin, W., 1987. Eastern Australia—4000 kilometres of mantle samples. *Mantle Xenoliths*, 267-280.
- O'Reilly, S.Y., Zhang, M., 1995. Geochemical characteristics of lava-field basalts from eastern Australia and inferred sources: connections with the subcontinental lithospheric mantle? *Contributions to Mineralogy and Petrology* 121, 148.
- O'Neill, H.S.C., McCammon, C., Canil, D., Rubie, D., Ross, C., Seifert, F., 1993. Mössbauer spectroscopy of mantle transition zone phases and determination of minimum Fe³⁺ content. *American Mineralogist* 78, 456-460.
- O'Neill, H.S.C., Pownceby, M.I., McCammon, C.A., 2003. The magnesiowüstite: iron equilibrium and its implications for the activity-composition relations of (Mg,Fe)₂SiO₄ olivine solid solutions. *Contributions to Mineralogy and Petrology* 146, 308-325.
- O'Reilly, S.Y., Griffin, W., 2000. Apatite in the mantle: implications for metasomatic processes and high heat production in Phanerozoic mantle. *Lithos* 53, 217-232.
- Oze, C., Sharma, M., 2005. Have olivine, will gas: serpentinization and the abiogenic production of methane on Mars. *Geophysical Research Letters* 32, 4.
- Palme, H., 2002. A new solar system basalt. *Science* 296, 271-273.
- Palme, H., O'Neill, H.S.C., 2003. Cosmochemical estimates of mantle composition. *Treatise on geochemistry* 2, 568.
- Paster, T.P., Schauwecker, D.S., Haskin, L.A., 1974. The behavior of some trace elements during solidification of the Skaergaard layered series. *Geochimica et Cosmochimica Acta* 38 (10), 1549-1577.
- Patera, E., Holloway, J.R., 1982. Experimental determination of the spinel-garnet boundary in a Martian mantle composition. *Journal of Geophysical Research: Solid Earth* 87, A31-A36.
- Pertermann, M., Hirschmann, M.M., 2003. Partial melting experiments on a MORB-like pyroxenite between

2 and 3 GPa: Constraints on the presence of pyroxenite in basalt source regions from solidus location and melting rate. *Journal of Geophysical Research: Solid Earth* 108.

- Pieters, C., 1978. Mare basalt types on the front side of the moon-A summary of spectral reflectance data, *Lunar and Planetary Science Conference Proceedings*, pp. 2825-2849.
- Pilet, S., Baker, M.B., Müntener, O., Stolper, E.M., 2011. Monte Carlo simulations of metasomatic enrichment in the lithosphere and implications for the source of alkaline basalts. *Journal of Petrology* 52, 1415-1442.
- Pilet, S., Baker, M.B., Stolper, E.M., 2008. Metasomatized lithosphere and the origin of alkaline lavas. *Science* 320, 916-919.
- Pilet, S., Baker, M.B., Stolper, E.M., Müntener, O., 2010. Alkaline magma-oceanic lithosphere interaction: a key to understand the nephelinite-alkali basalt transition observed in oceanic islands, *EGU General Assembly Conference Abstracts*, p. 3904.
- Powell, W., O'Reilly, S., 2007. Metasomatism and sulfide mobility in lithospheric mantle beneath eastern Australia: implications for mantle Re–Os chronology. *Lithos* 94, 132-147.
- Prelević, D., Foley, S., 2007. Accretion of arc-oceanic lithospheric mantle in the Mediterranean: evidence from extremely high-Mg olivines and Cr-rich spinel inclusions in lamproites. *Earth and Planetary Science Letters* 256, 120-135.
- Prelević, D., Jacob, D.E., Foley, S.F., 2013. Recycling plus: a new recipe for the formation of Alpine-Himalayan orogenic mantle lithosphere. *Earth and Planetary Science Letters* 362, 187-197.
- Presnall, D.C., Gudfinnsson, G.H., Walter, M.J., 2002. Generation of mid-ocean ridge basalts at pressures from 1 to 7 GPa. *Geochimica et Cosmochimica Acta* 66, 2073-2090.
- Price, R., Gray, C., Wilson, R., Frey, F., Taylor, S., 1991. The effects of weathering on rare-earth element, Y and Ba abundances in Tertiary basalts from southeastern Australia. *Chemical Geology* 93, 245-265.
- Prouteau, G., Scaillet, B., Pichavant, M., Maury, R., 1999. Fluid-present melting of ocean crust in subduction zones. *Geology* 27, 1111-1114.
- Rapp, R.P., Shimizu, N., Norman, M.D., 2003. Growth of early continental crust by partial melting of eclogite. *Nature* 425, 605-609.
- Rapp, R.P., Watson, E.B., Miller, C.F., 1991. Partial melting of amphibolite/eclogite and the origin of Archean trondhjemites and tonalites. *Precambrian Research* 51, 1-25.
- Ravna, K., 2000. The garnet–clinopyroxene Fe²⁺–Mg geothermometer: an updated calibration. *Journal of metamorphic Geology* 18, 211-219.
- Reguir, E., Chakhmouradian, A., Halden, N., Malkovets, V., Yang, P., 2009. Major-and trace-element compositional variation of phlogopite from kimberlites and carbonatites as a petrogenetic indicator. *Lithos* 112, 372-384.
- Reiners, P.W., 2002. Temporal-compositional trends in intraplate basalt eruptions: Implications for mantle heterogeneity and melting processes. *Geochemistry, Geophysics, Geosystems* 3, 1-30.
- Renggli, C., King, P., Henley, R., Guagliardo, P., McMorrow, L., Middleton, J., Turner, M., 2019. An experimental study of SO₂ reactions with silicate glasses and supercooled melts in the system anorthite–diopside–albite at high temperature. *Contributions to Mineralogy and Petrology* 174, 3.
- Rhodes, J., Vollinger, M., 2004. Composition of basaltic lavas sampled by phase-2 of the Hawaii Scientific Drilling Project: Geochemical stratigraphy and magma types. *Geochemistry, Geophysics, Geosystems* 5.
- Roeder, P., Emslie, R., 1970. Olivine-liquid equilibrium. *Contributions to mineralogy and petrology* 29, 275-289.
- Rohrbach, A., Ballhaus, C., Golla–Schindler, U., Ulmer, P., Kamenetsky, V.S., Kuzmin, D.V., 2007. Metal saturation in the upper mantle. *Nature* 449, 456-458.
- Rohrbach, A., Schmidt, M.W., 2011. Redox freezing and melting in the Earth's deep mantle resulting from

- carbon-iron redox coupling. *Nature* 472, 209-212.
- Rosenthal, A., Yaxley, G.M., Green, D.H., Hermann, J., Kovács, I., Spandler, C., 2014. Continuous eclogite melting and variable refertilisation in upwelling heterogeneous mantle. *Scientific reports* 4.
- Rudnick, R.L., McDonough, W.F., Chappell, B.W., 1993. Carbonatite metasomatism in the northern Tanzanian mantle: petrographic and geochemical characteristics. *Earth and Planetary Science Letters* 114, 463-475.
- Ryan, J.G., Langmuir, C.H., 1987. The systematics of lithium abundances in young volcanic rocks. *Geochimica et Cosmochimica Acta* 51, 1727-1741.
- Sachtleben, T., Seck, H., 1981. Chemical control of Al-solubility in orthopyroxene and its implications on pyroxene geothermometry. *Contributions to Mineralogy and Petrology* 78, 157-165.
- Sack, R.O., Walker, D., Carmichael, I.S., 1987. Experimental petrology of alkalic lavas: constraints on cotectics of multiple saturation in natural basic liquids. *Contributions to Mineralogy and Petrology* 96, 1-23.
- Scaillet, B., Holtz, F., Pichavant, M., 1998. Phase equilibrium constraints on the viscosity of silicic magmas: 1. Volcanic – plutonic comparison. *Journal of Geophysical Research: Solid Earth* 103, 27257-27266.
- Seitz, H.-M., Woodland, A.B., 2000. The distribution of lithium in peridotitic and pyroxenitic mantle lithologies—an indicator of magmatic and metasomatic processes. *Chemical Geology* 166, 47-64.
- Sekine, T., Wyllie, P.J., 1983. Experimental simulation of mantle hybridization in subduction zones. *The Journal of Geology* 91, 511-528.
- Schmidt, M.W., Poli, S., 1998. Experimentally based water budgets for dehydrating slabs and consequences for arc magma generation. *Earth and Planetary Science Letters* 163, 361-379.
- Shaikh, A.M., Patel, S.C., Bussweiler, Y., Kumar, S.P., Tappe, S., Ravi, S., Mainkar, D., 2019. Olivine trace element compositions in diamondiferous lamproites from India: Proxies for magma origins and the nature of the lithospheric mantle beneath the Bastar and Dharwar cratons. *Lithos* 324, 501-518.
- Shcheka, S.S., Wiedenbeck, M., Frost, D.J., Keppler, H., 2006. Carbon solubility in mantle minerals. *Earth and Planetary Science Letters* 245, 730-742.
- Shea, J.J., Foley, S.F., 2019. Evidence for a Carbonatite-Influenced Source Assemblage for Intraplate Basalts from the Buckland Volcanic Province, Queensland, Australia. *Minerals* 9, 546.
- Skae, A., 1998. The petrology of the Buckland volcanic province, Central Queensland, Australia. University of Oxford.
- Smithies, R.H., 2000. The Archaean tonalite–trondhjemite–granodiorite (TTG) series is not an analogue of Cenozoic adakite. *Earth and Planetary Science Letters* 182, 115-125.
- Sobolev, A.V., Hofmann, A.W., Kuzmin, D.V., Yaxley, G.M., Arndt, N.T., Chung, S.-L., Danyushevsky, L.V., Elliott, T., Frey, F.A., Garcia, M.O., 2007. The amount of recycled crust in sources of mantle-derived melts. *Science* 316, 412-417.
- Sobolev, A.V., Hofmann, A.W., Sobolev, S.V., Nikogosian, I.K., 2005. An olivine-free mantle source of Hawaiian shield basalts. *Nature* 434, 590-597.
- Sobolev, N.V., Logvinova, A.M., Zedgenizov, D.A., Pokhilenko, N.P., Kuzmin, D.V., Sobolev, A.V., 2008. Olivine inclusions in Siberian diamonds: high-precision approach to minor elements. *European Journal of Mineralogy* 20, 305-315.
- Sokol, A.G., Palyanova, G.A., Palyanov, Y.N., Tomilenko, A.A., Melenevsky, V.N., 2009. Fluid regime and diamond formation in the reduced mantle: Experimental constraints. *Geochimica et Cosmochimica Acta* 73, 5820-5834.
- Song, S., Su, L., Niu, Y., Lai, Y., Zhang, L., 2009. CH₄ inclusions in orogenic harzburgite: evidence for reduced slab fluids and implication for redox melting in mantle wedge. *Geochimica et Cosmochimica Acta* 73, 1737-1754.

- Spandler, C., Yaxley, G., Green, D.H., Rosenthal, A., 2007. Phase relations and melting of anhydrous K-bearing eclogite from 1200 to 1600 C and 3 to 5 GPa. *Journal of Petrology* 49, 771-795.
- Stagno, V., Frost, D.J., 2010. Carbon speciation in the asthenosphere: Experimental measurements of the redox conditions at which carbonate-bearing melts coexist with graphite or diamond in peridotite assemblages. *Earth and Planetary Science Letters* 300, 72-84.
- Stanley, B.D., Hirschmann, M.M., Withers, A.C., 2014. Solubility of COH volatiles in graphite-saturated martian basalts. *Geochimica et Cosmochimica Acta* 129, 54-76.
- Stracke, A., Salters, V.J., Sims, K.W., 2000. Assessing the presence of garnet - pyroxenite in the mantle sources of basalts through combined hafnium - neodymium - thorium isotope systematics. *Geochemistry, Geophysics, Geosystems* 1.
- Sun, S.-S., 1987. Chemical composition of Archaean komatiites: implications for early history of the earth and mantle evolution. *Journal of volcanology and geothermal research* 32, 67-82.
- Sun, S.-S., McDonough, W.F., 1989. Chemical and isotopic systematics of oceanic basalts: implications for mantle composition and processes. *Geological Society, London, Special Publications* 42, 313-345.
- Sutherland, F.L., 2011. Diversity within geodiversity, underpinning habitats in New South Wales volcanic areas, *Proceedings of the Linnean Society of New South Wales*. Linnean Society of New South Wales, p. 37.
- Sutherland, F.L., Graham, I.T., Meffre, S., Zwingmann, H., Pogson, R.E., 2012. Passive-margin prolonged volcanism, East Australian Plate: outbursts, progressions, plate controls and suggested causes. *Australian Journal of Earth Sciences* 59, 983-1005.
- Swartzendruber, L., 1984. The Fe-Ir (iron-iridium) system. *Bulletin of alloy phase diagrams* 5, 48-52.
- Takahashi, E., Shimazaki, T., Tsuzaki, Y., Yoshida, H., E., 1993. Melting study of a peridotite KLB-1 to 6.5 GPa, and the origin of basaltic magmas. *Philosophical Transactions of the Royal Society of London. Series A: Physical and Engineering Sciences* 342, 105-120.
- Tappe, S., Foley, S.F., Jenner, G.A., Heaman, L.M., Kjarsgaard, B.A., Romer, R.L., Stracke, A., Joyce, N., Hoefs, J., 2006. Genesis of ultramafic lamprophyres and carbonatites at Aillik Bay, Labrador: a consequence of incipient lithospheric thinning beneath the North Atlantic craton. *Journal of Petrology* 47, 1261-1315.
- Taura, H., Yurimoto, H., Kurita, K., Sueno, S., 1998. Pressure dependence on partition coefficients for trace elements between olivine and the coexisting melts. *Physics and Chemistry of Minerals* 25, 469-484.
- Taylor, S.R., McLennan, S., 2009. *Planetary crusts: their composition, origin and evolution*. Cambridge University Press.
- Taylor, W.R., 1985. The role of COH fluids in upper mantle processes: a theoretical, experimental and spectroscopic study. PhD thesis, University of Tasmania.
- Taylor, W.R., Green, D.H., 1988. Measurement of reduced peridotite-COH solidus and implications for redox melting of the mantle. *Nature* 332, 349-352.
- Tian, F., Toon, O.B., Pavlov, A.A., De Sterck, H., 2005. A hydrogen-rich early Earth atmosphere. *Science* 308, 1014-1017.
- Tiepolo, M., Oberti, R., Zanetti, A., Vannucci, R., Foley, S.F., 2007. Trace-element partitioning between amphibole and silicate melt. *Reviews in mineralogy and geochemistry* 67, 417-452.
- Till, C.B., Grove, T.L., Withers, A.C., 2012. The beginnings of hydrous mantle wedge melting. *Contributions to Mineralogy and Petrology* 163, 669-688.
- Toplis, M., 2005. The thermodynamics of iron and magnesium partitioning between olivine and liquid: criteria for assessing and predicting equilibrium in natural and experimental systems. *Contributions to Mineralogy and Petrology* 149, 22-39.
- Trail, D., Watson, E.B., Tailby, N.D., 2011. The oxidation state of Hadean magmas and implications for early Earth's atmosphere. *Nature* 480, 79.

- Ulmer, P., 1989. The dependence of the Fe^{2+} - Mg^{2+} cation-partitioning between olivine and basaltic liquid on pressure, temperature and composition. *Contributions to Mineralogy and Petrology* 101, 261-273.
- Veter, M., Foley, S.F., Mertz-Kraus, R., Groschopf, N., 2017. Trace elements in olivine of ultramafic lamprophyres controlled by phlogopite-rich mineral assemblages in the mantle source. *Lithos* 292, 81-95.
- Vickery, N., Dawson, M., Sivell, W., Malloch, K., Dunlap, W., 2007. Cainozoic igneous rocks in the Bingara to Inverell area, northeastern New South Wales. *Quarterly Notes Geological Survey of New South Wales* 123, 1-31.
- Wadhwa, M., 2008. Redox conditions on small bodies, the Moon and Mars. *Reviews in Mineralogy and Geochemistry* 68, 493-510.
- Wagner, T., Grove, T., 1997. Experimental constraints on the origin of lunar high-Ti ultramafic glasses. *Geochimica et Cosmochimica Acta* 61, 1315-1327.
- Wallace, M.E., Green, D.H., 1988. An experimental determination of primary carbonatite magma composition. *Nature* 335, 343.
- Waltenburg, K., 2006. Geochronology of weathered basaltic flows at Carnavon Gorge. Honours thesis, University of Queensland.
- Walter, M.J., Sisson, T.W., Presnall, D.C., 1995. A mass proportion method for calculating melting reactions and application to melting of model upper mantle lherzolite. *Earth and Planetary Science Letters* 135, 77-90.
- Wänke, H., Dreibus, G., 1988. Chemical composition and accretion history of terrestrial planets. *Philosophical Transactions of the Royal Society of London. Series A: Mathematical, Physical and Engineering Sciences* 325, 545-557.
- Wass, S.Y., Rogers, N.W., 1980. Mantle metasomatism—precursor to continental alkaline volcanism. *Geochimica et Cosmochimica Acta* 44, 1811-1823.
- Weaver, B.L.J., 1991. The origin of ocean island basalt end-member compositions: trace element and isotopic constraints. *Earth and Planetary Science Letters* 104, 381-397.
- Weir, C., Lippincott, E., Van Valkenburg, A., Bunting, E., 1959. Infrared studies in the 1-to 15-micron region to 30,000 atmospheres. *Journal of Research of the National Bureau of Standards. Section A, Physics*
- Wellman, P., Cundari, A., McDougall, I., 1970. Potassium-argon ages for leucite-bearing rocks from New South Wales, Australia, *Journal and Proceedings of the Royal Society of New South Wales*, pp. 103-107.
- Wellman, P., McDougall, I., 1974. Cainozoic igneous activity in eastern Australia. *Tectonophysics* 23, 49-65.
- Wetzel, D.T., Rutherford, M.J., Jacobsen, S.D., Hauri, E.H., Saal, A.E., 2013. Degassing of reduced carbon from planetary basalts. *Proceedings of the National Academy of Sciences* 110, 8010-8013.
- Wijbrans, C.H., Rohrbach, A., Klemme, S., 2016. An experimental investigation of the stability of majoritic garnet in the Earth's mantle and an improved majorite geobarometer. *Contributions to Mineralogy and Petrology* 171, 50.
- Williams, H.M., Wood, B.J., Wade, J., Frost, D.J., Tuff, J., 2012. Isotopic evidence for internal oxidation of the Earth's mantle during accretion. *Earth and Planetary Science Letters* 321, 54-63.
- Wilson, L., Head III, J.W., 1981. Ascent and eruption of basaltic magma on the Earth and Moon. *Journal of Geophysical Research: Solid Earth* 86, 2971-3001.
- Woodland, A., O'Neill, H.S.C., 1997. Thermodynamic data for Fe-bearing phases obtained using noble metal alloys as redox sensors. *Geochimica et Cosmochimica Acta* 61, 4359-4366.
- Wyllie, P.J., 1978. Mantle fluid compositions buffered in peridotite- CO_2 - H_2O by carbonates, amphibole, and phlogopite. *The Journal of Geology* 86, 687-713.
- Wyllie, P.J., 1980. The origin of kimberlite. *Journal of Geophysical Research: Solid Earth* 85, 6902-6910.

- Wyllie, P.J., Huang, W.J., 1976. High CO₂ solubilities in mantle magmas. *Geology* 4, 21-24.
- Yang, X., Gaillard, F., Scaillet, B., 2014. A relatively reduced Hadean continental crust and implications for the early atmosphere and crustal rheology. *Earth and Planetary Science Letters* 393, 210-219.
- Yang, Z.-F., Li, J., Liang, W.-F., Luo, Z.-H., 2016. On the chemical markers of pyroxenite contributions in continental basalts in Eastern China: implications for source lithology and the origin of basalts. *Earth-science reviews* 157, 18-31.
- Yang, Z.-F., Zhou, J.-H., 2013. Can we identify source lithology of basalt? *Scientific Reports* 3, 1856.
- Yasuda, A., Fujii, T., Kurita, K., 1994. Melting phase relations of an anhydrous mid - ocean ridge basalt from 3 to 20 GPa: Implications for the behavior of subducted oceanic crust in the mantle. *Journal of Geophysical Research: Solid Earth* 99, 9401-9414.
- Yaxley, G.M., Crawford, A.J., Green, D.H., 1991. Evidence for carbonatite metasomatism in spinel peridotite xenoliths from western Victoria, Australia. *Earth and Planetary Science Letters* 107, 305-317.
- Yaxley, G.M., Green, D.H., 1998. Reactions between eclogite and peridotite: mantle refertilisation by subduction of oceanic crust. *Schweiz. Mineral. Petrogr. Mitt* 78, 243-255.
- Yaxley, G.M., Green, D.H., Kamenetsky, V., 1998. Carbonatite metasomatism in the southeastern Australian lithosphere. *Journal of Petrology* 39, 1917-1930.
- Yoder Jr, H., Tilley, C.E.J., 1962. Origin of basalt magmas: an experimental study of natural and synthetic rock systems. *Journal of Petrology* 3, 342-532.
- Zeng, G., Chen, L.-H., Xu, X.-S., Jiang, S.-Y., Hofmann, A.W., 2010. Carbonated mantle sources for Cenozoic intra-plate alkaline basalts in Shandong, North China. *Chemical Geology* 273, 35-45.
- Zhang, J., Herzberg, C., 1994. Melting experiments on anhydrous peridotite KLB-1 from 5.0 to 22.5 GPa. *Journal of Geophysical Research: Solid Earth* 99, 17729-17742.
- Zhang, M., O'Reilly, S.Y., 1997. Multiple sources for basaltic rocks from Dubbo, eastern Australia: geochemical evidence for plume—lithospheric mantle interaction. *Chemical Geology* 136, 33-54.
- Zhang, M., Stephenson, P., O'reilly, S.Y., McCulloch, M.T., Norman, M., 2001. Petrogenesis and geodynamic implications of late Cenozoic basalts in North Queensland, Australia: trace-element and Sr–Nd–Pb isotope evidence. *Journal of Petrology* 42, 685-719.
- Zolotov, M.Y., 2011. On the chemistry of mantle and magmatic volatiles on Mercury. *Icarus* 212, 24-41.
- Zolotov, M.Y., Sprague, A.L., Hauck, S.A., Nittler, L.R., Solomon, S.C., Weider, S.Z., 2013. The redox state, FeO content, and origin of sulfur - rich magmas on Mercury. *Journal of Geophysical Research: Planets* 118, 138-146.
- Zuber, M.T., 2001. The crust and mantle of Mars. *Nature* 412, 220-227.

Versicherungen und Erklärungen (§ 6 Abs. 2, Nr. 4, 5, und 6)

Name der Doktorandin / des Doktoranden: Zairong Liu

Hiermit versichere ich, dass ich bin bisher noch keinen Promotionsversuch unternommen habe.

Münster, 06.03,2020, Zairong Liu

Hiermit versichere ich, dass ich die vorgelegte Dissertation selbst und ohne unerlaubte Hilfe angefertigt, alle in Anspruch genommenen Quellen und Hilfsmittel in der Dissertation angegeben habe und die Dissertation nicht bereits anderweitig als Prüfungsarbeit vorgelegen hat.

Münster, 06.03,2020, Zairong Liu

Hiermit erkläre ich, dass ich nicht wegen eines Verbrechens, zu dem ich meine wissenschaftliche Qualifikation missbraucht habe, rechtskräftig verurteilt worden bin.

Münster, 06.03,2020, Zairong Liu

Curriculum vitae

Name: Zairong Liu

Address: Gescherweg 62, 48161, Münster, Germany

Born: 04th July 1989, in Rizhao, China

Nationality: Chinese

Education

10.2014 – present: Ph.D. student in Petrology

Institut für Mineralogie, University of Münster, Germany

Supervisor: Prof. Dr. Stephan Klemme

07. 2017 – 08. 2019: Cotutelle PhD. in geochemistry

Supervisor: Prof. Dr. Stephen Foley

Macquarie University, Australia

07. 2011 – 06. 2014: M.Sc. in computational simulation geochemistry

Institute of Geology and Geophysics, Chinese Academy of Sciences

Beijing, China

09. 2007 – 06. 2011: B.Sc. in Hydrology and Water Resources Engineering

Shandong University of Science and Technology

Qingdao, China

Publications

Liu Z, Rohrbach A, Klemme S. (2016). The effect of C-O-H fluid on partial melting of eclogite and lherzolite under reducing conditions. In EMPG XV, Zürich , p. 42.

Zhang Z, Liu Z. (2015). High pressure equation of state for molten CaCO₃ from first principles simulations. Chinese Journal of Geochemistry, 34(1), 13-20. doi: 10.1007/s11631-015-0036-8.

Liu Z, Zhang Z. (2015). Densities and compressibilities of calcium-carbonate melts under the mantle condition. Journal of University of Chinese Academy of Sciences, 32(3), 356-362. doi: 10.7523/j.issn.2095-6134.2015.03.010.

Signature, Münster